PHOSPHORIC ACID FUEL CELL
STACK AND SYSTEM DEVELOPMENT

FINAL TECHNICAL REPORT

OCTOBER 1981

CONTRACT NO. DE-AC01-78ET15366

by:

ENGELHARD

Research and Development Department
Engelhard Industries Division
Engelhard Corporation
Menlo Park, Edison, New Jersey 08818

Authors:

J. J. Early
G. K. Johnson
A. Kaufman
G. A. Smith
R. M. Yarrington

ACKNOWLEDGMENTS

The authors gratefully acknowledge the substantial contributions of B. S. Beshty, W. Buchanan, A. K. P. Chu, C. J. Dettling, V. Elkin, H. Feigenbaum, E. Fekete, J. Miller, A. Stawsky, P. L. Terry, and J. A. Whelan in performing the tasks of this contract; the subcontract contributions of D. Bloomfield of Physical Sciences Inc. and R. Froberg of Pfizer Inc.; as well as the assistance of M. Teja in the preparation of this report. The authors wish to thank Technical Manager Robert B. King, NASA/Lewis Research Center Fuel Cell Project Office, for his valuable guidance and support throughout the course of the program.

SUMMARY

The present report summarizes the progress made under the DOE/NASA Phase II Contract over a period of 28 months. Task I of the Contract was devoted to the development of phosphoric acid fuel cell stack components, Task II to fuel selection and processing, Task III to integrated system design and development, and Task IV to large stack design and development. Task V, directed toward electrocatalyst improvement, was wholly sponsored by Engelhard as a cost contribution. The following paragraphs present highlights of work accomplished under these tasks.

A large number of carbon materials were screened for conductivity, strength, gas permeability and corrosion resistance to hot phosphoric acid. As a result, suitable materials have been chosen for service as bipolar plate components, electrode supports, acid-transport layers and sealants. Two versions of ABA bipolar plates were developed -- one with porous, non-grooved reticulated vitreous carbon A-elements and non-woven fabric precursor B-elements; the other a plate consisting of unitized needled-felt A-elements. The latter is potentially of lower cost.

An improved laminated matrix configuration based on silicon carbide has been formulated which exhibits far lower IR-drop and greater high-temperature stability than the membrane structure used previously. Substantial success has been realized in the maintenance of acid inventories during stack operation.

Advanced cathode catalyst formulations have shown improved corrosion resistance and greater platinum surface-area stability. Anode catalyst formulations exhibited signs of improved tolerance to carbon monoxide in the fuel.

In addition to the many single-cell and 3-cell stack tests that were utilized to develop the above materials and components, five 10-cell and 12-cell stacks were built and tested; the longest duration of testing was 3200 hours. Intercell cooling plates were utilized during this stack sequence, with a recent improvement being the incorporation of an effective corrosion-protection layer.

Stack hardware was designed and built at the 5kW power level, including coolant manifolding, reactant manifolding and stack compressive loading. A 5kW stack was constructed and successfully tested for over 860 hours with variable-load operation.

After thermodynamic and cost study, methanol was selected as the fuel for this program. Several low-temperature water-gas shift catalysts were evaluated for methanol/steam reforming; and one catalyst, U.C.I. T2107RS, was selected for use during the balance of the contract.

Development of the fuel processing subsystem included the design and construction of a 5kW reformer and an anode vent gas burner, as well as various ancillary components. The design of the 5kW reformer was based on a mathematical model and full-size experimental test unit results. Subsequent test results for the 5kW reformer were in good agreement with the model. Diagnostic tests were first completed in the non-reactive mode using inerts in the catalyst tubes. The initial run with catalyst T2107RS at full-design load gave complete methanol conversion at design space-velocity and temperature.

Analysis of various integrated system configurations has been facilitated through the use of a steady-state integrated system computer program. This was prepared under subcontract by Physical Science, Incorporated (PSI) and transferred to Engelhard's Computer Services Section. System electrical and heat utilization efficiencies and stack size were determined as a function of various

parameters using this program. Also, the energy distribution has been compared for various configurations to study suitability for on-site integrated energy system applications. A power conditioning subsystem (DC to AC Inverter) has been acquired for the 5kW integrated system. The required control functions have been defined and a complete description of the sequential (start-up and shutdown) and process (steady-state) control system has been prepared. The micropressor-based control system will be implemented in the 5kW integrated system early in the Phase III contract.

In anticipation of scale-up from 5kW systems in Phase II to 50kW systems in Phase III, advance component preparation has been accomplished during the present contract. Electrode/matrix combinations in full-scale size (13 x 22 inches) have been successfully fabricated and tested.

TABLE OF CONTENTS

LIST OF FIGURES

LIST OF FIGURES

LIST OF FIGURES

LIST OF FIGURES

LIST OF FIGURES

LIST OF TABLES

TASK I

PHOSPHORIC ACID STACK COMPONENT DEVELOPMENT

Task I of the Phase II program was devoted to upgrading of the phosphoric acid stack components. The progress is reported in the following sections, whereby the individual component efforts are described separately. The final section under Task I presents the test results for multi-cell stacks in which upgraded components were utilized. Highlights of achievements under Task I are as follows:

- Performance goals demonstrated in single-cells, approached in stacks
- Development of electrocatalysts with improved surface-area stability
- Successful implementation of high-temperature, laminated electrolyte-matrix
- Acid replenishment methods used effectively in stacks
- Successful development of multi-element bipolar plate
- 60-cell 5kW stack successfully tested over 36-day period

SECTION I

ELECTROCATALYSTS

The formulation and preparation of electrocatalysts for the program were conducted in Task V under Engelhard sponsorship. The results of these electrocatalyst efforts are reported below.

A. SUPPORTS

The rates of corrosion of carbons used as catalyst supports were studied as a function of time and potential. Figure I-1 shows the rates of electrochemical corrosion of the base-line support and several supports modified for stability by heat and other treatments. These results were obtained at a constant potential of 1000 mV versus the reversible hydrogen electrode (RHE). The corrosion current for each support diminishes quite rapidly in the early minutes as the more active species are oxidized. The stabilized support materials exhibited improved corrosion resistance over that of the base-line carbon, indicating potential advantage for long-term catalyst stability. Figure I-2 indicates the effect of potential by showing the corrosion current of one of the stabilized supports at potentials of 700 mV, 850 mV and 1000 mV, respectively.

A comparison was made of rates of corrosion of the base-line support with and without Pt to determine if the presence of Pt catalyzes corrosion. Figure I-3, obtained at 1000 mV (RHE) shows that the rates are essentially the same for the two materials.

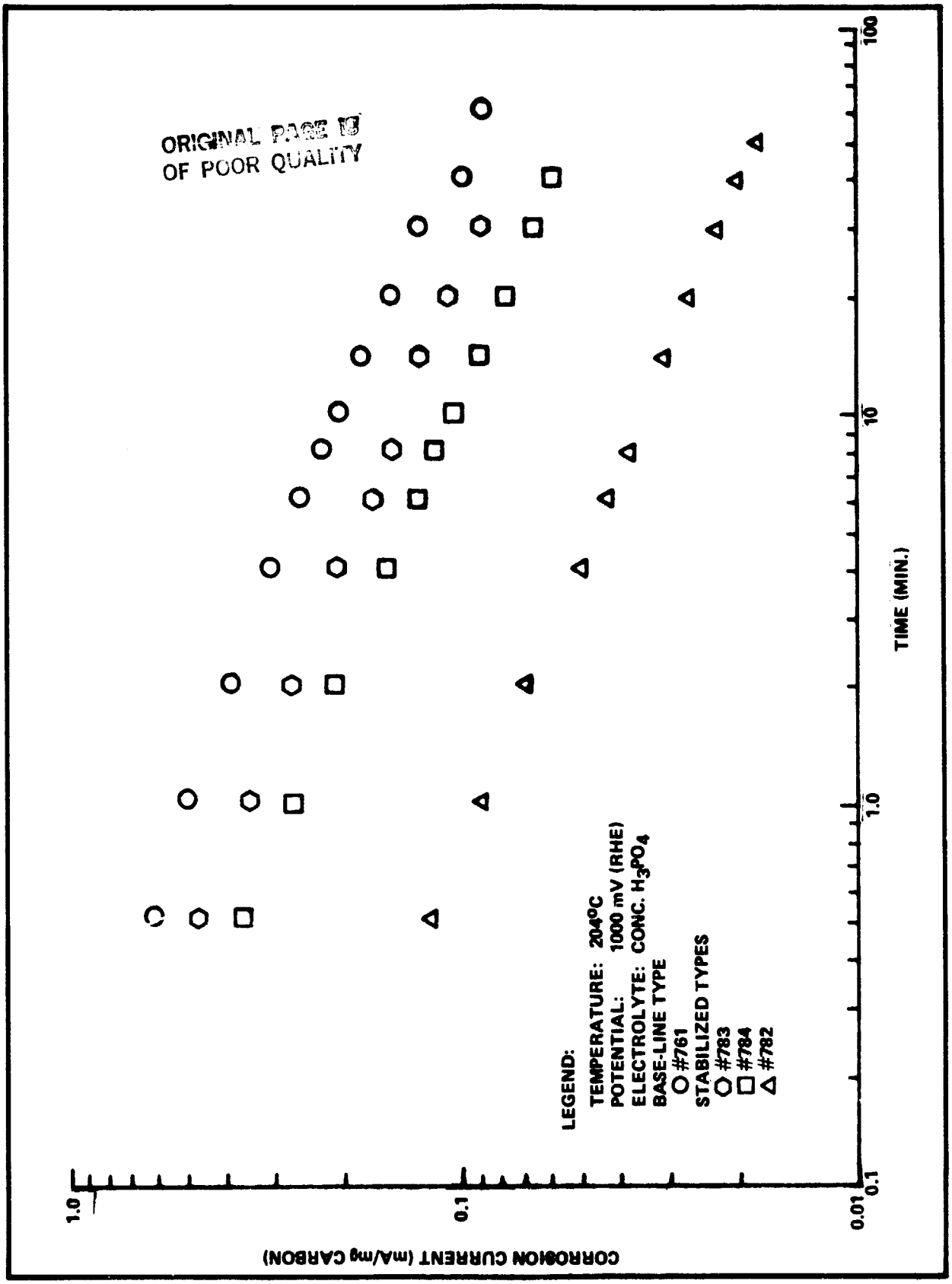

FIGURE I-1. CORROSION CURRENT OF CARBON SUPPORTS

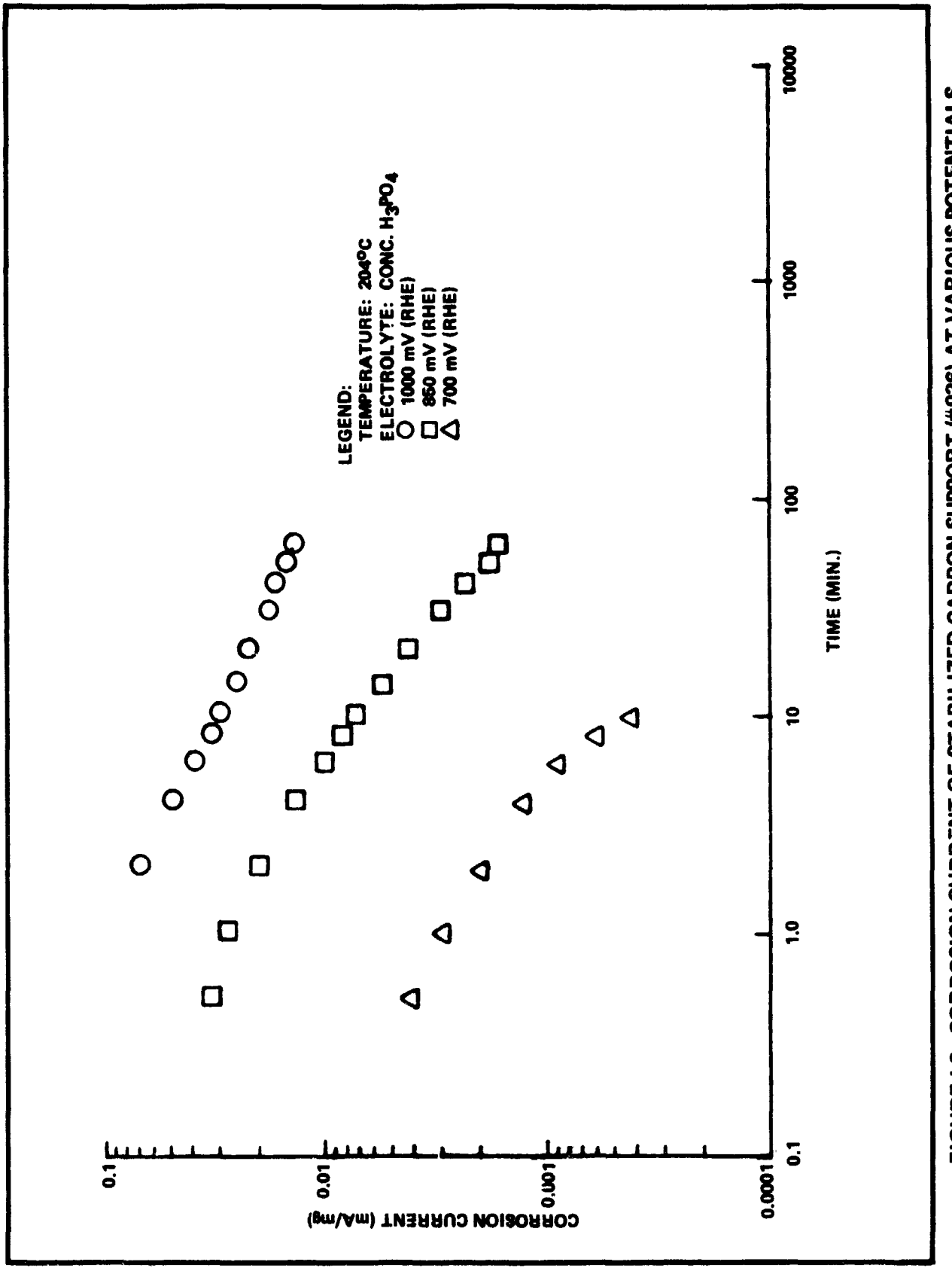

FIGURE I-2. CORROSION CURRENT OF STABILIZED CARBON SUPPORT (#926) AT VARIOUS POTENTIALS

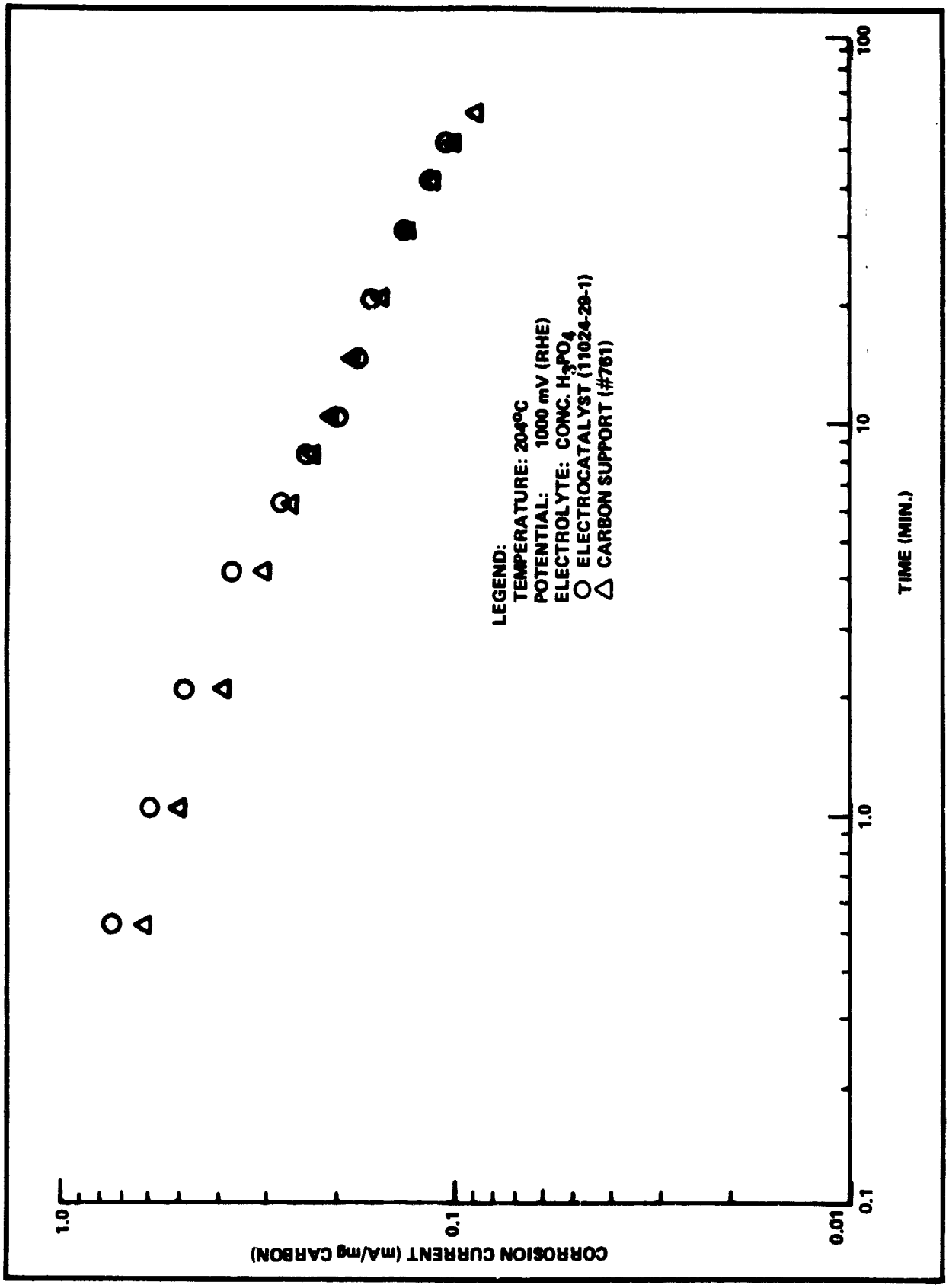

FIGURE I-3. CORROSION CURRENT OF ELECTROCATALYST AND CARBON SUPPORT

B. CATHODE CATALYST EVALUATION

A main objective of the cathode catalyst development program was to enhance platinum surface area stability. The basic technique used for determination of surface areas of fresh and aged catalysts was cyclic voltammetry. The Teflon test cell shown in Figure I-4 was constructed for use in the cyclic-voltammetric studies. The electrode holder is illustrated in Figure I-5.

A characteristic cyclic-voltammogram is shown in Figure I-6. This figure illustrates the current peaks corresponding to the Faradaic processes occurring during sweeps between the hydrogen potential and the oxygen potential. The area of the hydrogen deposition peaks, less the area due to double layer charging, was used to compute the active platinum area. A platinum black catalyst was used in this example to accentuate the current peaks.

Aging tests were conducted by exposing electrode samples to phosphoric acid in potentiostatic aging stations of the type shown in Figure I-7. Samples were withdrawn periodically, and the platinum surface area loss was monitored by cyclic-voltammetric analysis. Aging tests were carried out at a potential of 700 mV (RHE) to simulate cathode conditions in an operating fuel cell.

Early in the program platinum on carbon catalysts having Pt concentrations in the nominal 10-30% range were studied. The 30% Pt on carbon catalysts generally had specific surface areas in the 70-100 m^2/g Pt range, as compared to 100-150 m^2/g Pt for 10% Pt on carbon catalysts. Figure I-8 illustrates the tendency for rapid sintering (especially at higher temperatures) by comparing cyclic-voltammograms of a 30% Pt on carbon catalyst before and after a 48 hour potentiostatic aging cycle. Figure I-9 indicates that the relative sintering rates for 30% Pt on carbon and 10% Pt on carbon catalysts are similar, although the initial surface area of the 10% Pt catalysts is typically somewhat higher.

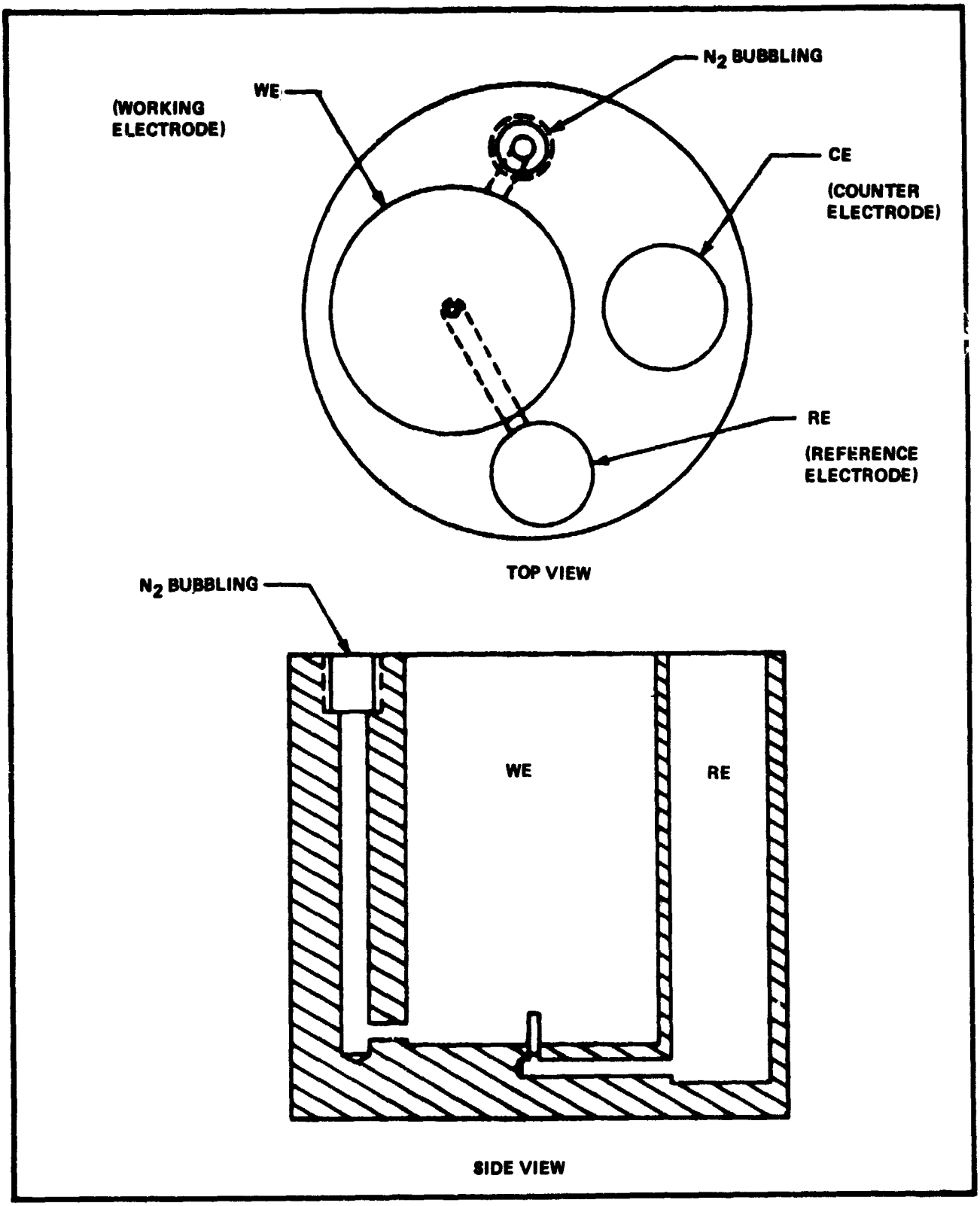

FIGURE I-4. TEFLON TEST CELL

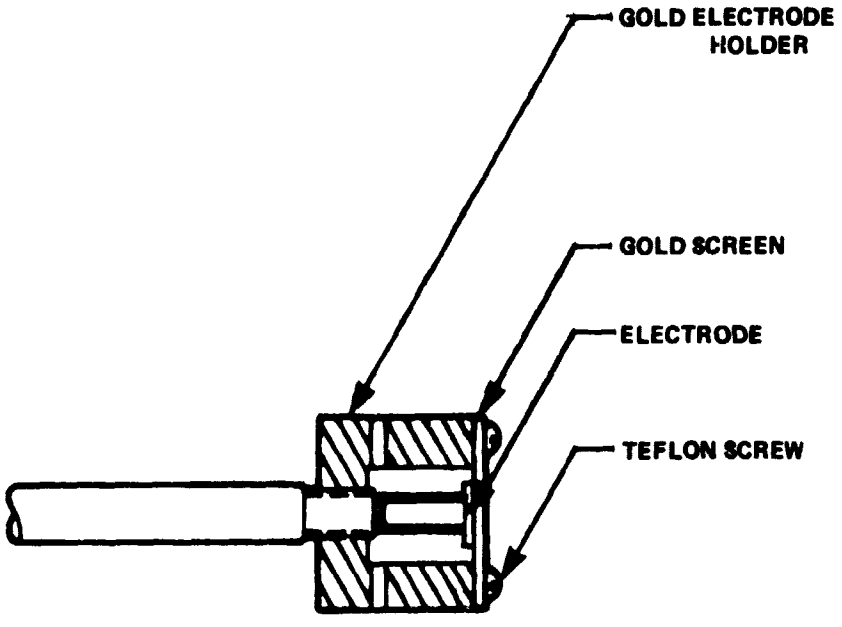

FIGURE I-5. ELECTRODE HOLDER

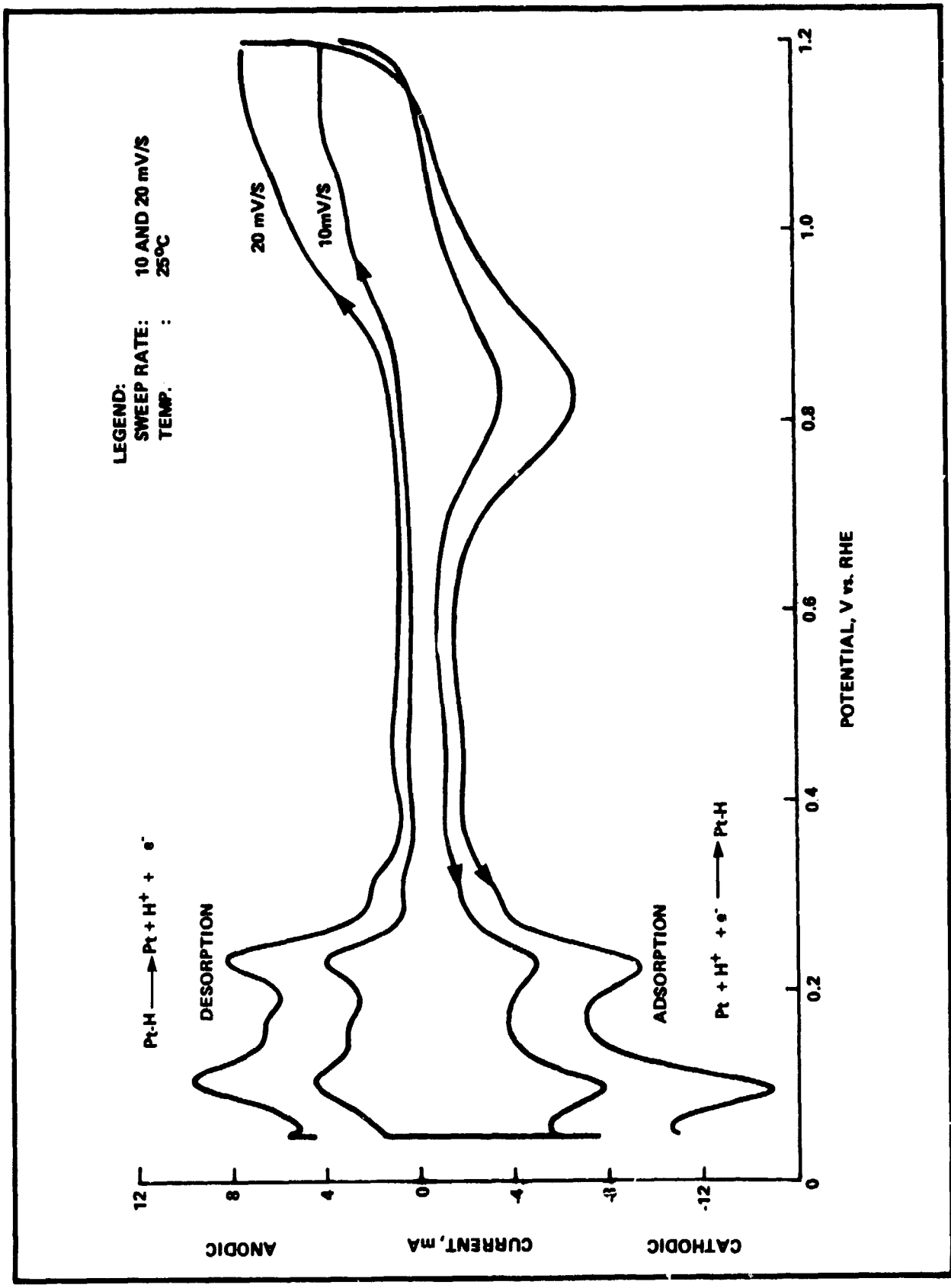

FIGURE I-6. VOLTAMMOGRAM FOR Pt BLACK ELECTROCATALYST IN 25 W/O H_3PO_4

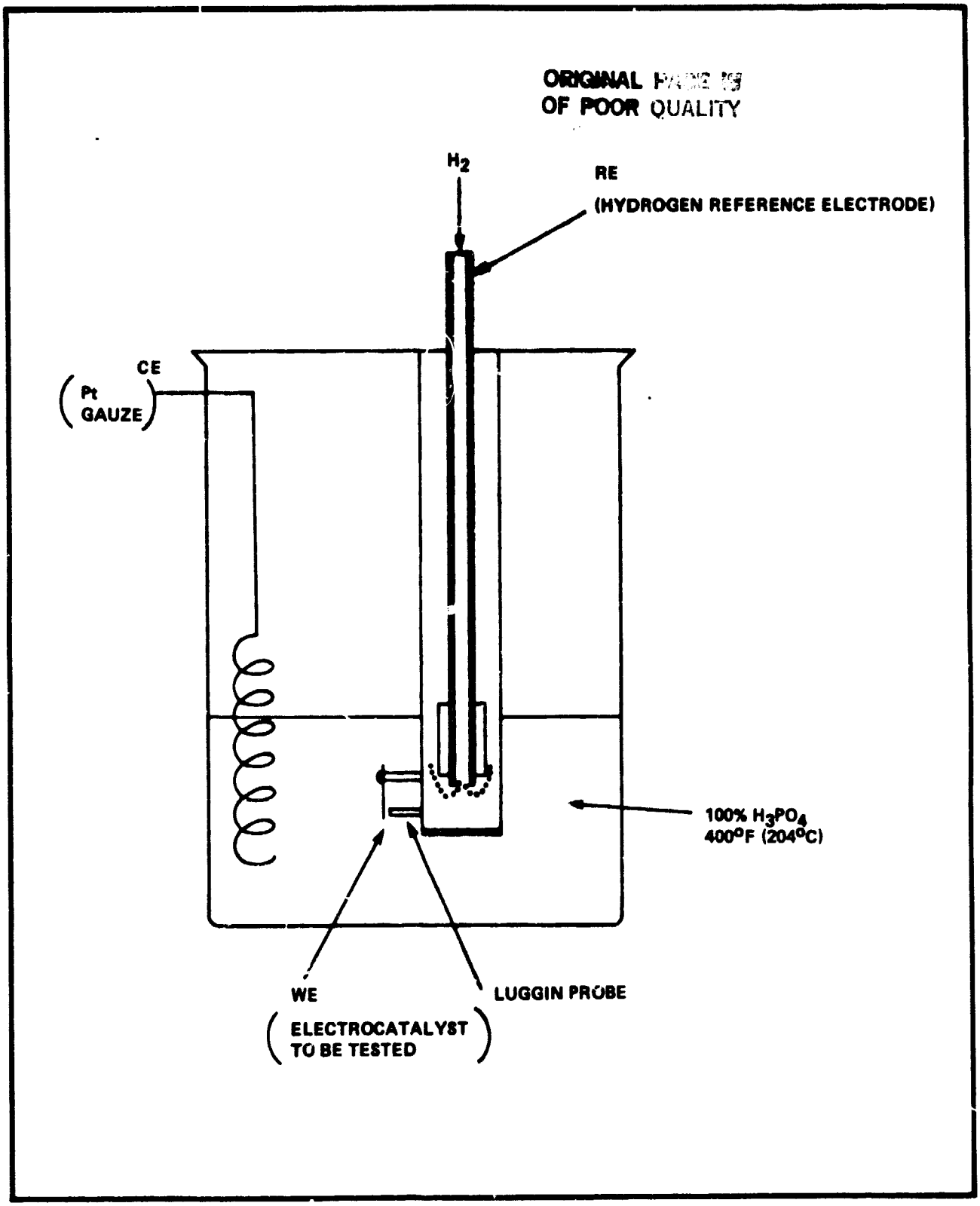

FIGURE I-7. POTENTIOSTATIC AGING TEST CELL

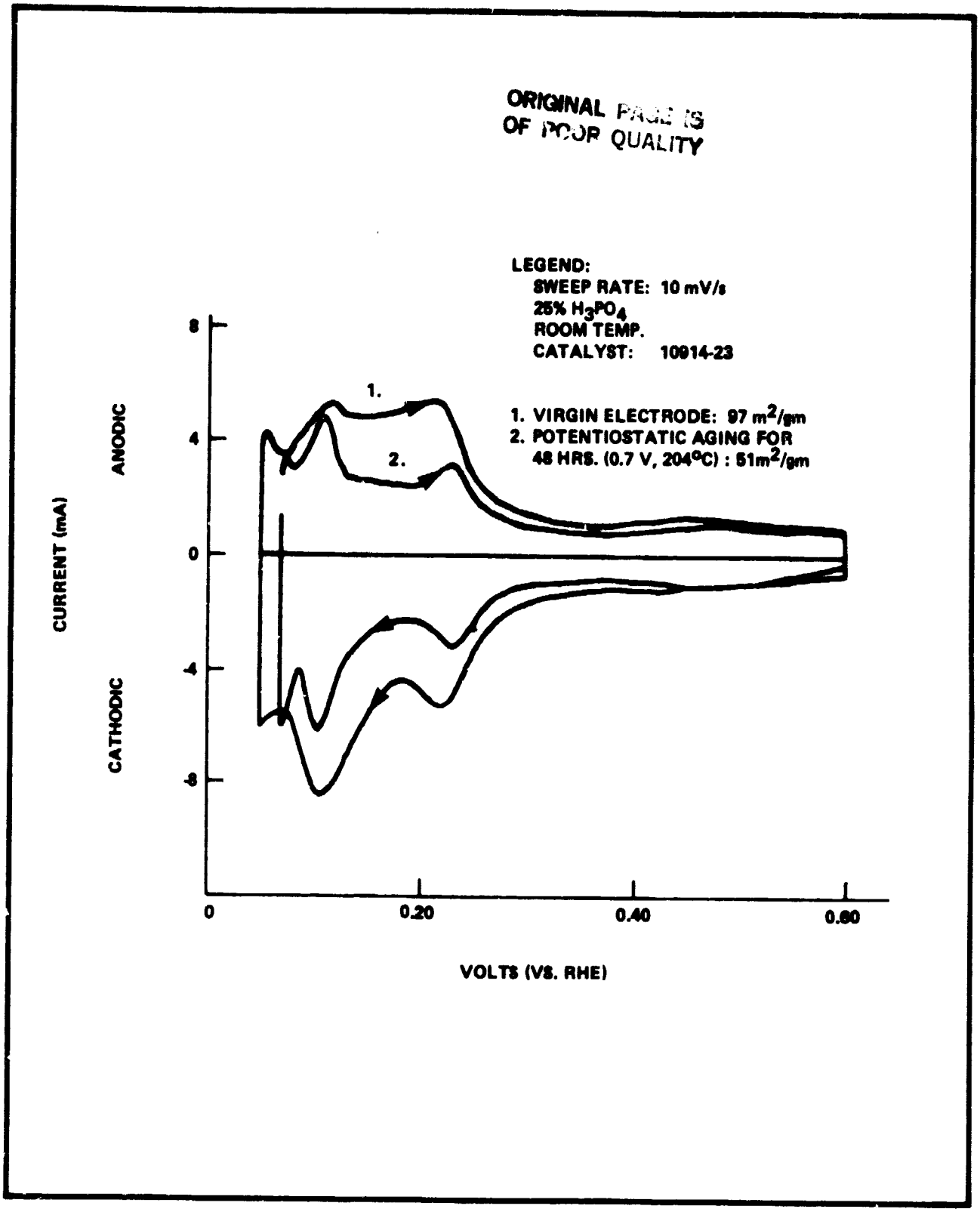

FIGURE I-8. CYCLIC-VOLTAMMOGRAM OF 30% Pt ON CARBON CATHODE

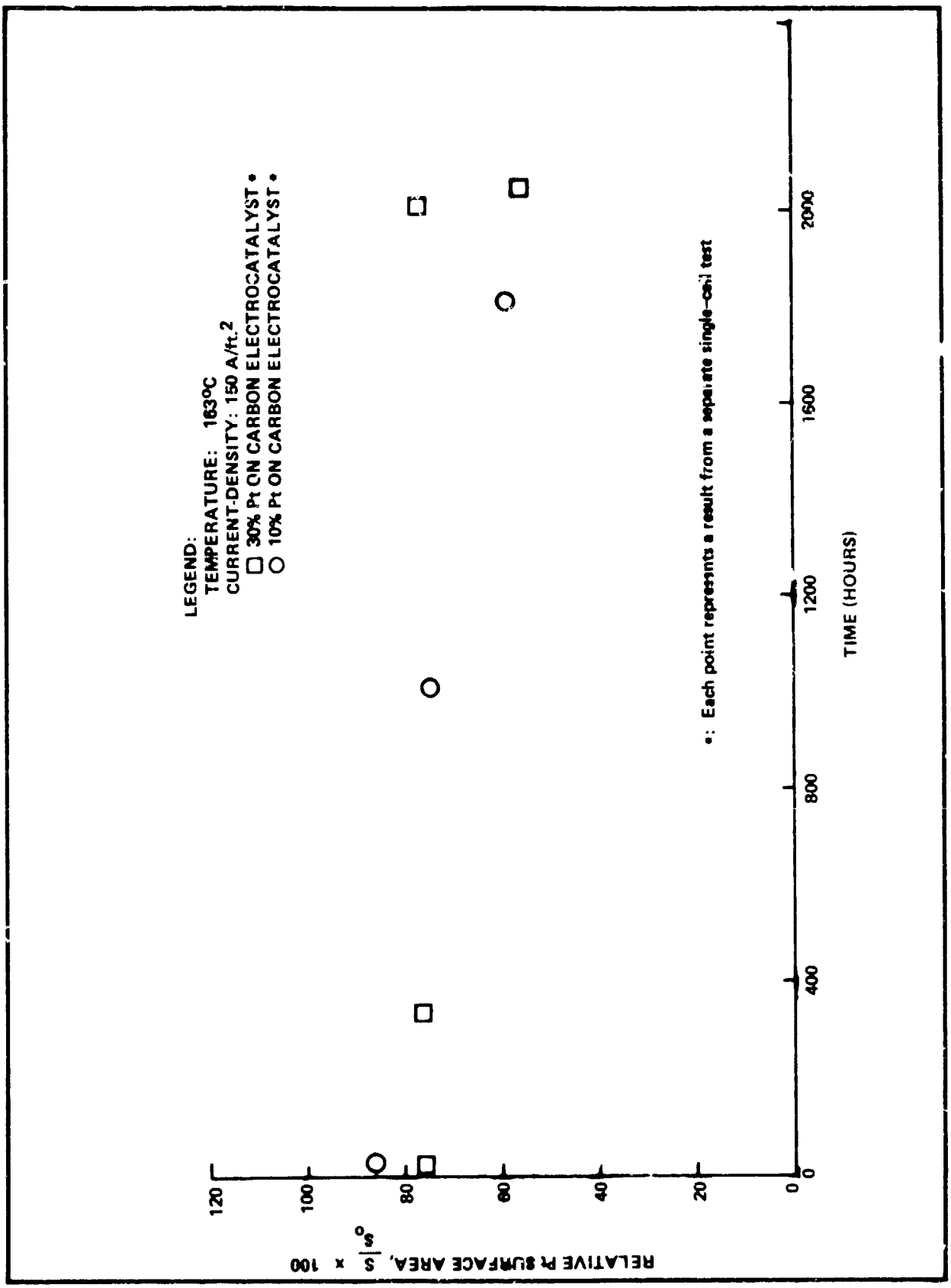

FIGURE I-9. PLATINUM SURFACE-AREA LOSS UNDER SINGLE-CELL AGING CONDITIONS

The effect of temperature on sintering rate during the early hours of test is illustrated in Figure I-10. The data of Figure I-11, obtained using electodes fabricated from the same 10% Pt on carbon base-line catalyst, indicate that the disparity in sintering rates between 163°C and 204°C dampens out considerably by the 1000-hour point; however, an appreciably higher surface area is maintained at the lower temperature.

Another electrode fabricated from this base-line catalyst was tested as a cathode in a 3-inch x 3-inch single cell for 1800 hours at 163°C. It was subsequently analyzed for platinum surface area by cyclic-voltammetry and found to have a specific surface area of 85 m^2/g Pt, as compared to 144 m^2/g Pt for the fresh catalyst. This cathode was also analyzed by transmission electron microscopy to observe the degree of platinum crystallite growth. Sections of the fresh and aged catalyst are shown in Figures I-12 and I-13, respectively.

Catalyst development efforts led to a cathode formulation of the stabilized-Pt/stabilized-support type that improved platinum surface area stability, while providing performance levels equivalent to or greater than those of base-line catalysts. Figure I-14 shows the platinum surface area as a function of time for a base-line and a developmental catalyst of this type at 204°C. The developmental catalyst maintained a specific surface area of about 70 m^2/g Pt through 2000 hours of testing, whereas the base-line catalyst lost surface area rapidly to approach 40 m^2/g Pt within a few hundred hours.

Figure I-15 shows the 3-inch x 3-inch single-cell performance for a cathode catalyst of the stabilized-Pt/stabilized-support type. This figure illustrates the respectable performance capabilities of this catalyst, despite the decline during the 24-36 day period; this decline is attributed to acid deficiency due to the absence of acid-management procedures in single cells.

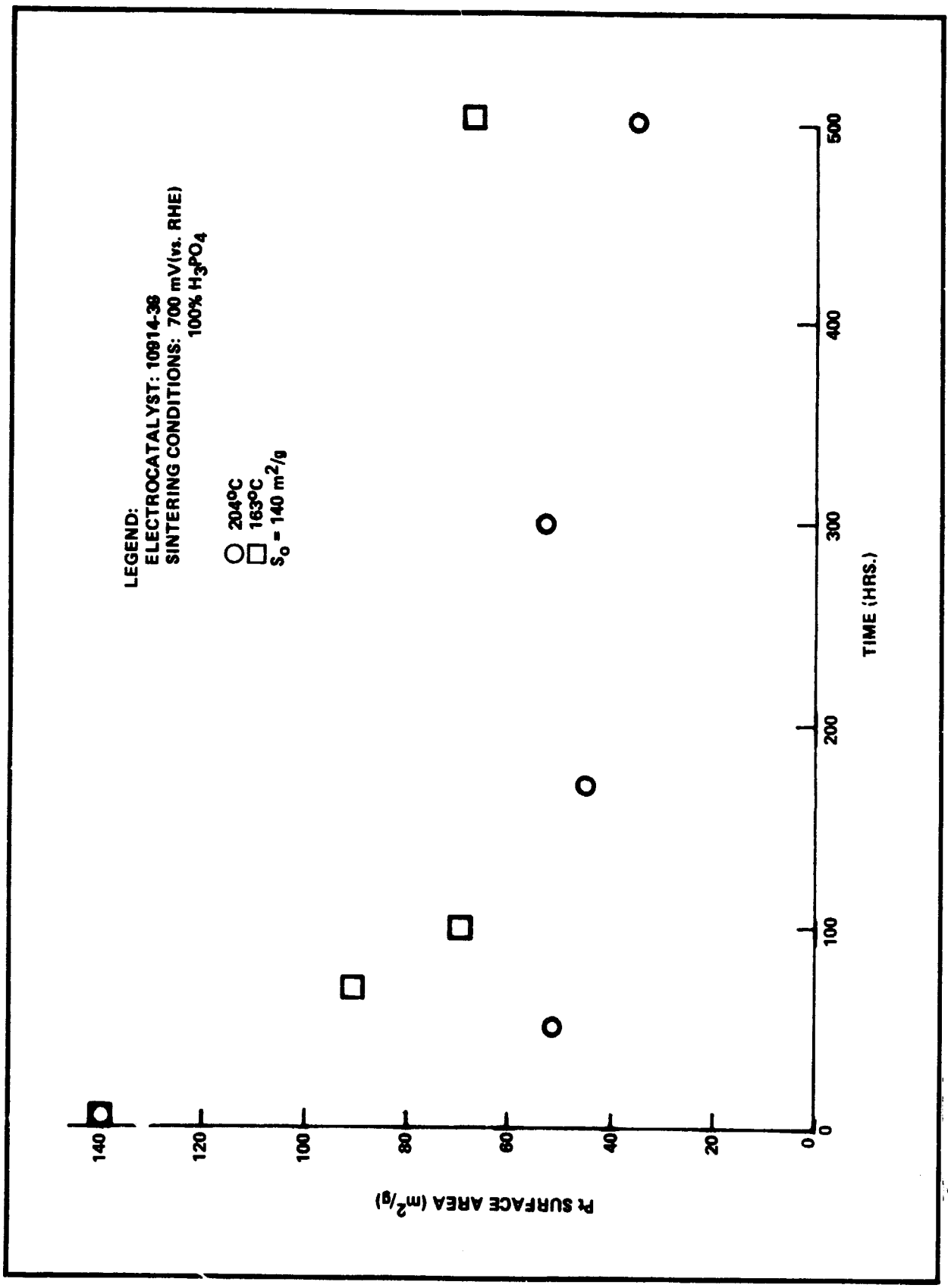

FIGURE I-10. EFFECT OF TIME ON Pt SINTERING, 10% Pt ON CARBON BASE-LINE ELECTROCATALYSTS

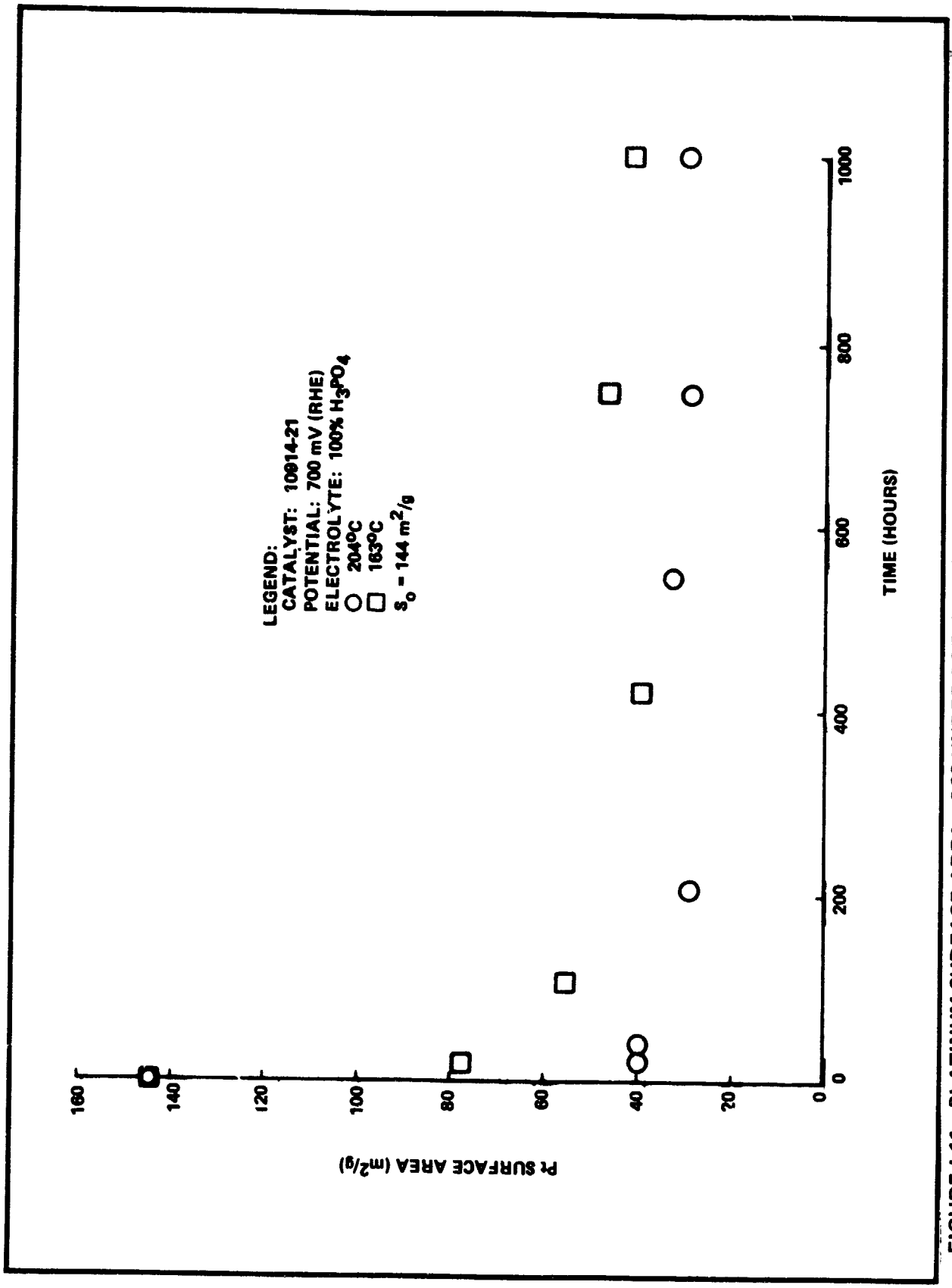

FIGURE I-11. PLATINUM SURFACE-AREA LOSS UNDER POTENTIOSTATIC AGING CONDITIONS, 10% Pt ON CARBON BASE-LINE ELECTROCATALYSTS

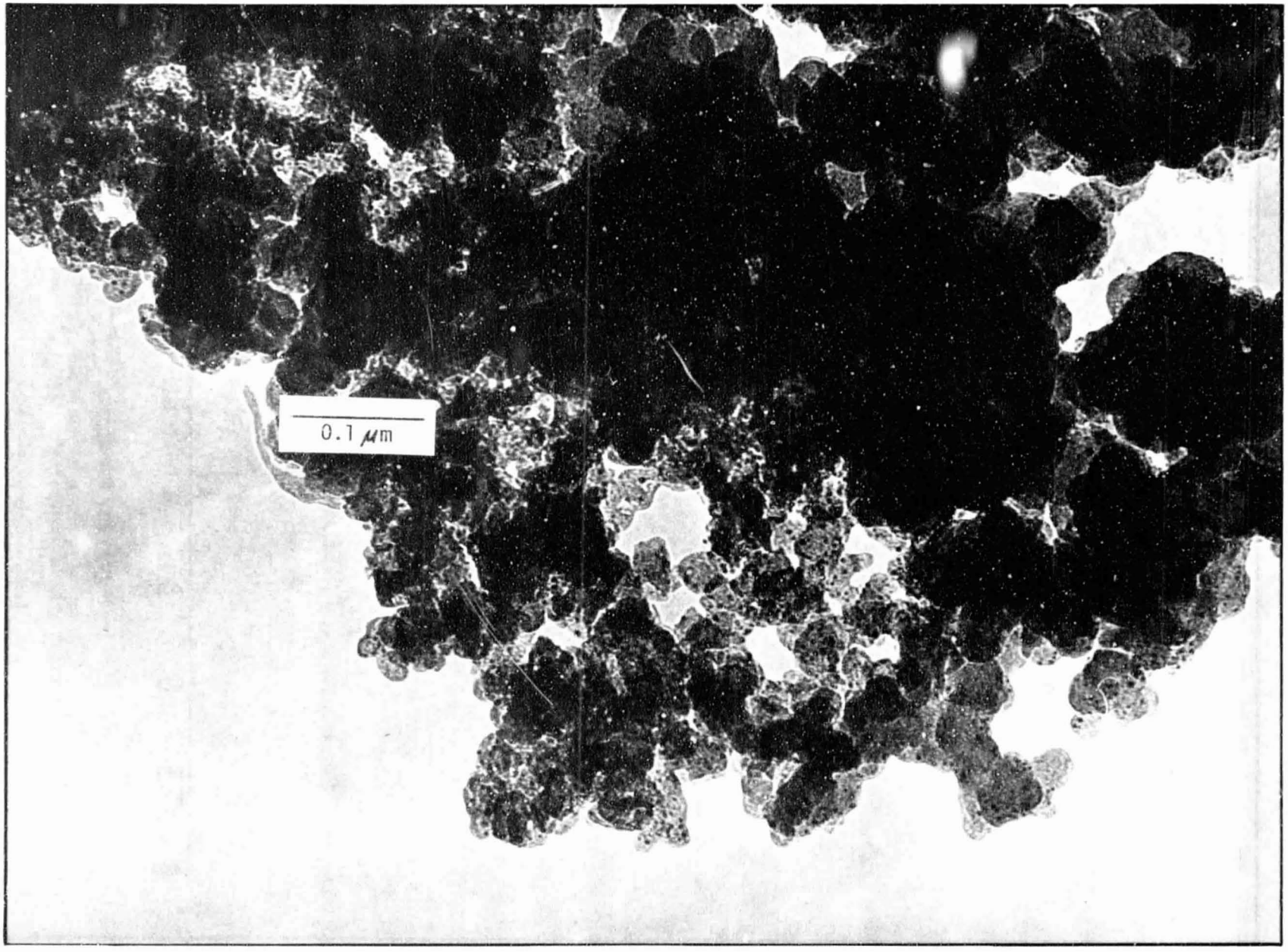

FIGURE 1-12. TRANSMISSION ELECTRON MICROGRAPH OF FRESH 10% Pt ON CARBON CATALYST (X 246,000)

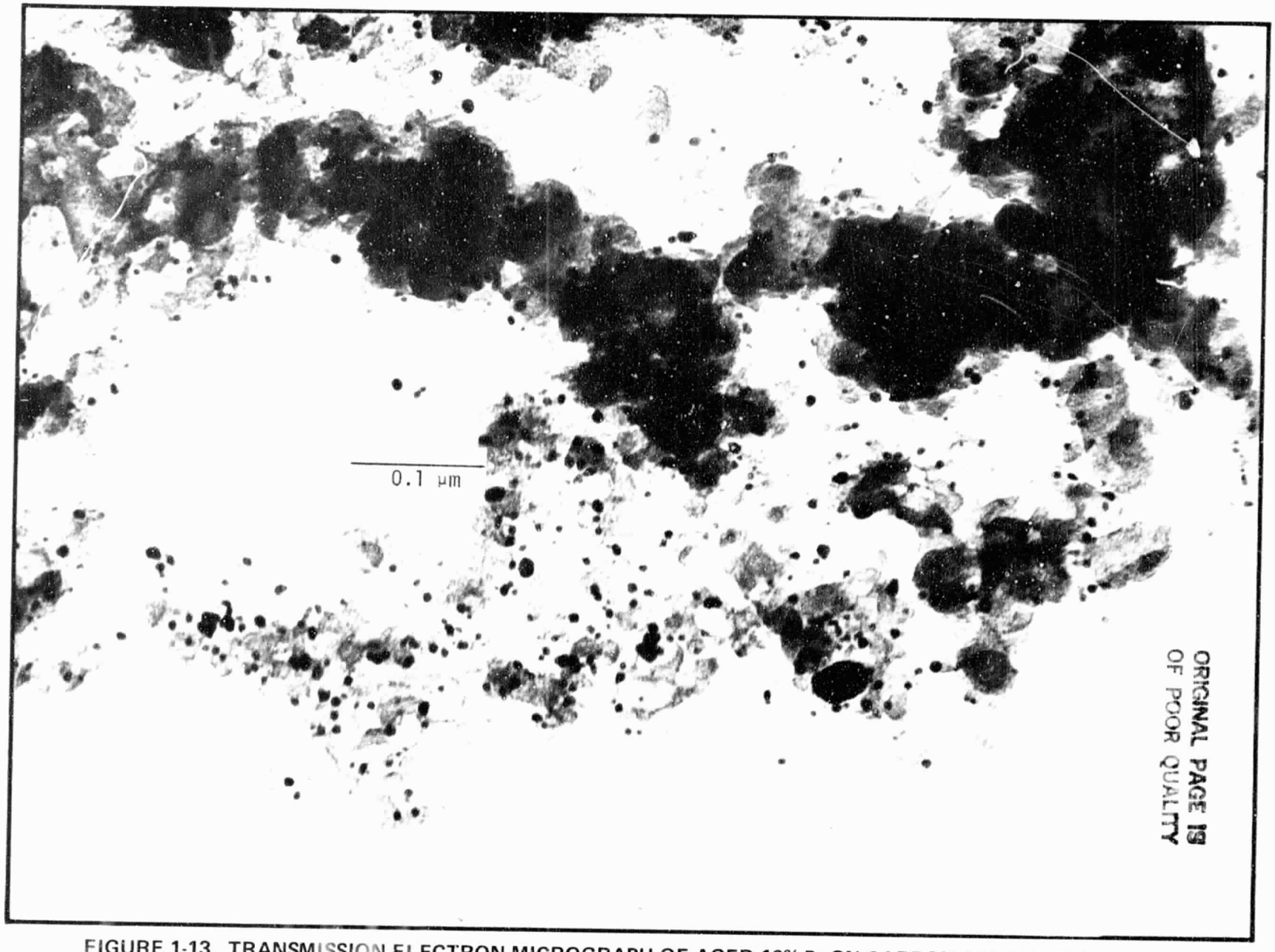

FIGURE 1-13. TRANSMISSION ELECTRON MICROGRAPH OF AGED 10% Pt ON CARBON CATALYST (X 246,000)

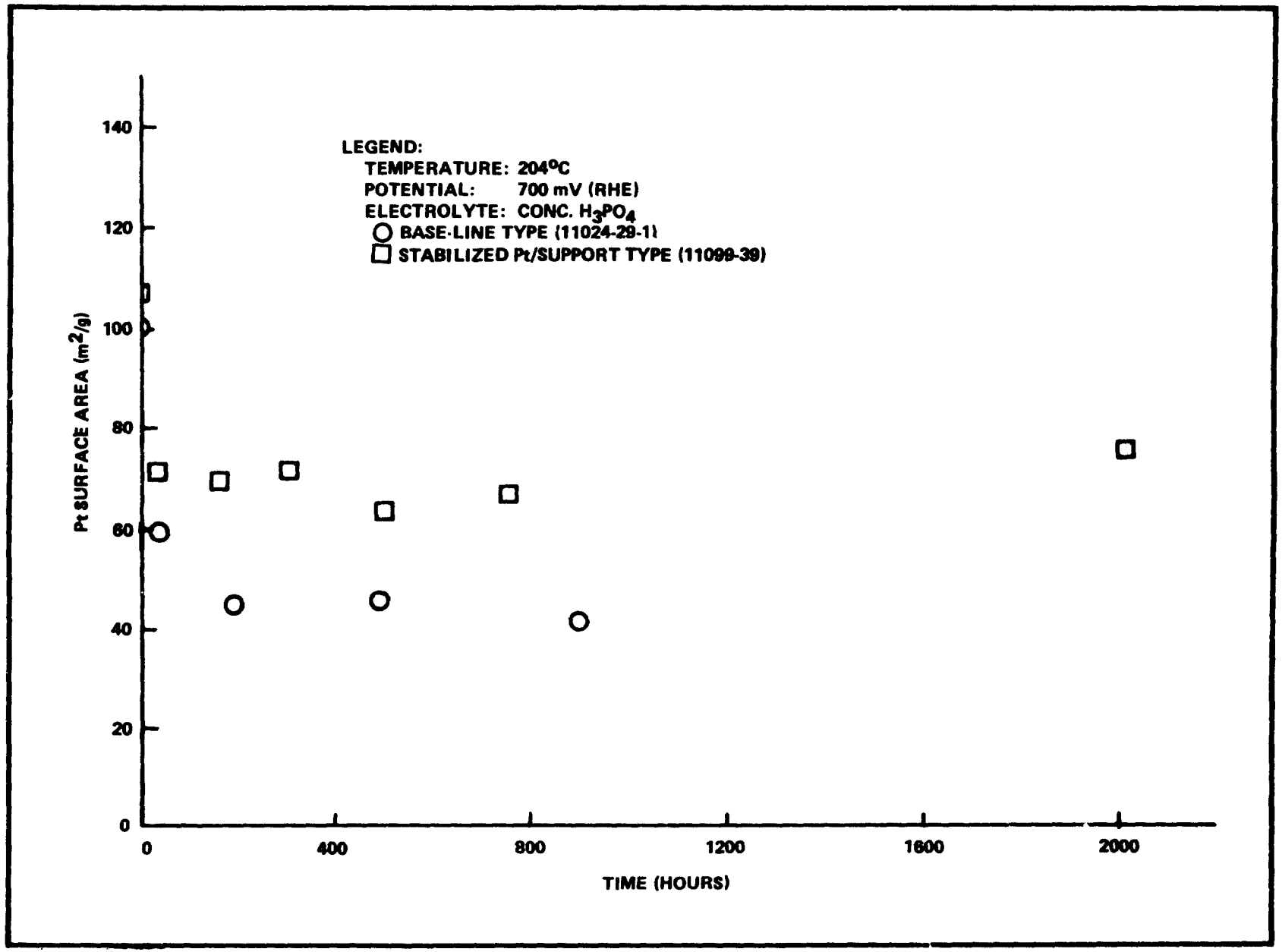

FIGURE I-14. PLATINUM SURFACE-AREA LOSS UNDER POTENTIOSTATIC AGING CONDITIONS FOR Pt ON CARBON ELECTROCATALYSTS

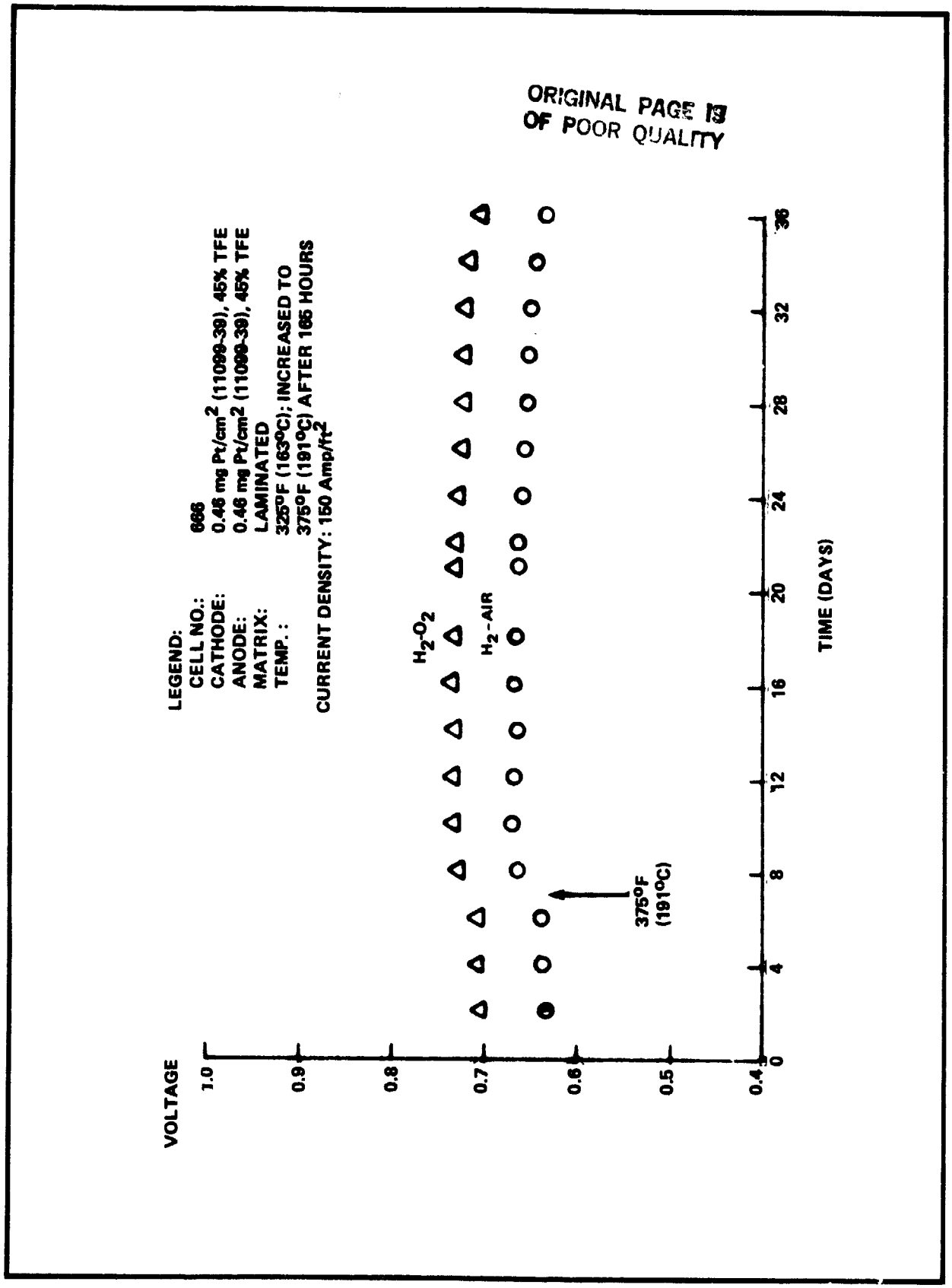

FIGURE I-15. PERFORMANCE STABILITY OF SINGLE-CELL USING DEVELOPMENTAL CATALYST OF THE STABILIZED-SUPPORT/STABILIZED-Pt TYPE

The above results for stabilized-Pt/stabilized-support catalysts led to the adoption of this type of formulation for cathodes through the latter portion of the program. This catalyst was utilized in Sub-Stack Nos. 3, 4, and 5 as well as in 5kW Stack No. 1 (see below).

C. ANODE CATALYST EVALUATION

Base-line catalysts (nominal 10% Pt on carbon) were used for anodes throughout the program. This included all stacks and the great majority of single cells. Late in the program developmental bimetallic catalysts were tested in single cells to evaluate their tolerance to carbon monoxide in the fuel stream (see below).

Figure I-16 illustrates the loss in single cell performance for a base-line anode catalyst as the fuel is changed from hydrogen to a synthetic reformate gas (65% H_2, 2% CO, 23% CO_2, 10% H_2O). The losses range from 18 mV at 204°C to 28 mV at 163°C, indicating the effect of temperature on CO-tolerance.

Losses due to CO, although recoverable upon resumption of hydrogen flow, tend to increase with time. Figure I-17 shows the endurance of a single cell using a base-line anode catalyst and a fuel containing 1% CO. A slow, but steady performance decline was observed over the test period of about 1000 hours. The catalyst development program provided a bimetallic anode catalyst that appeared to result in improved CO-tolerance. Figure I-18 shows the single cell endurance for such a catalyst using a fuel containing 1% CO. The voltage levels remained essentially constant throughout the test (about 1000 hours). Because of these results, efforts are currently underway to scale up this bimetallic catalyst formulation in anticipation of its use in stacks.

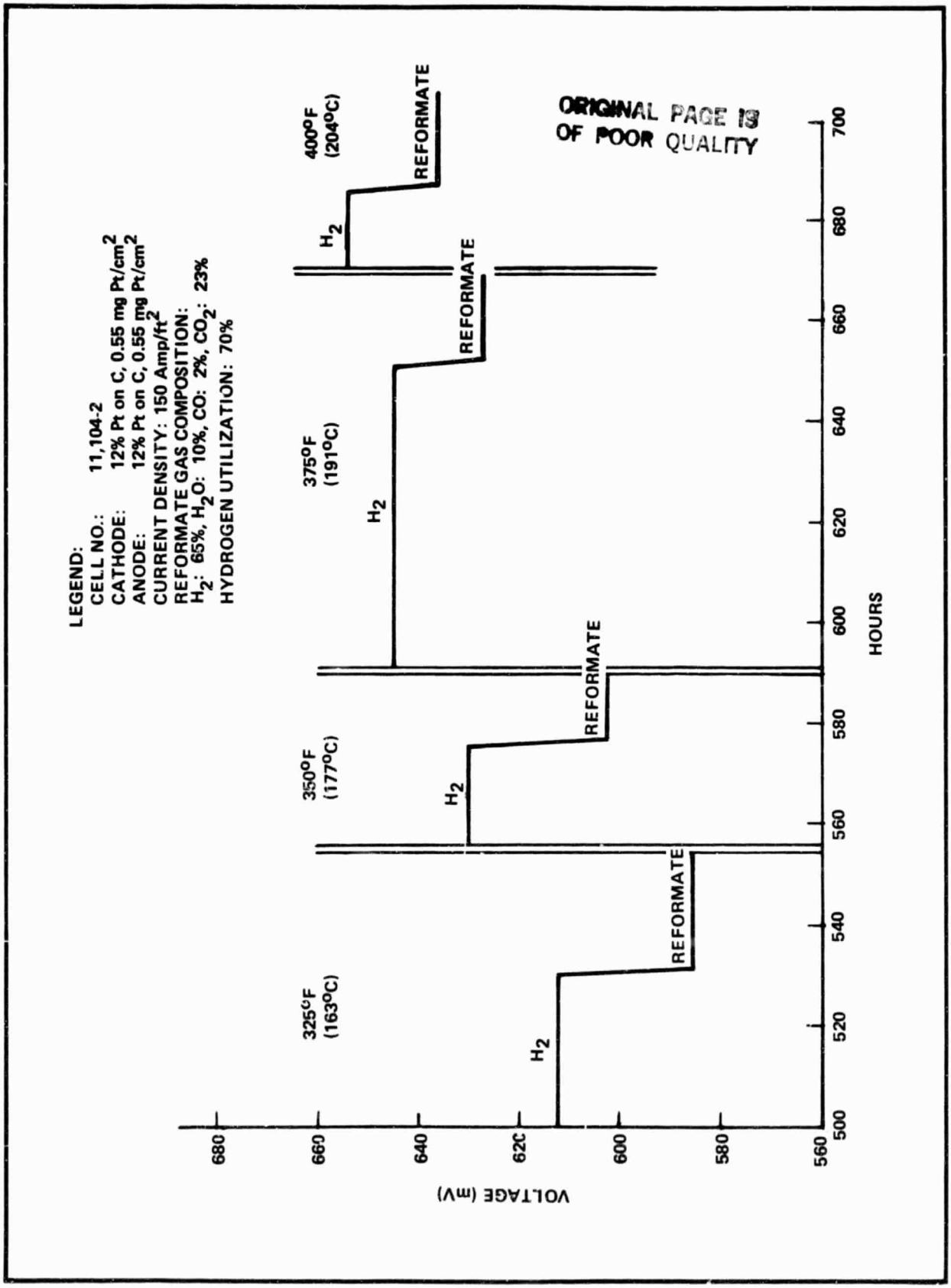

FIGURE I-16. EFFECT OF TEMPERATURE AND REFORMATE GAS ON 7 INCH x 10.7 INCH SINGLE-CELL PERFORMANCE

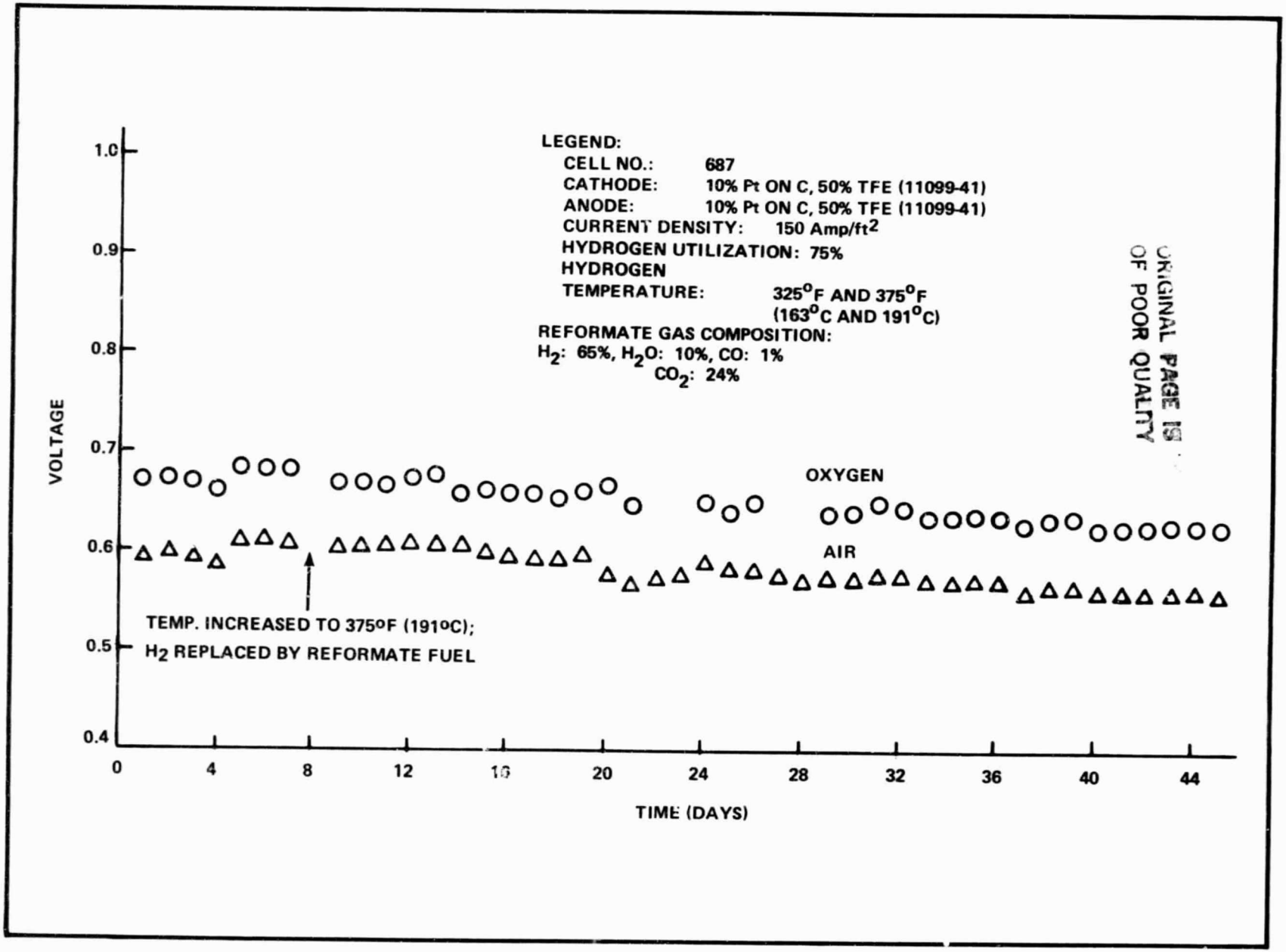

FIGURE I-17. EFFECT OF REFORMATE GAS ON SINGLE-CELL PERFORMANCE

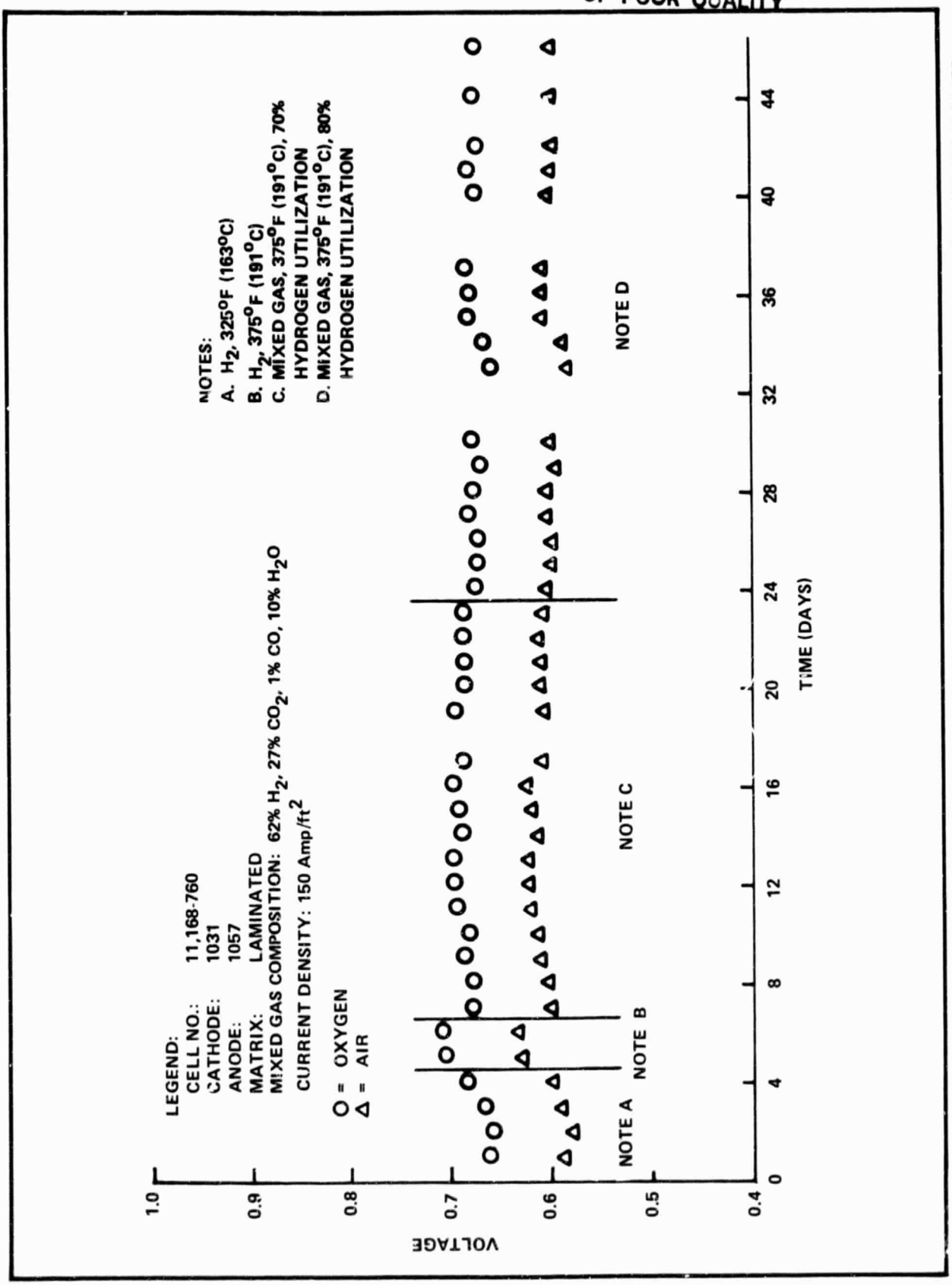

FIGURE I-18. PERFORMANCE OF SINGLE-CELL USING BI-METALLIC ANODE ELECTROCATALYST FOR IMPROVED CO-TOLERANCE

D. CONCLUSIONS

- The stability of carbon support materials against corrosion can be substantially enhanced through heat treatment and/or chemical treatment.

- Cathode catalyst preparations of the stabilized-support/stabilized-Pt type show promise of enhanced platinum surface-area stability.

- Follow-up work should be conducted on bimetallic anode catlaysts showing signs of improved CO-tolerance.

SECTION II

ELECTRODES

A. OBJECTIVES

The goals for the electrode development program during Phase II were as follows:

- 0.68 volt IR-free performance on hydrogen/air at 150 A/ft^2 (161 mA/cm^2) and 204°C
- Precious metal loading of 1.0 mg Pt/cm^2, total cell
- Non-PM projected high volume cost of $5/$ft^2$, total cell.

The performance goal above was achieved in single cells (see, for example, Figure I-15 in which the IR-free cell voltage exceeds 0.7 volt, even at the lower temperature of 191°C) and approached in stacks. Early in the program the major effort became focused on 10% Pt on carbon catalysts having a nominal loading of 0.46 mg Pt/cm^2. This loading thus became typical for cathodes and for anodes, resulting in a total cell loading less than 1.0 mg Pt/cm^2. The electrode manufacturing cost goals appear to be attainable, considering both the materials and projected labor costs. One key factor, however, will be the high volume cost of the carbon paper substrates, presently purchased from suitable manufacturers.

B. SUBSTRATES

Two types of carbon paper were used as electrode substrates in this program -- one from a woven fabric precursor, made by Pfizer, Inc., and the other from a non-woven fiber precursor, made by Stackpole Carbon Co. Catalysts were co-deposited with Teflon onto these porous substrates.

Figure II-1 shows the corrosion behavior of the Pfizer and Stackpole substrate materials in concentrated phosphoric acid at 204°C and 1.0 volt (RHE). It is seen that the Pfizer material is more corrosion resistant than the Stackpole; however, both approach very low corrosion currents within a short period of time at that potential.

Because of the relatively large macropore size of the woven carbon paper (Pfizer), the catalyst layer typically penetrated into or though this element to a certain degree, resulting in incomplete utilization of the catalyst. This is illustrated in the cross-sectional optical micrograph of Figure II-2. Use of the finer-pore non-woven paper (Stackpole) yielded catalyst layers with improved continuity.

The carbon paper substrates are wetproofed prior to catalyst deposition. The use of TFE-30 fluoropolymer dispersion as the wetproofing agent resulted in appreciable oxygen diffusion losses in single cells, even after short times at 163°C. Early in the program FEP-120 fluoropolymer dispersion was explored as a substitute for TFE-30. Acid uptake tests indicated that the FEP-120 wetproofing agent was more effective, even at lower loadings (about 5 mg fluoropolymer/cm^2). Figure II-3 shows the initial IR-free performance plot for a cell with FEP-120 wetproofed non-woven cathode and anode substrates. This figure illustrates the acceptably low oxygen diffusion polarization that was obtained through the use of FEP-120.

C. CATALYST LAYER

Catalysts were co-deposited with Teflon onto substrates according to Engelhard-developed techniques. TFE-30 fluoropolymer dispersion was used as the wetproofing agent for the catalyst layer. The main catalyst layer optimization effort involved the degree of Teflon loading in cathodes. A series of sub-scale (3-inch x 3-inch) single cell tests were run at 191°C to examine the effect of Teflon content.

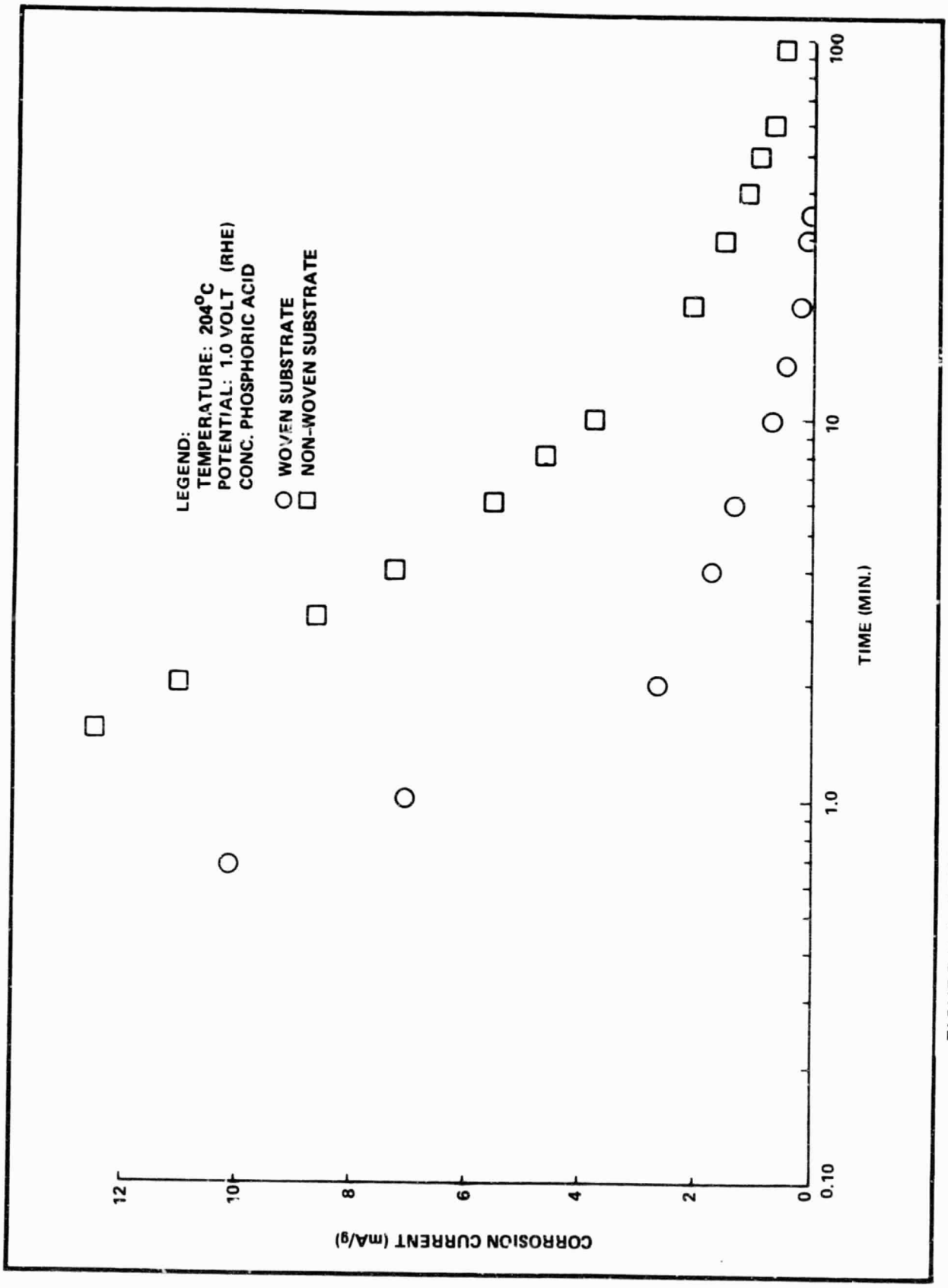

FIGURE II-1. CORROSION CURRENT OF CARBON PAPER SUBSTRATES

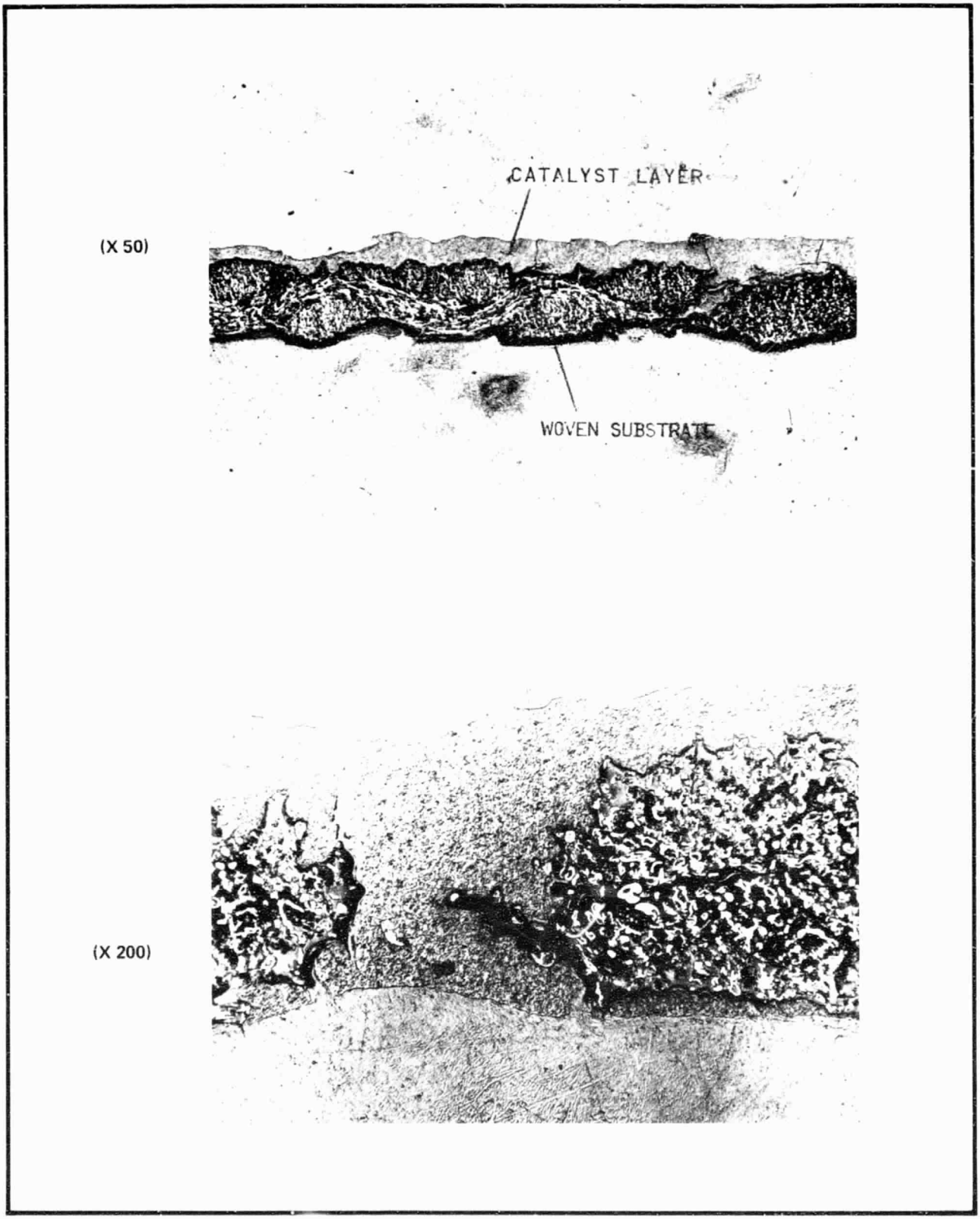

FIGURE II-2. CROSS-SECTION OF FUEL CELL ELECTRODE SHOWING CATALYST LAYER AND WOVEN SUBSTRATE

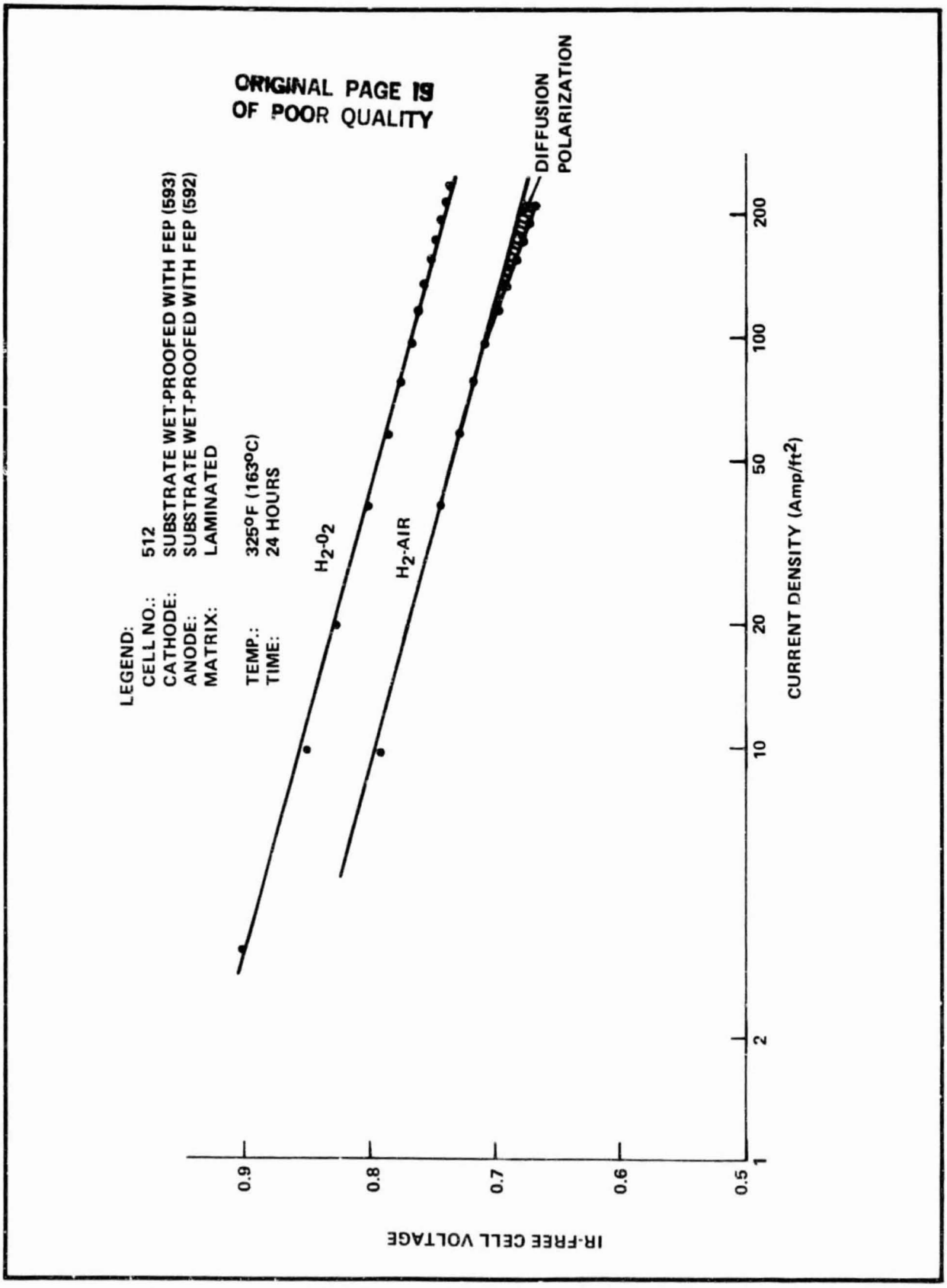

FIGURE II-3. SINGLE-CELL PERFORMANCE OF 10% Pt ON CARBON ELECTRODES WITH FEP-WETPROOFED SUBSTRATES

Figure II-4 shows the performance characteristics of cathodes having 40, 45, and 50% Teflon in the catalyst layers. It is seen that performance improves markedly as Teflon content is increased, especially from 40% to 45%. Testing of cathodes with 55% Teflon in the catalyst layer indicated inadequate ionic conductance, with slow improvement over several hundred hours.

As the result of this test series, subsequent stack tests employed cathodes with 50% Teflon in the catalyst layer. However, maximum hydrophobicity is desirable for long-term stability, and further optimization of Teflon content in the range 50-55% is planned. On the other hand, hydrophobicity is far less critical for anodes, and stack tests employed anodes with 45% Teflon in the catalyst layer.

D. CONCLUSIONS

- Non-woven carbon paper wetproofed with FEP-120 fluoropolymer dispersion is an acceptable electrode substrate.

- The optimum Teflon content for cathodes is higher than that for anodes.

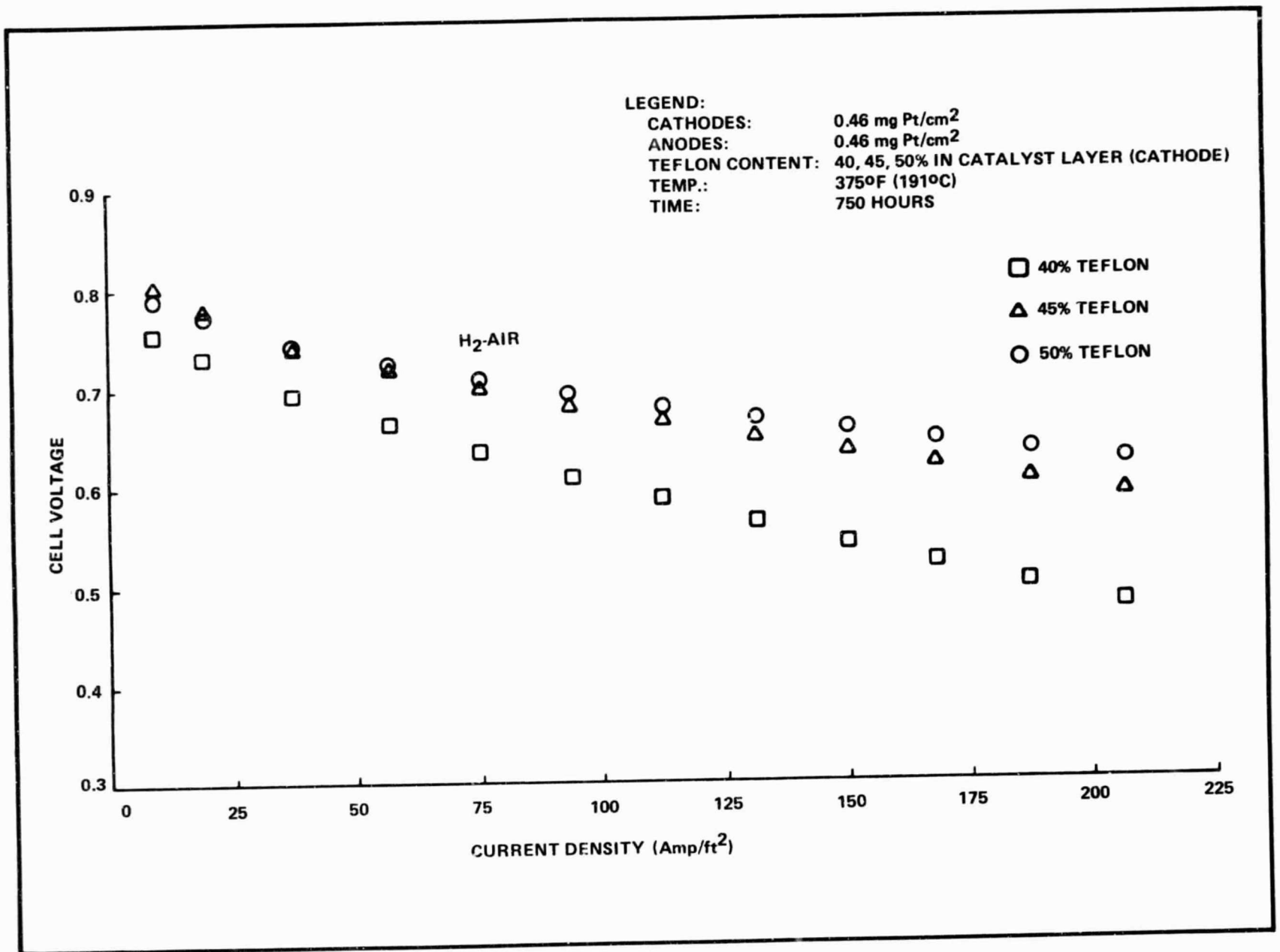

FIGURE II-4. EFFECT OF TEFLON CONTENT ON ELECTRODE PERFORMANCE

SECTION III

MATRIX

Goals for the matrix development program during Phase II were as follows:

- 30 mV IR-loss at 150 A/ft^2
- Operability in phosphoric acid at 177-204°C
- Projected high-volume cost of $\$3/ft^2$

Effort under this program has involved two approaches:

- Formulations based on the existing Engelhard membrane-type matrix (U.S. Patent 3,453,149)
- Formulations based on lamination of matrix layers onto other cell components.

The matrix effort in the early stages was directed toward modification of the existing membrane-type Engelhard matrix. Modifications were necessary to achieve reduced IR-losses and higher-temperature operation. One approach, based on a zirconium phosphate gel, was found to have attractive chemical stability in high-temperature phosphoric acid. Membranes of this type were tested in single cells, but these exhibited a tendency toward increasing IR-drop with time. This problem was traced to a physical characteristic of the membrane whereby creep would occur during cell operation, eventually resulting in loss of cell compression.

Emphasis was subsequently shifted to the laminated-type matrix. Various inorganic compounds -- mostly carbides and nitrides -- were examined as candidate filler materials. Silicon carbide fillers were used throughout the series of stack tests. Matrix pastes were prepared using the filler material, Teflon and polyethylene oxide. These were applied to both cell electrodes initially by manual blade-coating or screen printing. The combined matrix thickness was 0.008-0.010 inch. Samples prepared in this manner passed bubble-pressure screening tests in excess of 30 inches of H_2O. Evaluation then proceeded to the single-cell stage where open-circuit voltage was the key indicator of matrix integrity.

The open-circuit voltages of cells using this matrix were found to increase as the average particle size of the silicon carbide decreased. This trend is shown in Table III-1.

The open-circuit voltage characteristics of single cells using laminated matrix elements were found to be attractive over temperature range 163-204°C. The open-circuit voltage level depended in part on the paricle size of the filler material, with finer particles enhancing capillarity and, hence, the effectiveness of gas separation. This is illustrated in Table III-1 where decreasing filler particle size results in higher open-circuit voltage.

Since the laminated matrix layers are relatively thin, their acid inventory is quite low. It is therefore necessary to implement the means for acid replenishment in this type of cell (see Acid Management section later in this report). The sub-scale (3-inch x 3-inch) single cells generally did not have provisions for acid replenishment, and therefore these were not used for the purpose of evaluating open-circuit voltage stability. Such evaluations were conducted in stacks, and the test results of Sub-Stack No. 2 (see below) indicate long-term matrix integrity.

The laminated-matrix approach also provided the desired reduction in IR losses. Whereas cells using membrane-type matrix elements would typically have IR losses of about 70 mV at 150 A/ft^2 and 163°C, the laminated matrix would yield corresponding IR losses of 30-40 mV. In the temperature range 191-204°C this loss is generally about 30 mV.

Other advantages for the laminated matrix include superior acid acceptance and wicking properties and lower projected high volume cost. The acid acceptance and wicking properties are important in connection with acid management schemes (see below). The potential for low cost processing of this matrix type was demonstrated in part through preparation of matrix elements by automated techniques -- using both the blade-coating and screen-printing approaches. Furthermore, these processing techniques were found to be amenable to scale-up (see Task IV, below).

TABLE III-1

SiC LAMINATED MATRIX FILLER MATERIAL

CORRELATION BETWEEN CRYSTALLITE SIZE AND OPEN-CIRCUIT VOLTAGE

Crystallite Size (micrometers)			Open-Circuit
Average	Maximum	Minimum	Voltage*(mV)
17	28	8	860 ± 45
10	16	5	862 ± 15
6	12	2	880 ± 27
4	9	1.5	896 ± 25

*Measured at 325°F (163°C) after 24 hours with H_2-Air reactants.

CONCLUSIONS

- A laminated matrix configuration provides high-temperature tolerance and low IR-loss.

- Laminated matrix layers have superior acid-acceptance and wicking properties to those of membrane-type matrix elements.

SECTION IV

BIPOLAR PLATES

A. OBJECTIVES

The goals for the bipolar plate program during Phase II were:

- Electrical resistivity of 0.05 ohm-cm or less (about 3 mV IR-loss at 150 A/ft^2).
- Hydrogen permeability equivalent to 0.5 A/ft^2 or less at 204°C.
- Flexural strength of 4000 psi or greater (ref. ASTM-D790-71).
- Weight loss of 0.1% or less in phosphoric acid at 204°C and 1.0 volt (RHE).
- Projected high-volume cost of $4/ft^2.

The bipolar plate development effort fell into three general categories:

- All-carbon plates
- Resin-bonded and resin-sealed plates
- Multiple element plates (ABA-type)

B. ALL-CARBON PLATES

The all-carbon plates investigated and/or utilized in this program include carbon-sealed graphite (Tylan, U.S. Patent 3,854,979), vitreous carbon, and vitreous carbon impregnated graphite (Fluorocarbon Corp.). The disposition of these materials in terms of the properties of interest is presented in Table IV-1. Phosphoric acid tolerance is presented separately in Table IV-2.

As indicated in Table IV-1, all of the candidate materials are attractive with respect to electrical resistivity and flexural strength. The carbon-sealed graphite and the vitreous carbon materials have also shown hydrogen impermeability, and Table IV-2 indicates that their phosphoric acid tolerance is good. The projected cost for the carbon-sealed graphite, however, is high (about $30/ft^2). Likewise, the vitreous carbon material is too expensive (over $50/ft^2), and recent estimates of possible cost-reduction procedures by the processor do not indicate a change in this picture.

TABLE IV-1

PROPERTIES OF ALL-CARBON BIPOLAR PLATE MATERIALS

	Electrical Resistivity	Hydrogen Permeability	Flexural Strength
Carbon-sealed graphite	negligible(1)	negligible(2)	acceptable(3)
Vitreous carbon	negligible(1)	negligible(2)	acceptable(3)
Vitreous carbon impregnated graphite	negligible(1)	unacceptable(4)	acceptable(3)

Notes:

(1) less than 1 mV @ 150 mA/cm^2

(2) below detection level ($<<$ 0.5 mA/cm^2 equivalent, 204°C)

(3) greater than 4000 psi

(4) $>>$ [illegible] mA/cm^2 equivalent; includes four samples with varying levels of impregnation

TABLE IV-2

PHOSPHORIC ACID TOLERANCE OF ALL-CARBON BIPOLAR PLATE MATERIALS

	Immersion Tests(2)	Potentiostatic Tests* (204°C, 1.0 volt)	Remarks
Carbon-sealed graphite	0.07% weight-loss after 1000 hours at 175°C(3)	No measurable weight-loss after 1000 hours	
Vitreous carbon			
Vitreous carbon impregnated graphite			(1)

Notes:

(1) Testing not conducted because of failure to pass hydrogen impermeability tests.

(2) Fresh samples washed and oven-dried before weighing; aged samples hot-soaked, washed and oven-dried before weighing.

(3) Data obtained in prior contract.

In the case of vitreous carbon impregnated graphite, four levels of impregnation were examined. As shown in Table IV-1, none of these had sufficient hydrogen impermeability; therefore, phosphoric acid tolerance testing was not conducted. Furthermore, cost estimates from the processor -- based on preparation of these samples -- were not attractive. Effort on this material was discontinued.

Despite its high cost, the Tylan material continued to be used for some time in the program until more feasible approaches were developed. The performance of this material was excellent over many thousands of hours in single-cell and stack tests. Accordingly, it was most suitable for use in tests where electrodes or matrix elements were being evaluated.

C. RESIN-BONDED AND RESIN-SEALED PLATES

The relevant physical properties of the resin-bonded and resin-sealed materials evaluated in this program are shown in Table IV-3. The tolerance of the same materials to hot phosphoric acid at 1.0 volt (RHE) is given in Table IV-4.

The phenolic-bonded graphite was molded by Sparta Manufacturing Company at a resin content of 25% by weight. Electrical resistivity was acceptably low, but the phosphoric acid weight loss was unacceptably high. Accordingly, other tests were not conducted.

The polyphenylene sulfide bonded graphite material was also molded by Sparta Manufacturing Company at a resin content of 25%. It was found to have acceptable resistivity, permeability, and strength. The phosphoric acid tolerance, however, was poor under these demanding conditions of temperature and potential.

Graphite impregnated with Kearney Industries' CO-40 proprietary resin showed good physical properties. It can be noted from Table IV-4 that its degree of tolerance to phosphoric acid was somewhat uncertain for a period of time. A sample that had non-impregnated edges lost 0.7% of its weight after 1000 hours at

TABLE IV-3

PROPERTIES OF RESIN-BONDED AND RESIN-SEALED BIPOLAR PLATE MATERIALS

	Electrical Resistivity	Hydrogen Permeability	Flexural Strength	Remarks
Phenolic/graphite (25/75)*	acceptable(4)			(1)
Polyphenylene sulfide/graphite (25/75)	negligible(5)	negligible(6)	acceptable(8)	(1)
CO-40**/graphite	negligible(5)	negligible(6)	acceptable(6)	(2)
Polyether sulfone/graphite	negligible(5)	negligible(7)		(3)
Polyparabanic acid/graphite	negligible(5)	negligible(7)		(3)

Notes:

(1) molded composition

(2) resin impregnation

(3) lamination

(4) less than 3 mV @ 150 mA/cm^2

(5) less than 1 mV @ 150 mA/cm^2

(6) below detection level ($\ll$ 0.5 mA/cm^2 equivalent, 204°C)

(7) no leakage on basis of room-temperature bubble test, 10 psi

(8) greater than 4000 psi

* weight ratio

** Kearney Industries proprietary resin

TABLE IV-4

PHOSPHORIC ACID TOLERANCE OF RESIN-BONDED AND RESIN-SEALED BIPOLAR PLATE MATERIALS

	Immersion Tests[6]	Potentiostatic Tests[6] (204°C, 1.0 volt)	Notes:
Phenolic/graphite (25/75)[6]		4.6% weight-loss after 1000 hours	(1)
Polyphenylene sulfide/graphite (25/75)	0.19% weight-loss after 1000 hours at 175°C [7]	Disintegrated	(1)
CO-40[8]/graphite		0.7% weight-loss after 1000 hours; 10.2% weight-loss after 2000 hours	(2)
		1.9% weight-loss after 1000 hours	(3)
Polyether sulfone	0.56% weight-loss after 1000 hours at 204°C	0.1% weight-gain after 1000 hours	(4)
Polyether sulfone/graphite	0.18% weight-loss after 1000 hours	3.9% weight-loss after 1000 hours	(5)
Polyparabanic acid	9.7% weight-loss after 1000 hours at 204°C		(4)

Notes:

(1) molded composition
(2) resin impregnation, exposed edges
(3) resin impregnation, sealed edges
(4) resin only
(5) lamination
(6) fresh samples washed and oven-dried before weighing; aged samples hot-soaked, washed and oven-dried before weighing
(7) data obtained in prior contract
(8) Kearney Industries proprietary resin

204°C and 1.0 volt; however, in the next 1000 hours this sample lost an additional 9.5% of its weight. There was evidence of physical disengagement of carbonaceous particles in the acid-containing vessel, and the non-impregnated edges could have been a complicating factor.

A sample of the same material but with impregnated edges was subsequently tested. A weight loss of 1.9% was obtained during 1000 hours of potentiostatic testing. Also, in an extended single-cell test the rate of decay was well above average. Further work with Kearney CO-40/graphite was not considered justified.

A polyparabanic acid film of 0.010 inch thickness was tested, but it showed substantial weight loss in phosphoric acid. No further work was conducted with this material.

Other resins screened in the program, but not listed in Tables IV-3 and IV-4, included Torlon (polyamide/imide, Amoco) and Radel (polyphenyl sulfone, Union Carbide). The Torlon disintegrated during 312 hours immersion in phosphoric acid at 204°C, so it was excluded from further consideration. Radel gained 0.67% in weight after 1000 hours immersion and 0.86% after 1000 hours potentiostatic treatment. These data indicate some form of interaction with the hot acid, thus Radel also was considered unacceptable.

The immersion test data for polyether sulfone indicate low, but significant weight loss (air atmosphere). In the 1000 hour potentiostatic test at 1.0V (RHE) and 204°C the polyether sulfone/graphite structure showed substantial weight loss. This is borne out by the corresponding corrosion-current plot of Figure IV-1. However, the corrosion-current was found to be extremely potential-dependent. This is illustrated in the Tafel plot of Figure IV-2. It can be seen from this figure that the corrosion-current at 0.8V (RHE) is lower than that at 1.0V by about a factor of 50. Accordingly, the phosphoric acid tolerance of polyether sulfone falls into the acceptable range within potentials of practical fuel cell interest. This material was therefore considered promising for application in bipolar plates.

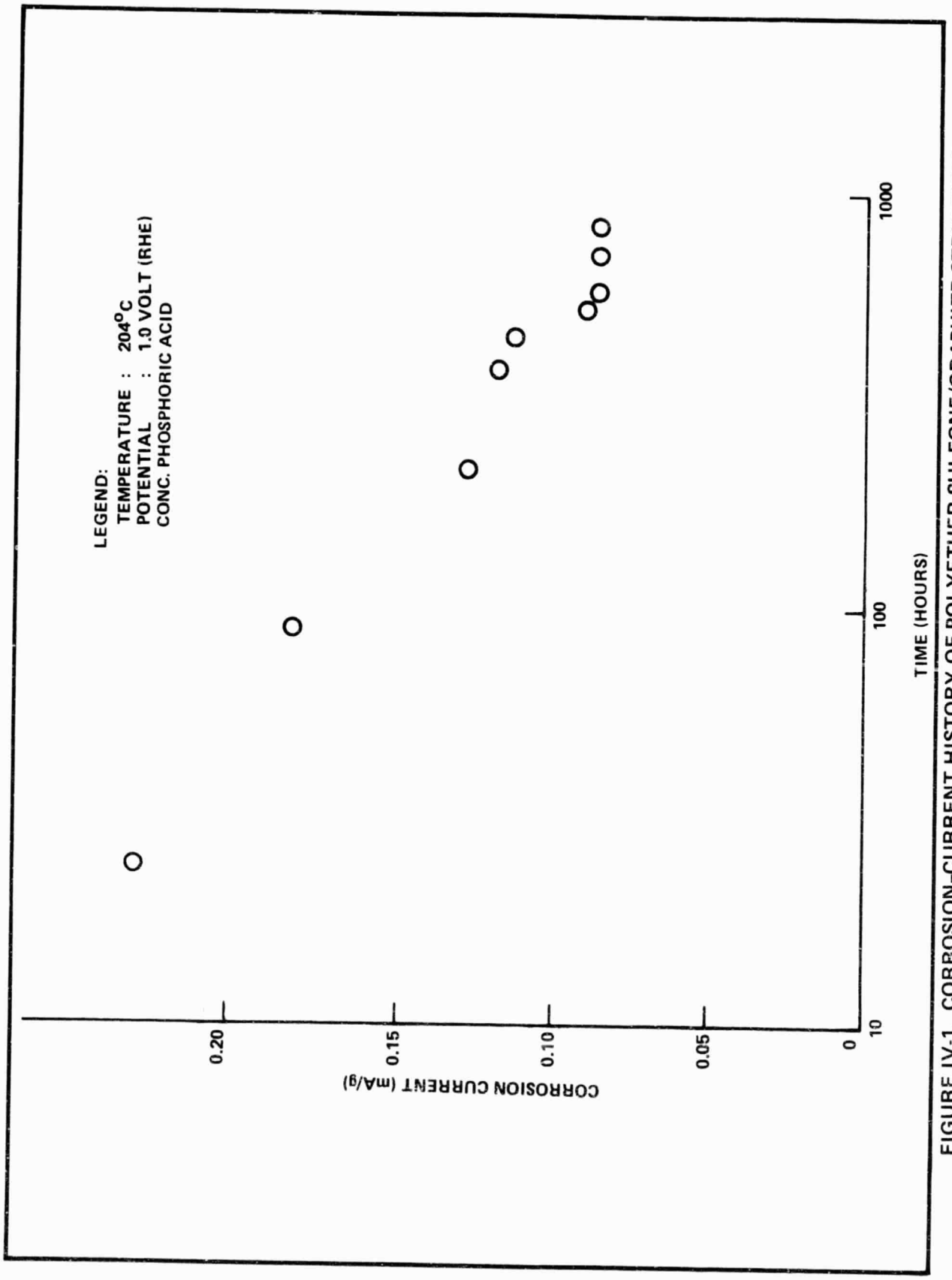

FIGURE IV-1. CORROSION-CURRENT HISTORY OF POLYETHER SULFONE/GRAPHITE STRUCTURE

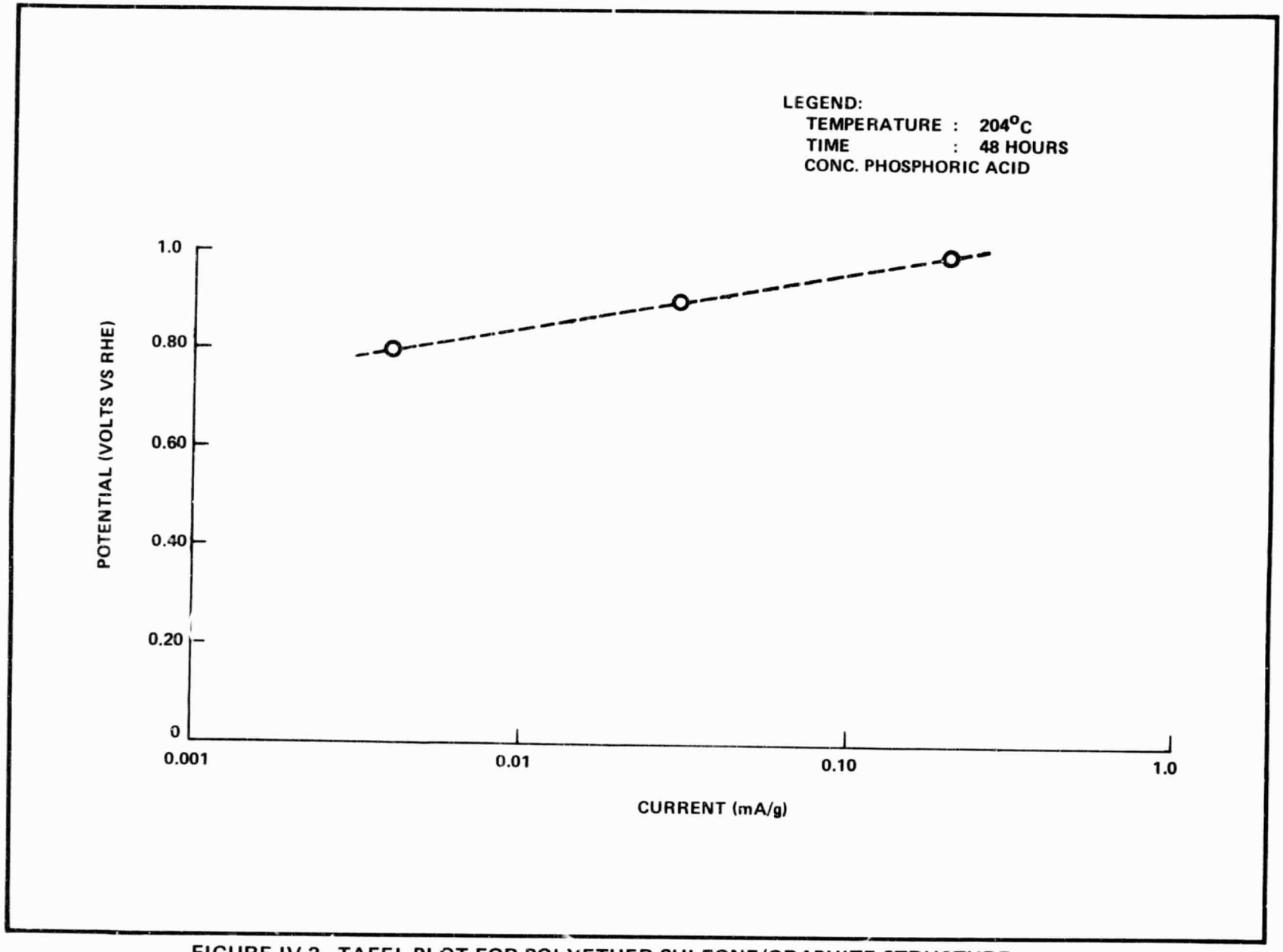

FIGURE IV-2. TAFEL PLOT FOR POLYETHER SULFONE/GRAPHITE STRUCTURE

D. MULTI-ELEMENT PLATES

The most extensive effort in the bipolar plate area during Phase II involved multi-element plates. The initial approach employed the non-grooved "ABA" configuration illustrated in Figure IV-3.

It follows from considerations of flow vs. pressure-drop in packed beds that a relatively large fiber diameter is needed to achieve acceptably low pressure-drops through non-grooved A-elements. Reticulated vitreous carbon (RVC, Chemotronics) satisfies this requirement, and various forms of this material were evaluated. In order to satisfy other requirements, such as electrical conductivity and mechanical strength, it was necessary to use RVC upgraded to 6-10 times its original weight by means of chemical vapor deposition (CVD) of carbon. Experience showed that RVC could be upgraded in such a manner and still maintain its flow characteristics for reactant gases. The mechanical and electrical properties of CVD-upgraded RVC are given in Table IV-5 and its corrosion properties in Table IV-6.

The weight loss of the first sample of CVD-upgraded RVC listed in Table IV-5 was a surprisingly high 9% after 1000 hours at 204°C and 1.0 volt. Subsequent observations indicated that attack on the RVC skeleton was responsible for the loss in weight. Microscopic examination of the aged material showed a loss of "crispness" in the RVC phase at the cut edges. Microporosity was found to be 0.08 cm^3/g in the aged sample as compared to zero in a fresh sample. Finally, a potentiostatic aging test of an untreated RVC sample resulted in disintegration of the sample.

Figure IV-4 shows the potentiostatic corrosion-current of two CVD/RVC samples, one with RVC exposed at the edges and the other in which the cut edges were protected with CVD coating. This comparison confirms that it is only the RVC skeleton which is susceptible to rapid attack in phosphoric acid. The rate of corrosion of the CVD coating is acceptably low.

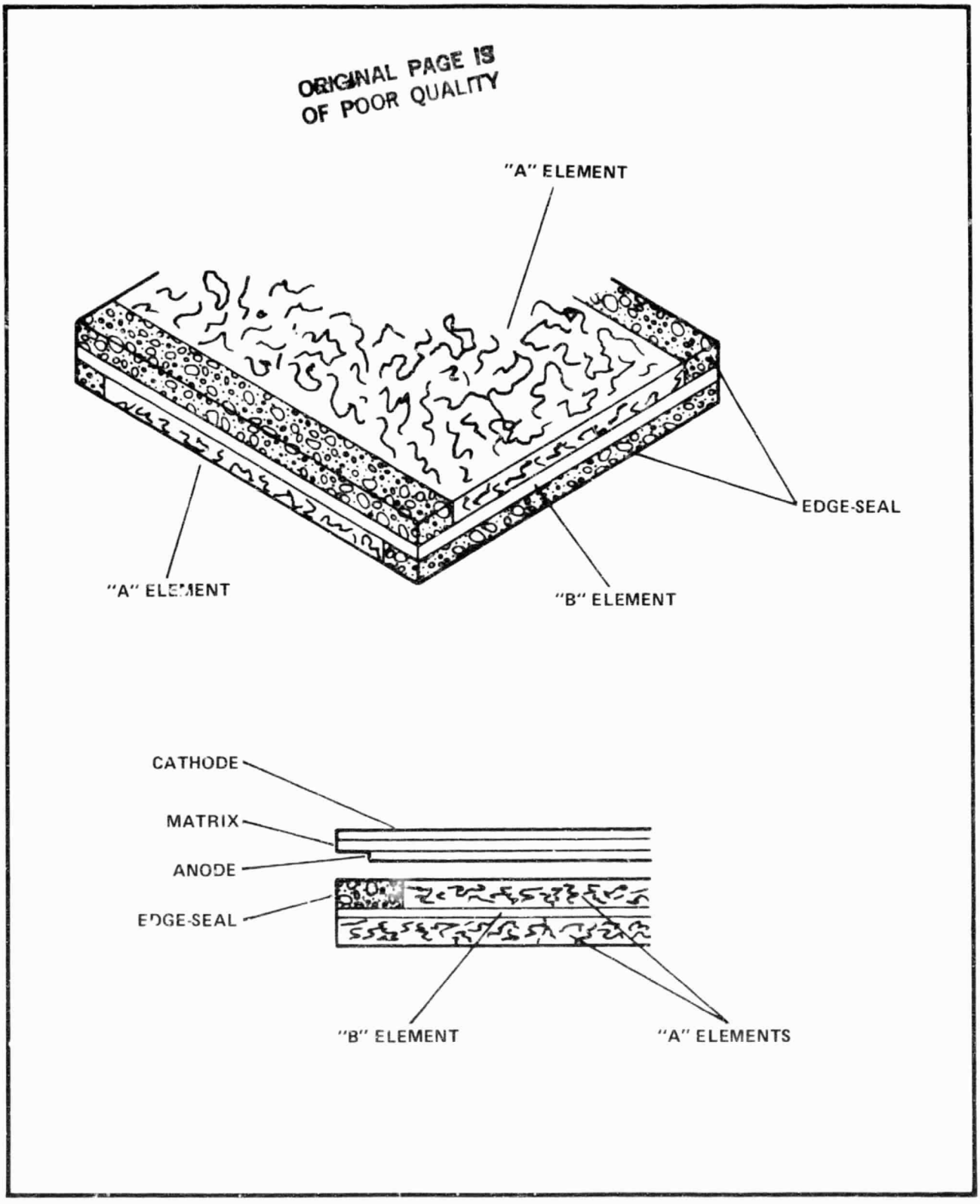

FIGURE IV-3. NON-GROOVED "ABA" BIPOLAR PLATE CONFIGURATION

TABLE IV-5

PROPERTIES OF CVD-UPGRADED [3] RETICULATED VITREOUS CARBON A-ELEMENTS

	Original Porosity	IR-Loss @ 150 mA/cm^2	Air Pressure-Drop[4]	Crush Strength
RVC @ 45 pores/inch	98%	2 mV	acceptable [2]	150 psi
RVC @ 60 pores/inch	98%	2 mV	acceptable [1]	

Notes:

(1) less than 2 in. H_2O

(2) less than 1 in. H_2O

(3) to 6-8 times the original weight; 3 samples of each type

(4) @ flow equivalent to 2x stoichiometric, 150 mA/cm^2; corrected to 6-inch length, 350°F (177°C)

TABLE IV-6

PHOSPHORIC ACID TOLERANCE OF ABA BIPOLAR PLATE MATERIALS

	Potentiostatic Tests (4) (204°C, 1.0 volt)	Remarks
Reticulated vitreous carbon	Disintegrated	
CVD-upgraded RVC	9.0% weight-loss after 1000 hours	(1)
	2.8 mA/g corrosion current after 387 hours	(2)
	0.07 mA/g corrosion current after 113 hours	(3)
Woven fabric precursor B-element	No measurable weight-loss	

(1) exposed at cut edges

(2) exposed at cut edges - second sample

(3) coated by CVD at edges

(4) fresh samples washed and oven-dried before weighing; aged samples hot-soaked, washed and oven-dried before weighing

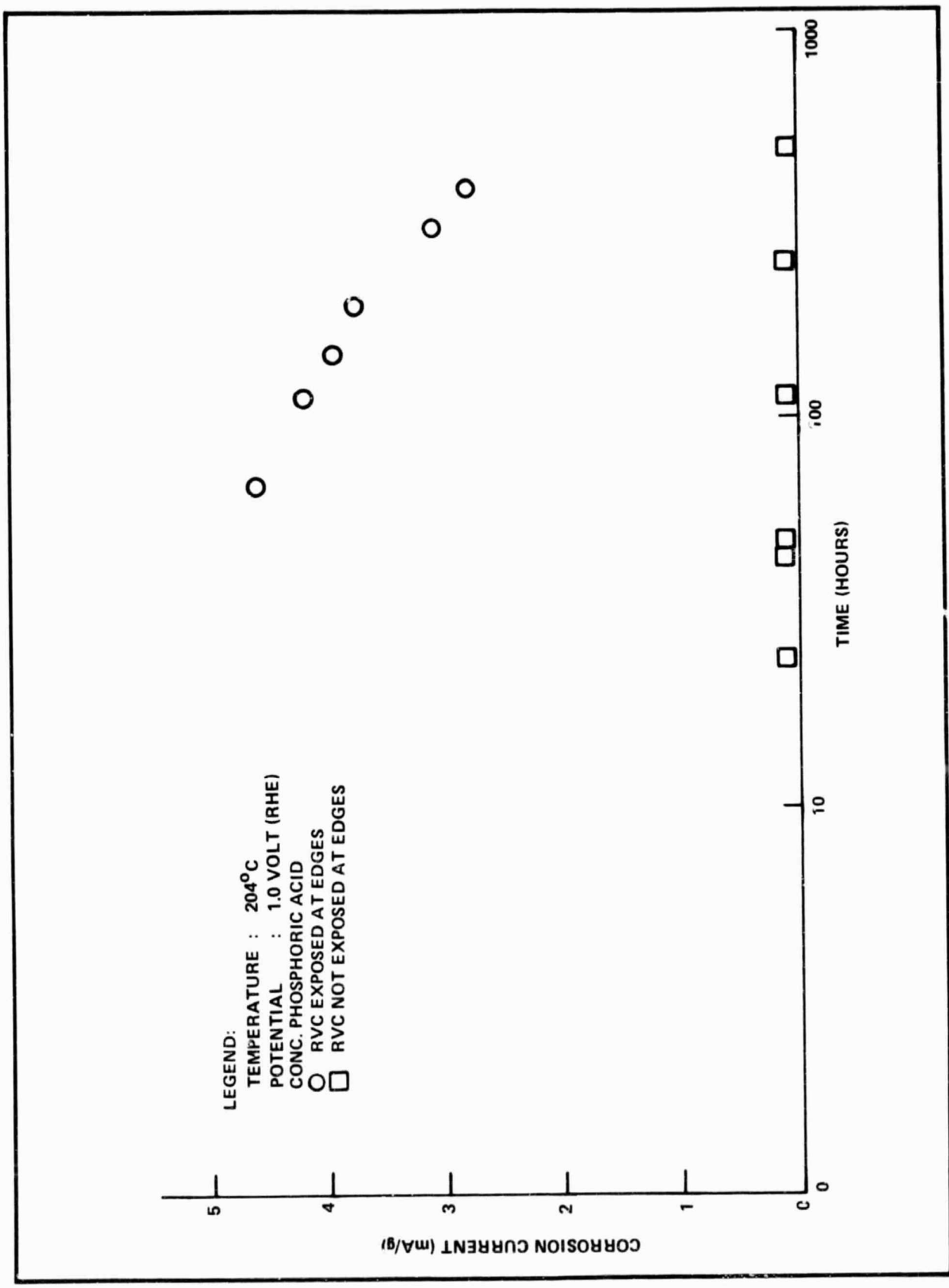

FIGURE IV-4. CORROSION-CURRENT HISTORY OF CVD-UPGRADED RVC A-ELEMENT

A graphitized woven fabric was selected as a precursor material for the B-element. Attempts to seal off the porosity of the B-element through the use of CVD alone were unsuccessful. Bubble tests indicated random pin-holes. Subsequent approaches to sealing employed graphite/resin-impregnation prior to CVD treatment. This procedure was eventually optimized to give acceptably impermeable material.

Electrical resistivity measurements on finished B-elements yielded an average IR-loss of about 1 mV at 150 A/ft^2, meeting the pre-established goal for this element. As indicated in Table IV-6, the phosphoric acid tolerance of this material is excellent.

The assembly of the CVD/RVC A-elements and the sealed B-elements into an ABA plate consisted of the following steps:

(1) A-elements edge-sealed as shown in Figure IV-3 with graphite adhesive.
(2) ABA sandwich bonded together with graphite/resin mixture.
(3) Graphitization

Plates prepared in this manner showed suitable adhesion and flatness. The performance of the first 3-cell stack incorporating these ABA plates is shown in Figure IV-5 (voltage on load) and Figure IV-6 (open-circuit voltage).

Later in the program emphasis shifted from CVD/RVC A-elements to needled-felt carbon plates upgraded by CVD. This was primarily motivated by the lower projected cost of the needled-felt plates. CVD-upgraded needled-felt was found to have excellent corrosion resistance in hot phosphoric acid. Mechanical and electrical requirements were also satisfactorily met by this material.

ABA assemblies utilized grooves in the relatively fine pore needled-felt A-elements to achieve adequate gas transport. The performance of a 3-cell stack constructed with needled-felt A-elements and Grafoil B-elements is shown in Figure IV-7. Testing was conducted with both pure H_2 and with synthetic reformate containing CO. The attractiveness of needled-felt as an A-element material was considered to be amply demonstrated by this stack.

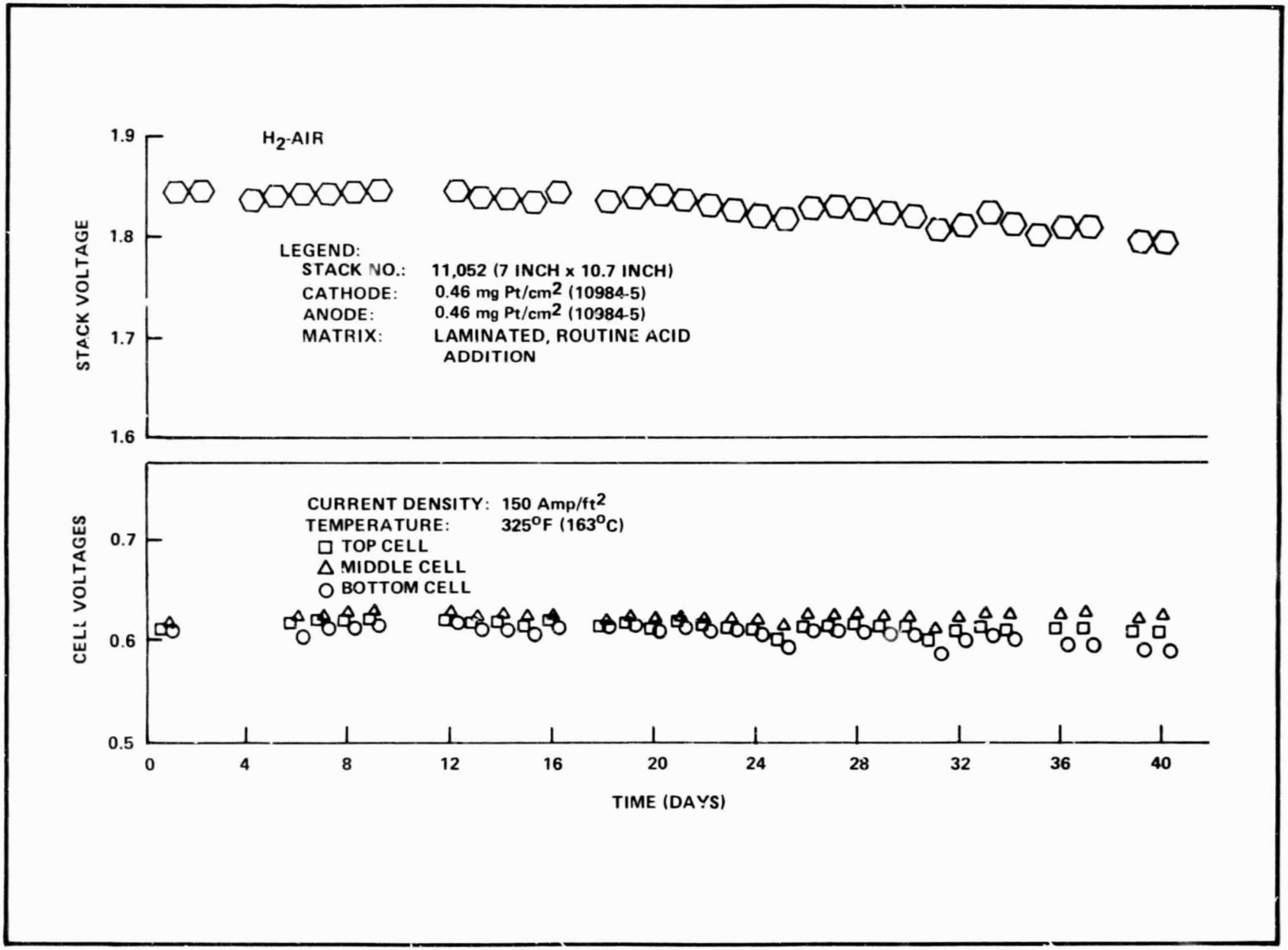

FIGURE IV-5. PERFORMANCE STABILITY OF 3-CELL STACK USING A–B–A CONSTRUCTION

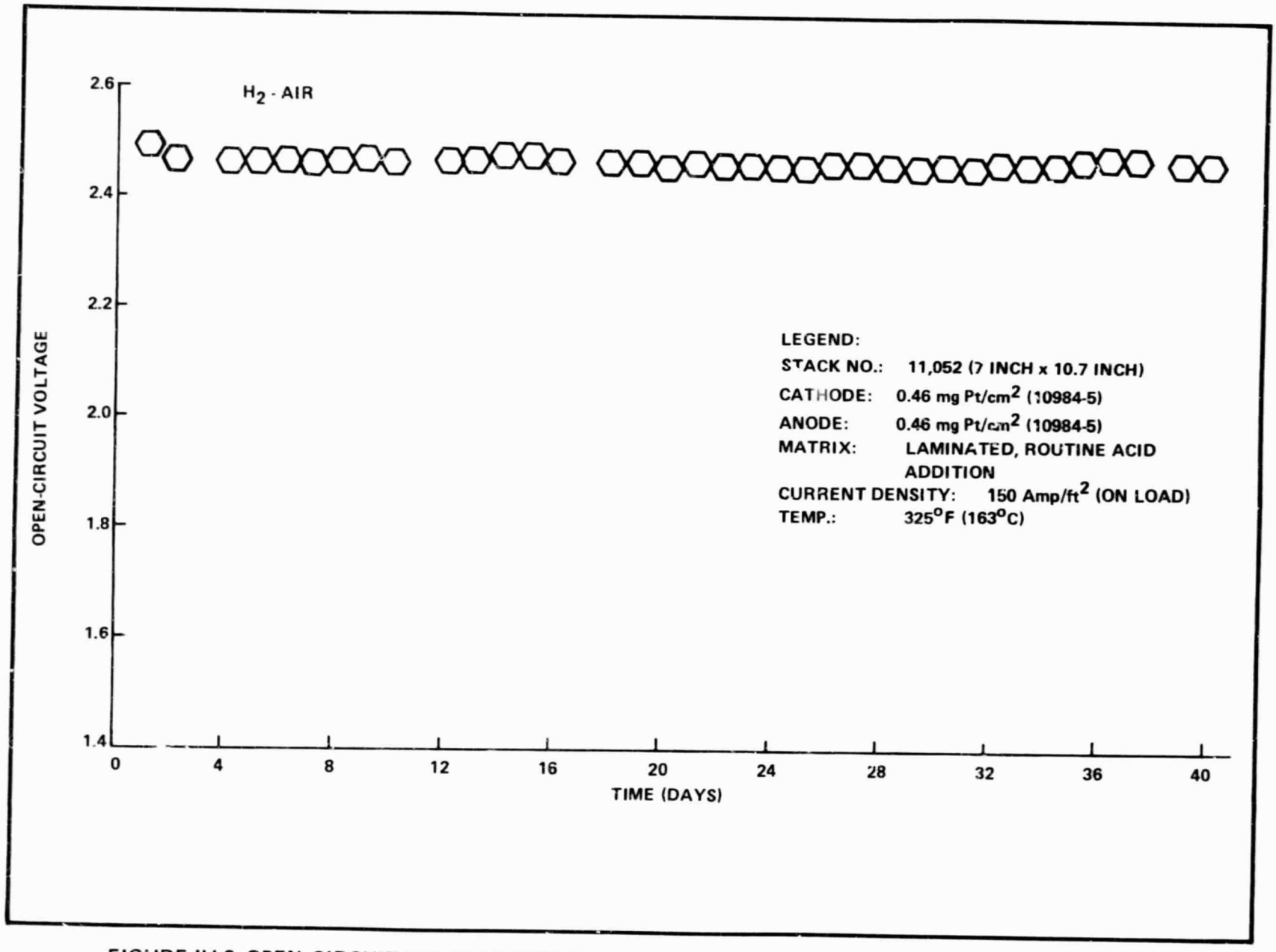

FIGURE IV-6. OPEN-CIRCUIT VOLTAGE STABILITY OF 3-CELL STACK USING A–B–A CONSTRUCTION.

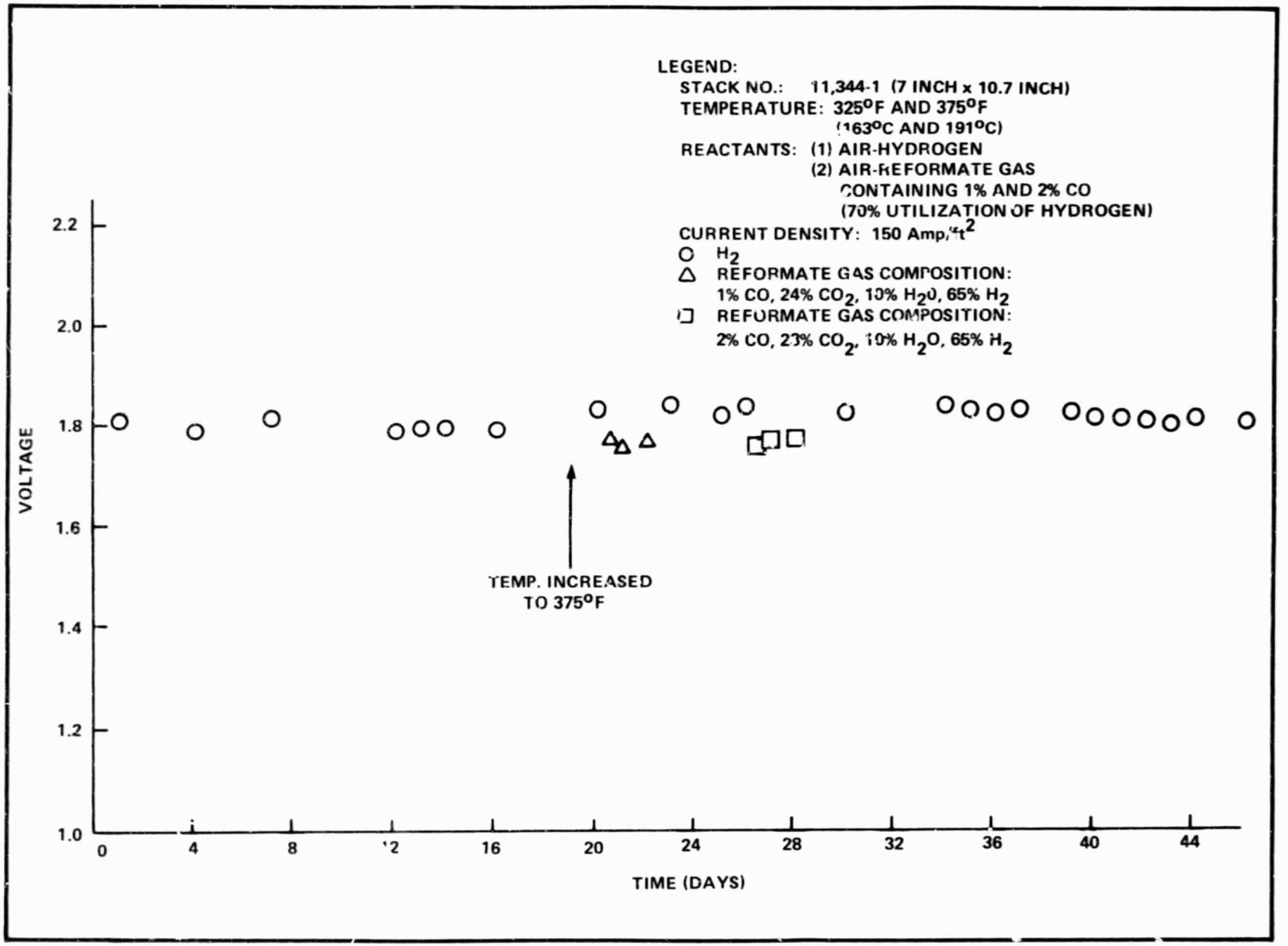

FIGURE IV-7. VOLTAGE STABILITY OF 3-CELL STACK CONSTRUCTED WITH NEEDLED-FELT CARBON PLATES

Toward the end of Phase II, experimentation was begun on a unitized needled-felt plate configuration. This approach would do away with discrete B-elements, provided satisfactory gas impermeability can be developed. Work in this direction will continue during Phase III.

E. CONCLUSIONS

- Multi-element bipolar plates of the ABA type meet all functional requirements for this component.

- Needled-felt bipolar plate A-elements perform well and offer the potential for low cost via continuous CVD processing.

SECTION V
COOLING PLATES AND COOLANT MANIFOLDS

The cooling plates used in this program were of the liquid-coolant spiral flow type, inserted into fuel cell stacks at 4-cell intervals. One cooling plate was also placed outboard of each current-collecting plate to maintain the temperature at the ends of the stack.

The simple, three-piece design of the aluminum cooling plates is shown in Figure V-1, prior to machining. The assembly to be brazed consists of the body, the cover sheet, and the manifolding connection. The last item is shown in one of two alternate positions.

A spiral flow path was machined into the body by a numerically controlled (N.C.) milling machine. The external shapes of the body and cover sheet were formed on the same N.C. machine.

In larger quantities, the body could either be stamped and formed from a thin sheet of aluminum or cast from aluminum. The casting could be either a precision die casting requiring no further machining or a low cost sand casting which would require grinding both surfaces to achieve the necessary flatness and surface finish. The cover sheet could be stamped out of the brazing sheet instead of using the N.C. mill. Further engineering is needed to reduce the cost of machining the manifolding connection while keeping the pressure drop low.

The external connections and orientations of the cooling plate were varied by rotating the cooling plate about its axis. With two different manifold connection locations, eight different cooling plate orientations could be obtained. Four of these had their

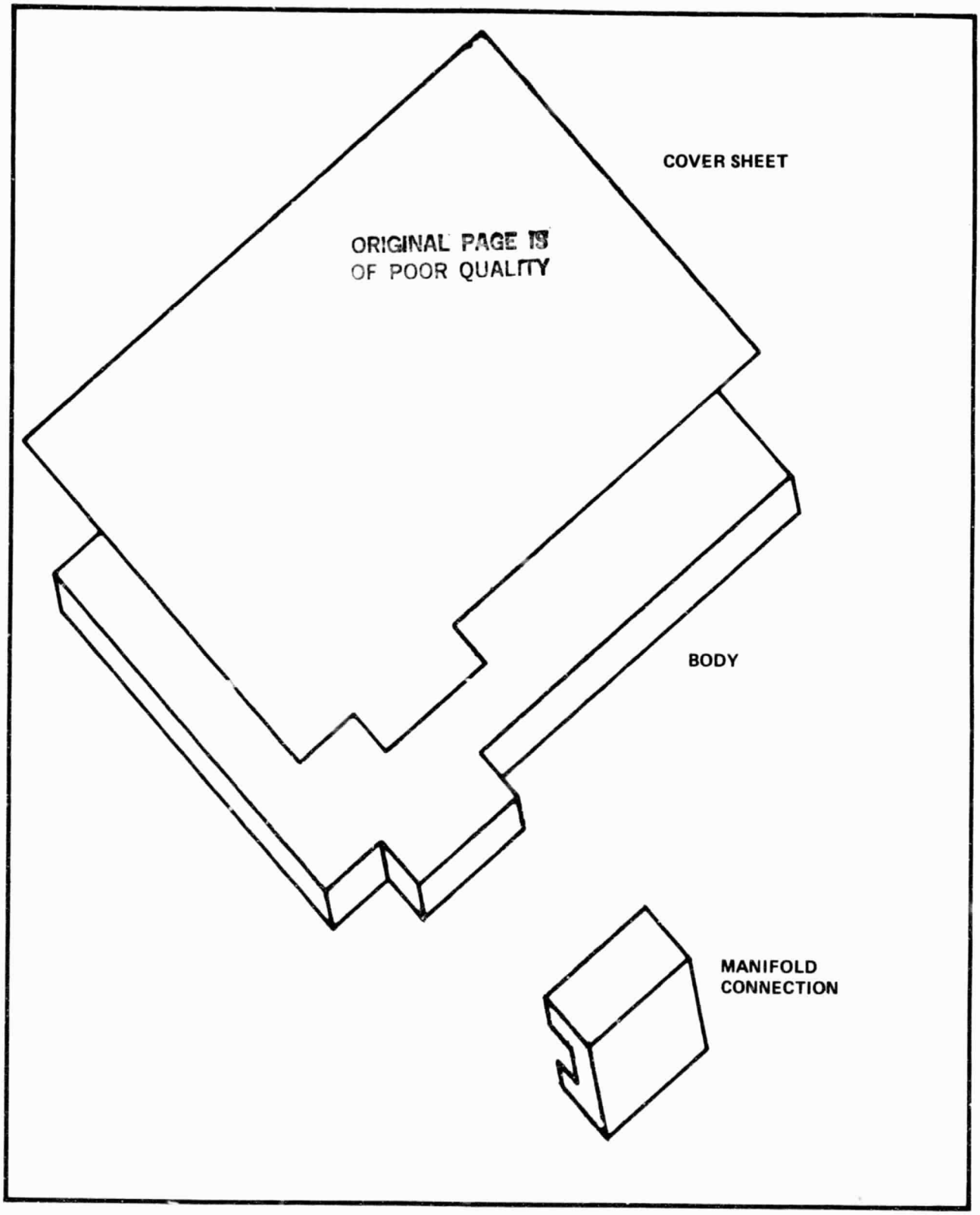

FIGURE V-1. COOLING PLATE

manifold connections on the air inlet side of the stack and the other four on the air exit side. The advantage of staggering the manifold connections was that it permitted them to be linked to each other within the confines of the air manifolds.

After machining and brazing of the cooling plates, they were plated with copper. The finished thickness was 5/16". Expanded copper screens were placed on both sides of the cooling plate, adjacent to bipolar plate B-elements in the stack to improve electrical contact.

The cooling plates of 5kW Stack No. 1 were interconnected by flexible hose assemblies. The connecting hoses ran vertically between cooling plate manifolding connections and terminated in manifolds within the top and the bottom end-plates. This arrangement is diagrammed in Figure V-2.

The hose was a 3/8 inch I.D., 1/32 inch wall Teflon tube reinforced by fiberglass braiding to give it the required high temperature strength. The hose assemblies had a machine-swaged swivel fitting attached to each end; these were factory pressure-tested to insure a leak-free connection. The swivel fitting was a 37° JIC standard with a metal seat. The swivel joints facilitated rapid installation of the hoses. The hose ends were angled 10° from the vertical to accommodate changes in stack height.

Coolant was distributed through the various cooling plates in multiple parallel paths to maintain low pressure drop (see Figure V-2). The total pressure drop across each of the main branches of the complete cooling system for 5kW Stack No. 1 was about 3 psi, which resulted in a parasitic power loss of only about one-half of one percent of the stack rated power. The coolant used in this system was Therminol 44.

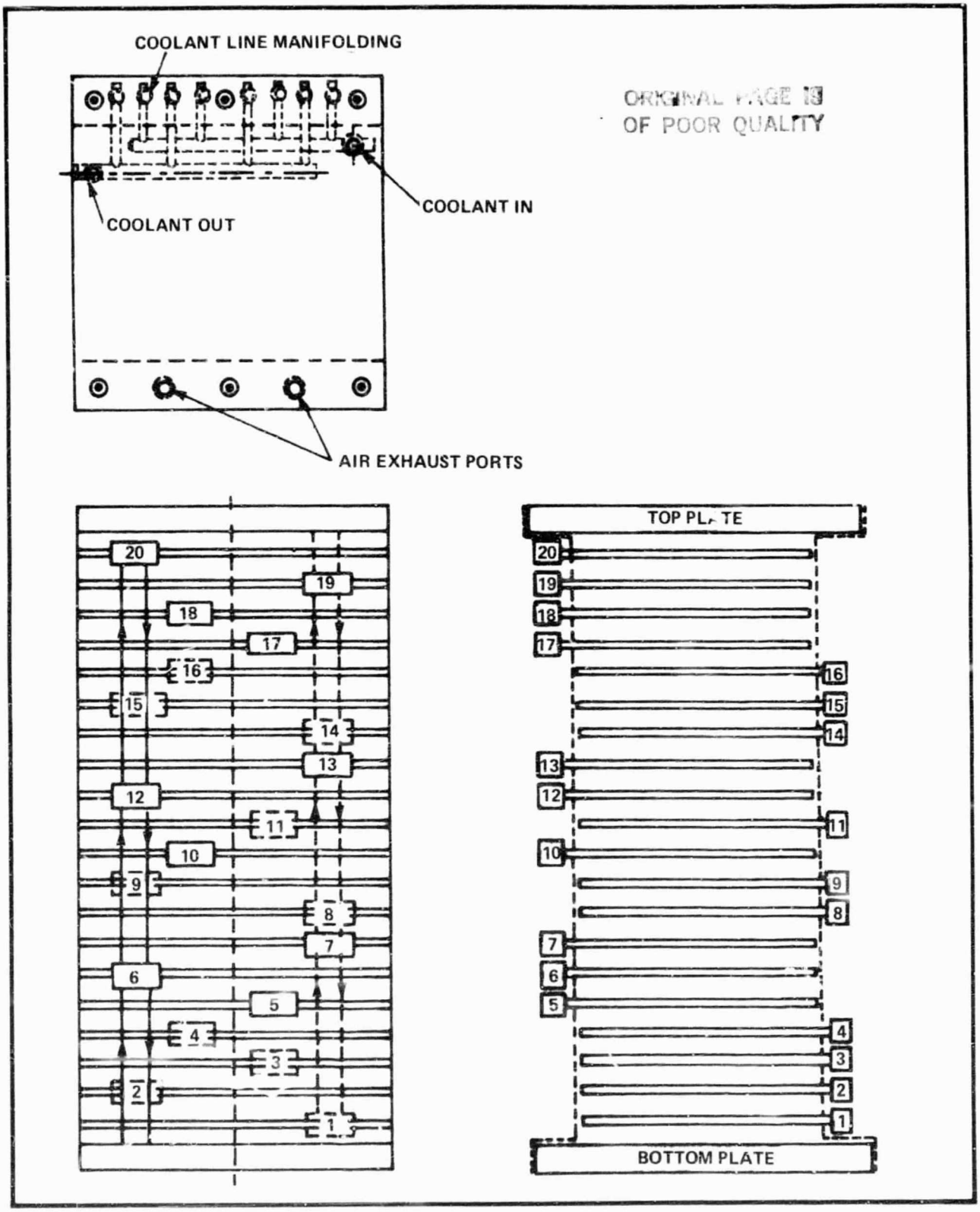

FIGURE V-2. STACK COOLING SYSTEM

The cooling scheme was effective in establishing uniform temperatures across the cells of each stack. This is illustrated by the temperature map of Figure V-3, taken from one of the mid-stack cells of Sub-Stack No. 1. Comprehensive temperature data were obtained for this stack of 7-inch x 10.7-inch cells because of the convenience of grooves in the Tylan bipolar plates.

Tear-down inspection of stacks subjected to long-term testing using ABA bipolar plates with Grafoil B-elements revealed a degree of corrosive attack at the cooling plate surfaces. Analysis of the corrosion products confirmed that phosphoric acid had penetrated into the interface. Late in Phase II a promising approach to achieve a corrosion-resistant interface was developed. Initial electrical conductance and corrosion resistance of plates prepared using this approach look attractive. This development will be pursued further in the early stages of Phase III.

CONCLUSIONS

- Aluminum-based intercell cooling plates utilizing a dielectric liquid coolant provide a relatively uniform temperature distribution across the surface of cells within the stack.

- A promising method of protecting the surfaces of cooling plates against corrosion has been developed.

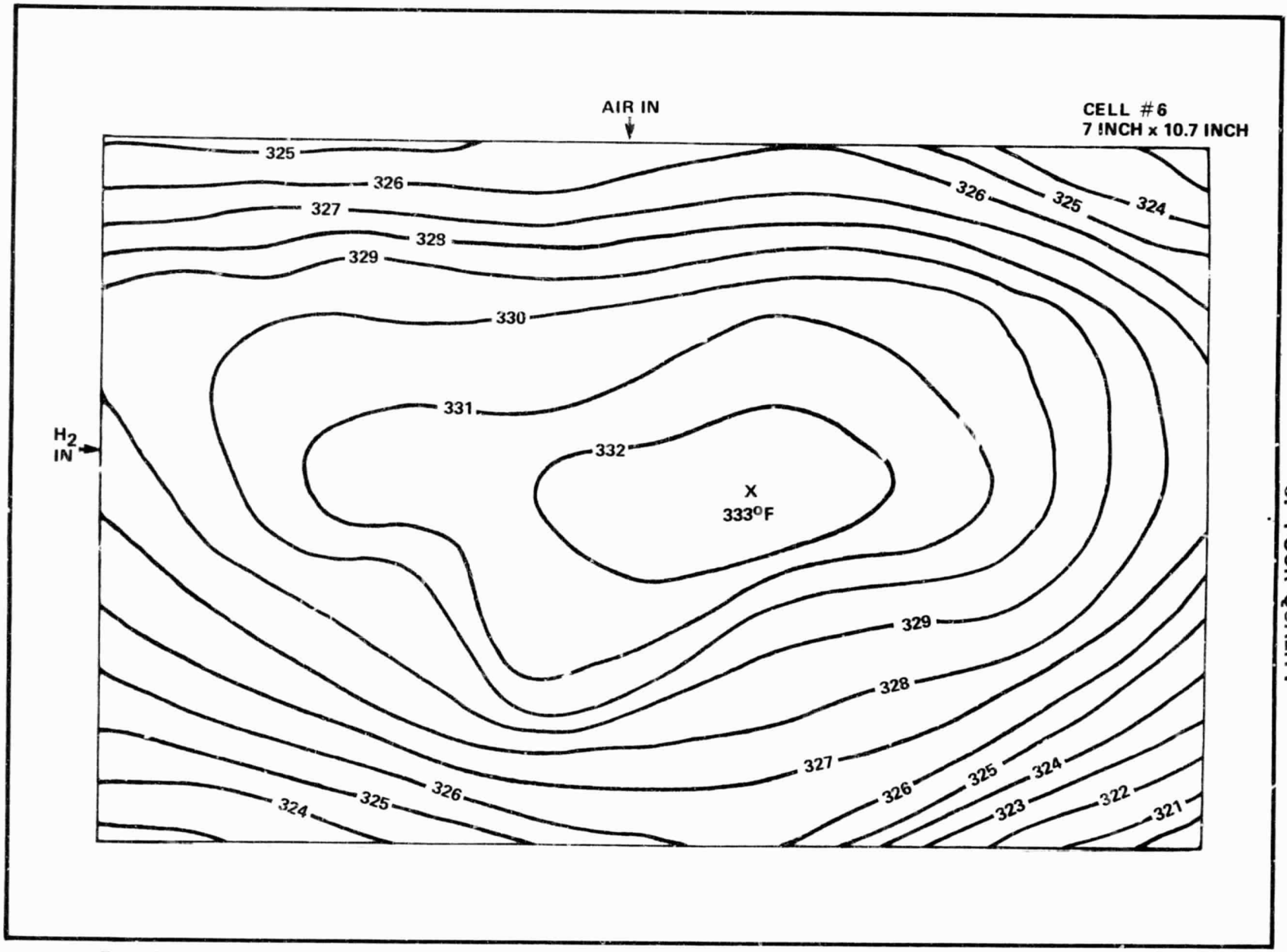

FIGURE V-3. TEMPERATURE PROFILE OF CELL #6 IN 10-CELL STACK; CURRENT DENSITY = 150 A/Ft^2

SECTION VI
ACID MANAGEMENT

A design requirement with phosphoric acid fuel cells is compensation for the acid electrolyte that is lost through evaporation, misting, and migration to other regions of the cell and stack. Electrolyte levels in the matrix and electrode catalyst layers must be maintained, either by internal storage or by periodic addition, if proper cell operation is to continue over long periods of time.

Since the laminated matrix layers used in most of the work of Phase II are quite thin, their acid-inventory capacity is low. It is therefore particularly necessary to implement the means for acid-replenishment in this type of cell. Figure VI-1 shows three candidate internal storage configurations for providing additional acid to the matrix. Single cell test results for configuration B were quite satisfactory over the short term, running on hydrogen/air at 163°C. Testing of configurations A and C was discontinued because of their relatively high IR-losses.

A configuration that utilizes the A-element for acid storage is shown in Figure VI-2. Single-cell test results in which the A-element was charged with acid during the cell assembly are shown in Figure VI-3. The initial high performance eroded sharply after 10 days. The cell was disassembled, and additional acid was charged to the A-element. This served to stabilize performance through the duration of the test (45 days). It appears that improvement in the acid communication between the A-element and the matrix would be required in order for this configuration to be suitable.

In the next stage of development a new acid-replenishment configuration was used in conjunction with acid storage in the A-element.

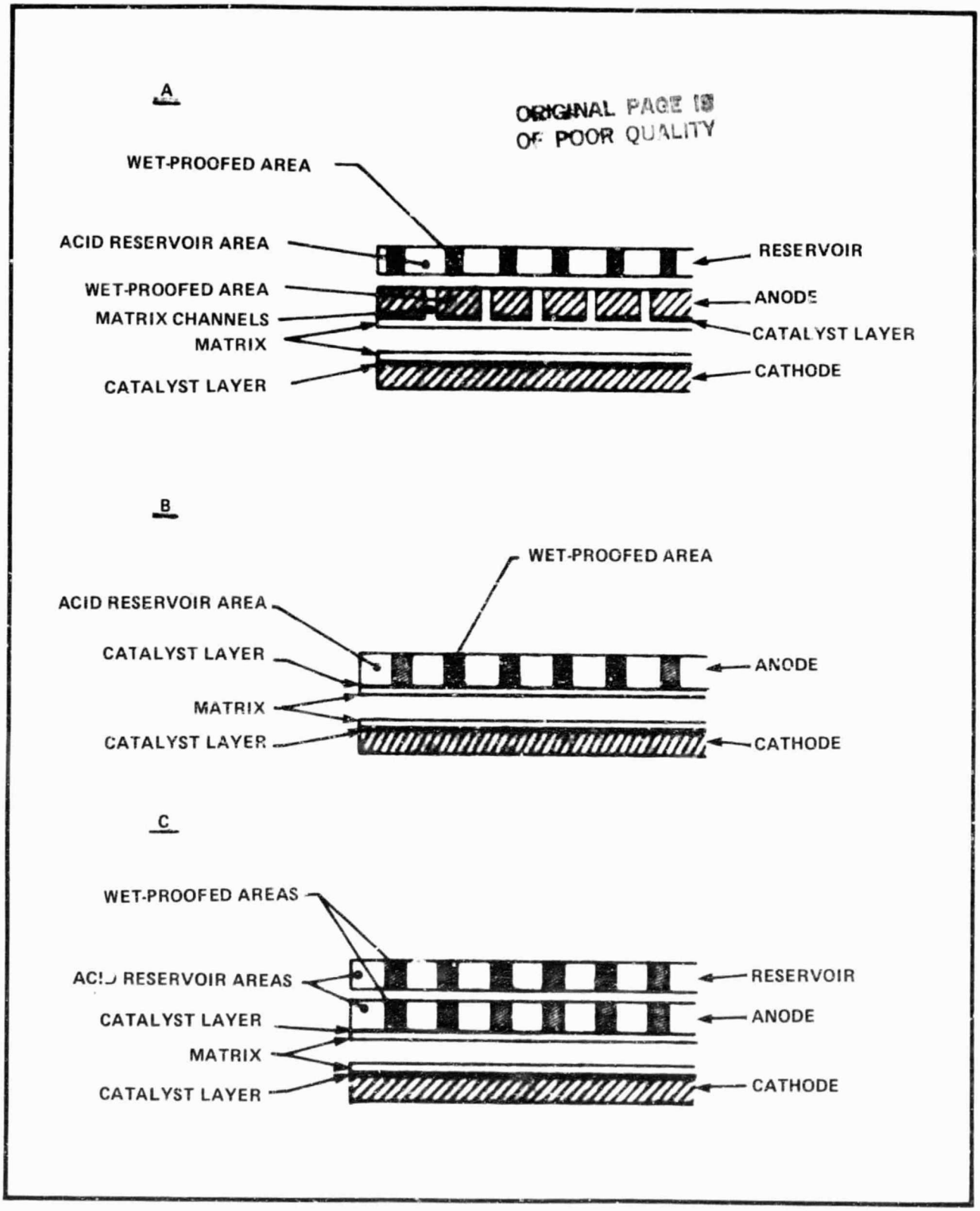

FIGURE VI-1. ACID-MANAGEMENT CONFIGURATIONS

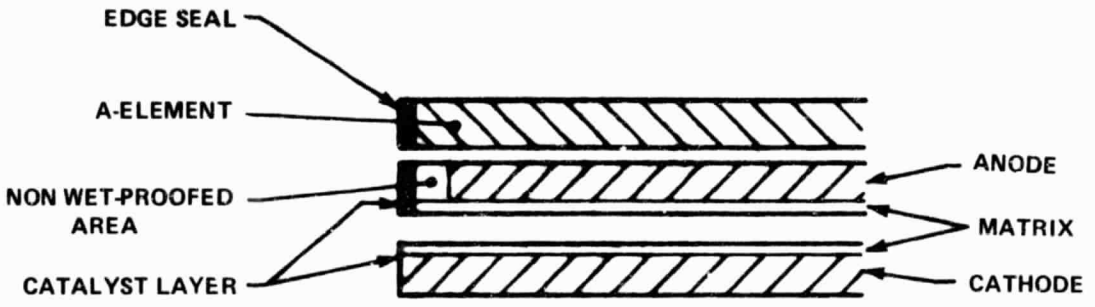

FIGURE VI-2. METHOD FOR UTILIZING A-ELEMENT FOR INTERNAL ACID STORAGE

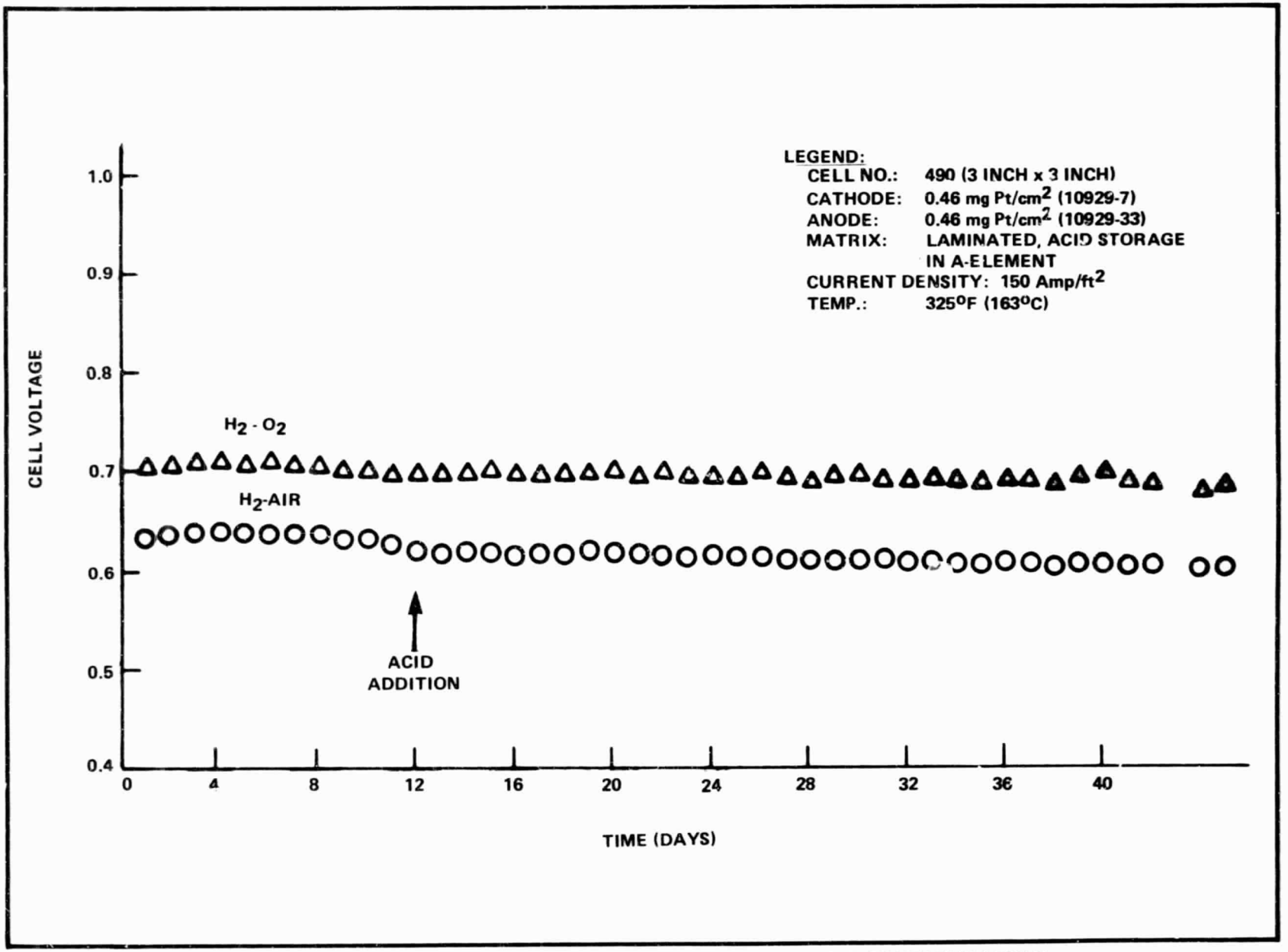

FIGURE VI-3. SINGLE-CELL EVALUATION OF ACID MANAGEMENT CONFIGURATION

The open-circuit voltage and performance on load of a single-cell using this arrangement were quite stable for over 2000 hours. The voltage under load for this cell is shown in Figure VI-4. Although there was an apparent loss of cathode wetproofing effectiveness (as indicated by increasing oxygen-gain), the H_2/O_2 performance (and hence the electrochemical activity as well as IR-drop) was extremely stable.

To further test the concept of acid storage in the A-element in conjunction with the acid-replenishment configuration a large single-cell (7" x 10.7") was constructed with these features. This test was started at 163°C and gradually raised to 191°C after three days. The voltage at 150 A/ft^2 for a total of 72 days of testing is shown in Figure VI-5. As indicated in the figure, the voltage under load declined significantly after about two weeks of operation, suggesting that the rate of acid uptake by the matrix was insufficient. Manual acid replenishment at a single point on the periphery of the matrix was conducted every two days thereafter for the duration of the run. Performance returned to its original level and remained there through the 1000 hour period (42 days). The implications for acid management by single-point replenishment are very positive.

The stable voltage due to external acid replenishment was abruptly interrupted at 47 days due to an accidental hydrogen supply shut down. For a period of time the cell was under a hot open-circuit condition, and this apparently caused an irreversible loss in performance.

Acid management by periodic manual addition was further tested in large stacks and is described in a later section of this report. Toward the end of Phase II the design for an automatic replenishing system was initiated.

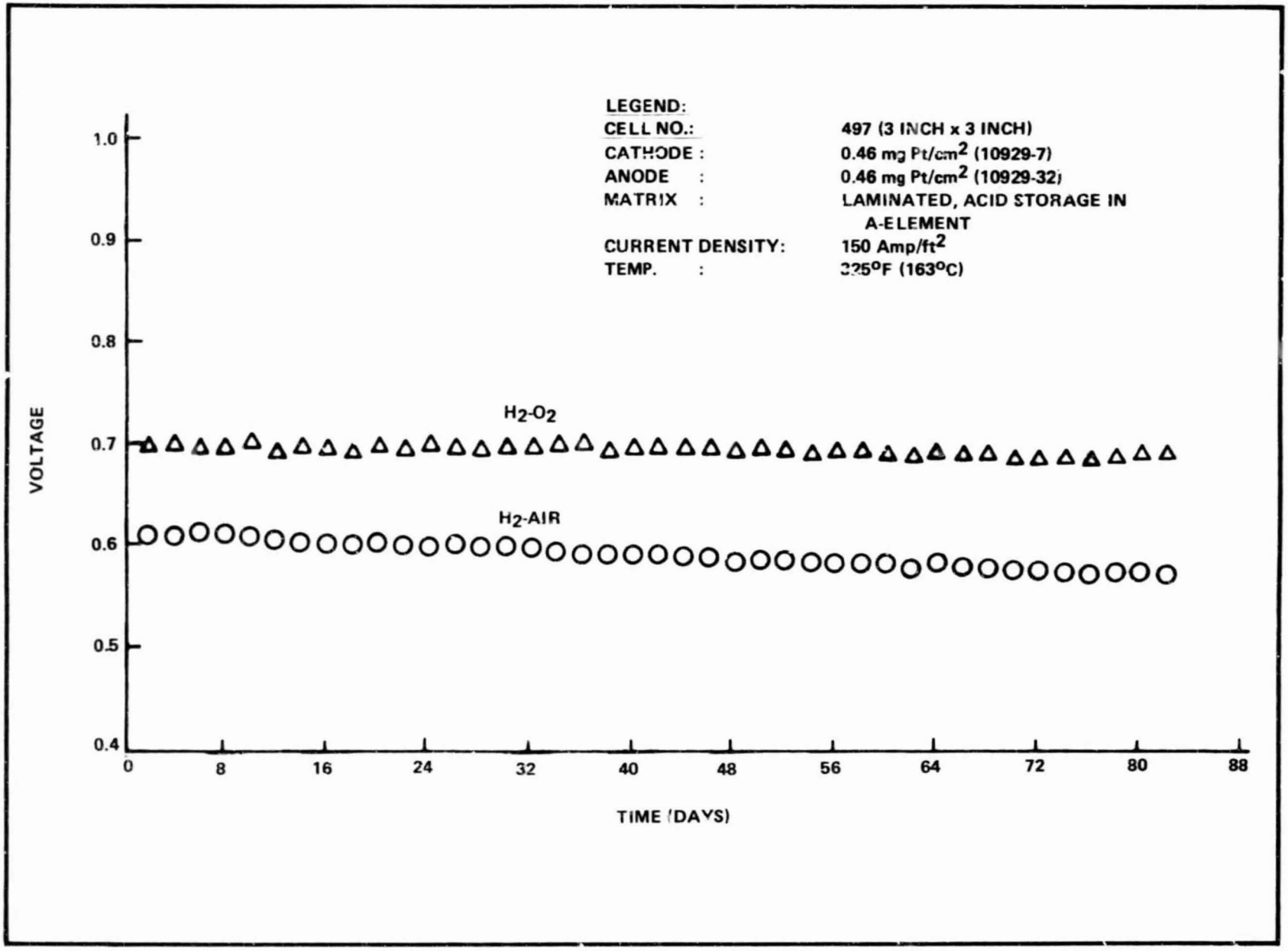

FIGURE VI-4. SINGLE-CELL EVALUATION OF ACID MANAGEMENT CONFIGURATION

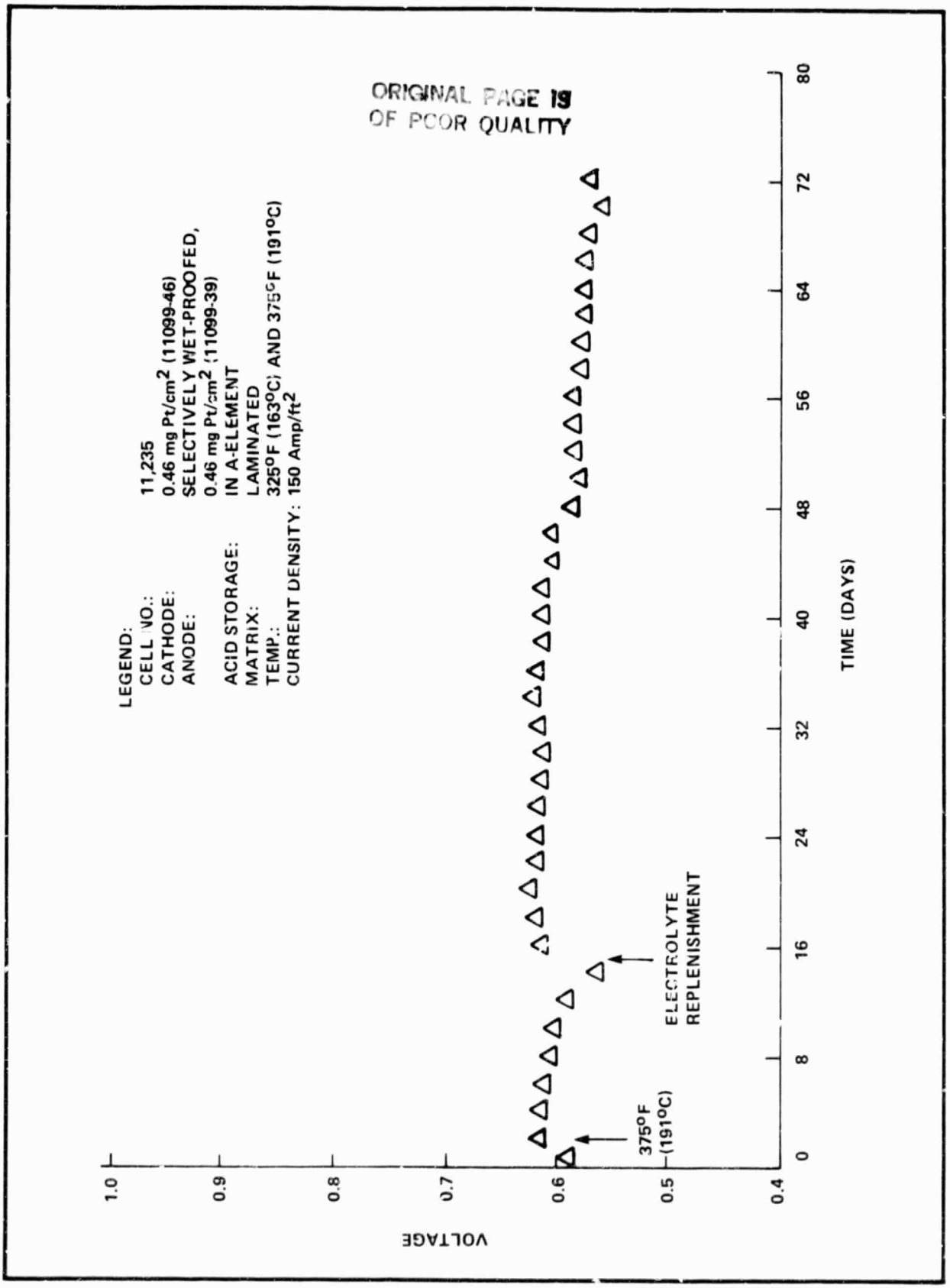

FIGURE VI-5. VOLTAGE STABILITY OF LARGE SINGLE-CELL (7 in. x 10.7 in.) WITH INTERNAL ACID STORAGE

CONCLUSIONS

- A cell configuration has been developed that is particularly amenable to external acid replenishment.

- Automated means of acid replenishment should be evaluated in future stacks.

SECTION VII

REACTANT MANIFOLDS

The reactant gas manifold design for 5kW Stack No. 1 provided all sealing surfaces in a vertical plane as shown in Figure VII-1. A stack of this size can be expected to exhibit appreciable creep in the direction perpendicular to the cell planes as the stack is gradually compressed, perhaps to the extent of 0.5 inch over the first few thousand hours of operation. Sealing the manifold between two horizontal planes, one at the top and one at the bottom, would require more compliance than could be expected of a gasket. By keeping all sealing surfaces in a vertical plane, this problem is alleviated.

The end plates were designed to be flush with the edges of the stack on the hydrogen inlet and outlet sides. The hydrogen manifold is a five-sided box-shaped structure which fits snugly against the edges of the end plates and the sides of the stack. The perimeter of the manifold was fabricated from four pieces of thin-wall rectangular tubing. The fifth side of the box was formed by welding a thin-gauge metal sheet over the frame formed by the rectangular tubes. The three sealing surfaces of each hydrogen manifold were subsequently ground to flatness. Wire rope assemblies with ends threaded left-handed and right-handed tied the two hydrogen manifolds together so as to support the mid-stack area.

The air manifold, also shown in Figure VII-1, is similar in concept to the hydrogen manifold. The perimeter of the manifold was fabricated from four pieces of structural angle. The pieces were welded together with the larger dimension forming a plane against the hydrogen manifold edges and the end plates. The air manifolds have a cover sheet which bolts in place and is removable to

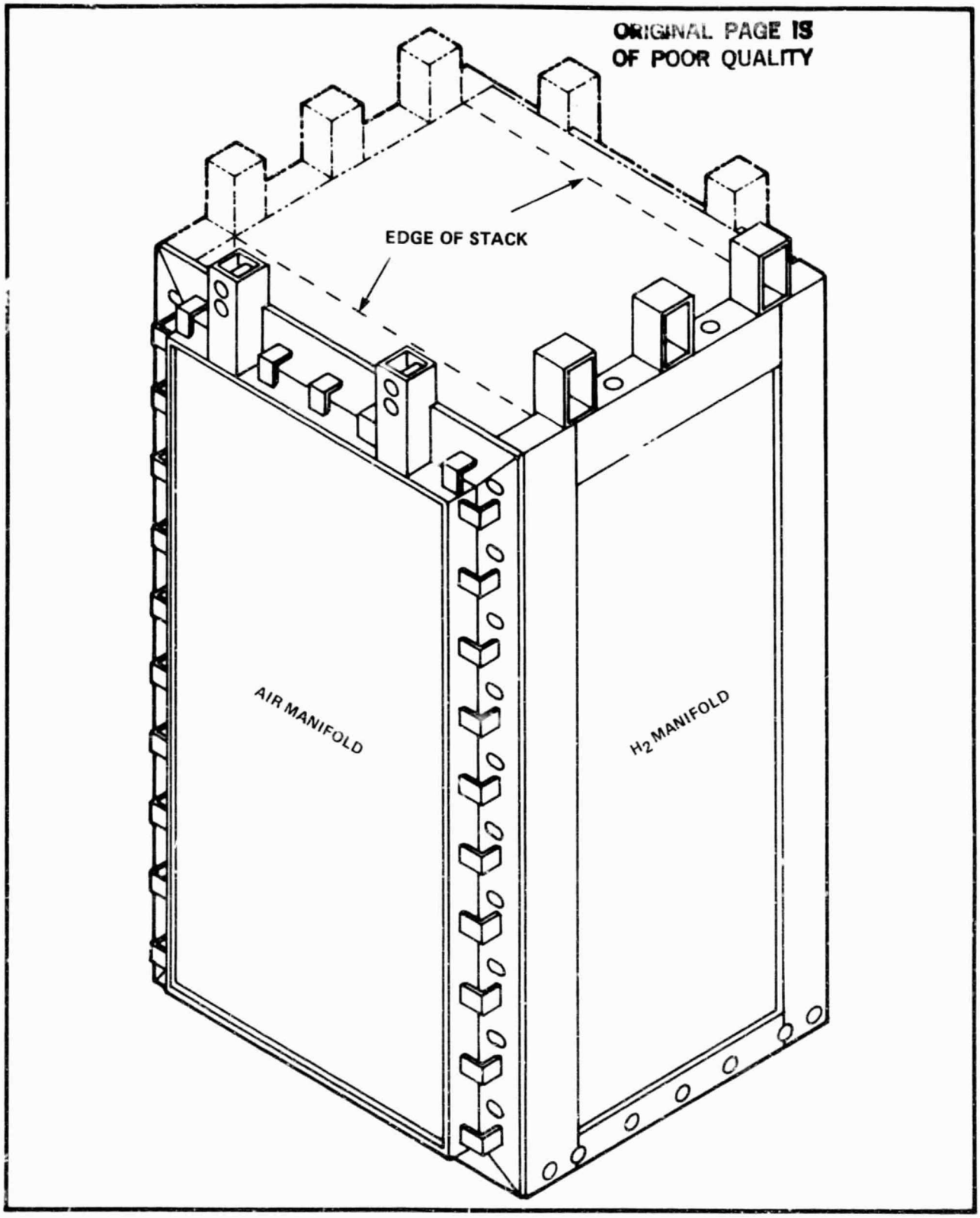

FIGURE VII-1. REACTANT MANIFOLDS

facilitate maintenance. The seal between the cover and frame is simple because there is no relative movement between these parts. After welding, the single sealing surface of each air manifold was ground to flatness.

The hydrogen manifold design for 5kW Stack No. 2 was modified to provide a corner seal as shown in Figure VII-2. This serves to prevent lateral leakage of hydrogen resulting from any misalignment between the manifold gasket and the edge-seals of the various cells.

Another modification has been adopted for the preliminary design of the 25kW stack that will be constructed during Phase III. This entails independently sealed hydrogen and air manifolds, thus avoiding the possibility (in case of seal failure) of intermixing of the two gases (see Task IV).

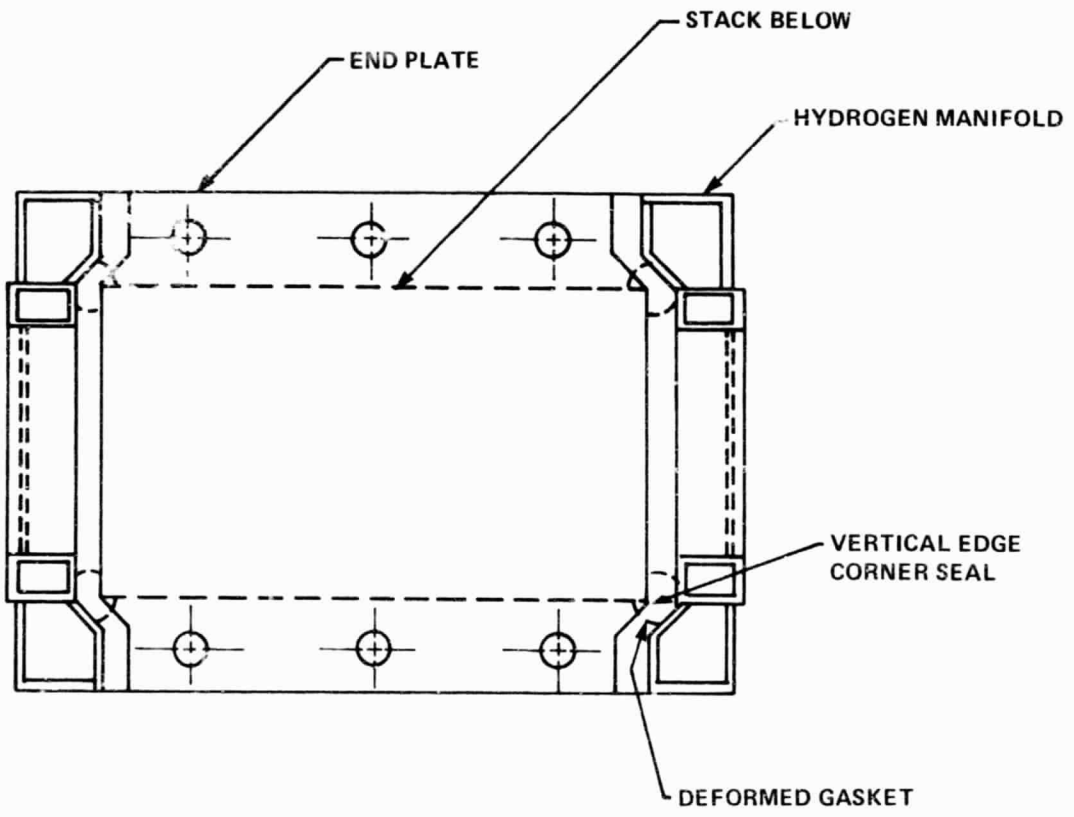

FIGURE VII-2. HYDROGEN MANIFOLD CORNER SEAL

SECTION VIII

SUB-STACK AND 5KW STACK TESTING

SUB-STACK NO. 1

A 10-cell stack was built and tested using 7 inch x 10.7 inch cells and Tylan all carbon bipolar plates. The stack was run for 500 hours at 150 A/ft^2 and a nominal temperature of 163°C. Individual cell performances were quite uniform, averaging about 0.615 volt. Stack performance variation over the course of the test was minimal as shown in Figure VIII-1, although an overnight hydrogen supply interruption after 19 days appears to have caused an average loss of a few millivolts per cell.

Open-circuit voltage remained steady throughout the test at about 8.1 volts as shown in Figure VIII-2. The voltage versus current density behavior of the stack is shown in Figure VIII-3. Although these curves show little variation over the course of the test, there appears to be a trend toward higher catalyst activity but greater oxygen diffusion losses with time. This is attributed to progressive wetting of the cathode catalyst with accompanying buildup of acid within the catalyst layer. The electrodes used in this stack were less hydrophobic than those in use later in the component development programs.

This stack was liquid-cooled (dielectric) using one cooling plate at the mid-point of the stack and one at either end. The temperature profiles of each cell were measured, and temperature uniformity across each cell and from cell to cell was good (see, e.g., Figure V-3). The temperature of Cell No. 10 (bottom cell) was somewhat low because it was adjacent to a relatively cool outside cooling plate.

After the 500-hour test and subsequent extensive temperature probing, the stack was shut down and held at room-temperature for about 1000 hours. The stack was then restarted, and performance at 163°C was about 20 mV lower on average than before shutdown.

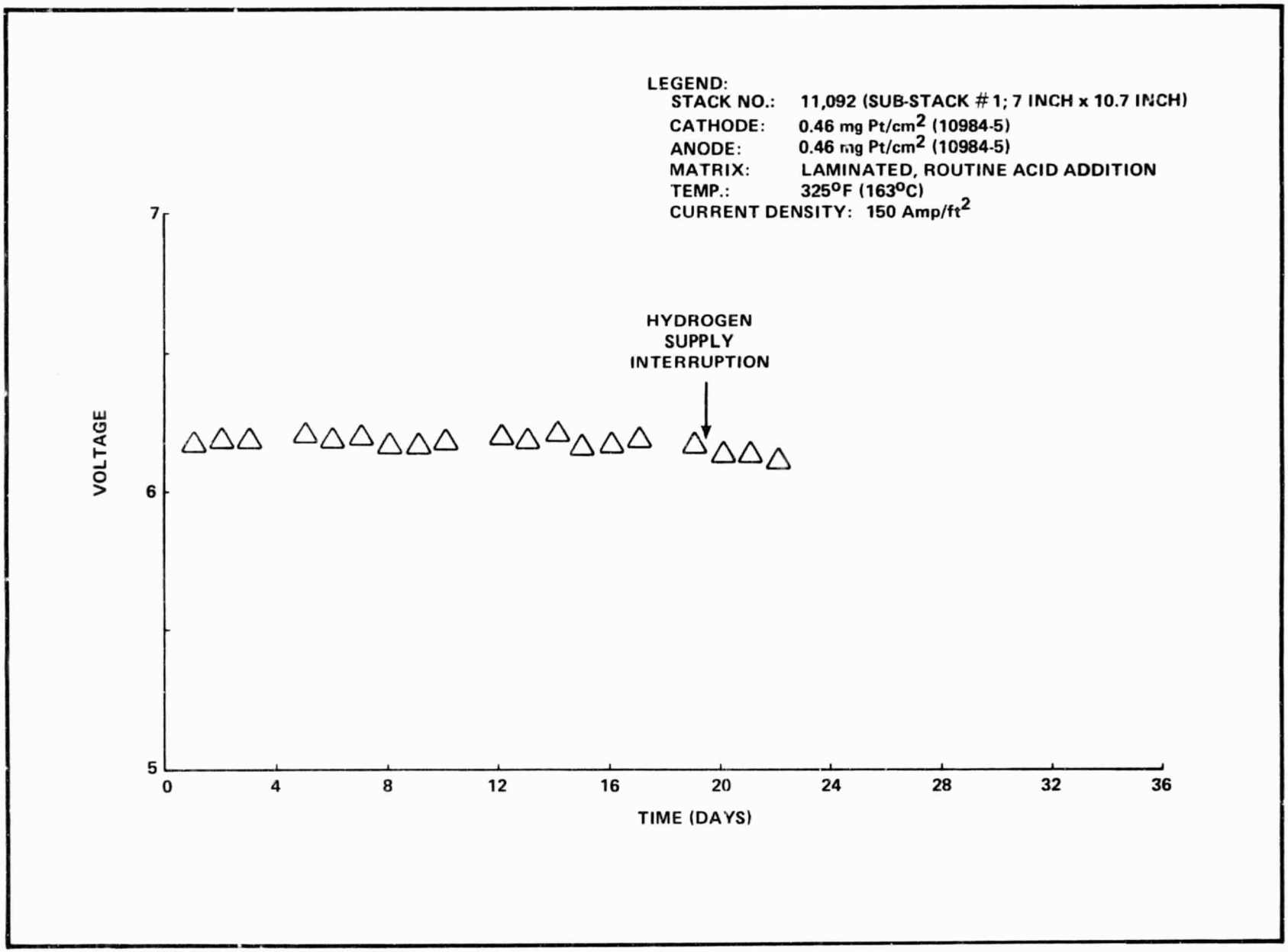

FIGURE VIII-1. PERFORMANCE STABILITY OF 10-CELL STACK

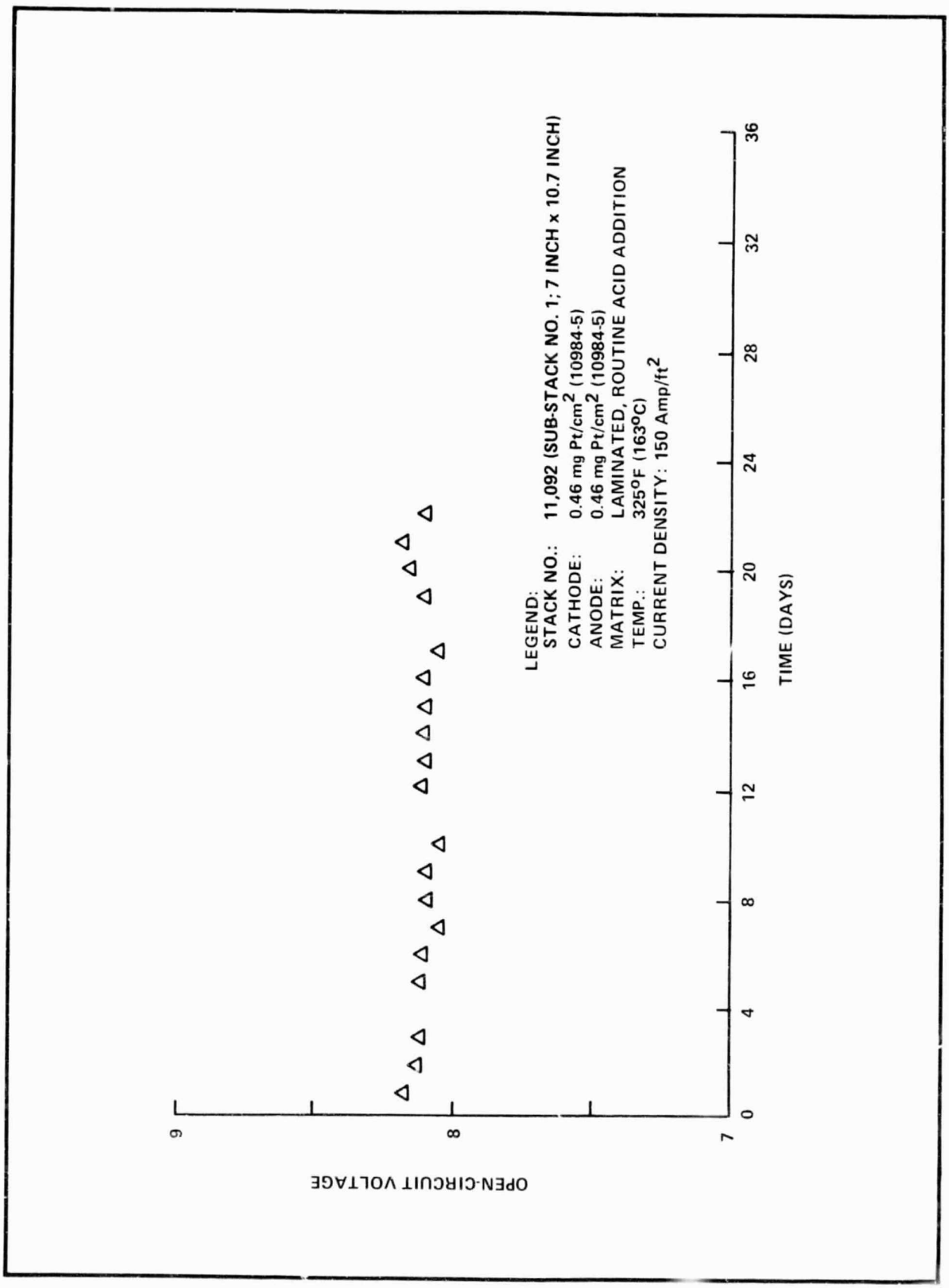

FIGURE VIII-2. OPEN-CIRCUIT VOLTAGE STABILITY OF 10-CELL STACK

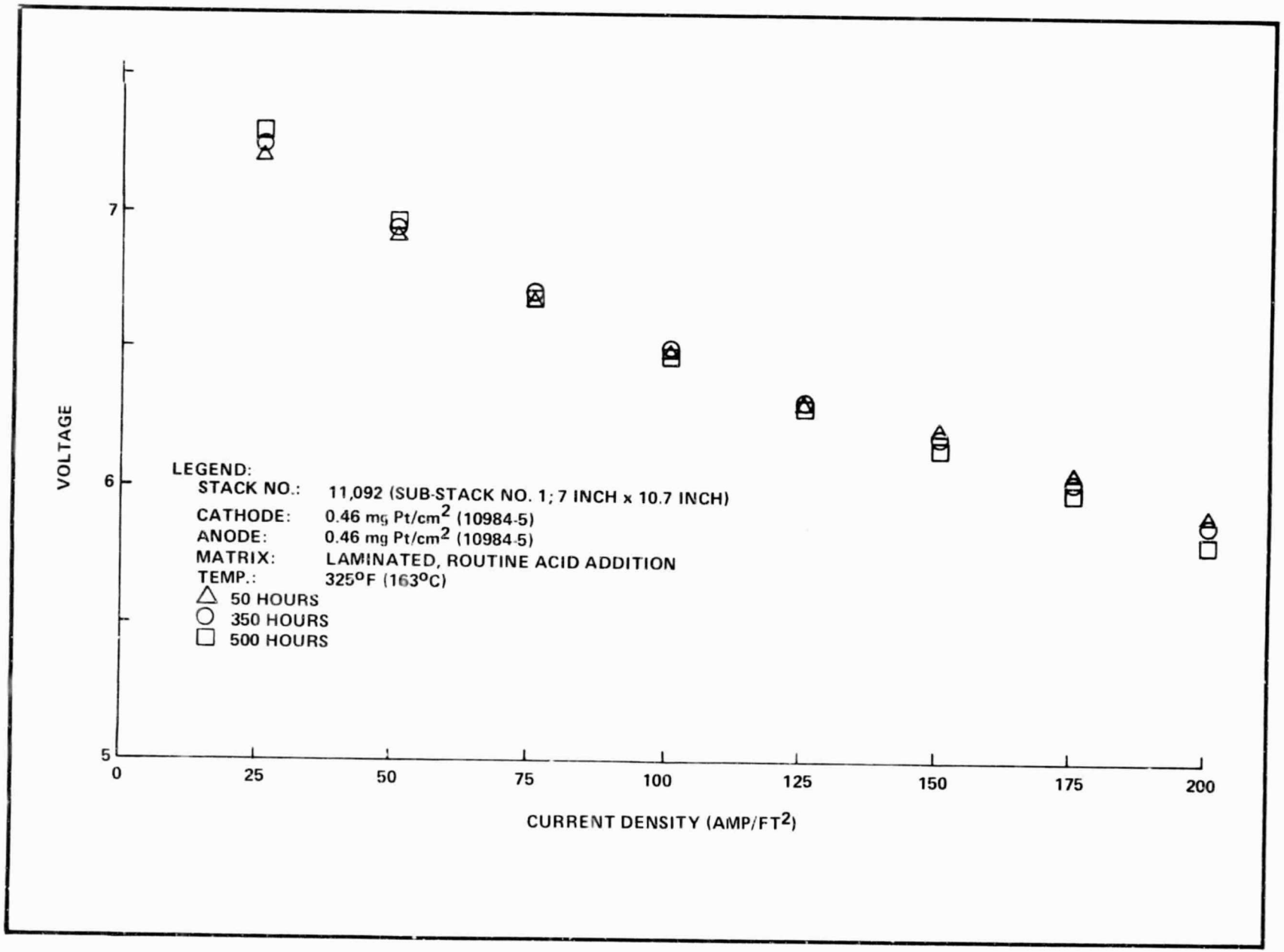

FIGURE VIII-3. 10-CELL STACK PERFORMANCE

This is attributed to incremental electrolyte flooding of the electrodes caused by the long shutdown, but loss in some cells might have resulted from physical damage inflicted during the temperature probing.

The temperature of the stack was raised to 191°C for several days before final shutdown. Performance increased to about 0.61 Volts per cell. Despite the shutdown and subsequent temperature increase, stack open-circuit voltage was maintained.

SUB-STACK NO. 2

This 12-cell stack was built with 10.7 x 14 inch cells (0.9 ft^2 active area) and non-bonded ABA-type bipolar plates. Non-grooved reticulated vitreous carbon A-elements were used along with Grafoil B-elements. The stack was run continuously on hydrogen/air for almost 3200 hours. The endurance plot at 150 A/ft^2 is shown in Figure VIII-4. Performance was quite stable through the first 2400 hours, averaging 0.60 volts per cell. Subsequent decay was almost entirely traceable to cell No. 9; diagnostic testing prior to shut-down suggested that anode poisoning might have been responsible for the decay in this cell.

Figure VIII-5 illustrates the open-circuit voltage of this stack, which was stable throughout the run; the average open-circuit voltage was about 0.85 volts per cell. This is attributed to the acid management procedures employed; acid was added routinely to an extended section of each cathode on the air exit side.

Figure VIII-6 presents current-voltage curves obtained at three different times over the course of the test. These show an increase in performance level from 48 to 1275 hours which is attributable to the 14°C temperature increase. The performance at 2000 hours indicates some decline at the higher current densities, suggesting increased electrolyte penetration of the cathode catalyst layer. This decline was virtually restricted to two of the cells.

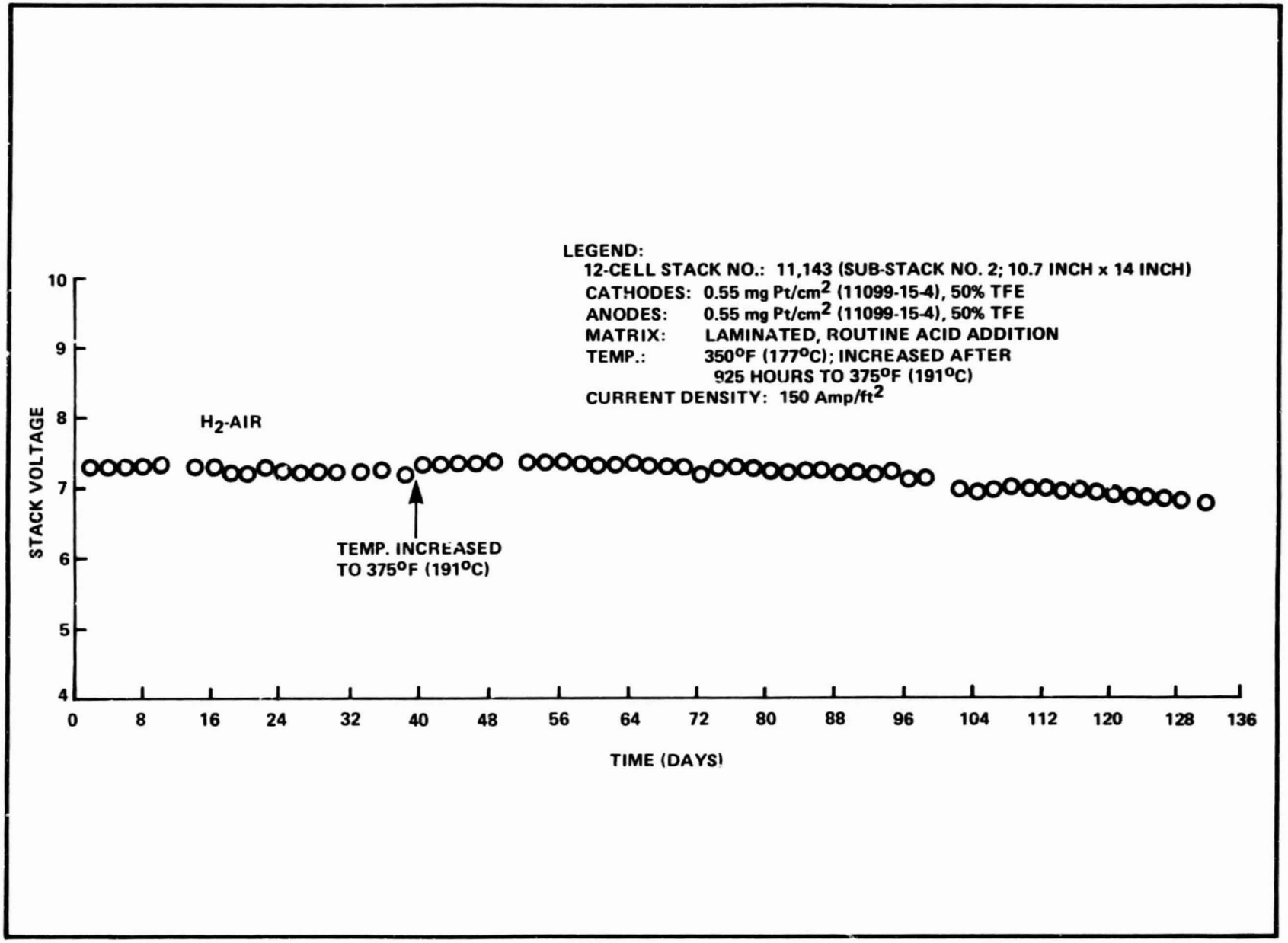

FIGURE VIII-4. VOLTAGE STABILITY OF 12-CELL STACK WITH A–B–A TYPE OF CONSTRUCTION

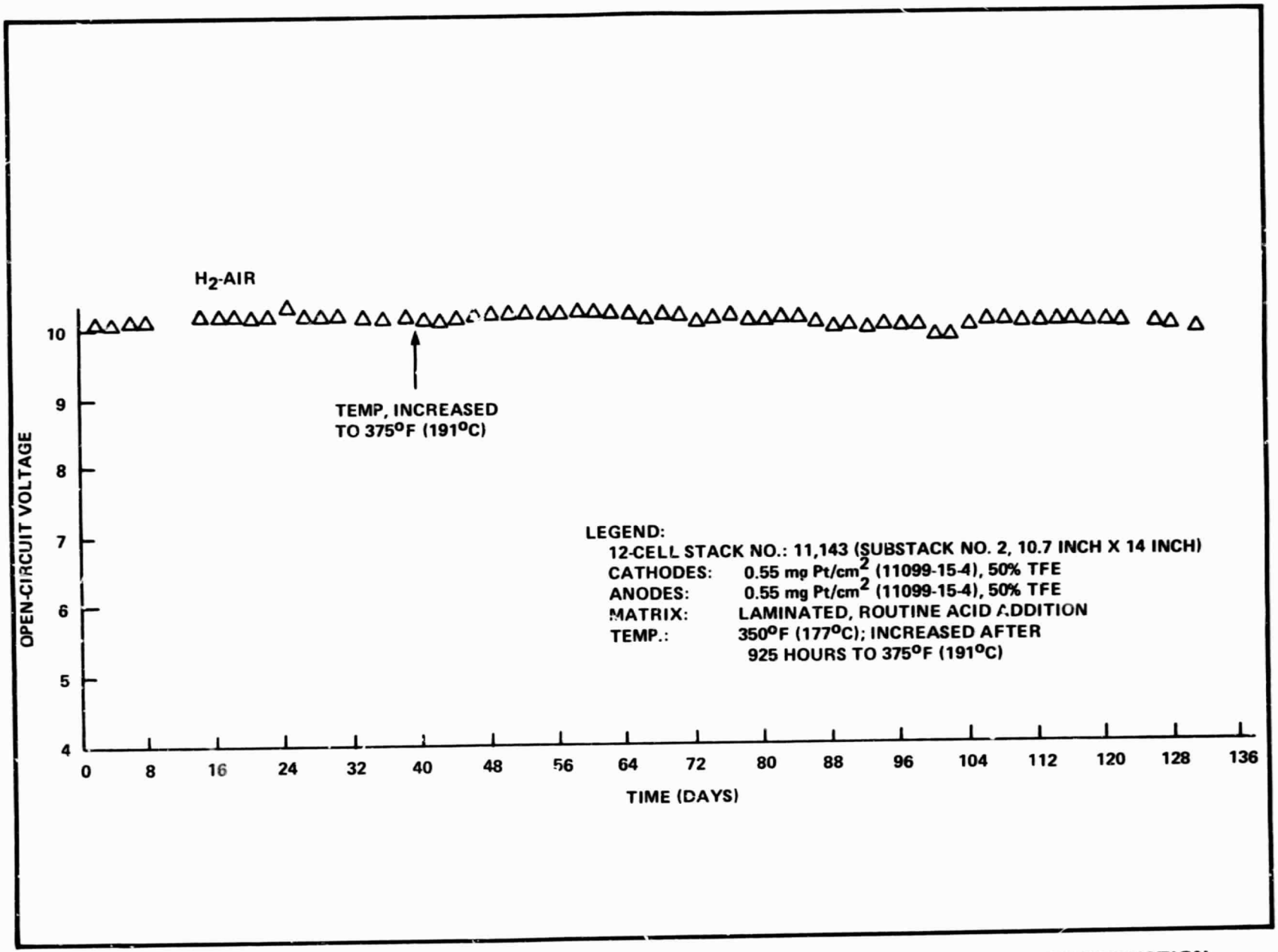

FIGURE VIII-5. OPEN-CIRCUIT VOLTAGE STABILITY OF 12-CELL STACK WITH A–B–A TYPE OF CONSTRUCTION

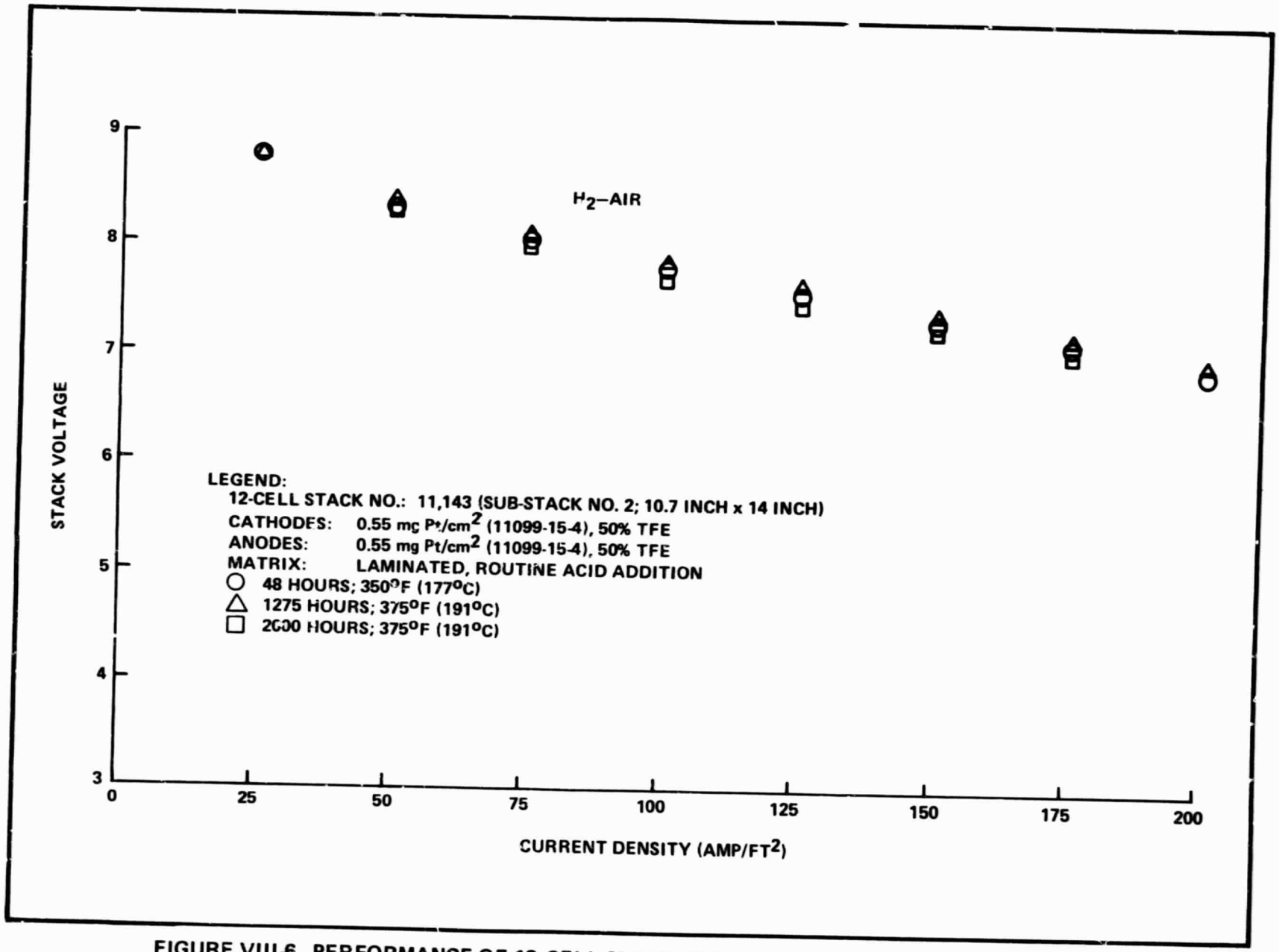

FIGURE VIII-6. PERFORMANCE OF 12-CELL STACK WITH A–B–A TYPE OF CONSTRUCTION

Figure VIII-7 illustrates the effect of air flow rate on stack performance with non-grooved ABA-type bipolar plates. Typical losses were obtained as the result of reduced air flow rate; i.e. there appeared to be no incremental loss in performance attributable to air flow within the non-grooved A-elements.

SUB-STACK NO. 3

Sub-Stack No. 3 was another 12-cell ABA-type stack. It was the first stack built with ABA plates that were fully bonded during processing. Also, this stack employed a developmental catalyst of the stabilized-Pt/stabilized-support type for the first time. It was found necessary to provide gas distribution grooves in the bipolar plate A-elements because the CVD loading was about twice the targeted amount (roughly 14 times original RVC weight, as compared to the typical seven times original weight).

Sub-Stack No. 3 was run for 500 hours at 150 A/ft^2. The average stack temperature was increased from 169°C to 191°C after one week. The performance history is shown in Figure VIII-8. Stack voltage was slightly lower than that of Sub-Stack No. 2. This resulted from a wide disparity in the performance of the individual cells. The disparity was apparently caused by non-uniform wetting of the anode catalyst layer in this relatively hydrophobic structure. The best cells exhibited good voltage levels, in the 0.63-0.64 volt range, but generally the quality of the developmental catalyst used for this stack was masked by the anode behavior. As a result of these findings, base-line (more hydrophilic) catalysts were used for anodes in subsequent stacks.

Figure VIII-9 shows the open-circuit voltage behavior for Sub-Stack No. 3. Once again, open-circuit voltage was quite acceptable, indicating continued successful operation in the areas of matrix integrity and acid management.

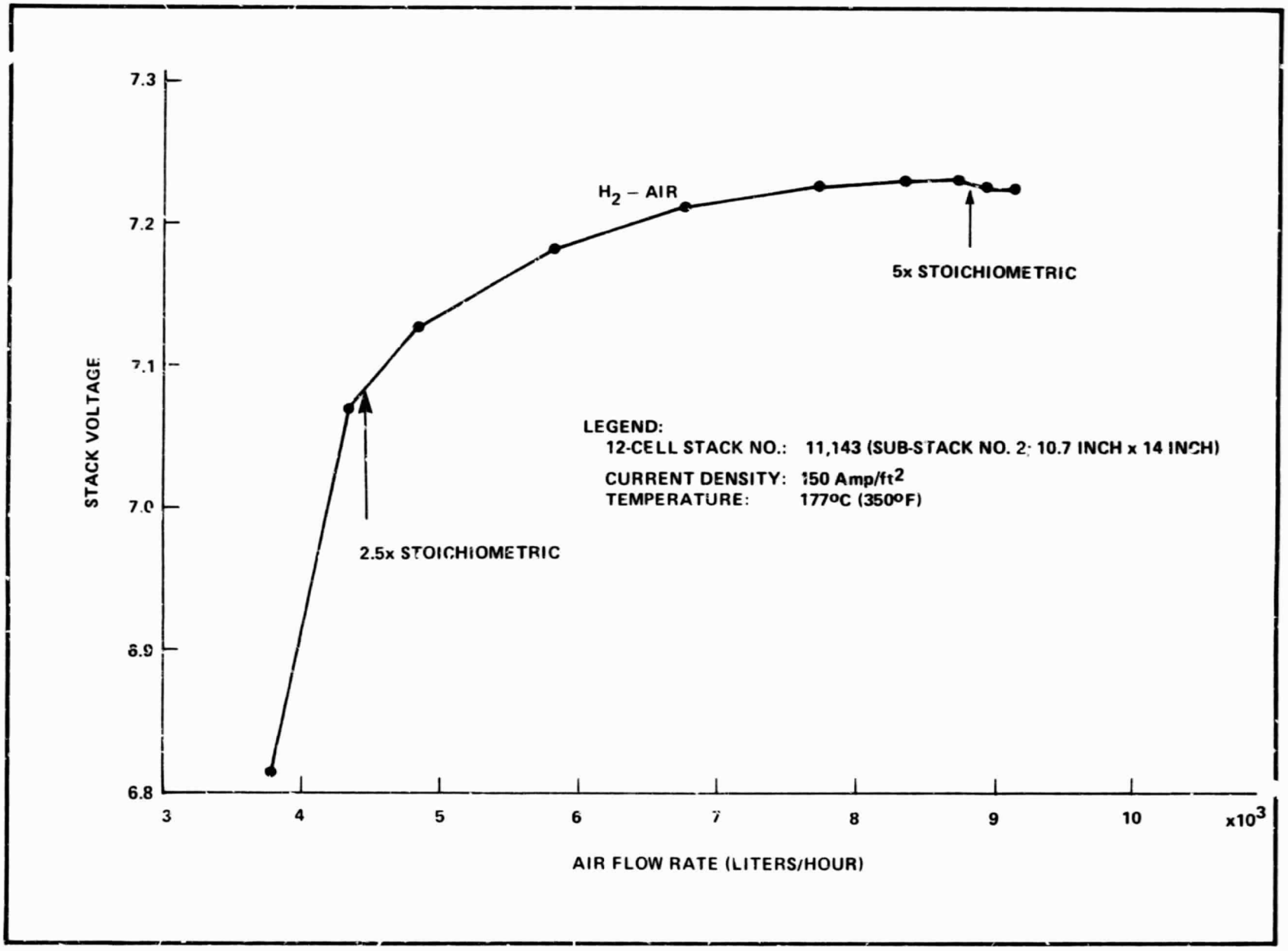

FIGURE VIII-7. THE EFFECT OF AIR FLOW RATE ON STACK PERFORMANCE

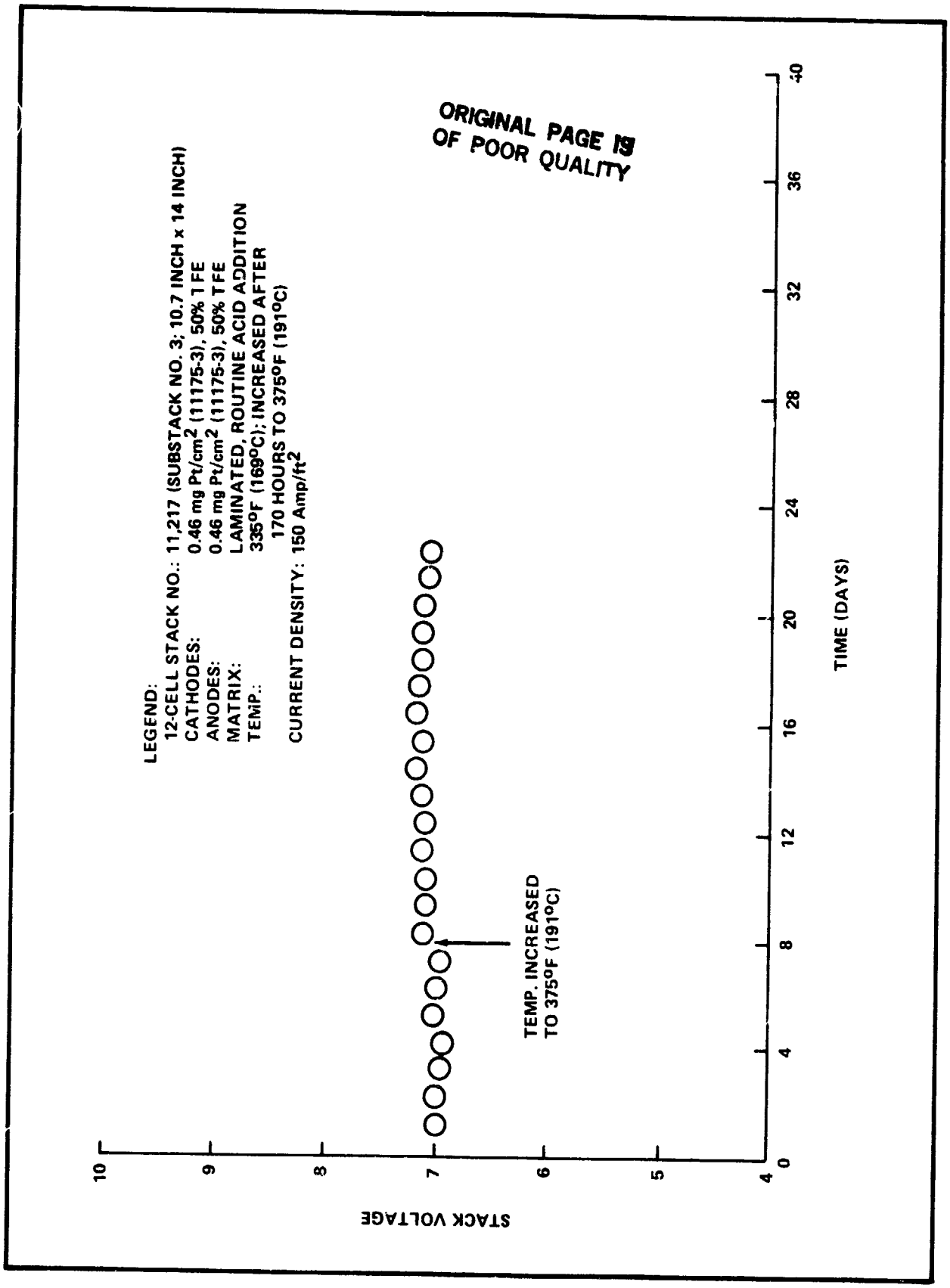

FIGURE VIII-8. VOLTAGE STABILITY OF 12-CELL STACK WITH A-B-A TYPE OF CONSTRUCTION

C - 2

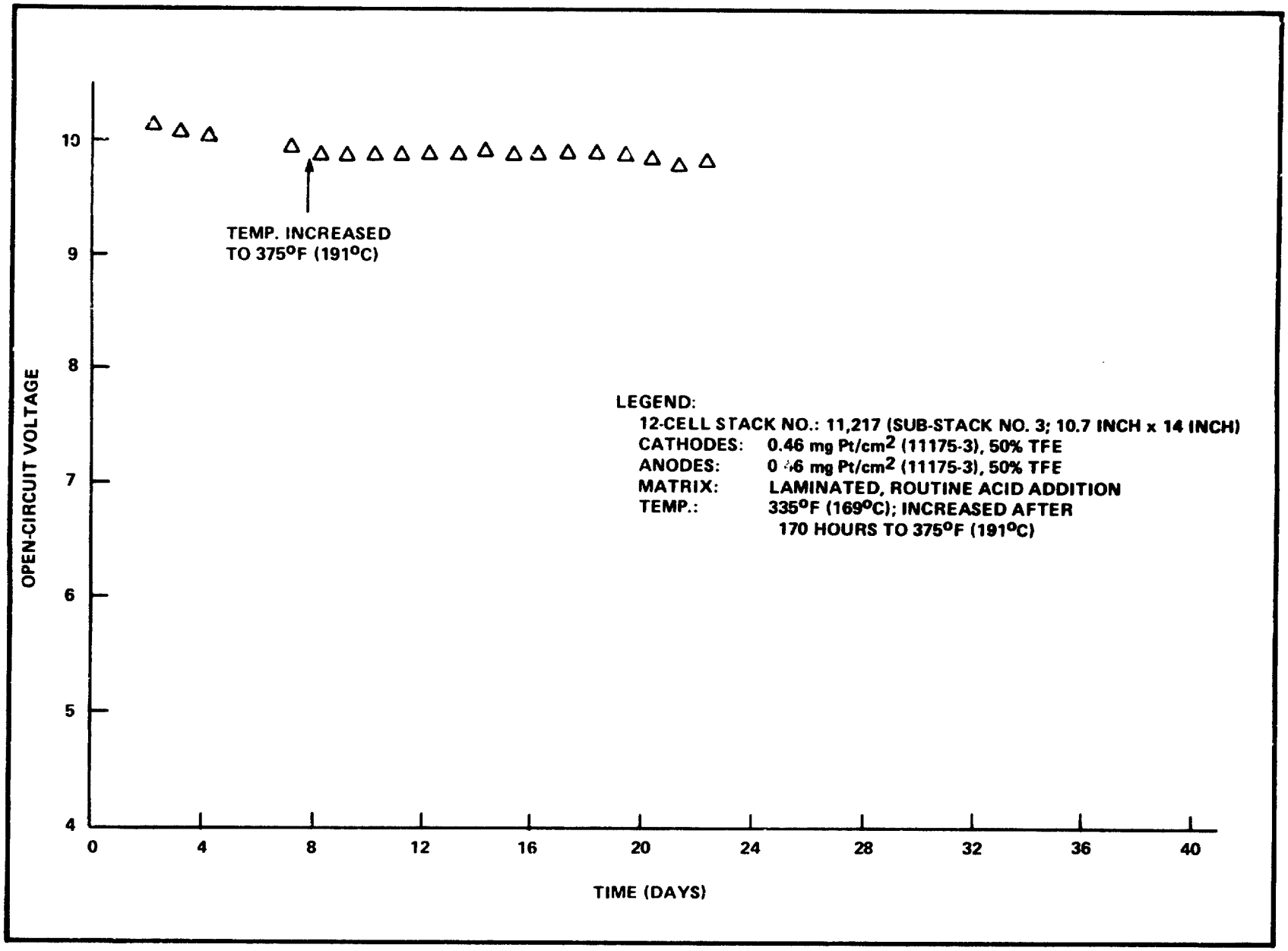

FIGURE VIII-9. OPEN-CIRCUIT VOLTAGE STABILITY OF 12-CELL STACK WITH A–B–A TYPE OF CONSTRUCTION

SUB-STACK NO. 4

This stack was a precursor to 5kW Stack No. 1. The components used in Sub-Stack No. 4 are summarized below:

Bipolar Plates: Fully bonded multiple-element plates of the non-grooved ABA type were used. The edge-sealing of the reticulated vitreous carbon A-elements was accomplished through impregnation using a graphite adhesive. The B-element was resin/CVD-treated woven fabric precursor material.

Cathodes: A 10% Pt on carbon developmental catalyst of the stabilized-support/stabilized-Pt type was employed, having a nominal loading of 0.46 mg Pt/cm^2. The electrode preparation was based on Engelhard-developed techniques. The Teflon content was 50%.

Anodes: A 10% Pt on carbon base-line catalyst was used with nominal loading of 0.46 mg Pt/cm^2. The Teflon content was 45%.

Matrix: The matrix consisted of silicon-carbide filler with TFE-30 binder. The matrix was laminated onto each electrode using screenless blade-coating methods. An acid-transport layer was placed between the electrodes with acid being added to an extension of the acid-transport layer (at air exit side) on a routine basis.

Cooling Plates: These were of the spiral flow type. Two were inserted into the stack, at four-cell intervals. Also, one was placed outboard of each current-collecting plate to retard heat-loss from the ends of the stack.

The main feature being tested in Sub-Stack No. 4 was the use of fully bonded, but non-grooved ABA plates.

The performance of Sub-Stack No. 4 during the 46 days of testing is shown in Figure VIII-10 (open-circuit voltage) and Figure VIII-11 (voltage at 150 A/ft^2). The open-circuit voltage, although

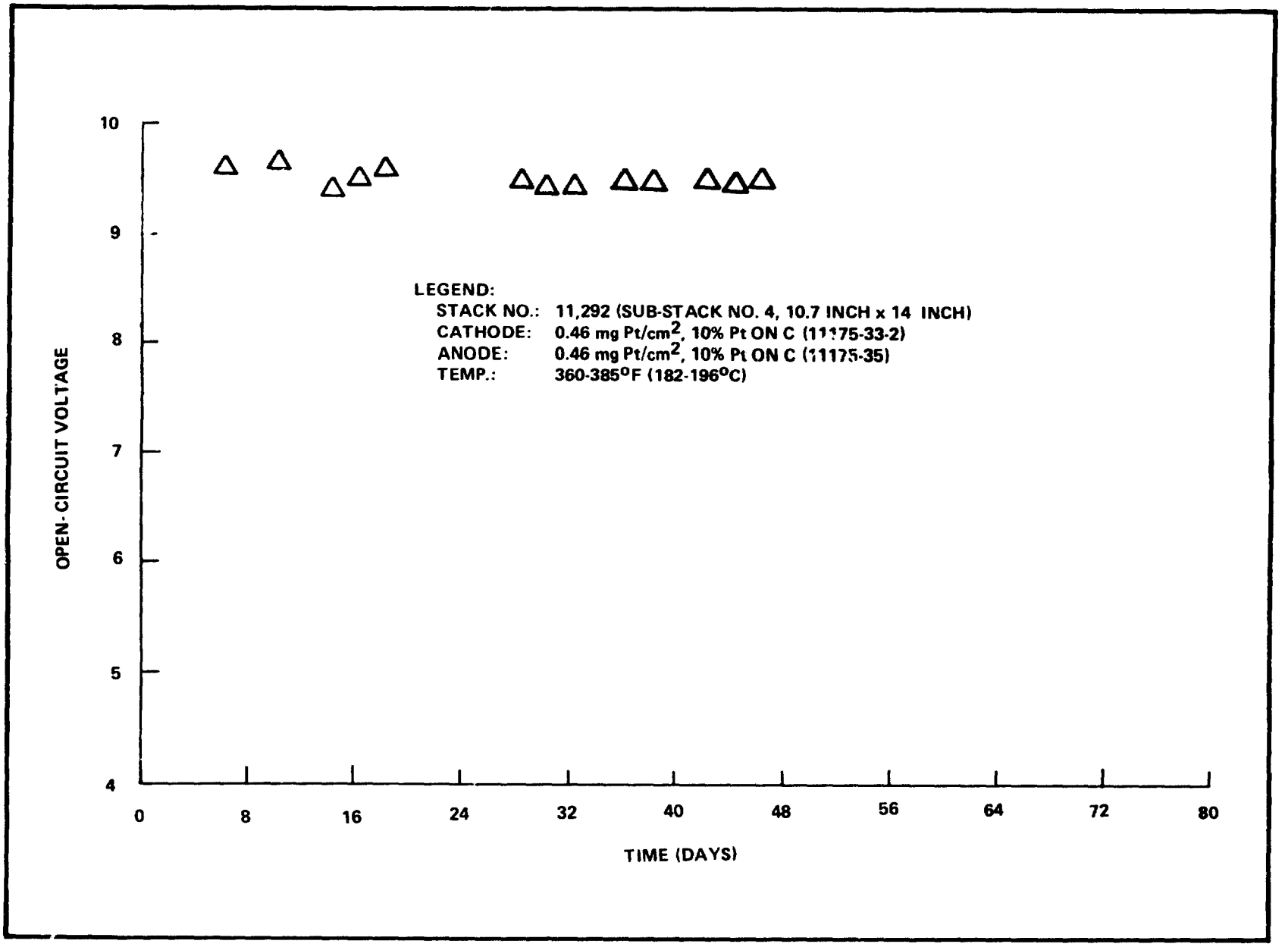

FIGURE VIII-10. OPEN-CIRCUIT VOLTAGE STABILITY OF 12-CELL STACK CONSTRUCTED WITH A–B–A CARBON PLATES

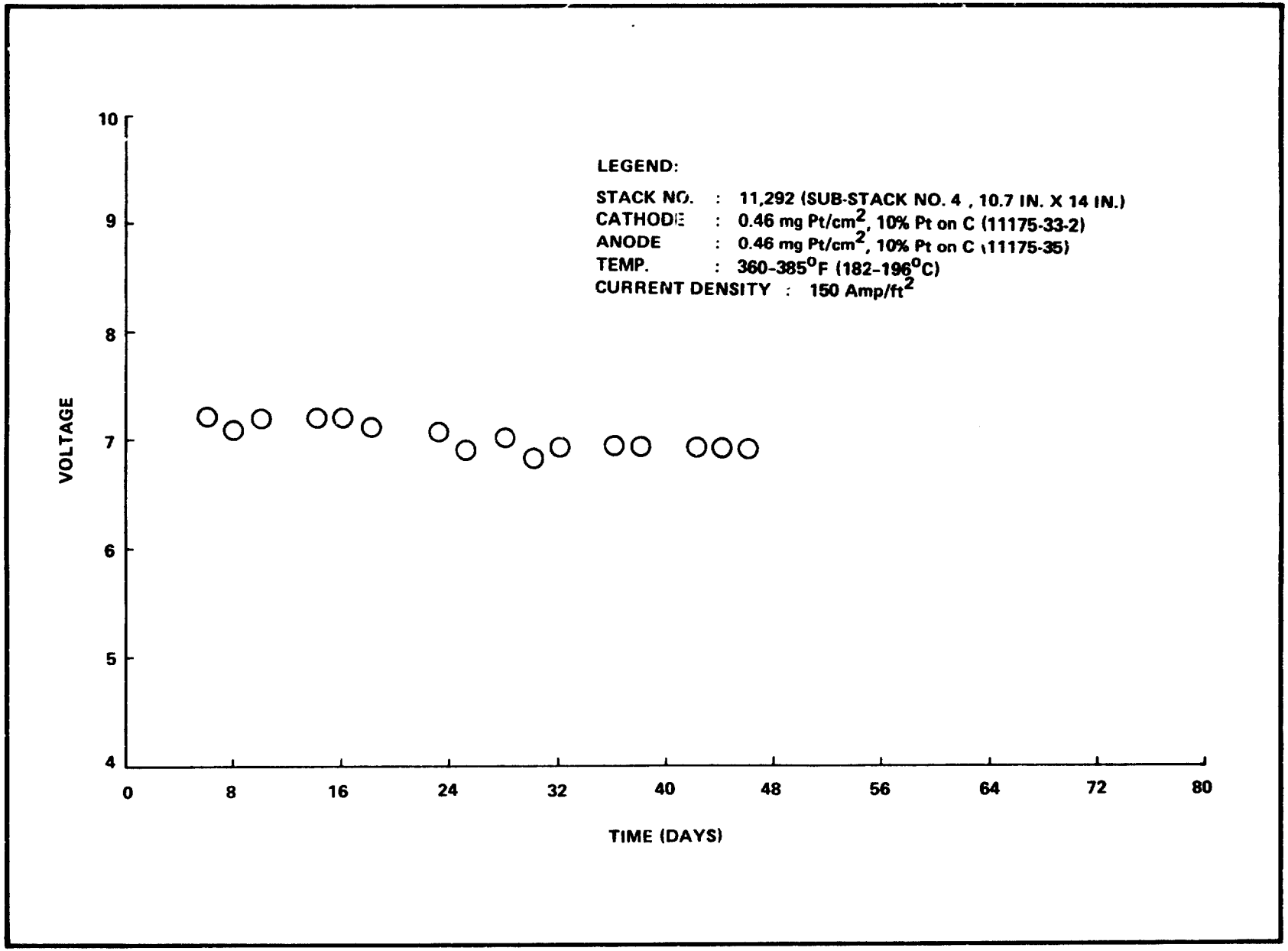

FIGURE VIII-11. VOLTAGE STABILITY OF 12-CELL STACK CONSTRUCTED WITH A--B--A CARBON PLATES

somewhat lower than in prior sub-stacks, was reasonably steady throughout the period, averaging just under 0.8 volts per cell. The voltage under load was steady at about 7.2 volts through the prescribed 500-hour (21 day) test period (H_2-air, 191°C). The test was continued; and over the first few days of the extended period, the voltage declined to just under 7.0 volts and remained there through the 46-day point. The voltage decline was for the most part traceable to two cells adjacent to cooling plates.

5KW STACK NO. 1

The principal purpose of this stack was to demonstrate and test in a 60-cell stack the progress that had been reflected in smaller stacks (i.e., Sub-Stack No. 1 through Sub-Stack No. 4). The cell-size in this stack was 14 inches by 10.7 inches.

5kW Stack No. 1 utilized fully bonded multiple-element plates of the non-grooved ABA type. The edge sealing of the A-elements was accomplished through impregnation using a graphite adhesive. This concept was successfully employed in 12-cell Sub-Stack Nos. 2, 3, and 4. The B-element was resin/CVD-treated woven fabric precursor material as in Sub-Stack Nos. 3 and 4. Key diagnostic indicators for bipolar plate effectiveness were open-circuit voltage and cell IR-loss, both of which proved to be satisfactory in this stack.

The cathodes, anodes, matrix, acid-management approach, and cooling plates were all as in Sub-Stack No. 4. There were 14 cooling plates inserted into the stack at four-cell intervals, with one placed at each end of the stack, inboard of the current-collecting plates, to retard heat loss.

The dielectric liquid coolant (Therminol 44) was distributed to the intercell cooling plates via channels in the end plates. Coolant flow among the various cooling plates was implemented through cooling plate manifolding connections and fiberglass-braided Teflon connector hoses.

The test program for 5kW Stack No. 1 was conducted through 860 hours of variable-load operation, including several shut-downs. Stack voltage at 150 A/ft^2 and 177°C (average) remained at approximately 35.5 volts throughout. The open-circuit voltage is shown in Figure VIII-12. Figure VIII-13 shows the voltage stability at 150 A/ft^2. Figure VIII-14 shows both the stack voltage and the power output as functions of current-density after 835 hours. The above results for this 60-cell stack are seen to be substantially consistent with those obtained in the previous testing of smaller stacks.

SUB-STACK NO. 5

Sub-Stack No. 5 was the first of two stacks intended for advanced technology trials prior to the construction of 5kW Stack No. 2. The major developmental item incorporated into this stack was the CVD-upgraded needled-felt bipolar plate A-element. This relatively fine-pore material requires gas distribution grooves, but the projected high volume cost is more attractive than that of the reticulated vitreous carbon material (and consistent with overall bipolar plate cost goals; see Section IV and Task IV).

Sub-Stack No. 5 was a 10 cell stack with 10.7 inch x 14 inch cells. The bipolar plates consisted of the needled-felt A-elements along with Grafoil as the B-element. (Fully bonded needled-felt bipolar plates are planned for Sub-Stack No. 6, which will be tested early in Phase III.) The cooling plates incorporated the film bonded interfaces for the first time in order to improve corrosion protection (see Section V). Aside from the bipolar plates and the cooling plates, the components used in this stack were as in Sub-Stack No. 4.

After initial assembly of Sub-Stack No. 5 it was discovered that substantial quantities of acid, that had been charged to the cell laminates, were absorbed by the needled-felt A-elements. This phenomenon had not been observed previously in smaller stacks because of the short time of contact among cell components prior to

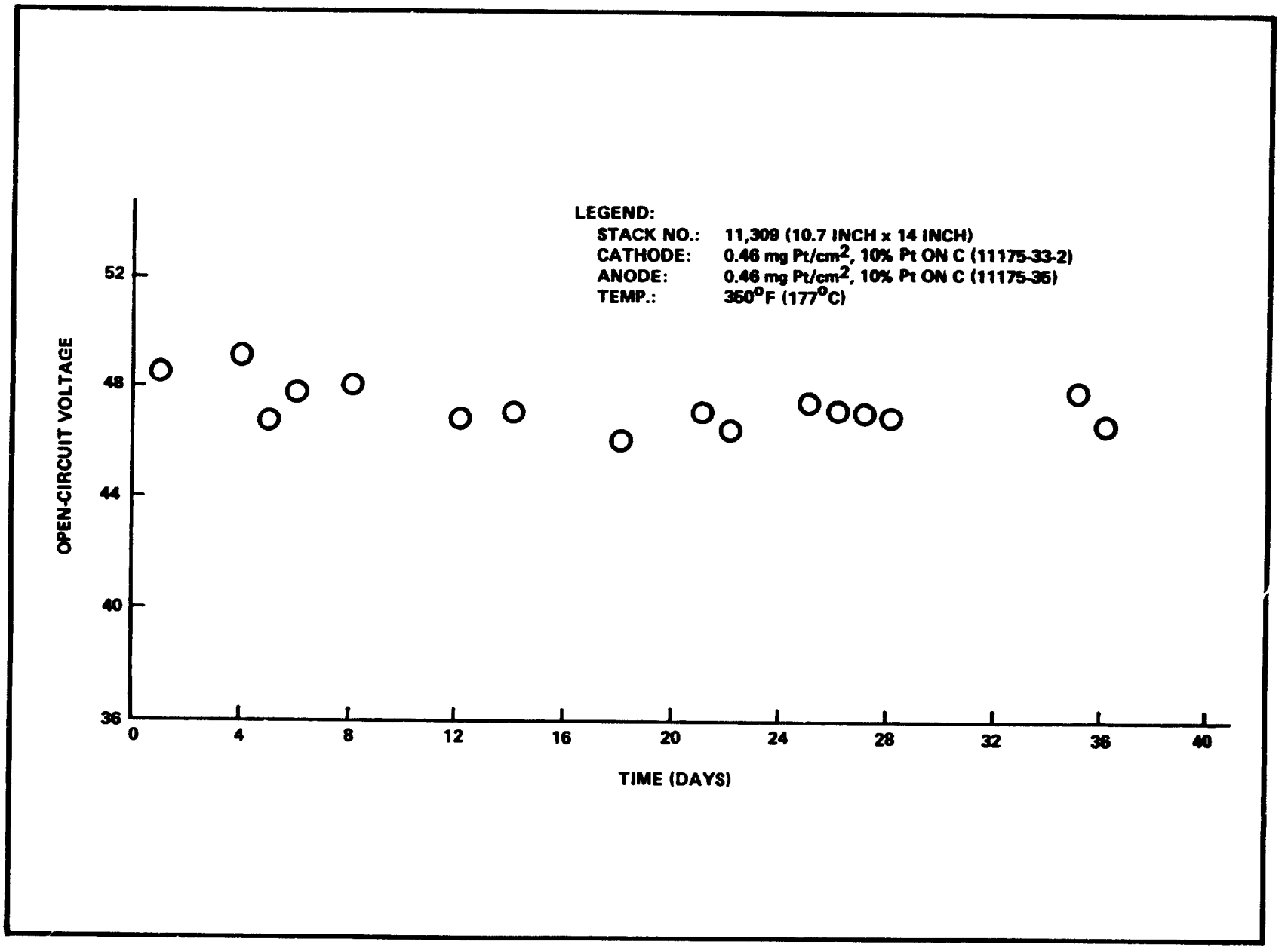

FIGURE VIII-12. OPEN-CIRCUIT VOLTAGE STABILITY OF 60-CELL STACK CONSTRUCTED WITH A–B–A CARBON PLATES

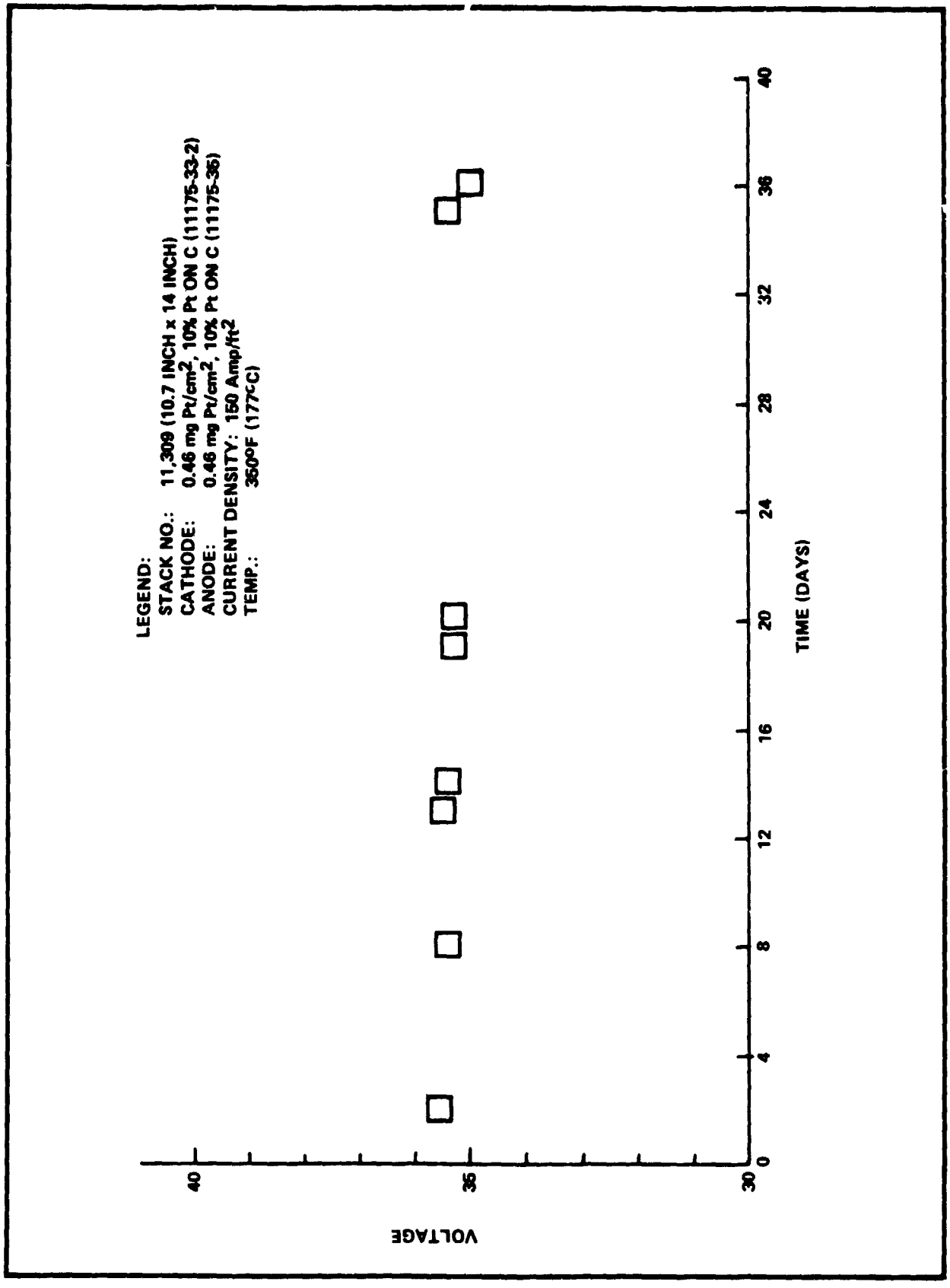

FIGURE VIII-13. VOLTAGE STABILITY OF 60-CELL STACK CONSTRUCTED WITH A–B–A CARBON PLATES

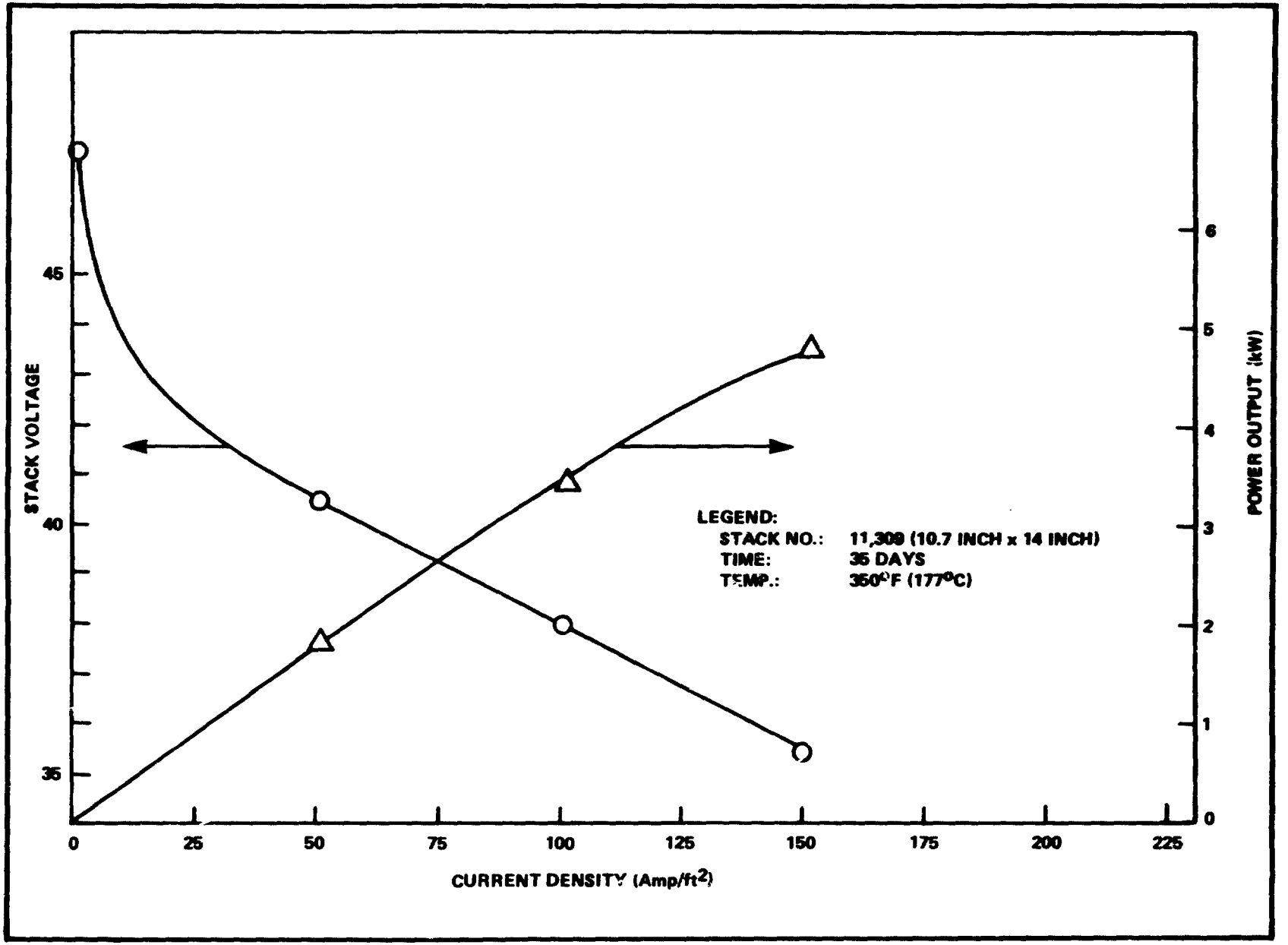

FIGURE VIII-14. PERFORMANCE OF 60-CELL STACK CONSTRUCTED WITH A-B-A CARBON PLATES

heat-up. In order to prevent this acid migration the stack was subsequently rebuilt with wetproofed A-elements. An alternative scheme would be to prefill the A-elements with acid prior to assembly; this approach will be evaluated during Phase III.

Testing of Sub-Stack No. 5 indicated that the A-element wetproofing caused excessive IR-loss between this element and the carbon paper substrate. The measured IR drop through the stack was about one volt greater than typical. As shown in Figure VIII-15, the voltage at standard load (150 A/ft^2) started very low and increased gradually in response to greater stack compressive load and higher temperature (204°C). However, the IR-loss did not decrease sufficiently to allow acceptable performance on load. The open-circuit voltage, as shown in Figure VIII-16, was quite steady throughout the 44-day run.

The problem of electrical contact between the wetproofed A-element and the carbon paper substrate was subsequently solved by simply applying a fluorocarbon spray to one side of the A-element, rather than employing an immersion procedure. This technique was tested in a 3-cell stack subsequent to the Sub-Stack No. 5 test. This 3-cell stack showed attractive performance and no excessive IR-loss.

Upon disassembly of Sub-Stack No. 5 the film bonded cooling plate interfaces were examined. Results were very encouraging; after over 1000 hours on test (mostly at 204°C) there was no evidence of corrosion. This approach will be pursued in Phase III.

CONCLUSIONS

- Substantial progress in component technology development has been demonstrated in several 10.7 inch x 14 inch 12-cell sub-stacks and a 5kW stack.

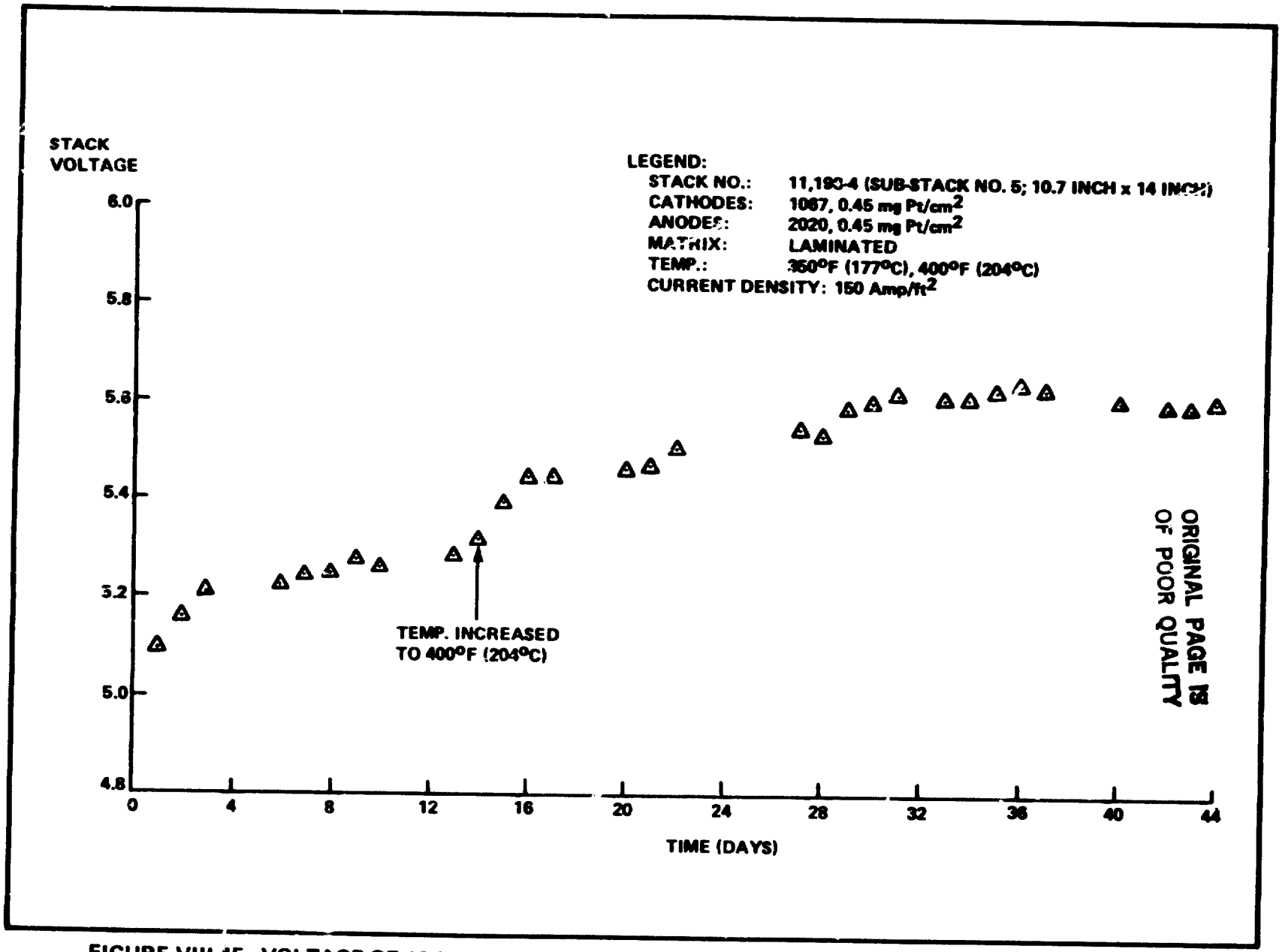

FIGURE VIII-15. VOLTAGE OF 10-CELL STACK CONSTRUCTED WITH NEEDLED-FELT CARBON PLATES

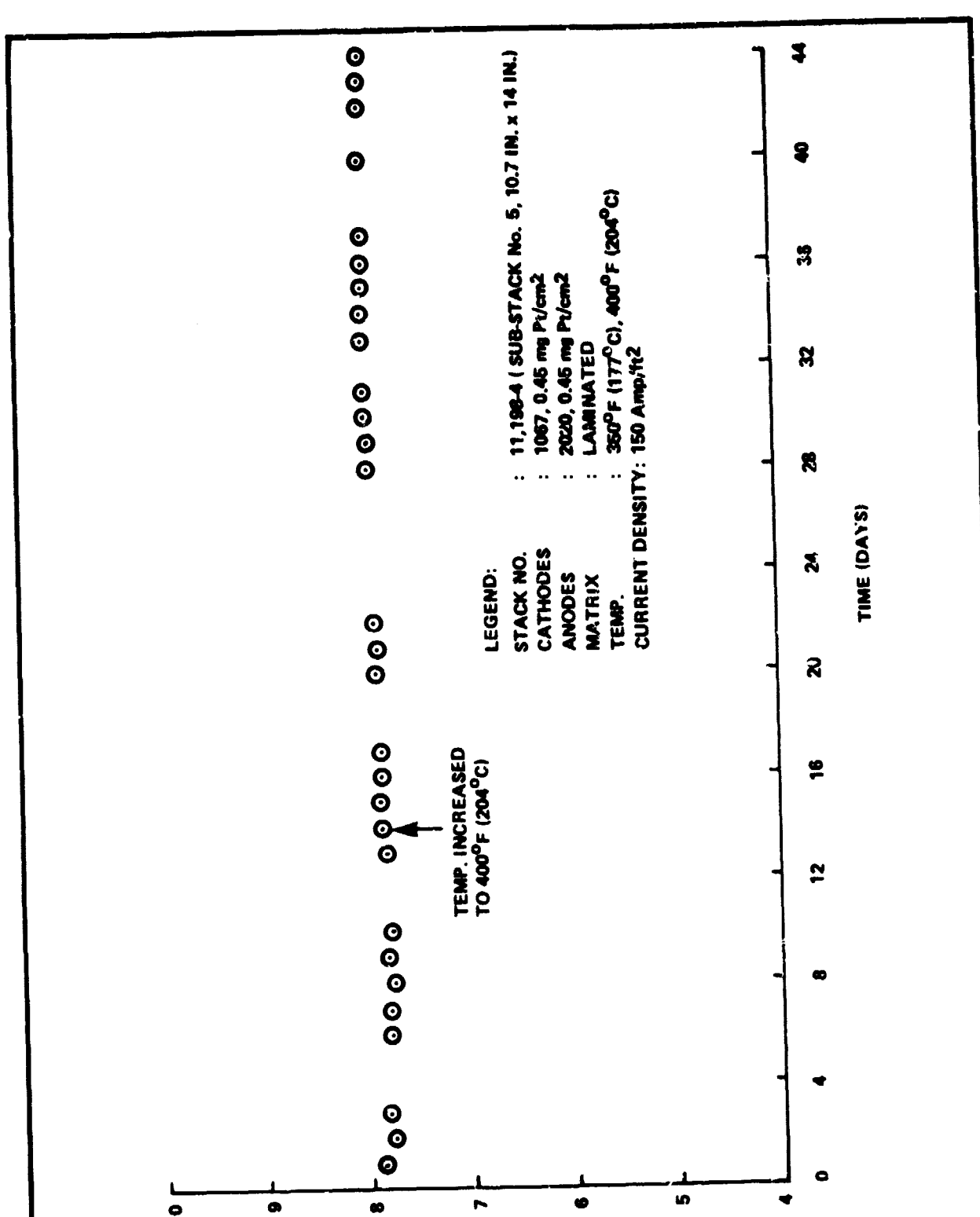

FIGURE VIII-16. OPEN-CIRCUIT VOLTAGE STABILITY OF 10-CELL STACK CONSTRUCTED WITH NEEDLED-FELT CARBON PLATES

CONCLUSIONS (cont'd)

- The stability of open-circuit voltage in the 12-cell sub-stacks and the 5kW stack attest to the integrity of the laminated matrix and acid-replenishment configuration.

- The performance of multi-element bipolar plates of the ABA type has been confirmed in a large stack.

- Intercell cooling plates using recirculating dielectric liquid perform well in a large stack; however, the need for a new approach to interfacial corrosion-protection has become apparent. (Preliminary results for a new configuration are encouraging.)

TASK II

FUEL PROCESSING SUBSYSTEM DESIGN AND DEVELOPMENT

The objective of this task was to develop a complete 5kW fuel processing subsystem including reformer, start-up furnace, fuel vaporizer, anode vent gas burner, and coolant loop. Highlights of work completed in this Task include the following:

- Selection of methanol as the feedstock.
- Evaluation of several low-temperature shift catalysts for use in the steam reforming of methanol. One catalyst, T-2107, was selected for use in the 5kW reformer.
- Selection of components for the fuel processing subsystem including the design and construction of a reformer and an anode vent gas burner.
- Evaluation of integrated fuel processor test unit. (Complete conversion of methanol was obtained at full design flow rate. Test results were in good agreement with the mathematical model of the reformer.)
- Design and construction of the 5kW reformer based on integrated test unit results and reformer mathematical model. (Diagnostic tests have been completed in the non-reactive mode with inerts in the tubes. The initial run with catalyst T-2107 at full design load gave 100% methanol conversion at design space velocity and temperature.)

Further details concerning these various activities are discussed in the following sections.

SECTION IX

THERMODYNAMIC ANALYSIS OF THE STEAM REFORMING PROCESS FOR THREE CANDIDATE FUELS

At the start of this work in 1978, three fuels were being considered for the fuel cell system being developed by Engelhard Industries; natural gas (methane), naphtha (C_xH_{2x}), and methanol. Hydrogen can be generated from these fuels by steam reforming followed by a water-gas shift reaction. (In the case of methanol, these two reactions occur within a single reactor.) The equilibrium compositions were calculated for each fuel. The calculated results included the reformer and shift effluent composition and the heat requirements for the steam reforming process. The equilibrium hydrogen concentrations for natural gas, naphtha, and methanol are shown in Figures IX-1, IX-2 and IX-3.

SECTION IX-A

FUEL SELECTION

Preliminary system and economic analysis was conducted for each fuel in order to provide background for the selection of a fuel. A computer program, written in APL language, was developed and utilized for system heat and material balance calculations. Equipment size and cost were calculated to estimate the system capital cost. Using 1978 fuel prices, the fuel cost (¢/kW-hour) was calculated.

Several factors were considered in selecting the candidate fuel other than capital and fuel costs. For example, as these estimates were being made, the supply of naphtha dropped and the price escalated. Thus the long-term price scenario was considered as well as availability from first generation coal processing. Other factors included consideration of geographical areas not having ready access to natural gas, such as rural New England. The desirability of developing an alternative system using a fuel other than natural gas was considered in the decision.

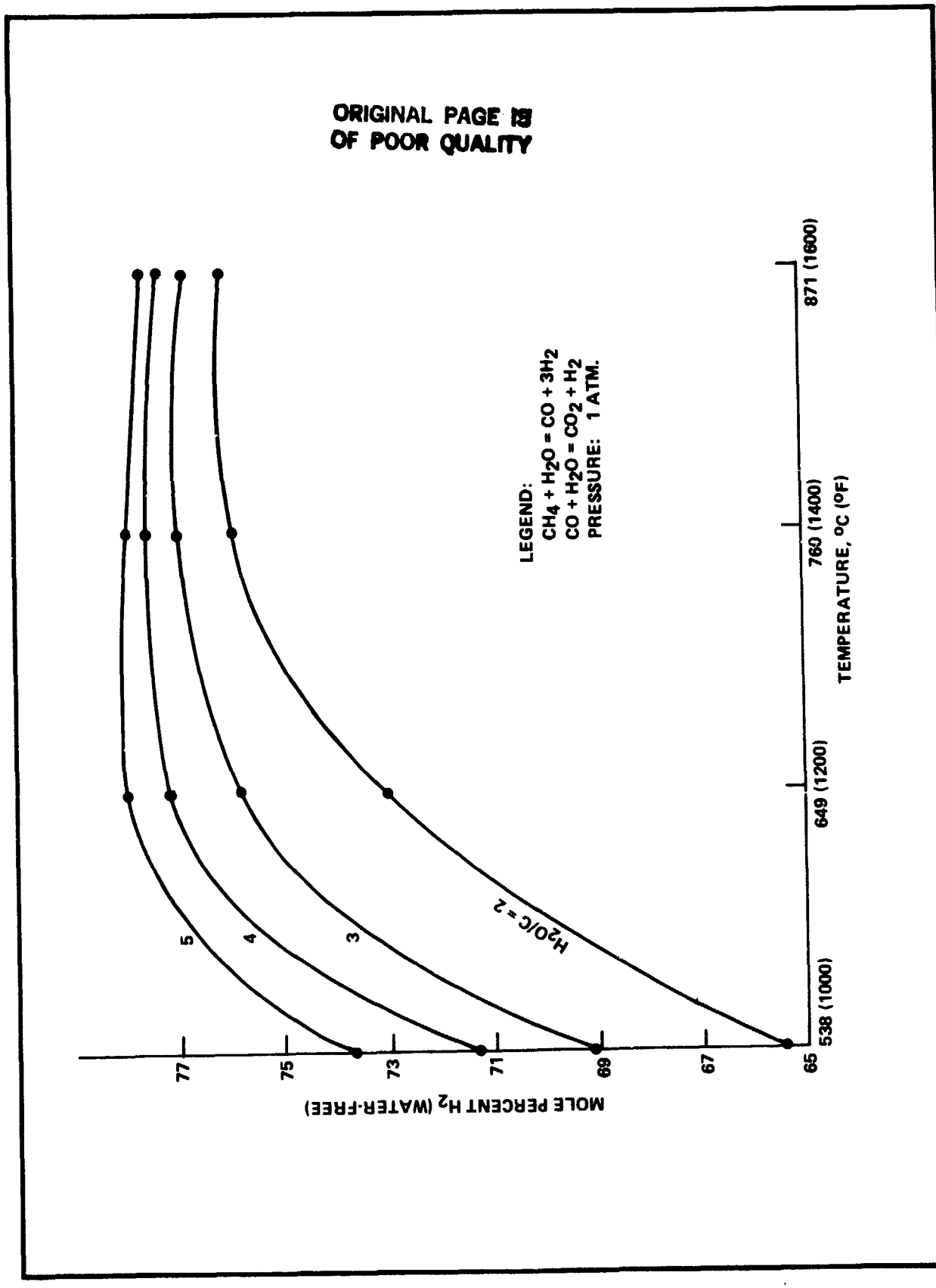

FIGURE IX-1. METHANE REFORMING EQUILIBRIUM

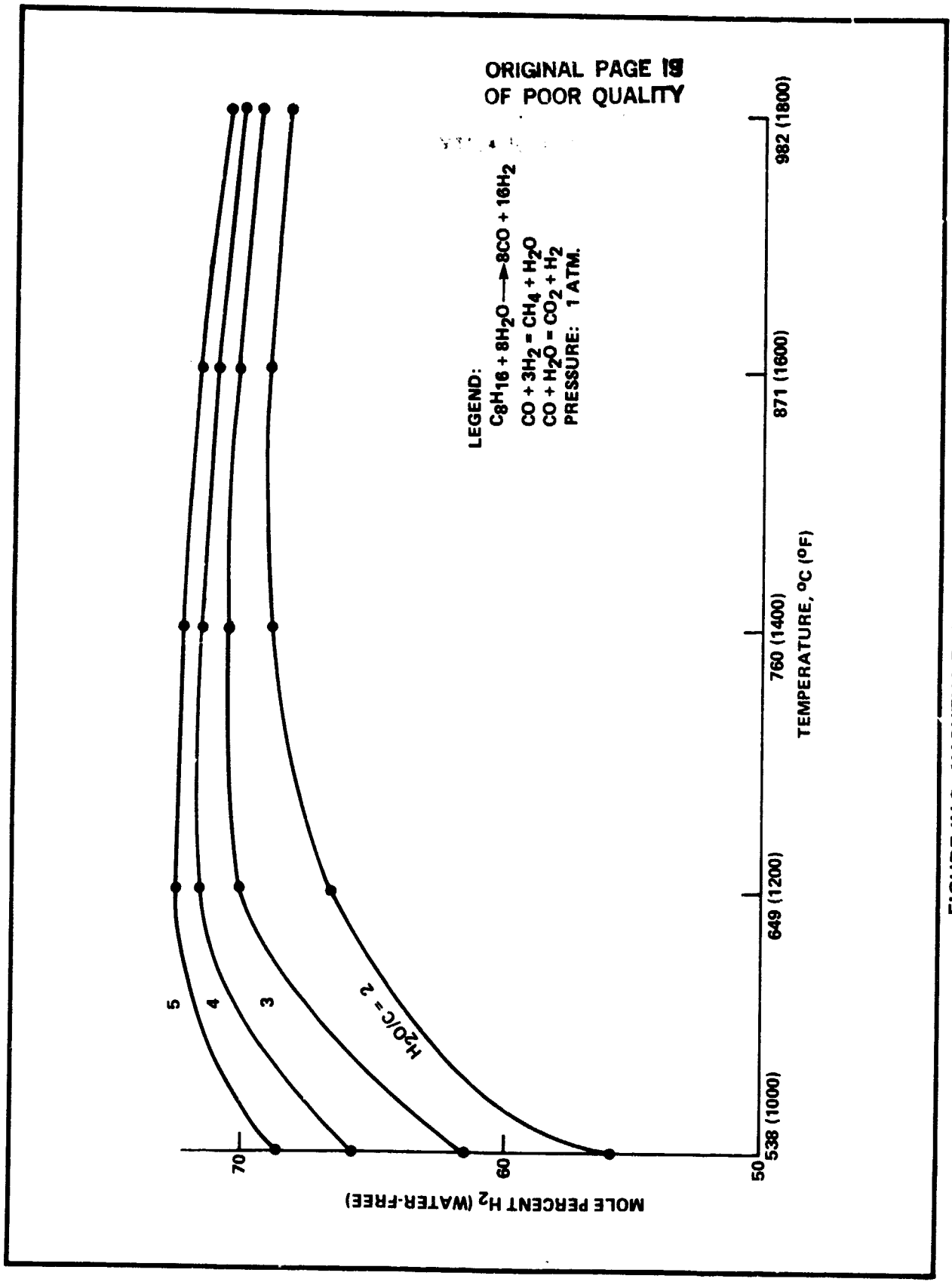

FIGURE IX-2. NAPHTHA REFORMING EQUILIBRIUM

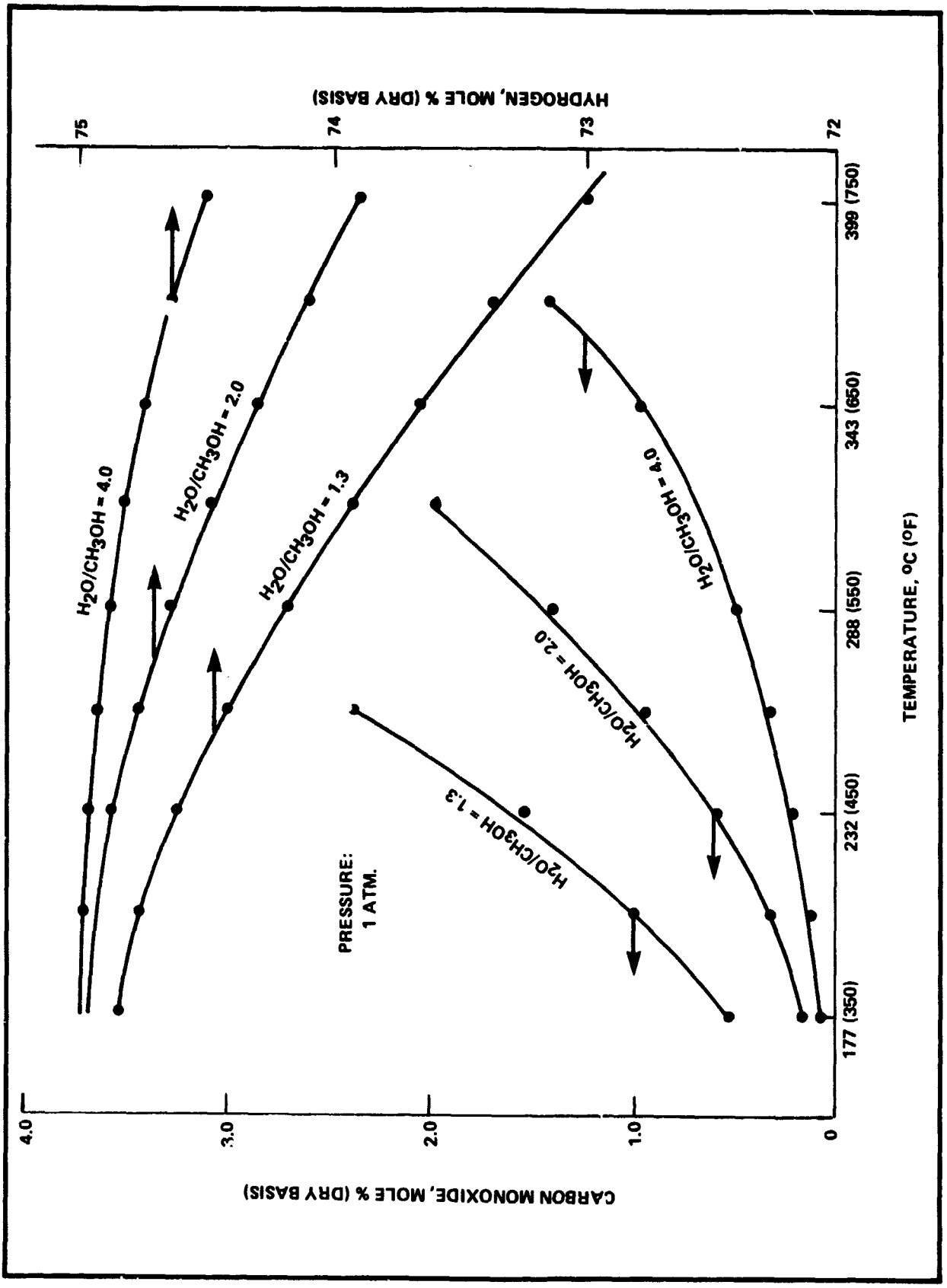

FIGURE IX-3. EQUILIBRIUM COMPOSITION FOR METHANOL/STEAM REFORMING

Table IX-1 lists the economic estimates for natural gas (methane) and methanol that resulted from the calculations described above. Although the methane system has an economic advantage with the fuel costs listed, both systems appear to be viable for on-site applications. The selection of methanol was made with the concurrence of the Department of Energy, and subsequent efforts were based on that decision.

CONCLUSIONS

- Natural gas is currently the most attractive fuel for fuel cell on-site integrated energy systems.

- Methanol is the most favorable alternative to natural gas for on-site fuel cell applications.

TABLE IX-1

COST FACTORS FOR ON-SITE SYSTEM
(1978 FUEL COSTS)

A. BASIS	METHANE	METHANOL
1. Auxiliary Power (% of net)	12	8
2. Inverter Efficiency (%)	95	95
3. H_2 Utilization in Fuel Cell (%)	80	85
4. Voltage Efficiency (%HHV)	43.9	43.9
5. Fuel Price	40¢/CCF	52¢/Gal
B. Fuel Cost (¢/KWH)(1)	4.4	7.1
C. System Capital Cost ($/KW)(1)	646	550
D. Life-Cycle Cost (¢/KWH)(1)	6.8	8.9

Notes:
(1) Costs are per unit electrical output

SECTION X

SUB-SCALE CATALYST TESTING AND PROCESS STUDIES

Once methanol was selected as the feedstock for Engelhard's development program, the sub-scale testing was directed towards selection of a catalyst for methanol/steam reforming.

A. INTRODUCTION

Previous work at Engelhard had shown that copper-zinc type low-temperature shift catalysts were effective for this reaction. This work was renewed on another DOE contract (DE-AC-03-79ET15383) in 1978. It was demonstrated that operating temperatures of about 250°C (482°F) were required to achieve nearly 100% methanol conversion with low temperature shift type catalysts.

B. CHEMISTRY OF METHANOL/STEAM REFORMING

With such catalysts the reaction appears to proceed in two steps:

$$CH_3OH + H_2O = 3H_2 + CO_2$$

This step is essentially irreversible at atmospheric pressure.

The second step is the reverse water-gas shift reaction:

$$H_2 + CO_2 = CO + H_2O$$

Results obtained in the course of this Task show low CO levels when methanol conversion is below about 95%. This suggests a competitive adsorption of methanol on the active sites for the shift reaction. Equilibrium calculations predict lower CO levels with water in excess of stoichiometric. Experimental results confirmed this prediction. No methane or higher hydrocarbons have been observed when using Cu/Zn catalysts, even though equilibrium would favor conversion of methanol to methane at this temperature.

C. COMPOSITION OF COMMERCIAL LOW-TEMPERATURE SHIFT CATALYSTS

Four commercial, low-temperature shift catalysts were selected for evaluation. Chemical analyses of the as-received material are listed in Table X-1.

TABLE X-1

Catalyst	Composition, Wt.% Cu	Zn	Cr	Al_2O_3
UCI-G66B	29.0	52.6	0.001	3.4
ICI 52-1	26.3	44.7	Nil	13.4
BASF K3-10	29.0	10.9	1.0	24.5
UCI T2107	27.5	11.6	1.0	29.9

These catalysts were supplied unreduced as the oxides with varying amounts of un-decomposed carbonate (or other anions) present. The catalysts are reduced in a temperature programmed schedule with ever increasing concentration of H_2. During the reduction procedure, the weight decreases due to reduction of the metal oxides and decomposition of the carbonates or nitrates. Engelhard plans to purchase these catalysts in the reduced and stabilized form so that this reduction step will not be required in the commercial reformer. These commercial catalysts are produced as 3/16" diameter tablets with a length of about 3/16". As a result of this work, we have requested special production of 1/8" diameter tablets 1/8" long.

D. TEST EQUIPMENT

The test equipment used for this catalyst evaluation work is shown in Figures X-1 and X-2. The methanol/water mix is vaporized and reacted in a 0.834" I.D. tubular reactor heated in a four zone electrical furnace. The gas is separated from the unreacted methanol and water and analyzed by chromatography. The condensate is weighed and the methanol content is determined by measuring the specific gravity. Excellent material and carbon balances are observed when a 24 hour material balance period is used.

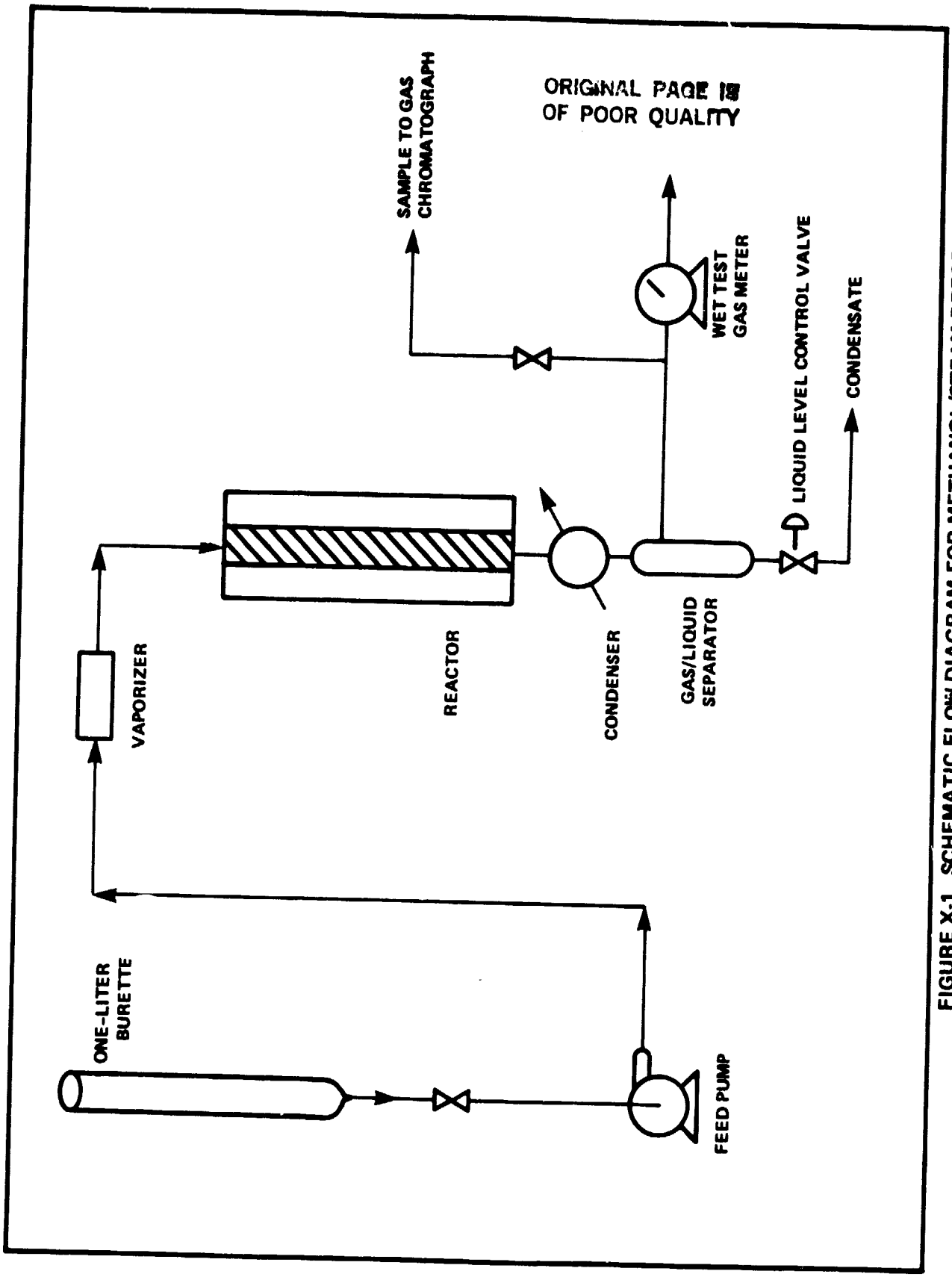

FIGURE X-1. SCHEMATIC FLOW DIAGRAM FOR METHANOL/STEAM REFORMING

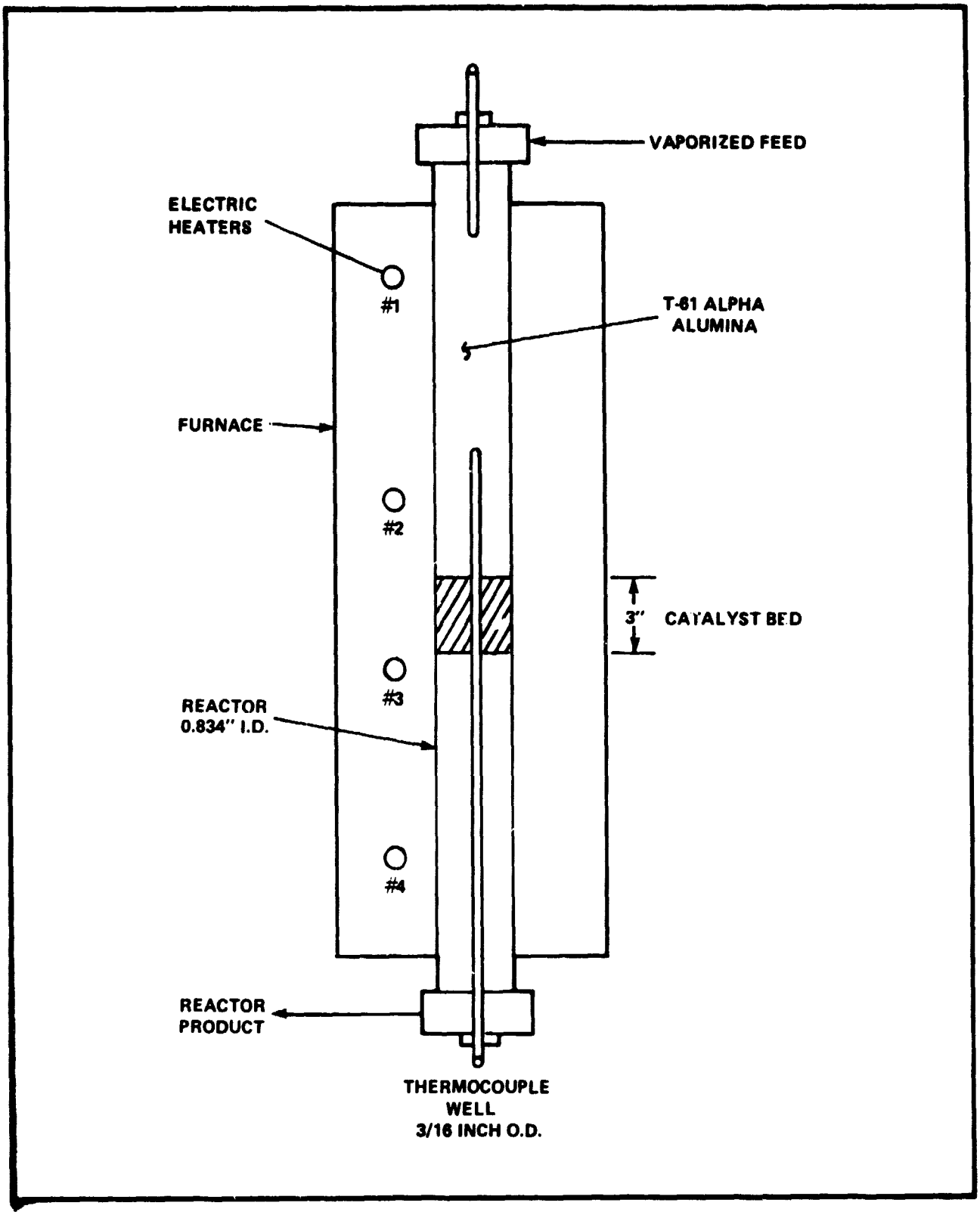

FIGURE X-2. SCHEMATIC DIAGRAM OF REACTOR FOR METHANOL/STEAM REFORMING

E. ISOTHERMAL TESTS AT TEMPERATURES BELOW 275°C

A series of isothermal tests was run to demonstrate the activity and stability of Cu/Zn catalysts when operated with temperatures below 275°C. Such runs were used for kinetic studies and process variable studies. In these tests the catalyst was ground to 14-20 mesh size and diluted with alpha alumina in a logarithmic fashion commonly used to operate highly endothermic reactions in an isothermal manner. Initial tests were made with an impure methanol obtained from a supplier of industrial solvents. The impurities were identified as toluene and xylenes. It was later shown that commercial methanol obtained directly from a methanol producer (in this case DuPont) could be used for prolonged periods without a loss in catalyst activity.

Tests were run for periods up to 2000 hours with 99% methanol conversion when the catalyst temperature was controlled at 274°C (525°F). A typical material balance is listed in Table X-2, and Figure X-3 shows the methanol conversion for the period of the test. Each point represents a material balance period. Figure X-4 shows the decline in CO concentration. These results, with ICI 52-1 catalyst, demonstrate good stability with commercial methanol when temperatures are controlled at 274°C.

F. KINETIC STUDY

Methanol conversion and dry gas composition were measured for a wide range of space velocities in the temperature range from 200-274°C (392-525°F). The catalyst used was ICI 52-1 ground to 14-20 mesh. A dilute packing was used to obtain isothermal operation even for very high conversion levels.

Methanol conversion was correlated with six mathematical models listed in Table X-3. Best fit was with a second order model in methanol and water. The second order model in methanol and water with an expansion term might be a better description of the process, even though the fit is not quite as good. The activation energy for the second order model (without expansion) was 26.3

ENGELHARD

TABLE X-2

TYPICAL MATERIAL BALANCE FOR METHANOL/STEAM REFORMING

PROJECT NO. G08-30 , RUN NO. 7236 , FEED ID 746-1931, DATE 10-13-79
CATALYST ICI-52-1, CATALYST VOLUME,ML 20.000 CATALYST WEIGHT, GMS 22.500
TIME AT START 52. TIME AT END 70. ELAPSED TIME,HRS 18.

********** INPUT **********

FEED MEOH CONTENT (WT.PCT.)	57.6000
FEED DENSITY (GM/ML AT 15 C)	0.9031
AVG. BED TEMPERATURE (C)	270.8000
BED PRESSURE (PSIG)	6.0000
EXIT BED TEMP. (C)	276.0000
VOLUME OF FEED USED (ML)	629.0000
H2O/CH3OH MOLAR RATIO	1.2980
PRODUCT CONDENSATE WT. (GM)	66.4000
PROD. COND DENSITY (GM/ML)	0.9952
UNREACTED MEOH IN COND.(WTPC)	2.1000
PRODUCT GAS VOLUME (CUBIC FEET)	35.2400
AMBIENT TEMP. (DEG C)	23.0000
BAROMETRIC PRESSURE (MM HG)	760.0000

GAS COMPOSITION, MOLE PCT

H2	74.2478
CO	1.6053
CO2	23.2365
H2O	0.8491
CH3OH	0.0613

********** CALCULATED RESULTS **********

METHANOL IN (GM MOLES/HR)	0.5700
CO+CO2+CH3OH (GM MOLES/HR)	0.5681
MEOH IN COND (GM MOLES/HR)	0.0024
C ACCOUNTABILITY (PCT)	100.0933

WEIGHT BALANCE

FEED IN (GM)	568.05
CONDENSATE (GM)	66.40
GAS MAKE (GM)	506.37
GAS AVG MW	12.3
WT. BALANCE, PCT	100.83

DRY GAS EQUILIBRIUM COMPOSITION

H2	74.28 (MOLE PERCENT)
CO	2.48
CO2	22.64

FEED RATE	34.94 ML/HR 31.37 GM/HR
HYDROGEN PRODUCTION (L/HR-STP)	37.94
MOLES H2 PRODUCED/MOLE MEOH FED	2.69
THEORETICAL H2 PRODUCTION L/HR STP	36.87
H2 SPACE VELOCITY (PER HR STP)	1843.55
PER CENT MEOH DISAPPEARANCE	99.33
PER CENT THEORETICAL HYDROGEN	102.91
WHSV	0.81

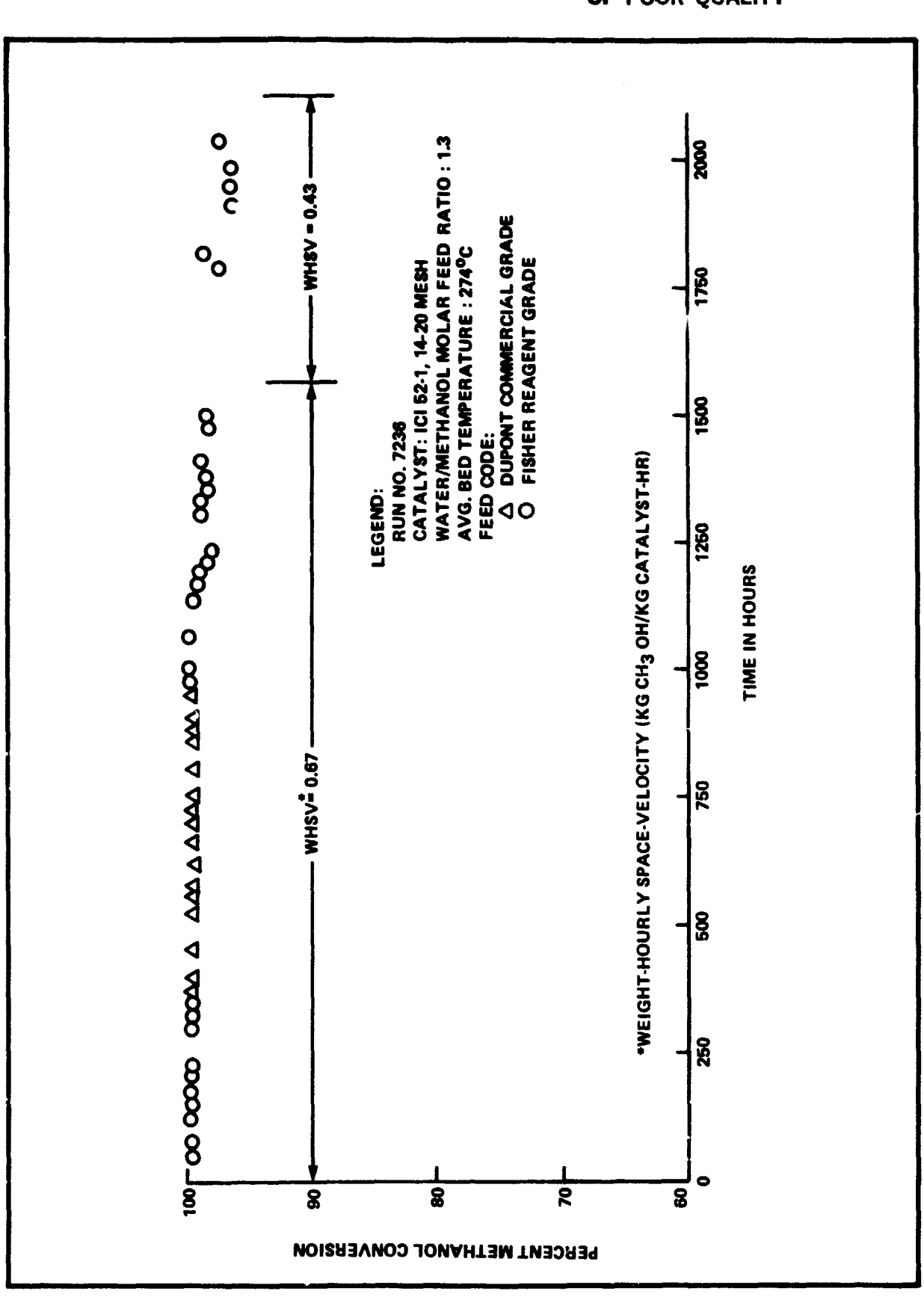

FIGURE X-3. METHANOL CONVERSION IN SUB-SCALE REFORMER

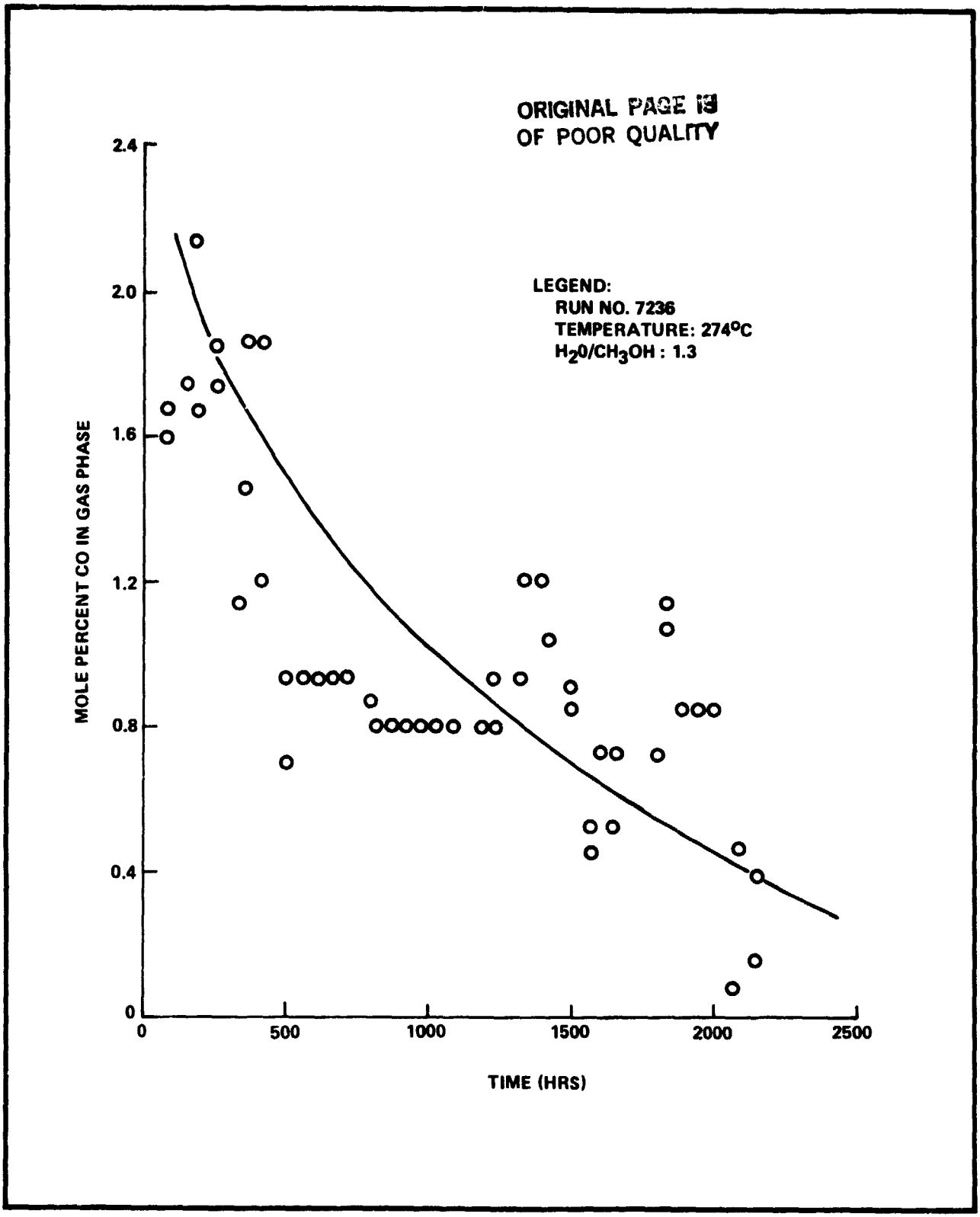

FIGURE X-4. CARBON MONOXIDE CONCENTRATIONS DURING METHANOL/STEAM REFORMING

TABLE X-3

COMPARISON OF MATH MODELS

	Mean % Error Between Experimental and Predicted Conversion, Xs
1. FIRST ORDER $-\ln (1-X_A) = k/WHSV$	10.7
2. FIRST ORDER NON-LINEAR $X_A = B1\ (1.0 - EXP\ (-(B2-B3/T)\ /WHSV)\ )$	7.8
3. SECOND ORDER IN METHANOL AND WATER $\ln \left[\frac{M-X_A}{M(1-X_A)}\right] = \frac{k\ C_{A0}\ (M-1)}{WHSV}$	3.5
4. Nth ORDER IN METHANOL $X_A = 1 - \left[\frac{(N-1)k}{(WHSV)C_{Ao}^{(1-N)}} + 1\right]^{\frac{1}{1-N}}$	5.35
5. PLUG FLOW – IRREVERSIBLE FIRST ORDER $k\ (WHSV) = (1+E_A)\ \ln \left(\frac{1}{1-X_A}\right) - E_A\ X_A$	79.5
6. SECOND ORDER IN METHANOL AND WATER WITH EXPANSION TERM, E_A $\ln \left[\frac{M-X_A}{M}\right]\ (1 + E_A\ M) - (1+ E_A)\ \ln (1-X_A) = \frac{C_{A0}\ (M-1)\ k}{WHSV}$	16.7

M = Water/Methanol molar feed ratio
X_A = Methanol fractional conversion
C_{A0} = Methanol initial concentration
E_A = Molecular expansion due to reaction
N = Reaction order

kcal/mole. The experimental data obtained in this study are listed in Table X-4 and the second order plot is shown in Figure X-5. We observe that the CO concentration approached the value predicted by equilibrium only as the methanol conversion approached 100%. (See Figure X-6.) For temperatures below 275°C, the activities of ICI 52-1, K3-10, and T2107 are similar as shown in Figure X-7.

G. TEMPERATURE STABILITY

In the 5kW refomer, part of the heat required for the endothermic reaction is supplied as sensible heat to the process stream. The process stream at the inlet may be about 100°C above the average bed temperature. To study the effect of this on catalyst stability, a series of tests was conducted with the temperature profile forced to give high inlet temperatures. This can be easily controlled in the electrically-heated sub-scale unit with a bronze block surrounding the reactor tube. The profile selected is listed below:

Location	Temperature °C	Temperature °F
Inlet Gas	400	752
Top of Bed	325	617
Bottom of Bed	303	577

This can be compared with results from a test run with the 5kW flue-gas heated reformer:

Location	Temperature °C	Temperature °F
Inlet	382	720
Average Bed Temperature	279	535
Exit Bed Temperature	296	565

The sub-scale test is far more severe than would be expected in operating the 5kW reformer. However, the purpose of the test is to screen the four commercial catalysts rapidly to select the

TABLE X-4

EXPERIMENTAL DATA AND PRODUCT CONSTITUENCY

Run No. 7318

CATALYST: ICI 52-1
H_2O/MeOH: 1.3

Time, Hrs.	Temp., °C	WHSV	%MeOH Conversion	Constituents in Product Moles Constituent/Mole MeOH Reacted			
				H_2	CO	CO_2	H_20
20	274.4	1.26	100.0	2.901	.099	.944	.418
92	273.8	1.19	99.65	2.751	.086	.898	.407
99	272.0	2.39	99.9	2.938	.092	.959	.341
115	271.6	2.33	99.66	2.903	.091	.948	.377
125	274.1	4.70	97.79	2.924	.028	.987	.352
139	276.6	4.38	98.01	2.884	.039	.974	.381
167	254.4	4.22	84.06	2.856	.016	.970	.355
188	253.0	4.47	84.52	2.955	.017	1.00	.375
190	252.0	4.38	82.98	2.970	.017	.969	.391
211	230.8	4.22	55.37	2.826	.023	.988	.469
214	232.8	4.29	58.07	2.652	.022	.927	.537
260	202.8	4.29	27.11	2.945	.0032	1.013	.279
261	205.4	4.29	26.20	2.485	.0026	.854	.813
262	203.8	4.29	23.59	2.392	.0026	.822	1.055
287	271.8	4.50	96.10	2.969	.039	1.007	.324
288	271.6	4.50	97.26	2.965	.039	1.005	.027
289	272.8	4.50	96.41	2.989	.039	1.019	.331
312	252.0	5.92	96.79	2.779	.0090	.982	.376
313	252.6	5.92	77.81	2.756	.0090	.974	.352
334	252.8	9.07	67.41	2.767	.0081	.919	.389
335	255.8	9.10	67.82	2.825	.0083	.939	.418
358	253.4	26.44	36.71	2.671	.0061	.887	.473

TABLE X-4, Cont'd.

EXPERIMENTAL DATA AND PRODUCT CONSTITUENCY

Run No. 7318

CATALYST: ICI 52-1
H_2O/MeOH: 1.3

Time, Hrs.	Temp., °C	WHSV	%MeOH Conversion	Constituents in Product Moles Constituent/Mole MeOH Reacted			
				H_2	CO	CO_2	H_2O
359	253.0	27.24	38.49	2.632	.0060	.874	.528
360	253.4	26.64	38.66	2.612	.0059	.867	.492
433	254.2	35.53	31.26	2.486	.0046	.820	.534
434	254.2	35.53	30.26	2.704	.0050	.892	.511
457	205.0	14.45	7.52	3.091	.0012	1.020	.360
458	202.0	15.99	7.02	2.656	.0053	.876	.194
481	203.6	1.19	37.37	2.949	.022	.962	.466
482	203.8	1.37	48.42	3.078	.038	1.00	.271
506	271.4	4.76	95.38	3.056	.013	.986	.357
524	298.6	4.21	99.57	3.005	.095	.932	.409
530	279.4	4.22	97.92	3.026	.030	.964	.388
622	274.0	5.09	93.12	2.954	.030	.981	.390
645	323.0	4.15	99.78	2.925	.160	.889	.002
669	274.2	4.36	91.82	2.898	.022	.941	.377
670	273.2	4.26	94.66	2.908	.022	.944	.339
693	354.4	4.76	99.55	2.319	.202	.847	.450
694	351.8	4.62	100.00	2.848	.204	.855	.449
764	275.0	1.70	98.63	3.004	.018	.982	.400
788	399.0	4.57	99.25	2.741	.256	.782	.551
817	272.5	4.60	76.33	2.848	.014	.932	.391
836	280.0	4.26	76.53	2.134	.0118	.732	.224

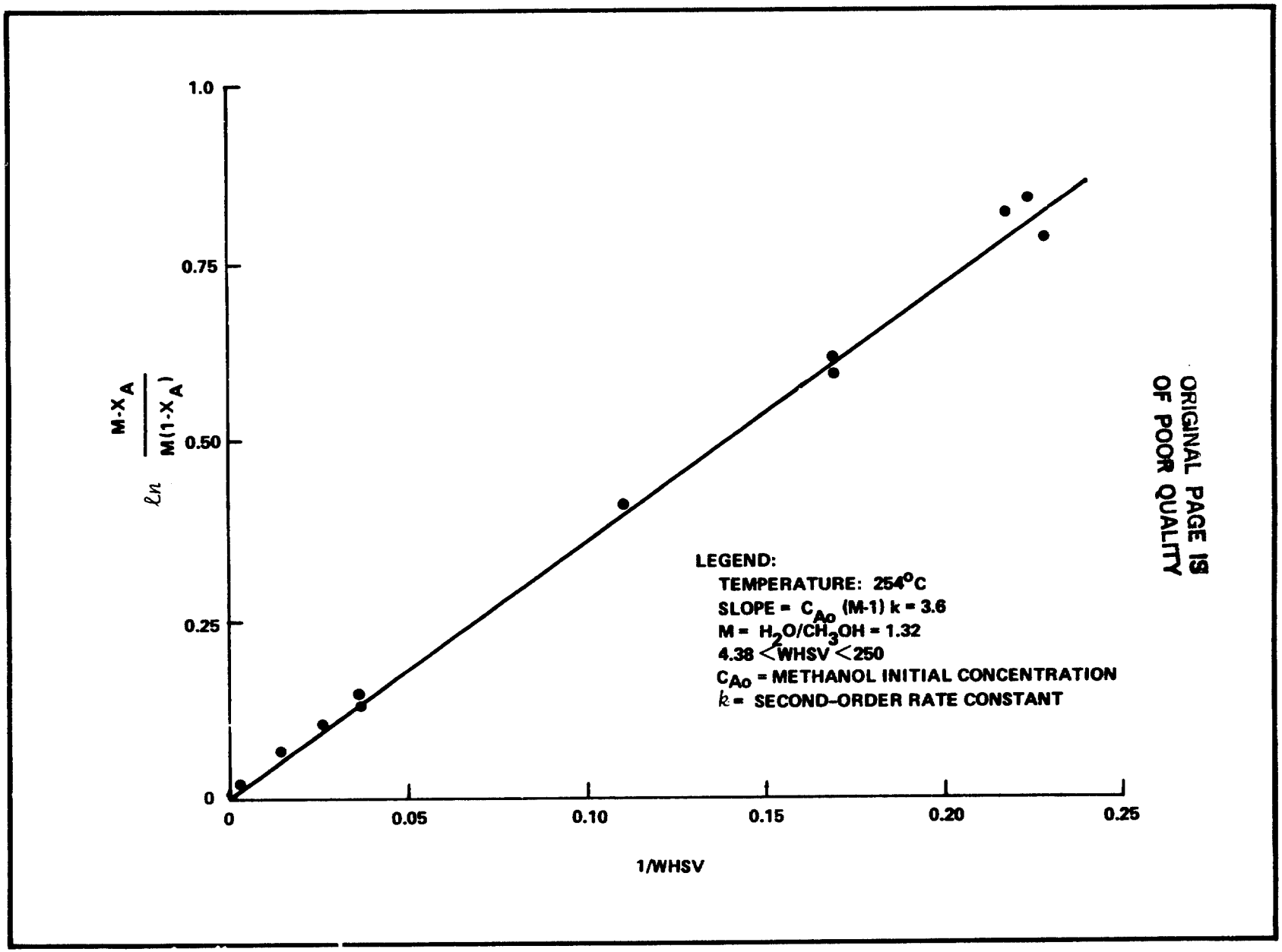

FIGURE X-5. SECOND-ORDER REACTION, METHANOL/STEAM REFORMING

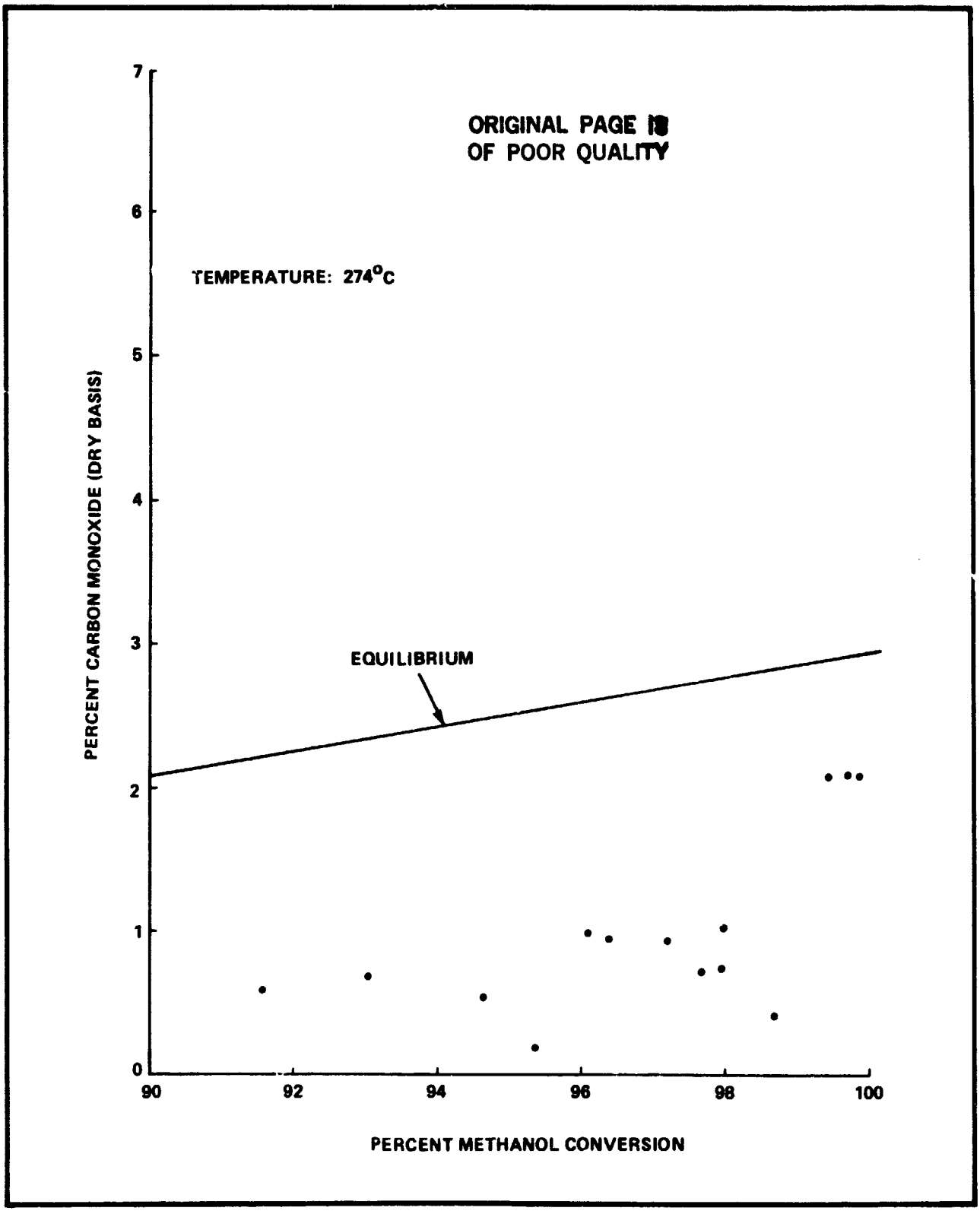

FIGURE X-6. CARBON MONOXIDE CONCENTRATION IN METHANOL/STEAM REFORMING

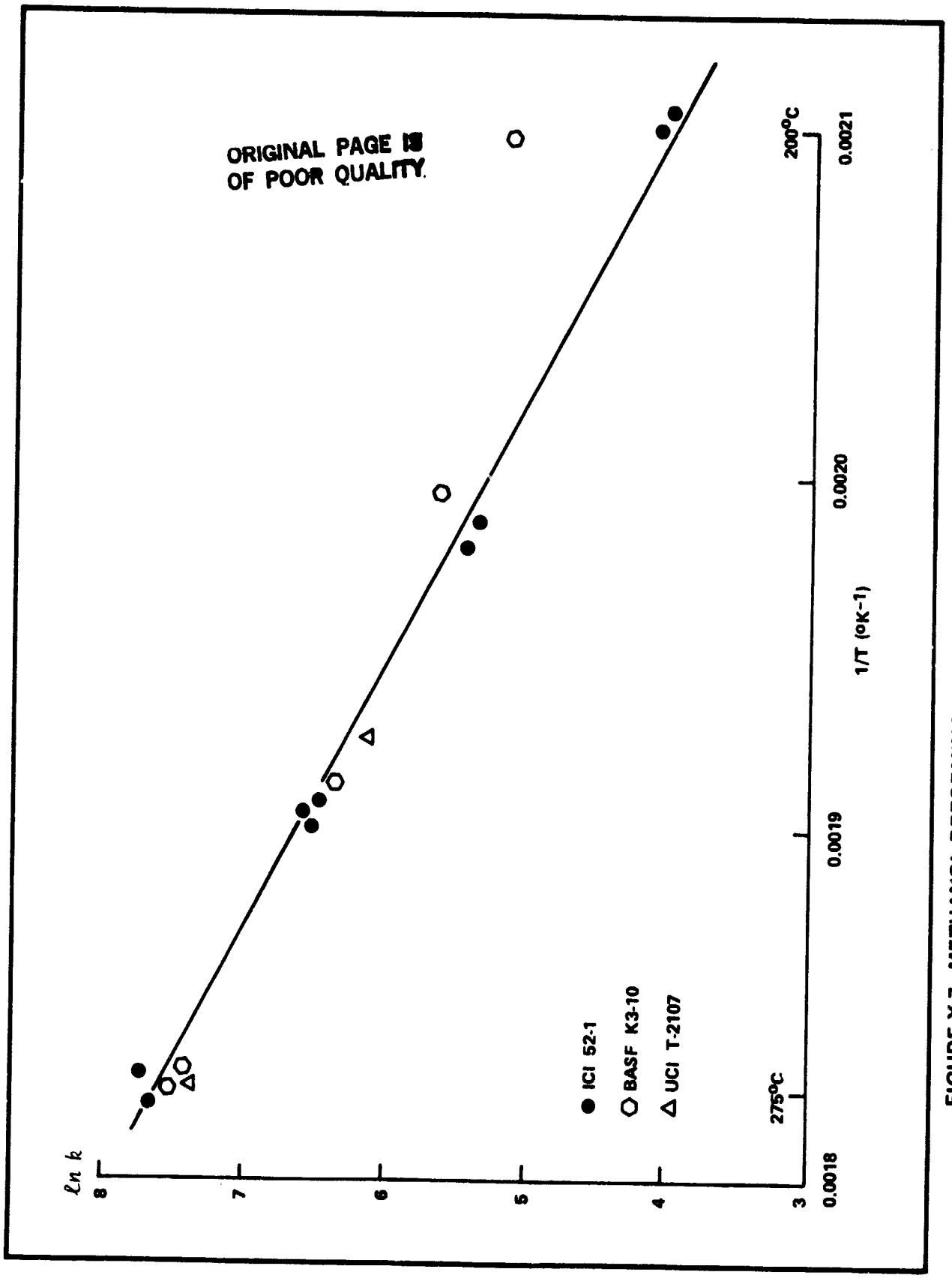

FIGURE X-7. METHANOL-REFORMING ACTIVITY FOR THREE COMMERCIAL CATALYSTS

most stable for use in the 5kW reformer. Higher space velocities were also used (about 2 WHSV* versus about 0.5 WHSV in the 5kW reformer).

The results are shown in Figure X-8 where the second order rate constants for the four catalysts are plotted versus time on stream. The two catalysts with higher alumina and chromium content, T-2107 and K3-10, are more stable than the catalysts with lower concentrations of these components. Table X-5 lists the average copper crystallite size of the used catalysts from these runs. Although T-2107 was the most stable of the catalysts, it exhibited the largest crystallite size. Thus other factors, such as chromium content, could be the key to catalyst performance at higher temperatures.

Based on these results, a 10 liter batch of reduced and stabilized T-2107 was obtained for the 5kW reformer.

H. PROCESS VARIABLE STUDIES AND RESULTS

1. Effect of Particle Size

Tests were run with ICI 52-1 catalyst of varying particle size with the following results:

Pellet Size	Activation Energy Kcal/mole	Apparent Second Order Rate Constant
14-20 Mesh	26.3	1848
Half Pellets, Cut on Diameter	18.9	858
Full Pellets 3/16"D x 1/8" Long	17.1	438

The results are shown as a function of temperature in Figure X-9. Because of the strong particle size effect (indicating mass-transport or pore-diffusion limitations), a large batch of catalyst was ordered at the smallest practical tablet size, 1/8" diameter x 1/8" long.

2. Effect of Water/Methanol Ratio in the Feed

As expected from the chemistry of the reaction, methanol conversion and dry gas CO concentration are affected by the water to methanol ratio in the feed. This is illustrated in Figure X-10.

* Weight-hourly space-velocity (lb. CH_3OH/lb. catalyst hr.)

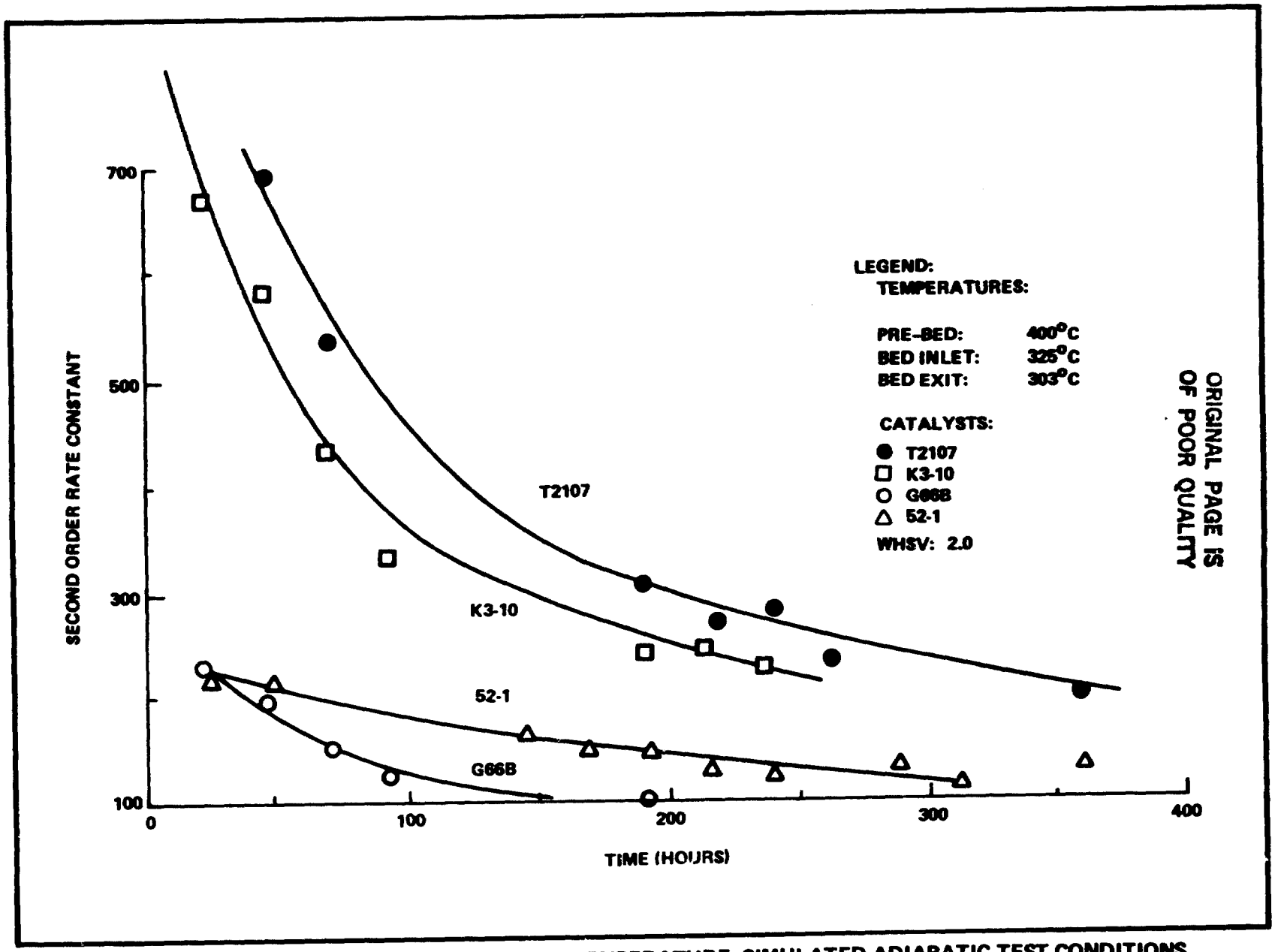

FIGURE X-8. CATALYST AGING UNDER HIGH-TEMPERATURE, SIMULATED ADIABATIC TEST CONDITIONS

TABLE X-5

SUB-SCALE METHANOL/STEAM REFORMING CATALYST

STABILITY TESTS

- Copper crystallite size of used Cu/Zn catalysts:

Catalyst	Run No.	Hours on Stream	EOR[a] Rate Const.	Average Cu Crystallite Size, A°
ICI 52-1	7457	358	120	95
G66BRS	7512	191	100	281
BASF K3-10	7517	236	250	293
UCI T 2107	7477	354	250	401

a. EOR = End of Run

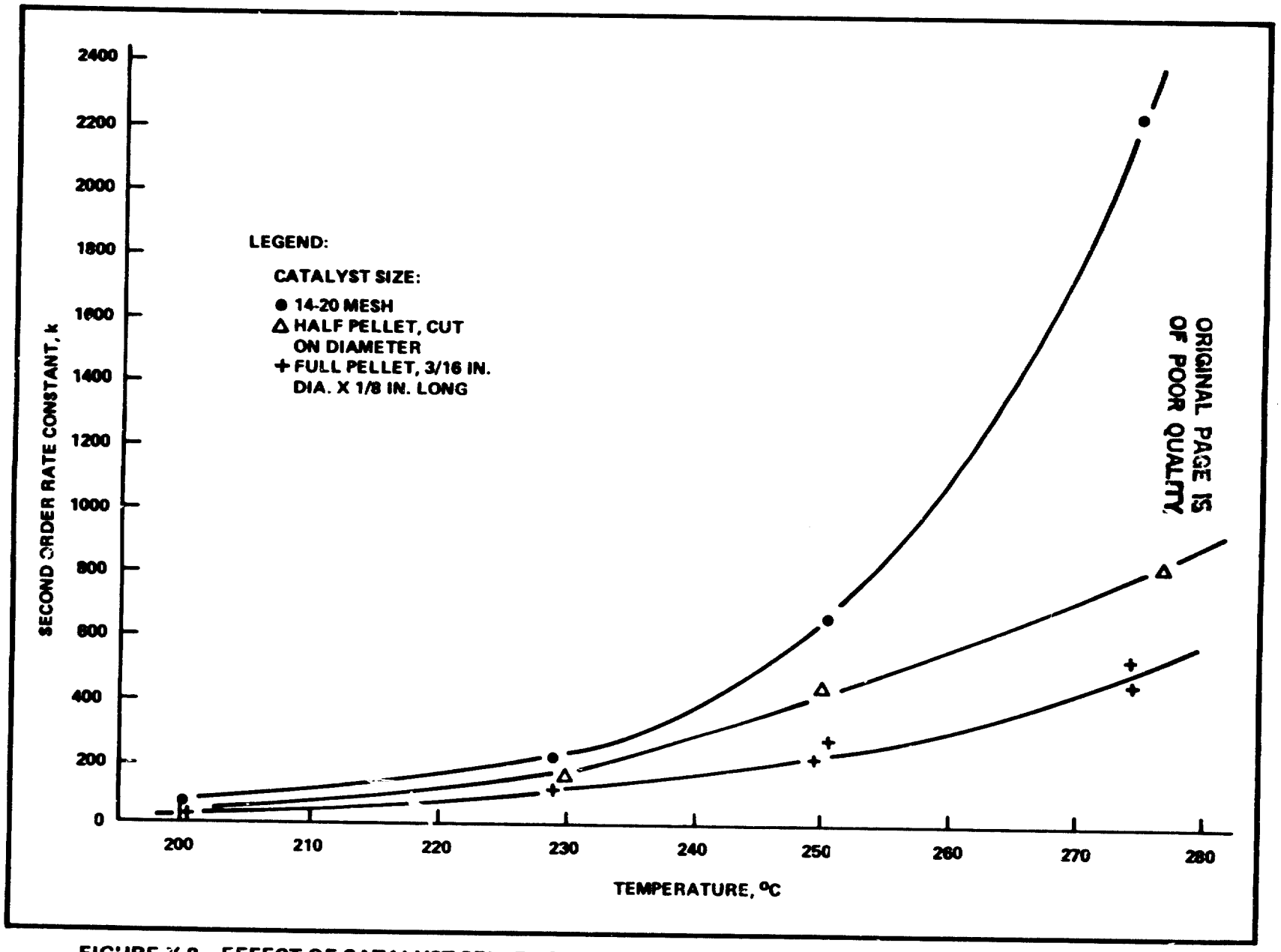

FIGURE X-9. EFFECT OF CATALYST PELLET SIZE ON APPARENT METHANOL REFORMING RATE CONSTANT

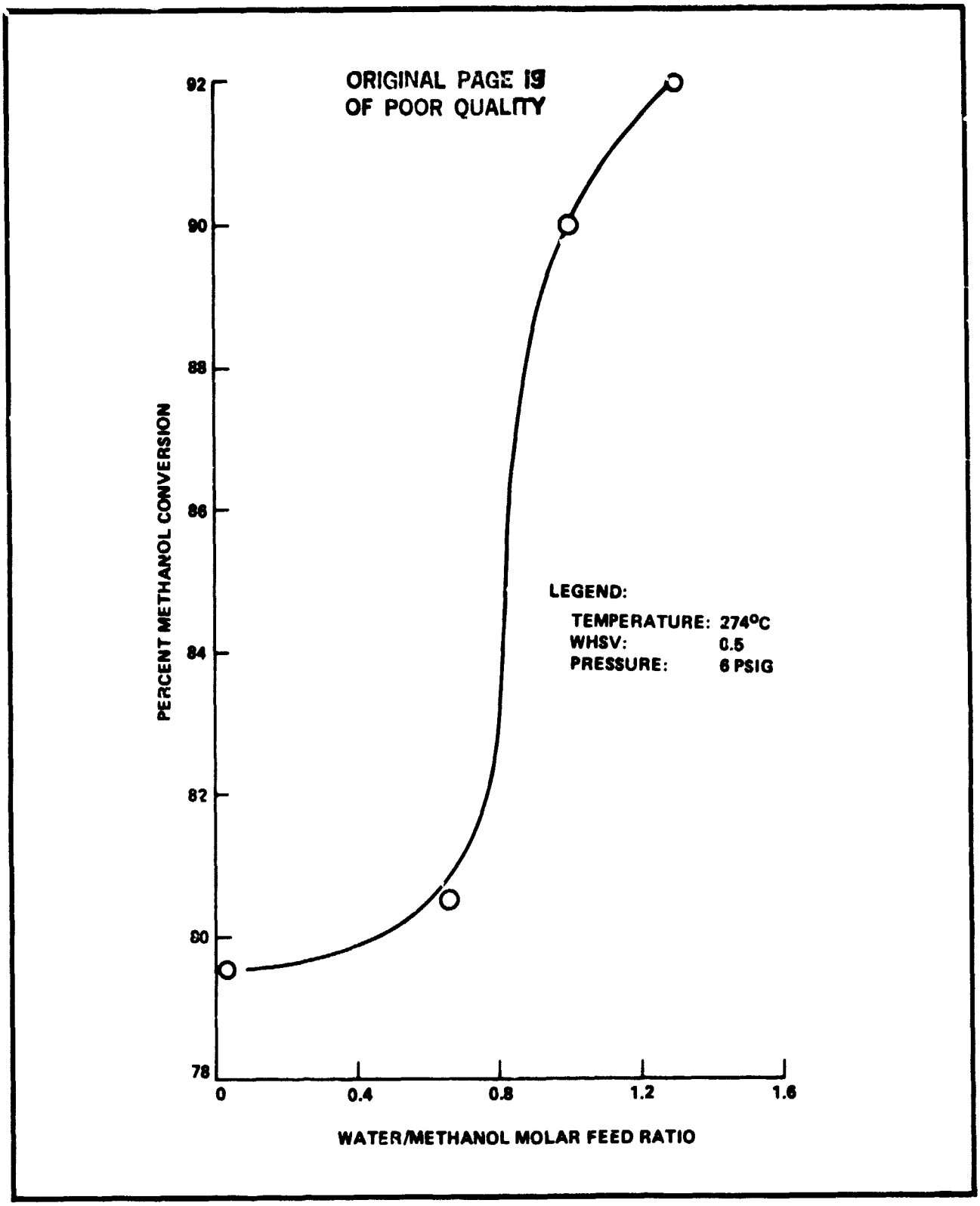

FIGURE X-10. EFFECT OF WATER/METHANOL RATIO ON CONVERSION

3. Effect of Shut-Down/Start-Up Cycles

On two occasions, methanol/steam reforming reactors were subjected to instantaneous shutdowns with accompanying isolation from the atmosphere. The reactors cooled to room temperature and remained there several hours before they were reheated and methanol-water feed was resumed. In both cases, methanol conversion retained the same level as before shutdown. More extensive examination of shutdown/start-up tolerance will be conducted during the Phase III program.

I. EVALUATION OF CATALYSTS OTHER THAN Cu/Zn TYPE

There are indications from this and other work that low-temperature shift catalysts of the Cu/Zn type have limitations in temperature stability and resistance to poisoning by higher alcohols. Near the end of this program, several other catalysts were screened at 400°C for activity, selectivity (CO content and possible methane formation) and stability.

Four catalysts were tested at 673 K (400°C) and WHSV 2 with the following results (H_2O/CH_3OH molar ratio = 1.3):

Catalyst	Methanol Conversion	Comment
Rh/Al_2O_3	98%	17% CH_4 and 17% CO in dry effluent gas. (Not selective.)
Mn/Al_2O_3	0%	Not active.
Fe/Cr (High temp. shift catalyst)	100%	12% CH_4 in dry effluent gas. (Not selective.)
Zn/Cr (High pressure methanol synthesis catalyst, Zn0312)	100%	No methane, CO below equilibrium value. Good stability.

The zinc chromium catalyst was selected for further testing. Results for a 1500 hour test at temperatures up to 500°C are listed

in Table X-6. Although less active than Cu/Zn catalysts, zinc-chromium is thermally stable and yields a low CO content. Further studies comparing Cu/Zn and Zn/Cr catalysts will be conducted during the Phase III program.

J. CONCLUSIONS

- Low-temperature shift catalysts of the Cu-Zn type are effective for the steam-reforming of methanol in the 500-550°F range.

- Zn-Cr catalysts have substantially lower activity than Cu-Zn catalysts for the steam-reforming of methanol, but these catalysts should be investigated further because of their ability to operate stably at high temperatures.

TABLE X-6

METHANOL/STEAM REFORMING ENDURANCE TEST RESULTS
USING ZINC–CHROMIUM CATALYST

Time, Hours	Temp., °C	WHSV	MeOH Conversion, %	CO, %	Second Order Rate Constant
18	404	1.41	99.84	3.94	1.31
91	401	1.50	99.61	2.35	1.21
163	394	1.65	99.81	2.03	1.56
260	395	1.35	99.63	1.81	1.10
330	397	1.56	99.55	2.51	1.21
426	399	1.61	99.82	2.28	1.54
522	399	1.49	99.62	2.22	1.21
619	399	1.34	99.49	2.50	1.01
691	392	1.45	99.42	1.43	1.06
808	397	1.62	99.68	1.30	1.37
858	373	0.57	99.28	1.25	0.39
980	375	0.49	99.44	2.09	0.36
1031	379	0.46	99.52	4.47	0.35
1101	370	0.40	99.62	1.31	0.32
1171	372	0.59	98.39	1.06	0.32
1292	500	0.50	100.00	–	–
1316	373	0.51	99.32	1.58	0.36
1459	375	0.51	99.40	1.32	0.37
1507	379	0.52	99.15	1.16	0.34

Notes:

Catalyst: 10 ml Harshaw Zn-0312 (Zn, Cr), 14-20 mesh, diluted with 90 ml alpha alumina.

Pressure: 115 kPa (2 psig).

H_2O/MeOH : 1.3

SECTION XI
INTEGRATED SUB-SYSTEM DESIGN

A. SIMULATED COOLANT LOOP

An experimental fuel cell coolant loop was set up as illustrated in Figure XI-1 to aid in evaluation of the fuel processing subsystem. Two 2.5kW electric furnaces were used to simulate the heat generated by the fuel cell. The coolant, Therminol 44, was circulated through heat exchangers in the furnaces and then through the vaporizer. This set-up also served to evaluate the type of coolant pump to be used in the final integrated system and to evaluate the methanol/water vaporizer. A gear pump with a DC motor drive was selected for endurance testing. The vaporizer was of the flat plate type with about 4 ft^2 of heat transfer surface. During the test runs the heat input was just adequate to vaporize 5.5 liters per hour of a mix with 1.3 moles of water per mole of methanol.

B. ANODE VENT GAS BURNER

Another sub-unit evaluated in this part of the work was the burner for the anode vent gas. The simulated composition of the fuel cell anode vent gas was as follows:

		Dry Basis
H_2	31.3 Mole %	39.1
CO	3.9 " "	4.9
CO_2	44.8 " "	56.0
H_2O	20.0 " "	-
	100.0	100.0

This represents the vent gas with the fuel cell operating at about 80% hydrogen utilization. Two burners were evaluated for this service and both are still under review for the integrated system testing. Burner HB3 is shown in Figure XI-2. The use of the monolithic catalyst downstream of the venturi assured ignition and good mixing over a wide range of air/fuel ratios as shown in Figure XI-3. This burner was used in the reformer/burner integration studies.

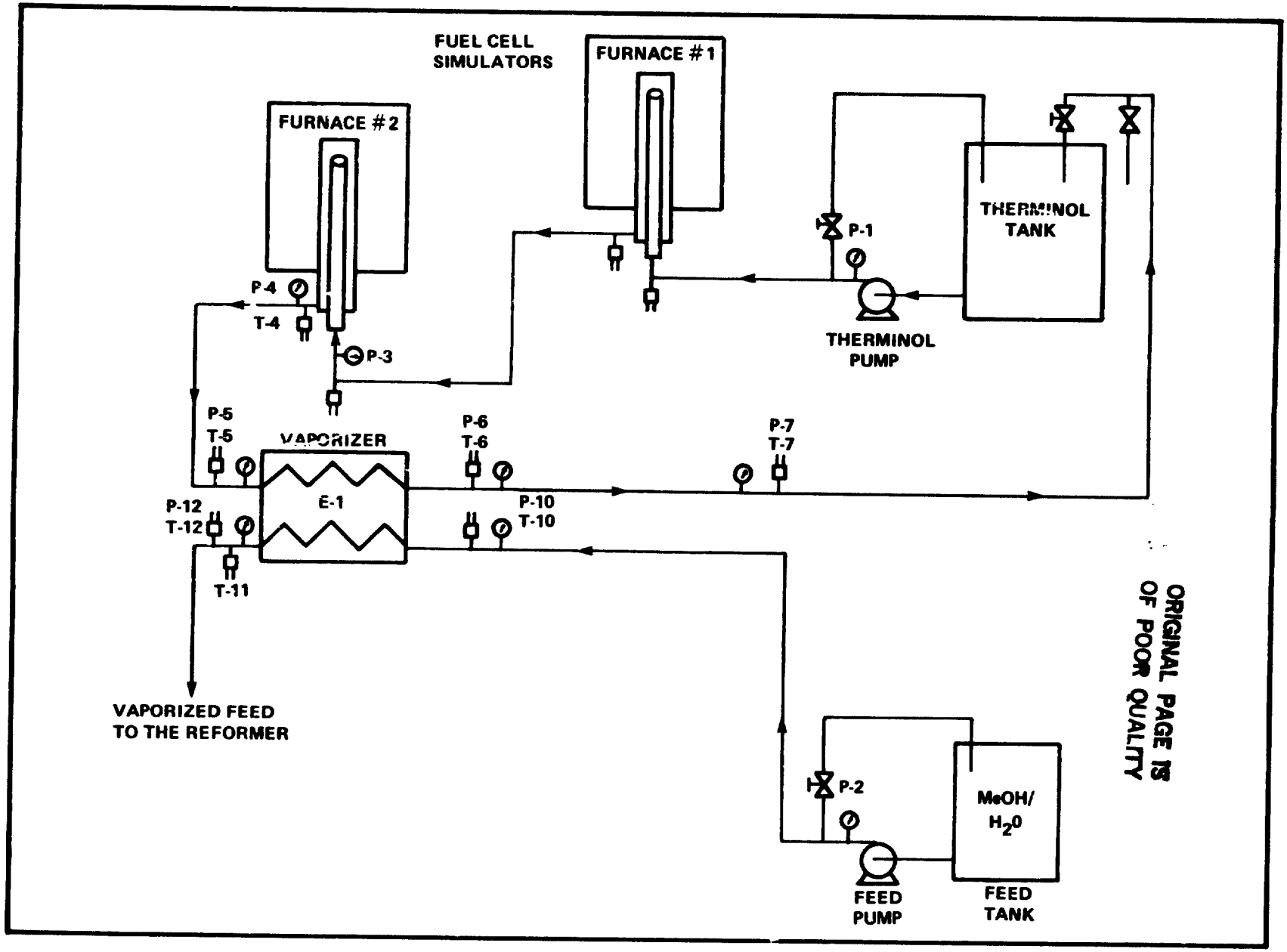

FIGURE XI-1. EXPERIMENTAL SET-UP TO SIMULATE THE FUEL CELL COOLANT LOOP

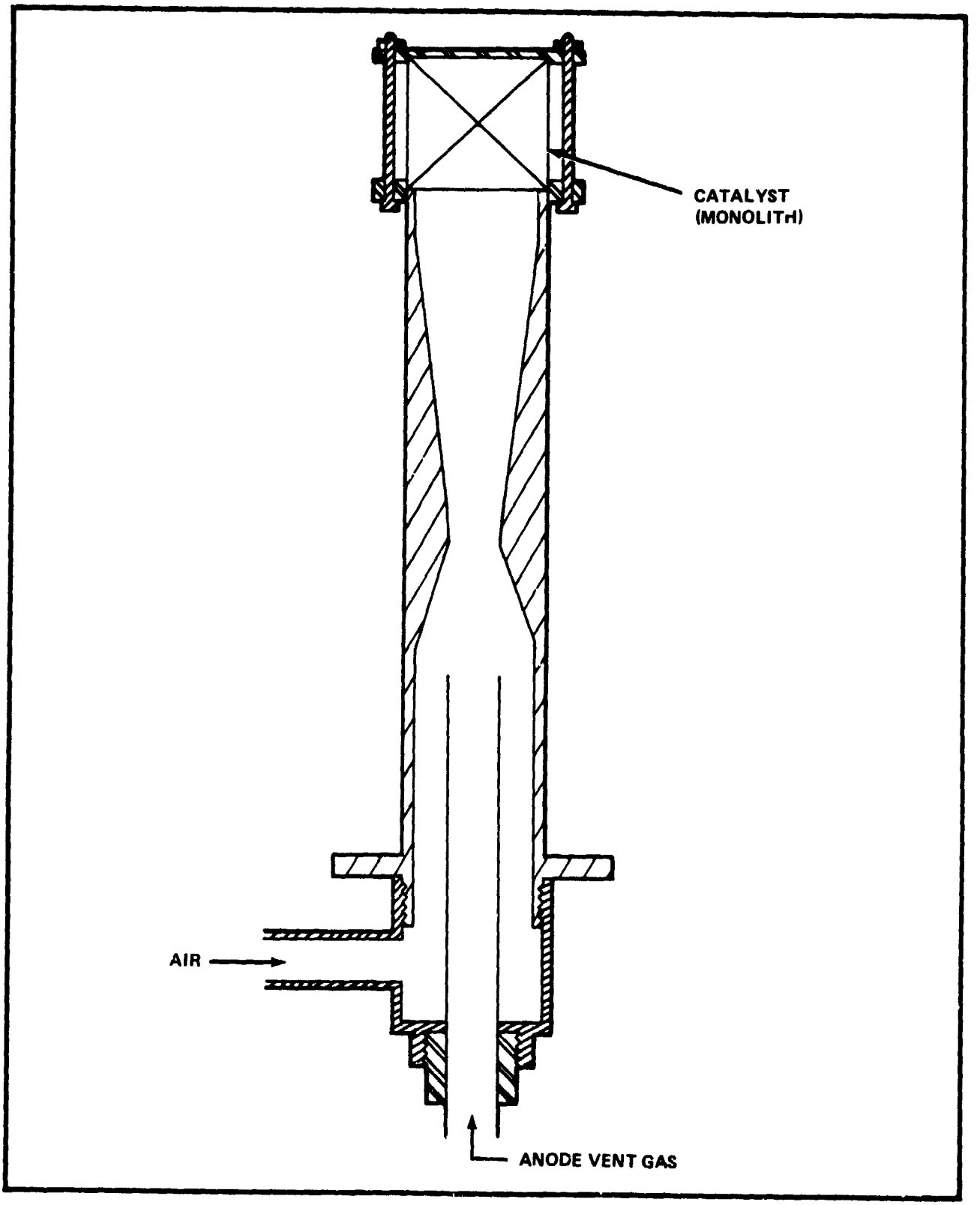

FIGURE XI-2. HYDROGEN BURNER HB3

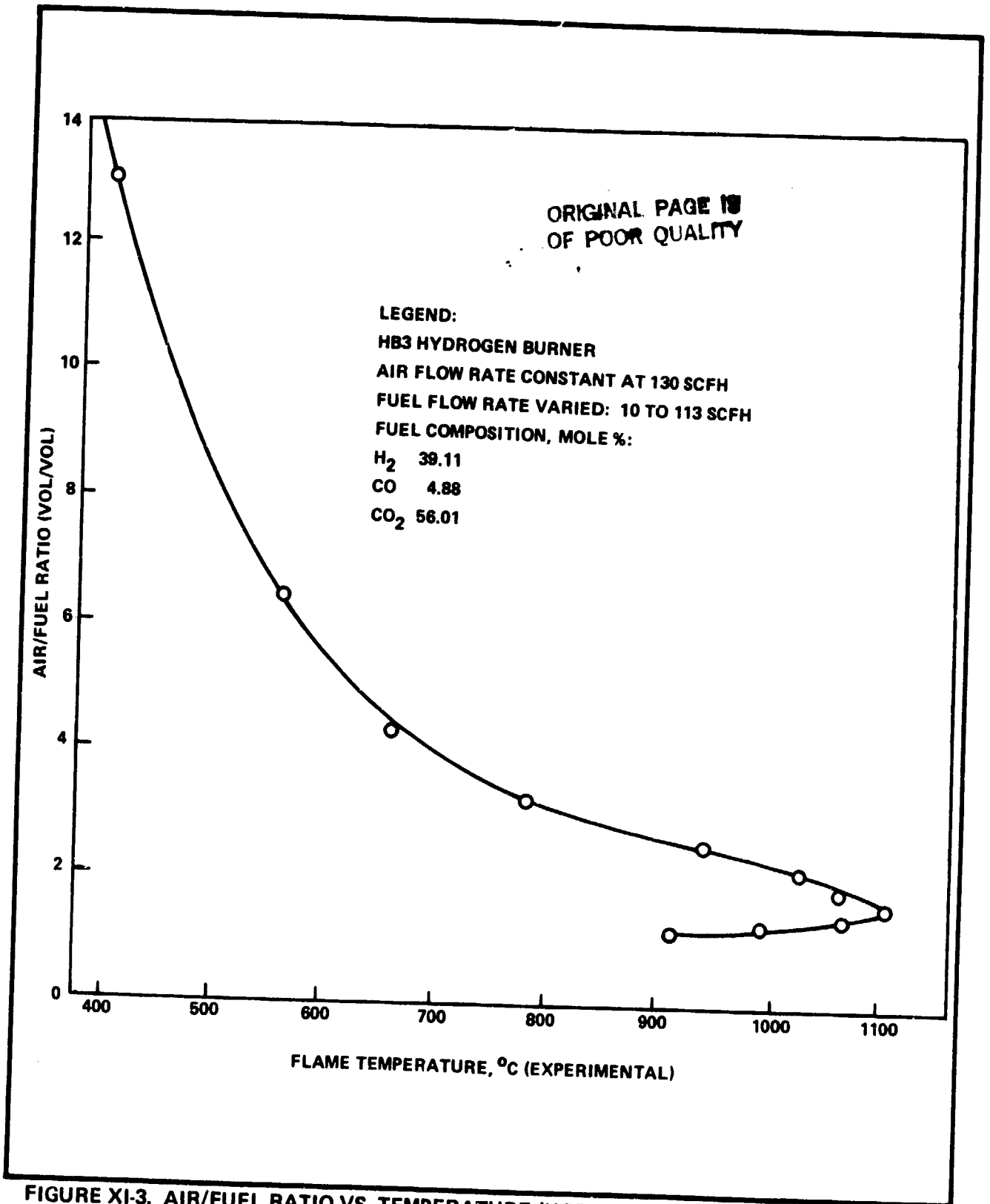

FIGURE XI-3. AIR/FUEL RATIO VS. TEMPERATURE (HORIZONTAL BURNER ORIENTATION)

A modified version of a home heating oil burner is also under development. It is possible that such a burner could be used for start-up on methanol and also for combusting anode vent gas. Simultaneous burning of methanol and anode vent gas is also possible. Such a burner would provide a simplified fuel processing subsystem.

C. START-UP FURNACE

Another aspect of this design work was the start-up furnace. In addition to the burner required to bring the reformer to operating temperature, a start-up furnace will be used to heat the Therminol that transfers heat to the fuel cell stack and the vaporizer. The current design (directed toward a nominal 20 minute start-up period) is shown in Figure XI-4. The Beckett burner is a home heating oil burner modified to burn methanol.

D. COMPUTER MODEL

Design of the start-up furnace was facilited by use of a computer model that determines heat transfer, pressure drop, and power consumption characteristics. Also, the film temperature limitations of the heating medium can be considered in design and parametric studies.

Table XI-1 illustrates the results of furnace design calculations. Results of the analysis of pressure drop, heat transfer and power consumption as a function of temperature of the liquid side of the furnace (Therminol side) are presented in Table XI-2.

The section of the program dealing with the analysis of pressure drop and power consumption is written in a general form. This allows for the analysis of a wide range of piping configurations. The furnace design section of the program determined the total heat transfer area (by trial and error) for a wide variety of finned tube types and geometric configurations. The program's flexibility was particularly useful for modifying the configuration to suit various requirements. Such design changes would have been extremely tedious to perform by hand calculation.

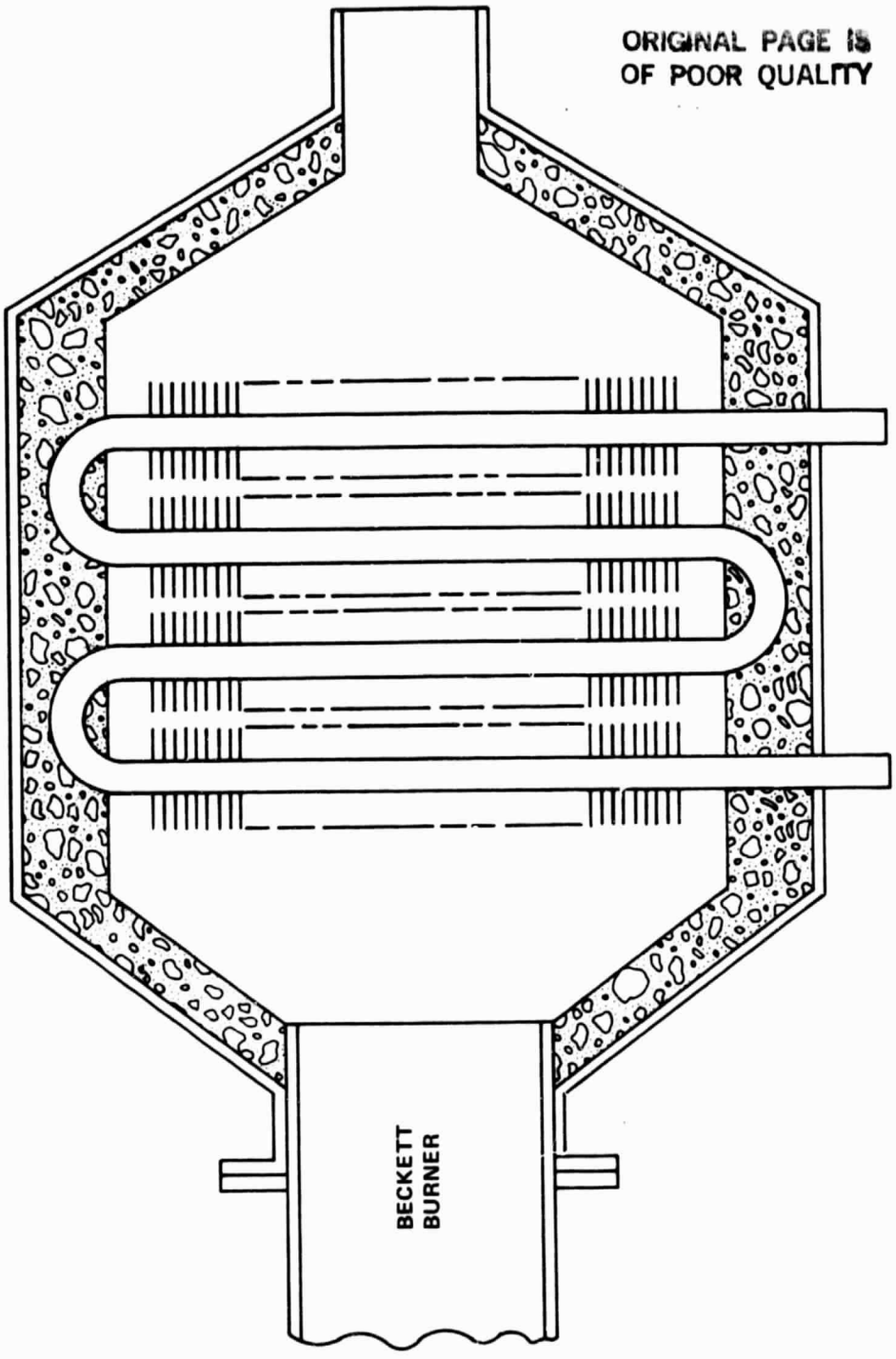

FIGURE XI-4. START-UP FURNACE DESIGN

TABLE XI-1

DESIGN OF START-UP FURNACE – COMPUTER MODEL ANALYSIS

OUTSIDE DIAMETER OF TUBE , IN, DO	= 0.50	
TUBE WALL THICKNESS,IN,WTH	= 0.060	
TRANSVERSE TUBE PITCH, IN,PT	= 2.00	
LONGITUDINAL TUBE PITCH, IN, PI	= 1.73	
FIN HEIGHT, IN, FH	= 0.50	
AVERAGE FIN THICKNESS,IN,FT	= 0.024	
NUMBER OF FINS PER UNIT LENGTH OF TUBE, 1/IN,FN	= 5.00	
FINNED LENGTH OF THE TUBE, FT,FL	= 0.75	
NUMBER OF TUBE ROWS IN DIRECTION OF FLOW,RN	= 2.62	
NUMBER OF TUBES PER ROW,NT	= 2	
FIN SEGMANT WIDTH,IN,WS	= 0.1560	
CROSS SECTIONAL OF FLOW OBSTRUCTIONS OTHER THAN FINNED TUBES,SQ. FT.,XC	= 0.17	
TOTAL INSIDE SURFACE AREA PER UNIT LENGTH OF TUBE,SQ.FT/FT.,AI	= 0.0995	
TOTAL OUTSIDE SURFACE AREA PER UNIT LENGTH OF TUBE,SQ.FT/FT.,AO	= 0.8861	
MEAN AREA OF TUBE WALL PER UNIT LENGTH OF TUBE,SQ.FT/FT.,AW	= 0.1152	
PRIME OUTSIDE SURFACE AREA PER UNIT LENGTH OF TUBE,SQ.FT/FT.,APO	= 0.1152	
FIN OUTSIDE SURFACE AREA PER UNIT OF TUBE,SQ.FT/FT.,AFO	= 0.7709	
FINNED TUBE PROJECTED CROSS SECTIONAL AREA PER UNIT LENGTH OF TUBE,SQ.FT/FT.,AC	= 0.0517	
NET FREE AREA IN A TUBE ROW,SQ.FT.,AN	= 0.1525	
TOTAL OUTSIDE SURFACE OF A BUNDLE,SQ.FT.,AT	= 3.49	
CROSS SECTIONAL FLOW AREA OF THE DUCT ENCLOSING THE BUNDLE,SQ.FT.,AD	= 0.4000	
OUTSIDE FLUID INLET TEMPERATURE, F,GT1	=1400.00	F
OUTSIDE FLUID OUTLET TEMPERATURE,F,GT2	= 800.00	
INSIDE FLUID INLET TEMPERATURE,F,TT1	= 70.00	
INSIDE FLUID OUTLET TEMPERATURE, F,TT2	= 250.00	
AVERAGE OUTSIDE FLUID TEMPERATURE,TB	=1100.00	
AVERAGE INSIDE FLUID TEMPERATURE,TI	=160.00	
AVERAGE FIN TEMPERATURE,TS	= 442.00	
AVERAGE TUBE WALL TEMPERATURE,TW	= 254.00	F
OUTSIDE FLUID MASS FLOW RATE, LB/HR,W	= 124.92	
TOTAL HEAT DUTY, BTU/HR,Q	= 22419.88	
HEAT CAPACITY,BTU/LB,F,CPW	= 0.2991	
AVERAGE OUTSIDE FLUID VISCOSITY,LB/HR,FT.,VISB	= 0.0899	
AVERAGE OUTSIDE FLUID DENSITY,LB/C.FT,RHOB	= 0.0245	
OUTSIDE FLUID INLET DENSITY,LB/CU.FT.,RHO1	= 0.0206	
OUTSIDE FLUID OUTLET DENSITY,LB/CU.FT.,RHO2	= 0.0304	
AVERAGE OUTSIDE FLUID THERMAL CONDUCTIVITY, BTU/HR FT.F,TKB	= 0.0344	
AVERAGE FIN THERMAL CONDUCTIVITY,BTU/HR,FT.F,TKF	= 28.10	
REYNOLD NUMBER CORRECTION TO J-FACTOR,C1	= 0.0313	
REYNOLD NUMBER CORRECTION TO F-FACTOR,C2	= 0.6225	
GEOMETRY CORRECTION TO J-FACTOR,C3	= 0.7165	
GEOMETRY CORRECTION TO F-FACTOR,C4	= 0.4608	
NON EQUILATRAL AND ROW CORRECTION TO J-FACTOR,C5	= 0.8747	
NON EQUILATERAL AND ROW CORRECTION TO F-FACTOR,C6	= 1.0395	
INSIDE FOULING RESISTANCE BASED ON INSIDE SURFACE AREA, HR. FT2 F/BTU,RFI	= 0.0010	
OUTSIDE FOULING RESISTANCE BASED ON TOTAL OUTSIDE SURFACE AREA,HR FT2 F/BTU,RFO	= 0.0030	
TOTAL INSIDE THERMAL RESISTANCE BASED ON TOTAL OUTSIDE AREA,HR.SQ.FT.F/BTU,RIO	= 0.0312	
TOTAL THERMAL RESISTANCE BASED ON TOTAL OUTSIDE AREA, HR FT2F/BTU,RTO	= 0.1437	
TUBE WALL THERMAL RESISTANCE BASED ON TOTAL OUTSIDE AREA,RWO	= 0.0013	
TOTAL OUTSIDE THERMAL RES. INCLUDING FIN EFF. BASED ON TOAL OUTSIDE AREA,HR.SQ.FT.F/BTU,RO	= 0.1111	
AVERAGE INSIDE CONVECTION HEAT TRANSFER COEFF.,BTU/HR.SQ.FT.F,HI	= 399.11	
AVERAGE OUTSIDE HEAT TRANSFER COEFF.,BTU/HR.SQ.FT.F,HO	= 11.20	
AVERAGE OUTSIDE CONVECTION HEAT TRANSFER COEFF.,BTU/HR.SQ.FT.F.,HC	= 11.25	
AVERAGE OUTSIDE RADIATION HEAT TRANSFER COEFF.,BTU/HR.SQ.FT.F.,HR	= 0.35	
EFFECTIVE OUTSIDE HEAT TRANSFER COEFF.,BTU/HR.SQ.FT.F.,HE	= 9.00	
REYNOLD NUMBER,RE	= 379.77	
MASS VELOCITY BASED ON THE NET AREA IN A TUBE ROW(AN),LB./HR.SQ.FT,GN	= 819.17	
FANNING FRICTION FACTOR,F	= 0.5164	
PRESSURE DROP ACROSS BUNDLE,INCHES OF WATER,DP	= 0.0314	

TABLE XI-2

DESIGN OF START-UP FURNACE – COMPUTER MODEL RESULTS

NUMBER OF SUDDEN CONT. SECTIONS,N1 = 0
NUMBER OF SUDDEN EXP. SECTIONS,N2 = 0
NUMBER OF SHARP EDGE ORIFICES,N3 = 0
NUMBER OF 90 DEG. ELBOWS(ROUNDED),N4= 0
NUMBER OF 90 DEG. ELBOWS(SQUARE),N5 = 0
NUMBER OF 180 DEG. BENDS,N6 = 6
NUMBER OF GLOBE VALVES,N7 = 0
NUMBER OF GATE VALVES,N8 = 0

ASSUMED PUMP EFFICIENCY = 0.55
TOTAL FLOW RATE = 38.500 CUBIC Feet PER HR.
TOTAL LENGTH OF TUBES = 10.00 Feet
FLOW RATE PER TUBES IN PARALLEL = 19.250 CUBIC Feet PER HR.

EFFECT OF TEMPERATURE AND TUBE DIAMETER

TEMP. DEG.F	DI.. IN.	RE.NO.	F.FACTOR	VELOCITY FT./SEC	P.DROP PSI	POWER HP.	PR.NO.	H.T.COEFF. BTU\HR.Sq.Ft.DEG.F
50.00	0.3800	1975.78	0.0080981	6.79	6.7779	0.0345	126.40	278.726
100.00	0.3800	5490.40	0.0091892	6.79	7.0407	0.0358	47.49	351.676
150.00	0.3800	10978.64	0.0072275	6.79	6.3448	0.0323	24.65	407.290
200.00	0.3800	17893.05	0.0068392	6.79	5.8706	0.0299	15.65	449.110
250.00	0.3800	26524.04	0.0061982	6.79	5.5151	0.0281	10.98	483.720
300.00	0.3800	37194.89	0.0056958	6.79	5.2140	0.0265	8.17	511.900
350.00	0.3800	45912.94	0.0054020	6.79	4.9759	0.0253	6.90	523.281
400.00	0.3800	56494.39	0.0051307	6.79	4.7486	0.0242	5.86	532.966
450.00	0.3800	68450.71	0.0048903	6.79	4.5340	0.0231	5.07	538.823
500.00	0.3800	78833.89	0.0047206	6.79	4.3521	0.0222	4.64	536.319

E. REFORMER/BURNER TEST UNIT DESIGN

The most important element of this design phase was the reformer design and development. The original design was accomplished using general reactor engineering principles applied to this specific requirement and was facilitated by the development of a mathematical simulation model. This computer model permits evaluation of important chemical and physical parameters such as:

- Methanol feed rate
- Water/methanol ratio
- Reactor tube diameter
- Number of reactor tubes
- Activation energy
- Overall heat transfer coefficient
- Space velocity
- Reactor length
- Catalyst density, mass, and volume
- Reactant inlet temperature
- Flue gas temperature and flow rate
- Reactor pressure

A number of simulation studies have been conducted to examine the effect of various design and operating parameters on the reactor performance. Two key studies of this type are discussed below.

1. Heat Transfer Coefficient: The overall heat transfer coefficient, U, was varied over the range 0 (adiabatic) to 7.35 BTU/hr ft^2 °F, while keeping the following constant:

a) Flue gas inlet temp. (782°C)
b) Reactant inlet temp. (299°C)
c) H_2O/MeOH (1.3)

Figure XI-5 shows the effect of change in the extent of heat transfer on methanol conversion and reactant temperature. Curves 1A and 2A correspond to adiabatic conditions where the

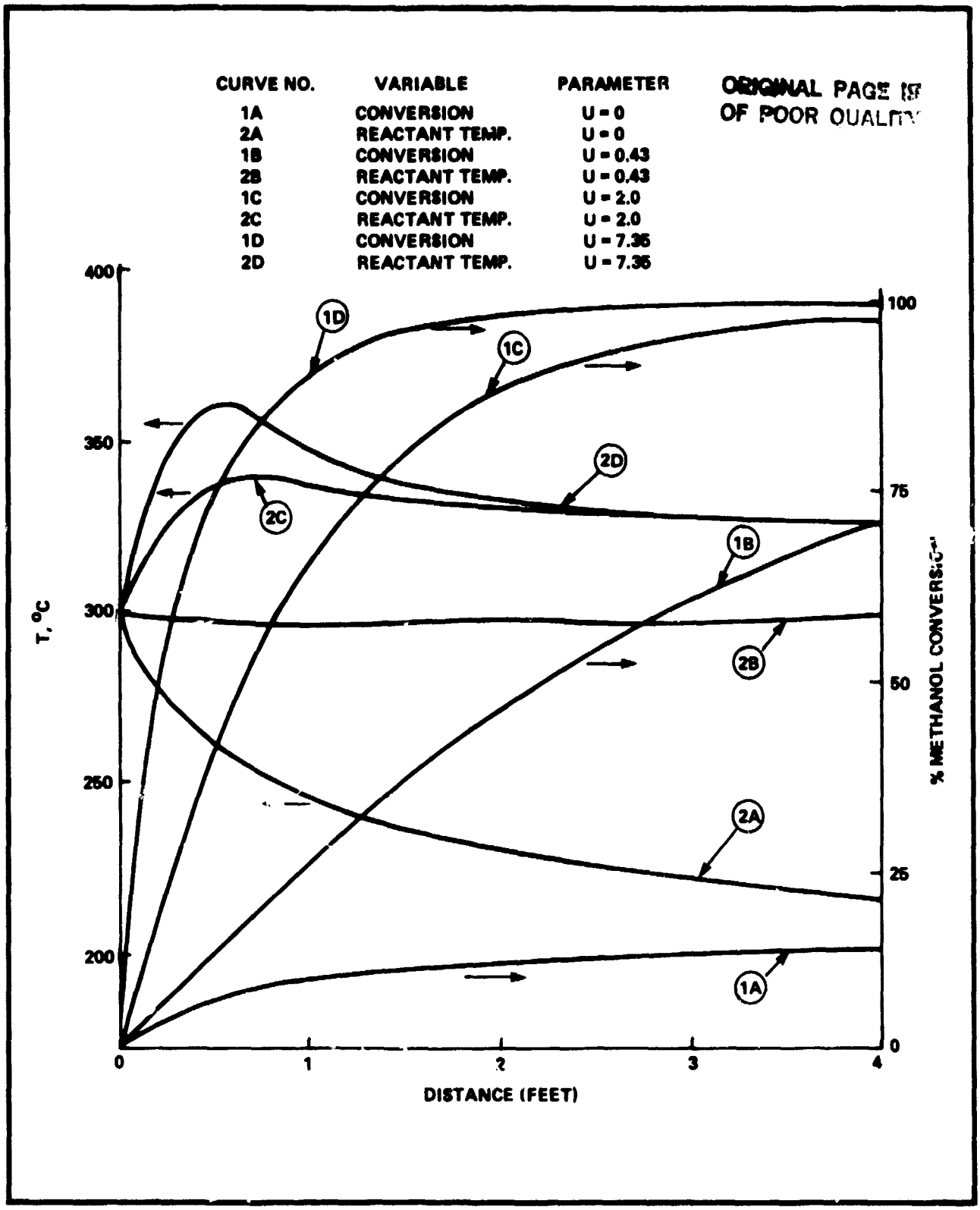

FIGURE XI-5. REACTANT TEMPERATURE AND CONVERSION PROFILES WITH OVERALL HEAT TRANSFER COEFFICIENT AS PARAMETER

heat of reaction is completely supplied by the sensible heat in the reactant. It is interesting to note that for a value of U = 0.43 it would be possible to achieve isothermal conditions within the reactor. The actual heat transfer coefficient is expected to lie between the 2.0 and 7.35 BTU/hr ft^2 °F values. Figure XI-6 shows the flue gas temperature profiles which correspond to the cases of Figure XI-5.

2. Reactant Inlet Temperature: The reactant inlet temperature was varied over the range 338°C to 505°C, while keeping the following constant:

a) U (2 BTU/hr ft^2 °F)
b) H_2O/MeOH (1.3)
c) Flue gas inlet temperature (671°C)

The results for this case are presented in Figure XI-7. It is interesting to note that it is possible to supply a substantial amount of the heat of reaction as sensible heat in the reactants, achieving high conversion even under poor heat-transfer coefficient and relatively low flue gas temperature conditions (compare Figure XI-7 with Figure XI-5). Also, the high inlet reactant temperature, which might exceed a safe operating value for the catalyst, drops very rapidly within a short distance in the reactor.

The reactor that evolved from this study is shown in Figure XI-8. The combustion chamber houses the burner plus two heat transfer coils. The bottom coil preheats the air for the fuel cell stack. This aspect of the design is still under review. At high hydrogen utilization, the anode vent gas heating value would be insufficient to support this heat duty. The second coil acts as the feed superheater to add the sensible heat required in this design. The catalyst is contained in 12 "U" tubes, each 48" long. The flue gas and process gas flow co-currently through the heat exchanger zone, with the flue gas on the shell side.

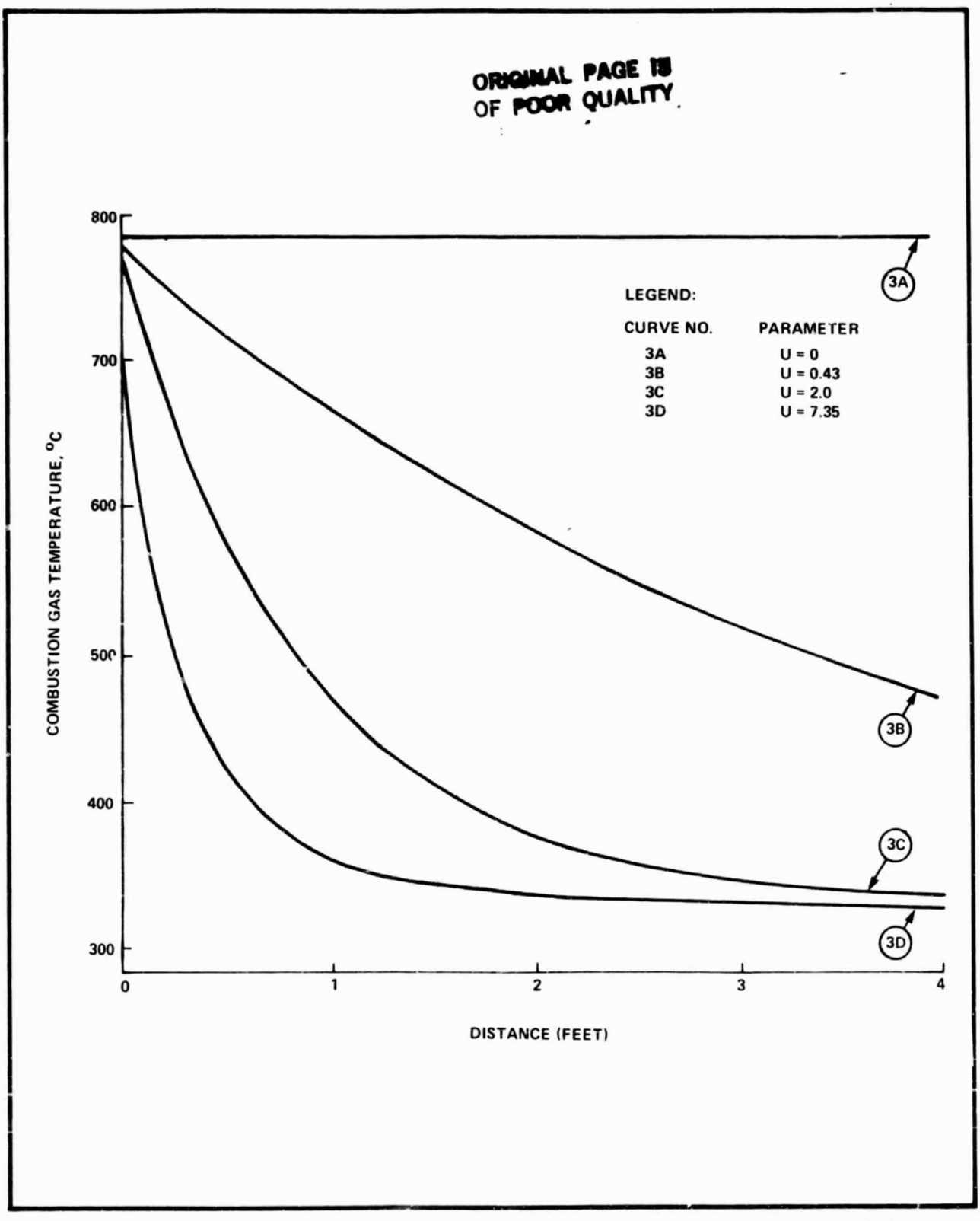

FIGURE XI-6. COMBUSTION GAS TEMPERATURE PROFILES WITH OVERALL HEAT TRANSFER COEFF., U, AS A PARAMETER

LEGEND:

CONST. FLUE GAS INLET TEMP., 671°C

CONST. H_2O/ MeOH, 1.3

CONST. OVERALL HEAT TRANSFER COEFF, U = 2

CURVE NO.	PARAMETER
1A 2A	T (INLET) = 338°C
1B 2B	T (INLET) = 394°C
1C 2C	T (INLET) = 449°C
1D 2D	T (INLET) = 505°C

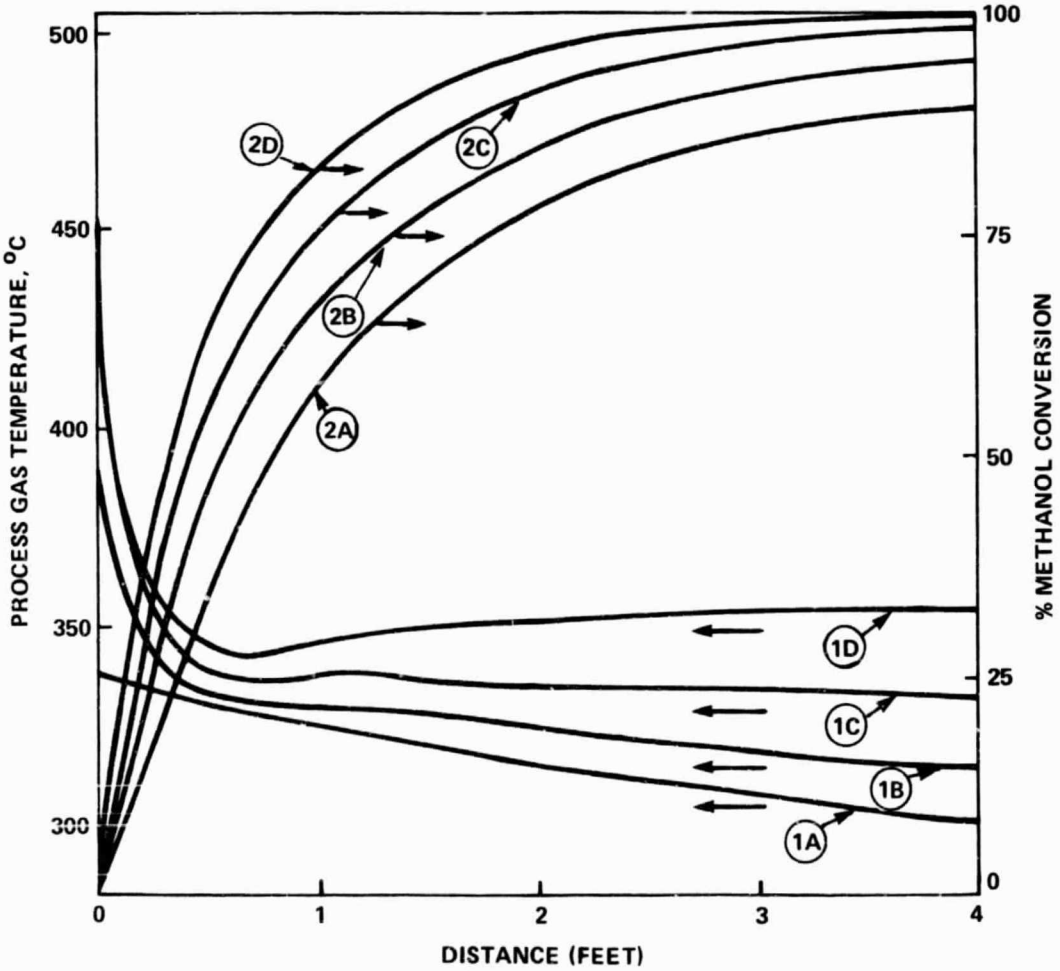

FIGURE XI-7. EFFECT OF REACTANT INLET TEMPERATURE ON CONVERSION

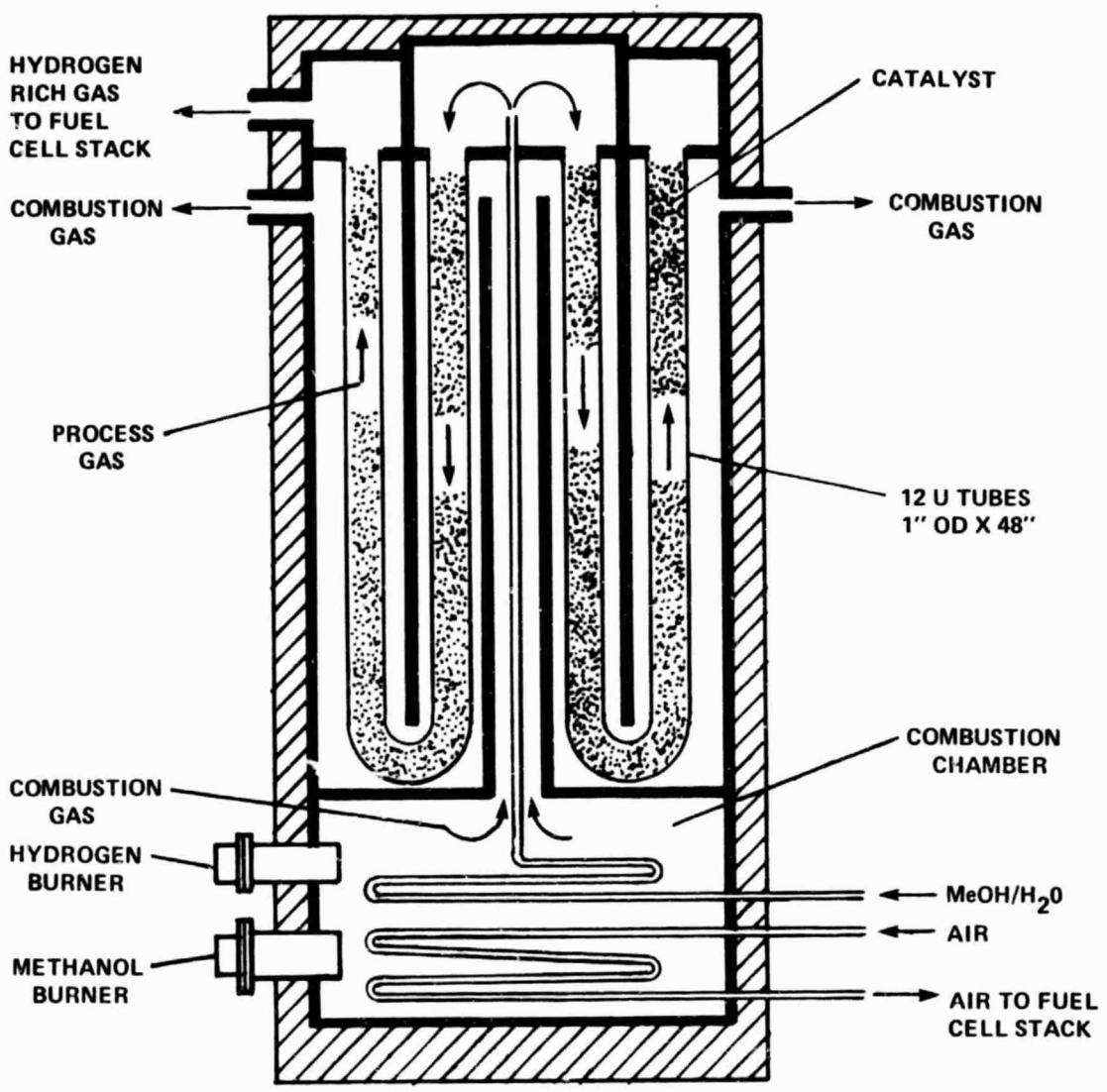

FIGURE XI-8. FUEL PROCESSING INTEGRATED TEST UNIT

SECTION XII

EVALUATION OF THE REFORMER/BURNER INTEGRATED TEST UNIT

Steady state and transient runs were conducted to confirm the design of the reformer and to study the dynamics of the integrated subsystem. Typical conditions for steady state operation at full load are listed below along with the results of Run 15.

Catalyst (ICI52-1 Pellets)

Total catalyst vol.	=	6.29
Catalyst weight (reduced)	=	6.05 kg
Catalyst bed bulk density	=	0.96 kg/

Feed

H_2O/MeOH (Molar)	=	1.3
Feed flow rate	=	5.5 /hr
Feed Sp. Gr.	=	0.894
Feed Composition, methanol wt %	=	57.7
Feed Composition, methanol vol %	=	63.2
Average start-up time	=	20 mins

Space velocity, mass basis (WHSV) = $\frac{0.47 \text{ gm MeOH/hr}}{\text{gm cat.}}$

Space velocity, vol. basis (VHSV) = $\frac{985 \quad \text{theor. } H_2 \text{ (STP)}}{\text{hr.} \quad \text{catalyst}}$

Operating Conditions of typical run (#15)

Temperature of MeOH/H_2O feed to superheat coil	=	196°C
Temperature of superheated MeOH/H_2O feed to reformer reaction tubes	=	382°C
Average catalyst bed temperature (all tubes)	=	279°C
Temperature of reactants leaving reformer	=	296°C

Flue gas temperature, inlet at the top of reformer	=	477°C
Flue gases leaving reformer (shell side)	=	286°C
Flow rate of flue gases leaving reformer (shell side)	=	14.0 kg/hr
Combustion air flow rate	=	8.6 kg/hr
Fuel flow rate to burner	=	5.4 kg/hr
Burner fuel composition (mole %): CO_2 56%, H_2 39% and CO 5%		
Average heat input rate to reformer	=	5,195 kcal/hr
	=	20,610 BTU/hr

Results

Conversion	=	100% (nominal)
Condensate Sp. Gr.	=	0.999
Dry gas produced (STP)	=	8,185 /hr

Product gas composition (mole %):

H_2	73.4
CO_2	24.0
CO	2.6

A. START-UP PROCEDURE

The reformer start-up procedure consists of rapid heating of the catalyst bed in nitrogen (using 250 SCFH air and 200 SCFH fuel feed to the burner). This normally takes 20-25 min. When the catalyst bed temperature reaches about 200°C, the feed is introduced, the nitrogen flow is stopped and the fuel flow rate to the burner is adjusted to maintain the required reaction temperature.

A modified version of this procedure was used in later runs. Nitrogen was not used since it would not be available in an integrated system. The catalyst was heated for a shorter period (10 minutes), under no-flow conditions, to a moderate temperature (150°C) prior to feed introduction. This temperature is low enough to insure that no hot-spots are created in the catalyst bed and sufficiently high to prevent feed condensation on the catalyst pellets. The procedure has been tested and proven successful.

B. STEADY STATE OPERATION

Figure XII-1 shows a comparison of experimental and model-predicted temperature profiles of reactants and flue gas. The experimental data plotted in this figure are from Runs 15 and 16. Experimental inlet conditions were used in the computer program to obtain the simulated curves in Figure XII-1. An overall heat transfer coefficient of 4.5 BTU/hr °F ft^2 was used in the simulation.

The chemical kinetic parameters used in the simulation were derived from previous experimental runs in the sub-scale unit. Figure XII-1 shows a reasonable agreement between the model predictions and the actual experimental profiles. An axial conversion profile, predicted by the model, is also shown in Figure XII-1.

C. TRANSIENT STUDIES

The transient and steady-state temperature behavior in the 5kW reformer/burner integration unit has been studied over a wide range of feed flow rates to the reformer and air and fuel flow rates to the burner. In these runs, anticipated operating conditions of the integrated system were simulated experimentally. The study examined the transient behavior of the reformer as the hydrogen demands of the fuel cell stack varied from part-load to full-load operation. These data showed the extent of interdependence among key operating parameters (feed flow rate to the reformer and air and fuel flow rate to the burner) and the transient temperature distribution in the various zones of the reformer.

In Run 23 (Figures XII-2 and XII-3), the air flow rate was kept constant at 250 SCFH while the flow of burner fuel was adjusted in response to a feed flow rate step change from 2.9 /hr to 5.5 /hr (baseline value). The 5.5 /hr feed flow rate was maintained for 78 minutes, followed by a step decrease to 1.5 /hr. The figures

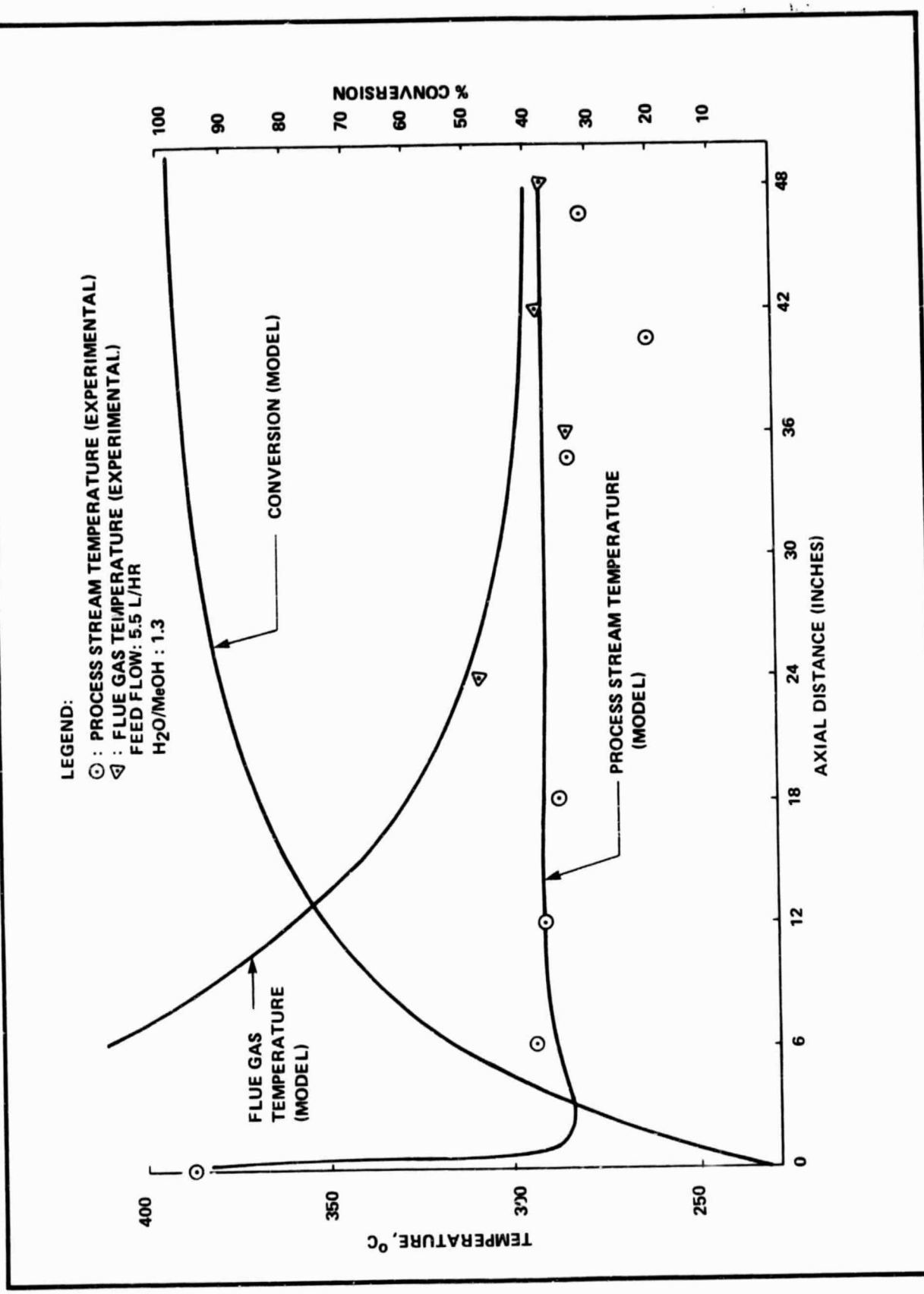

FIGURE XII-1. A COMPARISON BETWEEN EXPERIMENTAL AND MODEL-PREDICTED TEMPERATURE PROFILES

show both the feed flow rates and the corresponding changes in burner fuel flow rate. Transient changes in temperature in the various zones of the reformer, both within the catalyst bed and in the flue gas, are plotted in Figures XII-2 and XII-3 in order to show the response to changes in input parameters.

Figures XII-4 and XII-5 show the results of Run 25. In this run, while the reformer was maintained at baseline conditions, the temperature for a given heat load was adjusted by slightly changing the air to fuel ratio. However, changes in the air to fuel ratio were used only for "fine-tuning" of the temperature.

In one run the reformer was operated at baseline conditions for 27 hours. The purpose of the run was to confirm sound and stable performance of the reformer. Frequent monitoring of the gas produced and conversion during this run showed no decline in reformer performance over the 27 hours.

D. CONCLUSIONS

- The operation of the reformer/burner integrated test unit was in conformity with the design specifications.

- The mathematical simulation model for the reformer is a valuable tool in reformer design studies.

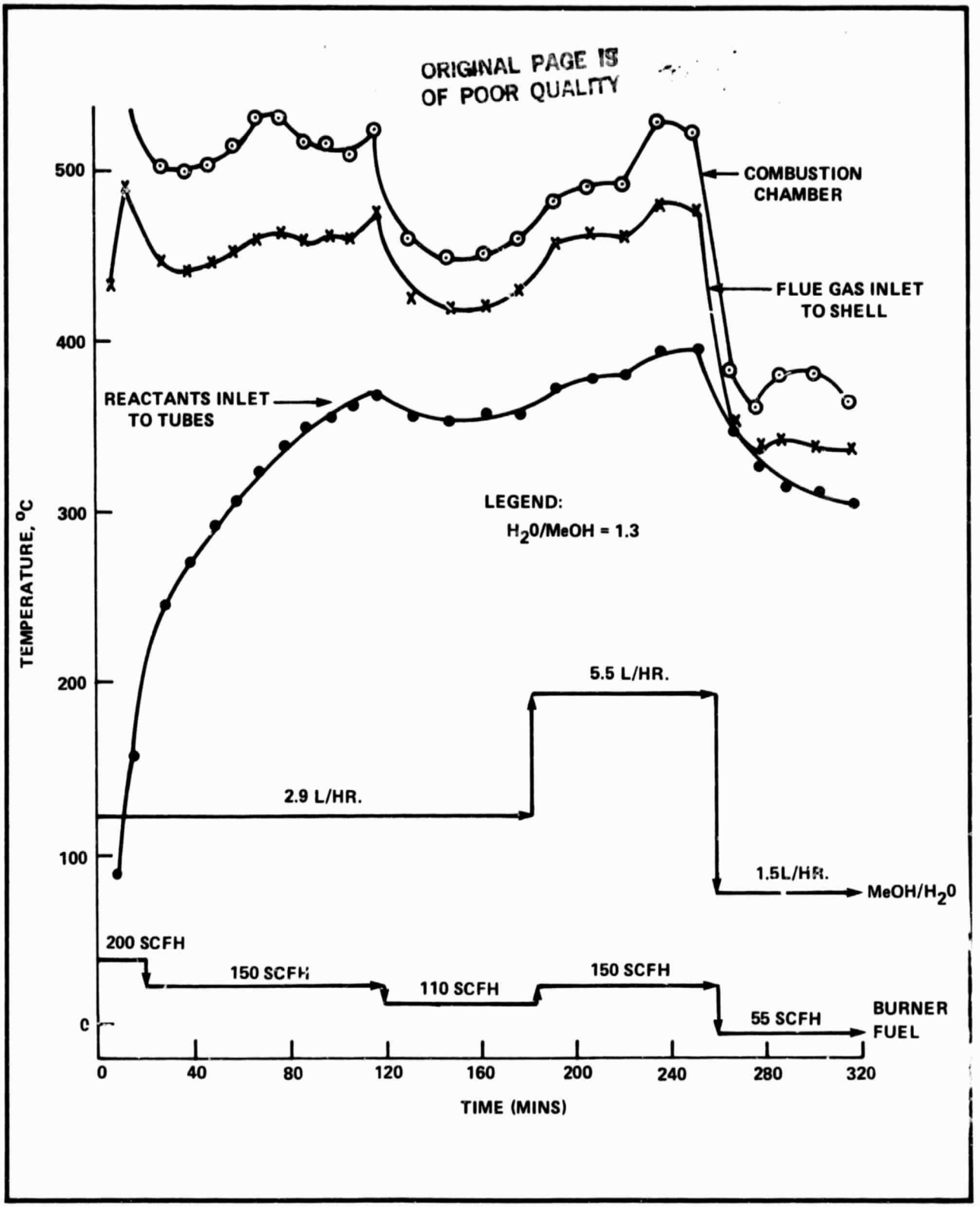

FIGURE XII-2. REFORMER TEMPERATURE – EFFECT OF CHANGES IN FEED FLOW RATE

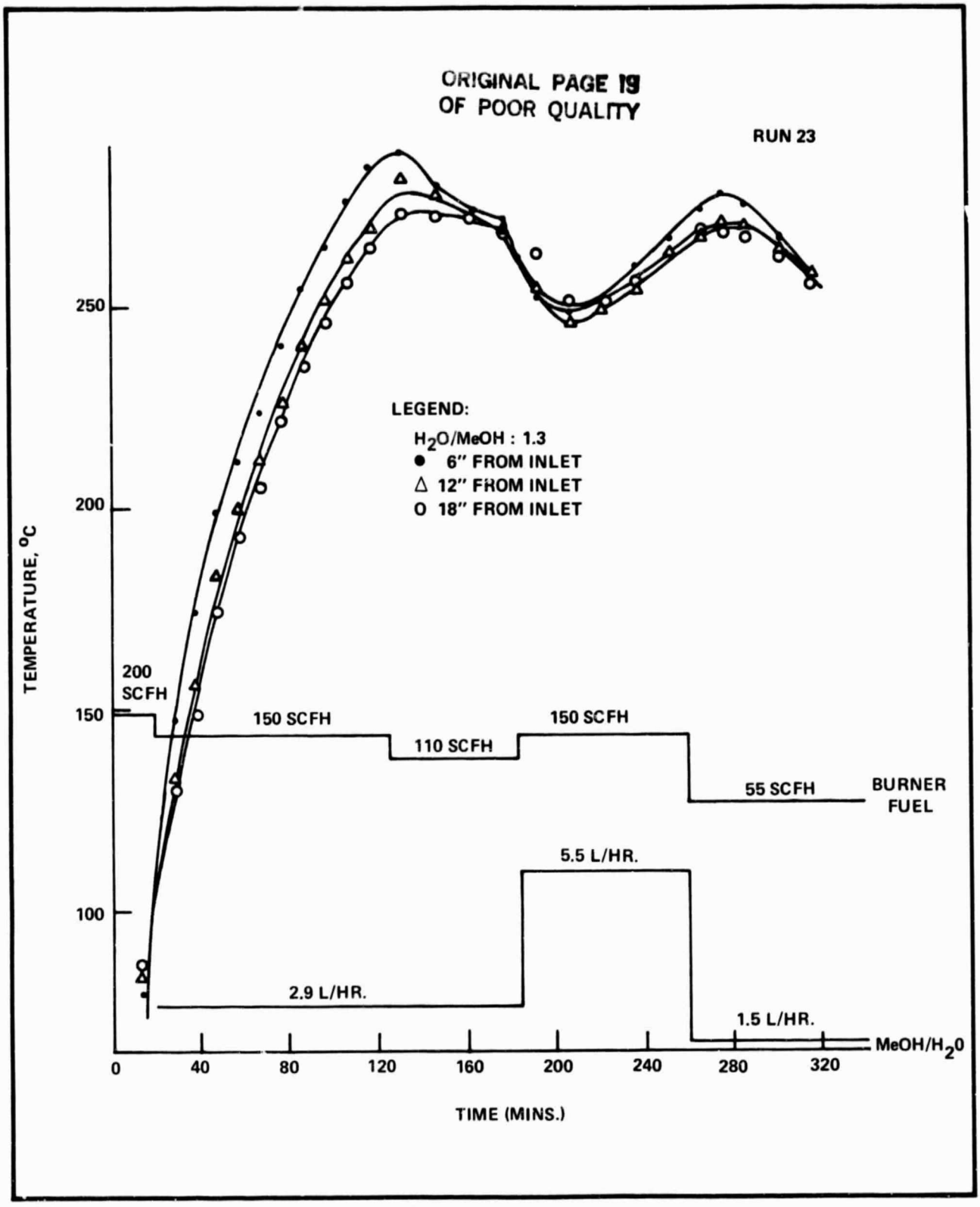

FIGURE XII-3. REACTANTS TEMPERATURE – EFFECT OF CHANGES IN FEED FLOW RATE

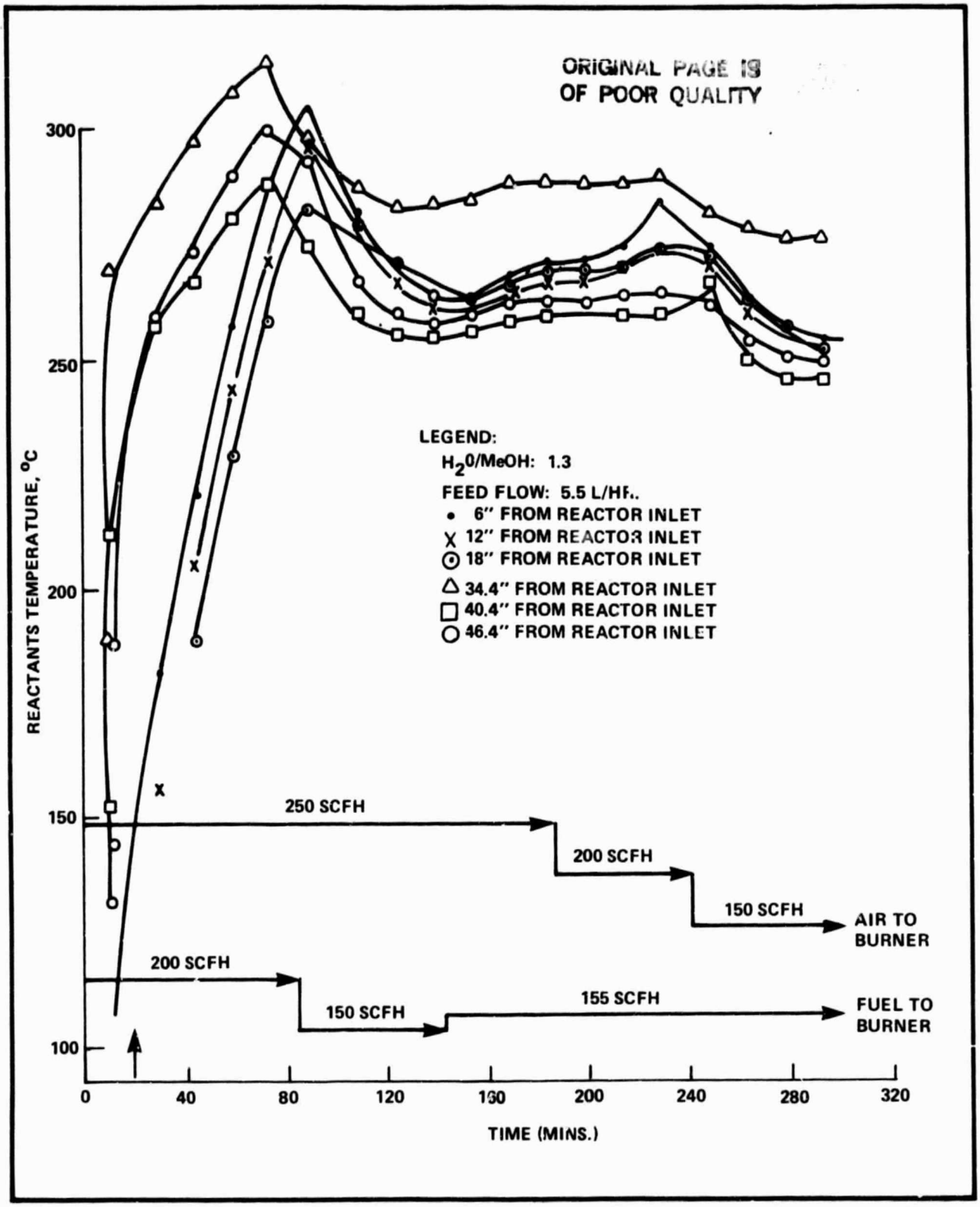

FIGURE XII-4. REACTANTS TEMPERATURE – EFFECT OF CHANGES IN AIR/FUEL RATIO

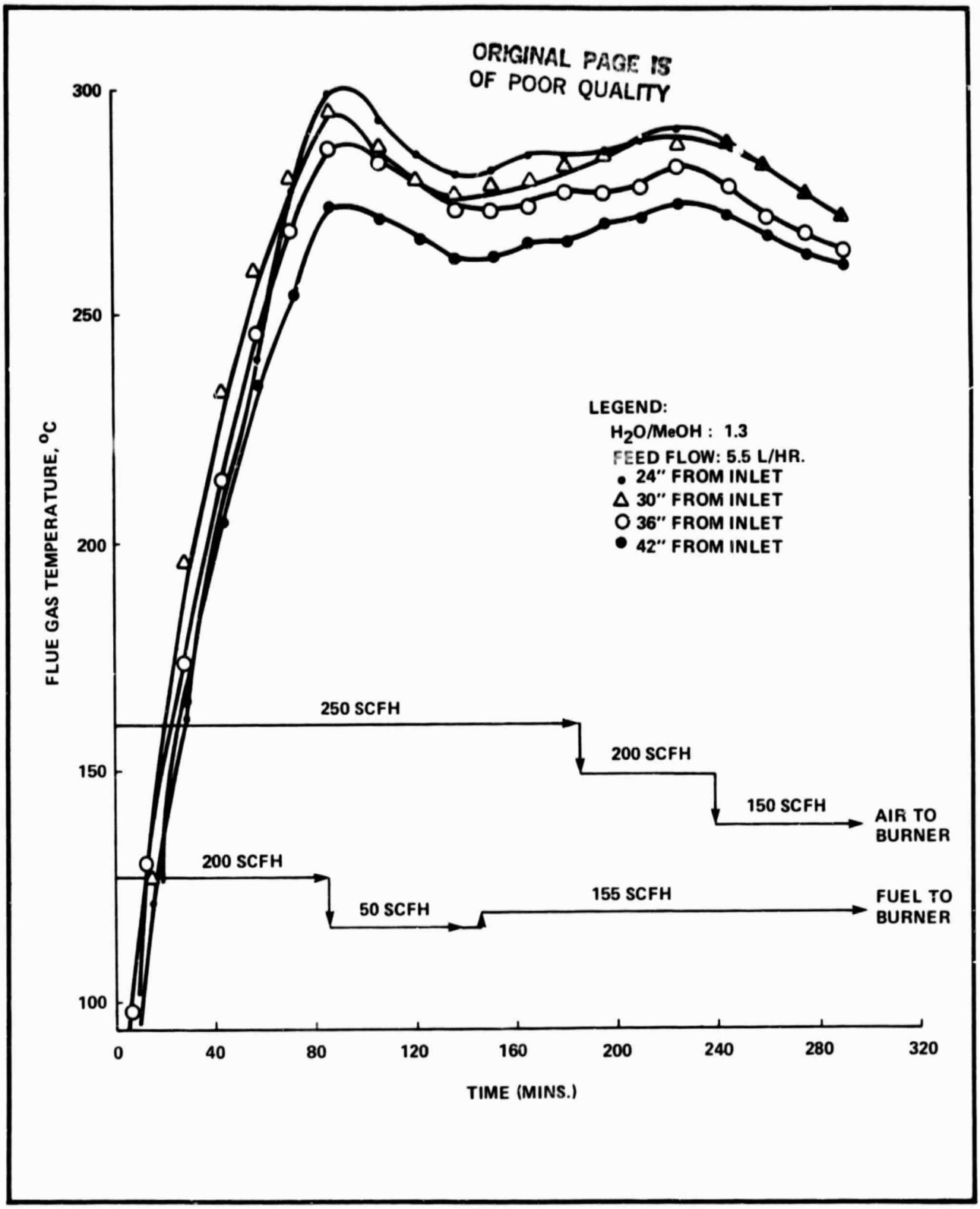

FIGURE XII-5. FLUE GAS TEMPERATURE, EXIT SIDE OF REACTOR – EFFECT OF AIR/FUEL RATIO

SECTION XIII

DESIGN AND PRELIMINARY EVALUATION OF THE 5KW REFORMER

The mathematical simulation model was used to show that the 12 "U" tubes could be replaced by 20 straight tubes (the volume of catalyst used in both cases being the same). Figure XIII-1 shows the predicted results for this reformer concept. Elimination of the "U" tubes allows a simplified and more compact unit.

The resulting reformer design, that will be used in the 5kW integrated system, is shown in Figure XIII-2. As in the previous design, the flue gas flows on the shell side co-currently with the process gas flowing in the tubes. A number of baffles have been included on the shell side to improve heat transfer from the flue gas to the reactor tubes. The design studies indicated that satisfactory performance could be anticipated with the 27 inches of tube length even if the overall heat transfer coefficient were as low as 2.0 BTU/hr ft^2 °F.

This reformer was fabricated and evaluated in the experimental set-up shown previously. Early tests showed the need for more insulation at the top and around the burner section. After this was corrected, tests were run with inert packing to study the heat transfer in the reformer.

Inert tests were run with varying air/fuel ratios at constant fuel flow. Nitrogen was used as the process gas; the flow rate was chosen to simulate the heat capacity with methanol and water. Figure XIII-3 shows the thermocouple locations in the reformer. Two inboard and two outboard tubes have thermocouples positioned axially. Table XIII-1 lists the temperatures for one set of data simulating full load conditions. Figure XIII-4 shows the flue gas and inert packing temperatures at steady state. Heat from the combustion zone is apparently being transferred to the bottom section of the tubes. (A similar observation was made later with catalyst present under steam/methanol reforming conditions.)

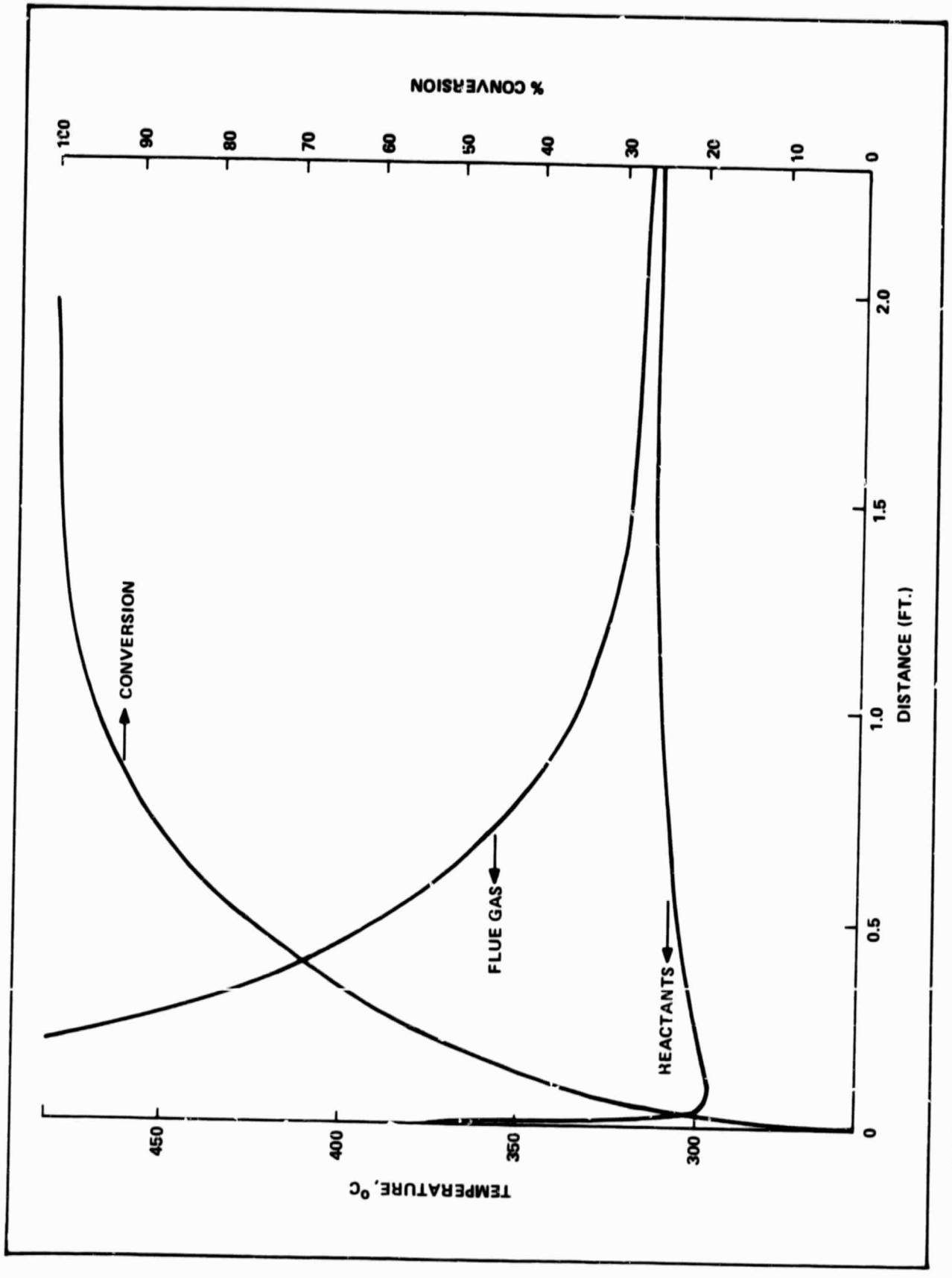

FIGURE XIII-1. 5kW REFORMER DESIGN-THEORETICAL MODEL SIMULATION

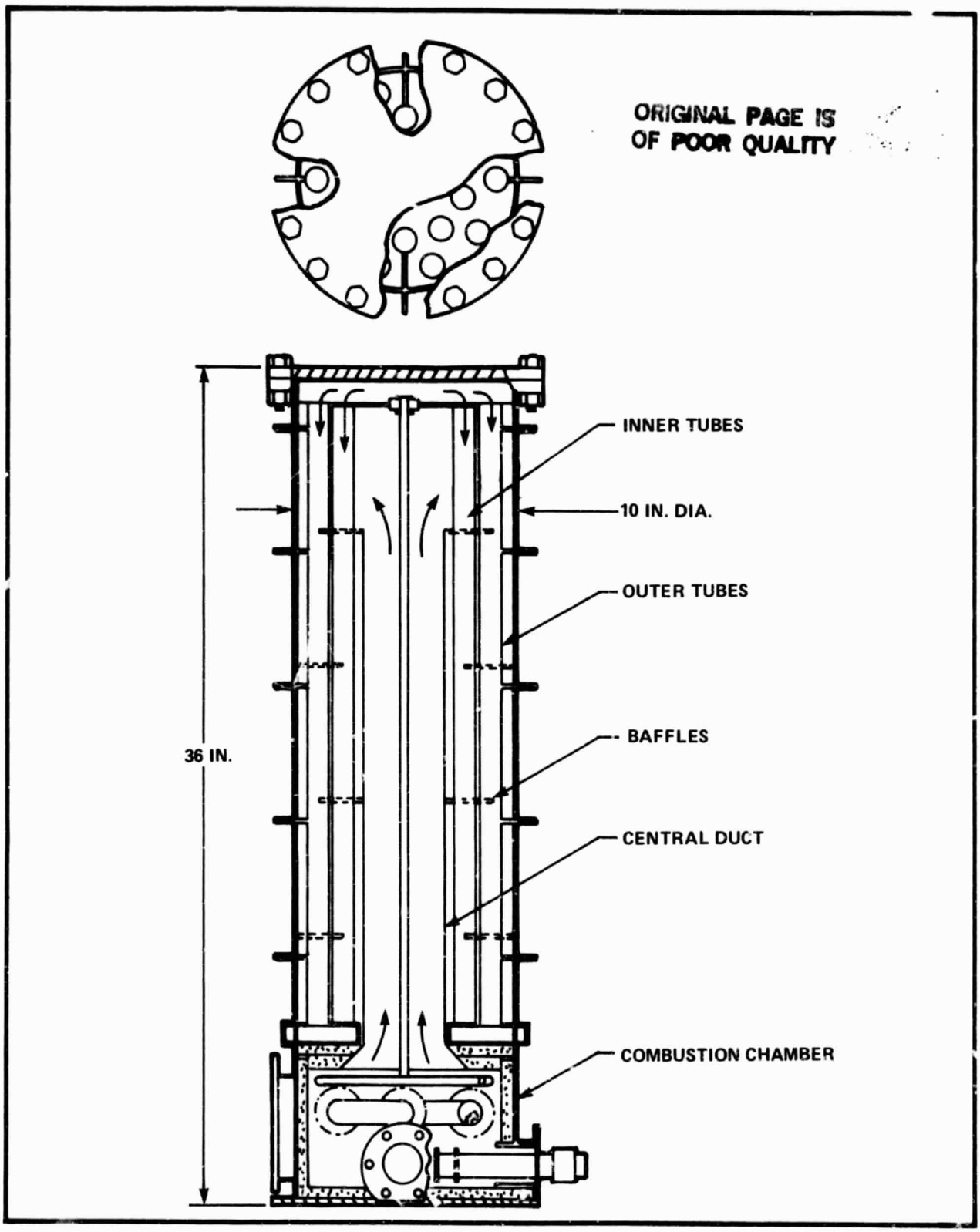

FIGURE XIII-2. 5kW METHANOL REFORMER

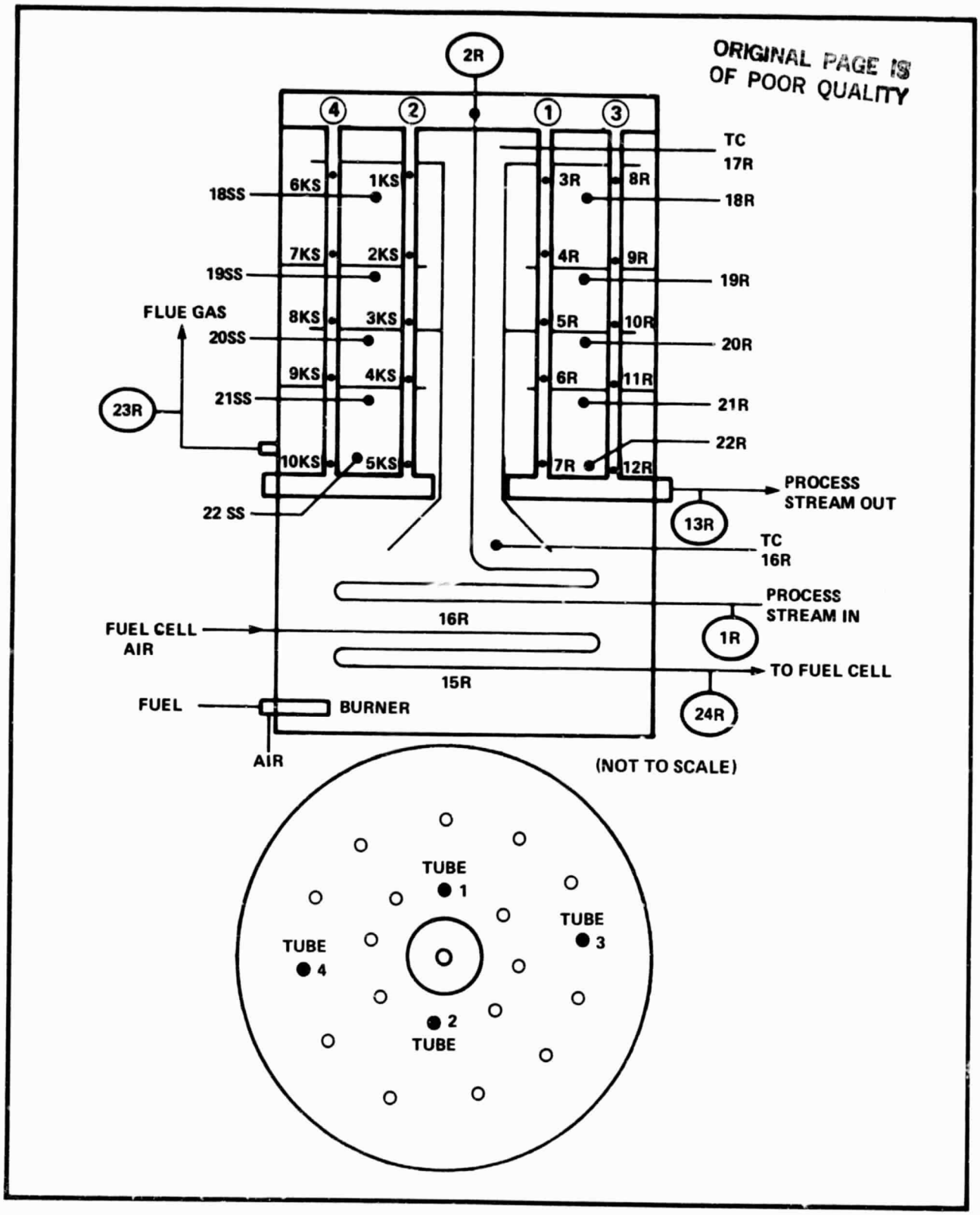

FIGURE XIII-3. THERMOCOUPLE LOCATION IN 5kW REFORMER

TABLE XIII-1
STEADY STATE RESULTS –
5kW FUEL PROCESSOR
RUN 10

- SIMULATED FULL LOAD
- INERT PACKING

Conditions: Burner Fuel: 40% H_2, 5% CO, 55% CO_2
Burner Fuel Flow: 85 SCFH
Burner Air Flow: 120 SCFH
Air to Preheat Coil: 900 SCFH
Process N_2: 120 SCFH

Temperatures (^oC)
(See Figure XIII-3 for TC locations)

Temp. Above Tubes (2R): 381^oC

Tube 1	Tube 3	Flue Gas	Tube 2	Tube 4	Flue Gas
3R:388	8R:363	18R:352	1KS:386	6KS:364	18SS:352
4R:371	9R:332	19R:341	2KS:366	7KS:334	19SS:352
5R:352	10R:327	20R:338	3KS:348	8KS:327	20SS:–
6R:357	11R:338	21R:338	4KS:350	9KS:343	21SS:341
7R:368	12R:346	22R:329	5KS:366	10KS:339	22SS:337

Process Stream Outlet (13R): 332
Flue Gas Outlet (23R): 332

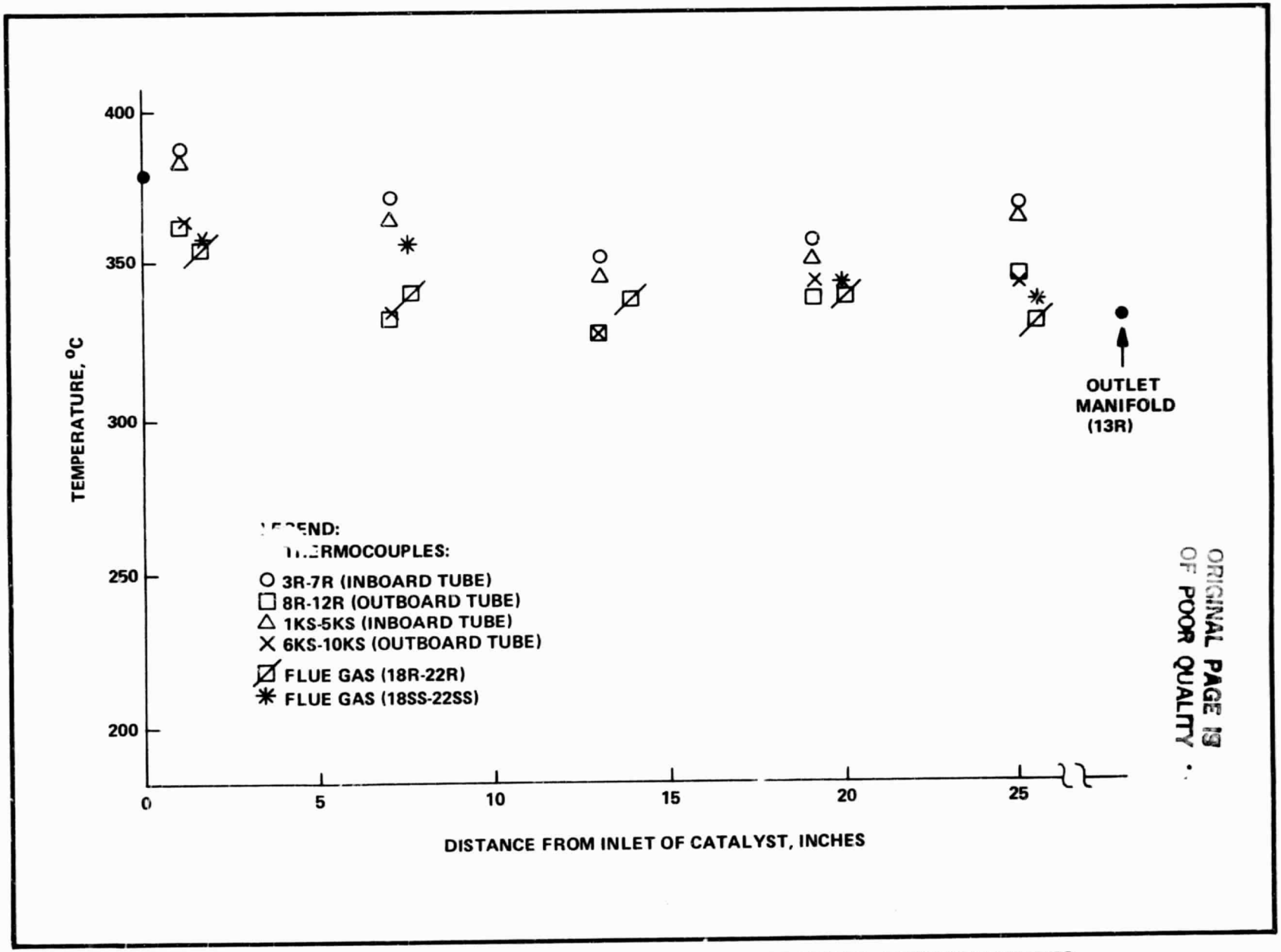

FIGURE XIII-4. TEMPERATURE PROFILE IN 5kW REFORMER, RUN WITH INERTS

After the inert runs, the reformer was charged with 5.885 kg of T2107RS (United Catalysts, Incorporated). These tablets were 5 mm dia. x 5 mm long and had a bulk density of 0.968 kg/liter. The T2107RS catalyst was slightly more dense than the ICI 52-1RS used in the previous reformer study. Table XIII-2 lists the results for one run conducted at full load using simulated fuel cell reactant air flow in the preheat coil. Essentially complete conversion was observed with an exit temperature of about 277°C (TC 13R). Figure XIII-5 shows the temperature profiles observed. Here again, the temperature rises near the bottom of the tubes, apparently because of heat conduction from the burner section. Several options are being considered to alleviate this characteristic since higher exit temperatures result in higher CO concentrations.

CONCLUSIONS

- The 5kW reformer provides essentially complete conversion of methanol at the design conditions.

- The design for the full-size (50kW) reformer should incorporate a modification that serves to thermally isolate the reformer catalyst from the combustion chamber.

TABLE XIII-2

STEADY STATE RESULTS – 5kW FUEL PROCESSOR RUN 5R

- FULL LOAD
- CATALYST: T2107RS

Conditions:	Burner Fuel Composition, Mole %:	H_2 : 40%
		CO : 5%
		CO_2 : 55%
	Burner Fuel Flow:	165 SCFH
	Burner Air Flow:	175 SCFH
	Fuel Cell Air Flow (Preheat Coil):	900 SCFH
	H_2O/CH_3OH Ratio, Molar:	1.3
	Feed Mixture Rates:	5.5 ℓ/hr

Temperatures, °C (280 Min. On Stream)

(See Figure XIII-3 for TC locations)

H_2O/MeOH Feed (1R): 88°C; Top, Above Tubes (2R): 360°C

Tube 1	Tube 3	Flue Gas	Tube 2	Tube 4	Flue Gas
3R:260	8R:266	18R:371	1KS:304	6KS:270	18SS:347
4R:221	9R:221	19R:263	2KS:238	7KS:232	19SS:297
5R:227	10R:204	20R:221	3KS:221	8KS:209	20SS:217
6R:238	11R:221	21R:243	4KS:232	9KS:214	21SS:238
7R:254	12R:243	22R:243	5KS:247	10KS:237	22SS:241

Process Stream Outlet (13R):	277
Flue Gas Outlet (23R):	249
Preheated Air Exit Temp. (24R):	177°C
Room Temp.:	23°C
Product Dry Gas Flow Rate:	8501 ℓ/hr
Product Dry Gas CO Concentration:	1.55%
Condensate Specific Gravity:	0.995 @ 8.5°C
Methanol Conversion:	~99.5%

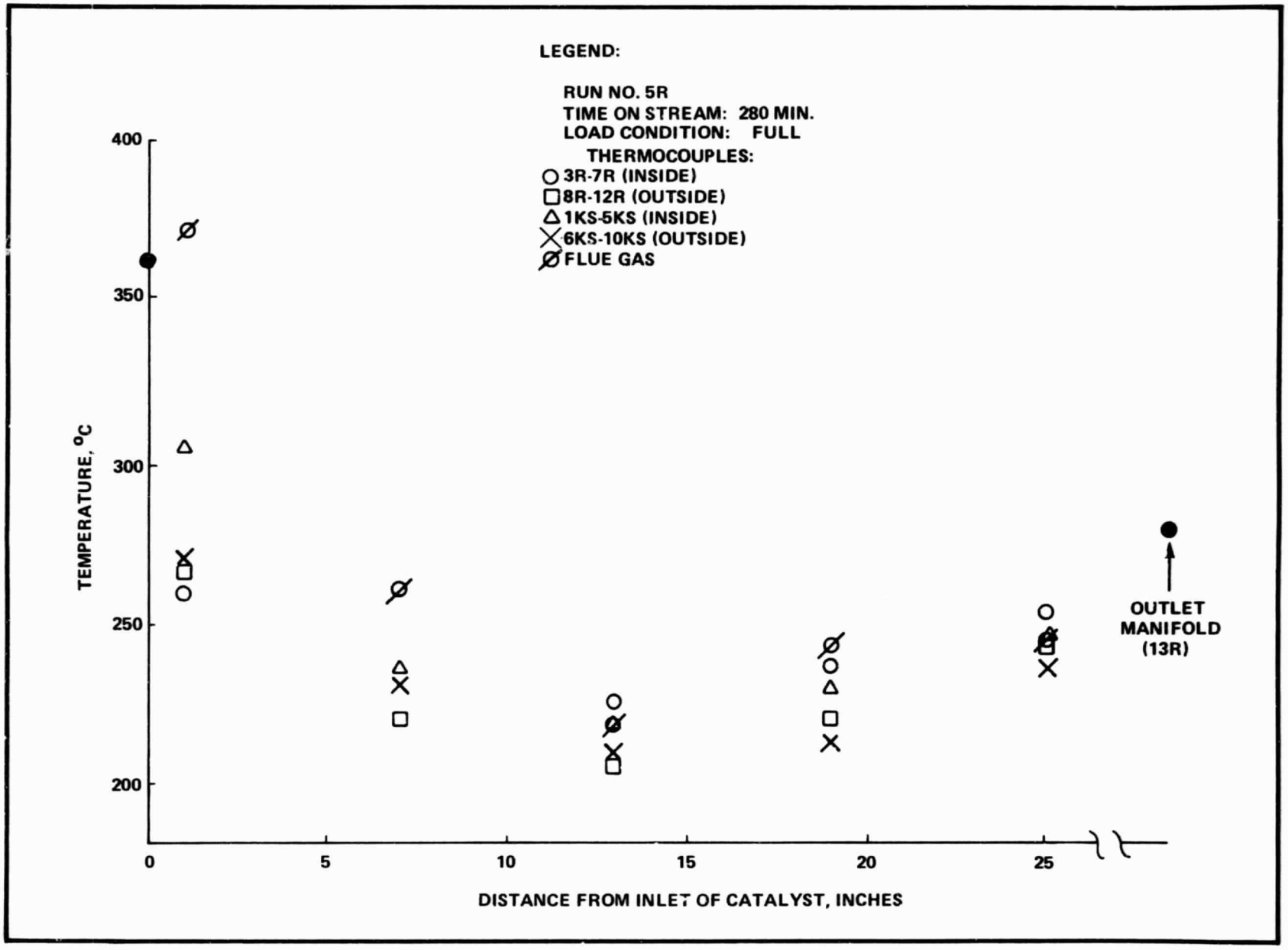

FIGURE XIII-5. TEMPERATURE PROFILE IN 5kW REFORMER

TASK III

INTEGRATED SYSTEM DESIGN AND DEVELOPMENT

Analysis of various integrated system configurations has been facilitated using a steady-state, integrated system computer program. This was prepared by Physical Science, Incorporated (PSI) under a subcontract and transferred to Engelhard's Computer Services Section. System electrical and heat utilization efficiencies and stack size were determined as a function of various parameters using this program. The energy distribution has been compared for different configurations to demonstrate how the system could be interfaced with an on-site heating, ventilation and air conditioning subsystem.

A power conditioning subsystem (DC to AC Inverter) has been acquired for the 5kW integrated system. The required control functions have been defined for the sequential (start-up and shutdown) and process (steady-state) system operations. More details about each of these items are provided in the following sections.

SECTION XIV

DESCRIPTION OF THE STEADY STATE INTEGRATED SYSTEM MODEL (PROVIDED BY PHYSICAL SCIENCES, INC.)

A. PURPOSE

Power plant systems analysis may be subdivided into steady-state design point, off design, and transient analysis. The PSI steady state design point systems analysis program is described. The purposes of this type of analysis are to:

1. Select and arrange powerplant components into a configuration which meets the powerplant performance goals at minimum cost, or maximum efficiency. In general, the technical feasibility of a powerplant is strongly dependent on the selection and arrangement of the components which together make a system.
2. Evaluate advanced concepts. A new technology concept may be considered advantageous if, and only if, it lowers the cost or improves the efficiency of the system as a whole. The steady-state design point systems analysis approach permits the quick evaluation of an advanced concept.
3. Evaluate the powerplant's response to changes in design or operating conditions. The sensitivity of a particular design to changes in operating conditions is an important consideration in selecting a powerplant configuration.
4. Define the operating conditions that a component will be subjected to during normal operation. Conversely, systems analysis may be used to determine how the malfunction of a component (e.g., a leaking valve or fouled heat exchanger) would affect the system. This may be particularly useful when received components do not meet performance specificati .

B. PROGRAM ELEMENTS

Since the number of components in a system may be large and the calculations required to analyze a single component may be considerable, the simulation of a system requires a computerized model. Moreover, in the optimization of a system, it is often necessary to perform interactive analyses over several components. The first few trial configurations seldom yield an optimum system. Hence, the simulation model must be easily modified to insert and remove components as required. For this reason a systems analysis program must be modular. Finally, a systems analyst using the code must be quickly made aware of how the analysis is progressing. This requires adequate output from the program at various points in the analysis. The systems analysis code must be interactive and graphic terminal displays are helpful. A more subtle effect is on the type of numerical analysis which is best employed, and this will be discussed under the section on operational modules. In summary, the requirements of the systems analysis code are that it be modular and interactive.

The PSI steady-state design point systems analysis code is comprised of a library of component modules, operational modules, and a main program which links these elements so as to simulate the operation of a powerplant operating at its steady state design point.

C. COMPONENT MODULES

A component is a subroutine which describes the output of a component in terms of its input. Components include fuel cells, reformers, turbines, compressors, etc; all of the major components normally found in a powerplant. Both inputs and outputs usually consist of a set of fluid characteristics like gas pressure, composition, temperature, enthalpy, and flow rates. In addition, component specific input/output may be defined. In the case of the fuel cell, this is comprised of current density, voltage and reactant utilization. Other components may have input/output parameters like shaft power, heat exchanger effectiveness, etc.

Each component module is connected to other modules by one or more nodes. The main program, in linking modules together will specify a node number for each of the component's nodes. The input node of one module is the output node of another module. The properties - temperature, pressure, enthalpy, and molar flow rates associated with each node - are stored in an array. By specifying the input and output nodes for a module, the main program tells the module where to obtain its input information and where to store its output. The Component Module Library section of this document lists the presently available component modules and their functions. If a component is not listed in the module library, one can be readily developed and added to the library.

D. OPERATIONAL MODULES

Operational modules are subroutines which perform various functions such as calculating thermodynamic properties, performing input/output functions, finding roots of equations, etc. Just as it is convenient to modularize components, it is equally convenient to modularize the housekeeping functions of the program. This also permits easy expansion of the program's capability to perform additional functions. The Operational Module Library section lists the presently available modules. As in the case of component modules, if an operational module function is not presently incorporated in the module library, one can be developed and added to the library.

A word should be mentioned concerning the operational module called "SECANT." This module finds the roots of equations using the secant method. When the equations describing a functional relationship are known, the Newton-Raphson method is often more expeditious. This method is, in fact, used in the "THERMO" module. In a systems analysis program, interactive analyses are often performed over several modules or over the entire system. The equations change from configuration to configuration. It is, therefore, impractical to use the Newton-Raphson method. In solving

large sets of equations it is often faster to use matrix solutions (e.g., Gauss-Seidel). This type of numerical analysis is being explored for the PSI program. However, in evaluating a new system, the analyst often chooses to optimize a dependent variable against an independent variable which is unrelated or weakly related ("stiff") to the dependent variable. A sequential systems analysis using SECANT quickly identifies these errors. Should this type of analyst error occur when using a matrix analysis, the error would yield a singular matrix. The result is no solution and no information as to where the error occurred. Matrix analysis is recommended for well defined systems but not for new, untried systems.

E. MAIN PROGRAM

The main program performs the following functions:

- Links the modules into a configuration simulating the power-plant configuration.

- Specifies the analysis order by defining which dependent variables are to be optimized against which independent variables and defining points in the program where these optimizations will occur.

- Calls for terminal displays of the status of an analysis. This may take the form of a graphic display of a numerical analysis or a screen print of the thermodynamic conditions at a node.

- Calls for the output printing of the node array or the system data.

- Defines the input value of various parameters not otherwise defined by the module.

The titles of the various modules are listed below:

THERMO	ACID FUEL CELL LIBRARY	DATABLOC
ATOMS	CATH	MFRAC
EQUIL	ANOD	BLWR
TOT	PERF	PUMP
ZERO	SPRNT	COND
SECANT	BURN	SGDIAG
SHIFT	SHICON	LABEL
EQUATE	HX MODULES	INDEX
ATR	GRAPHICS	FAN
COMP	LPRNT	DISCOPS
TURB	CH3OHR	
SPLT	VAPOR	
QBAL	BOIL	
MIX	SYSM	

F. CONCLUSIONS

- An integrated system computer model has been developed which provides for convenient and effective analysis of fuel cell systems at the steady-state design point.

- Further effort in the fuel cell system analysis area should focus on off-design and transient analysis.

SECTION XV
SYSTEM ELECTRICAL AND HEAT UTILIZATION EFFICIENCIES

The baseline system configuration being used for these studies is shown in Figure XV-1. Table XV-1 is a typical printout describing the various streams in the flow diagram. The node numbers correspond to streams as depicted in Figure XV-1.

The various parameters studied are listed below:

Parameter	Range
Inverter Efficiency	0.85-0.98
Oxygen Utilization Ratio	0.2-0.5
Water/Methanol Molar Feed Ratio	1.1-2.0
Fuel Cell Temperature	350-400°F
Ambient Air Temperature	35-105°F
Burner Excess Air	10%-40%
Hydrogen Utilization Ratio	0.7-0.85
Condenser Cooling Water Temperature	40-65°F
Burner Heat Loss	70%-30%

Many cases were run to determine the effect of these parameters on system electrical and thermal efficiencies. Representative results are listed in Table XV-2. These studies are particularly useful for sensitivity analysis.

In OS/IES Configuration #2 (See Figure XV-1), the heat is recovered in Stream 33 as hot water and in Stream 37 as warm water. In some systems this could be an ideal form of heat recovery. However, for other applications (e.g., where absorption air cooling is used) higher temperatures would be required. OS/IES Design #3 (Figure XV-2) shows a configuration where the combustion gas exhausted from the reformer is used to generate superheated 50 psig steam. The condensate return (from the HVAC subsystem) is vaporized using the fuel cell coolant loop prior to being superheated.

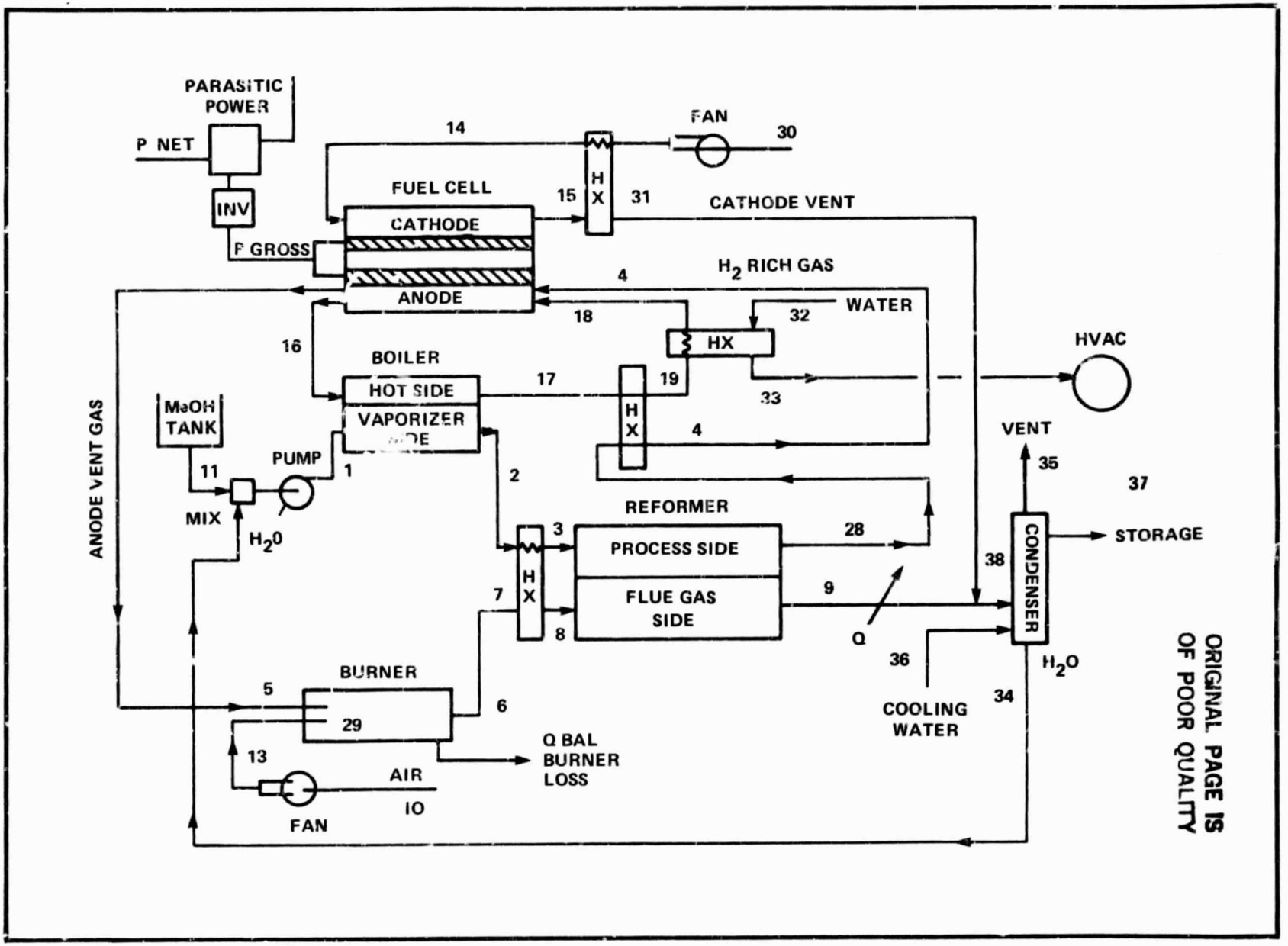

FIGURE XV-1. ON-SITE SYSTEM REFERENCE SCHEMATIC

TABLE XV-1

ON-SITE SYSTEM PROGRAM -- NODE PARAMETERS
(MOLAR FLOW RATES, LB-MOLE/HR)

NODE	H2	H2O	CH4	CO	CO2	O2	N2	FUEL	TOT	TEMP(DEGF)	ENTH(BTU/HR)	
1	0.0000	2.2429	0.0000	0.0000	0.0000	0.0000	0.0000	1.7253	3.9682	70.L	-424740.44	1
2	0.0000	2.2429	0.0000	0.0000	0.0000	0.0000	0.0000	1.7253	3.9682	280.	-345930.38	2
3	0.0000	2.2429	0.0000	0.0000	0.0000	0.0000	0.0000	1.7253	3.9682	720.	-326693.78	3
4	4.5986	0.7504	0.0000	0.2256	1.4825	0.0000	0.0000	0.0173	7.3843	375.	-296570.03	4
5	0.9797	0.7504	0.0000	0.2256	1.4825	0.0000	0.0000	0.0173	3.4655	375.	-318974.78	5
6	0.0000	1.8285	0.0000	0.0000	1.7081	0.1205	2.7288	0.0000	6.3858	1911.	-343263.63	6
7	0.0000	1.8285	0.0000	0.0000	1.7081	0.1205	2.7288	0.0000	6.3858	1911.	-343263.63	7
8	0.0000	1.8285	0.0000	0.0000	1.7081	0.1205	2.7288	0.0000	6.3858	1609.	-363098.44	8
9	0.0000	1.8285	0.0000	0.0000	1.7081	0.1205	2.7288	0.0000	6.3858	954.	-403731.13	9
10	0.0000	0.0983	0.0000	0.0000	0.0000	0.7232	2.7288	0.0000	3.5403	70.	4001.9114	10
11	0.0000	0.0000	0.0000	0.0000	0.0000	0.0000	0.0000	1.7253	1.7253	70.L	-160697.38	11
12	0.0000	0.0000	0.0000	0.0000	0.0000	0.0000	0.0000	0.0000	0.0000	0.	0.00000000	12
13	0.0000	0.0983	0.0000	0.0000	0.0000	0.7232	2.7288	0.0000	3.5403	70.	4001.9114	13
14	0.0000	0.5983	0.0000	0.0000	0.0000	4.8836	18.4839	0.0000	23.9808	275.	61523.645	14
15	0.0000	4.5172	0.0000	0.0000	0.0000	2.9392	18.4839	0.0000	25.9403	375.	-309523.78	15
16	0.0000	0.0000	0.0000	0.0000	0.0000	0.0000	0.0000	0.0000	65.0230	345.	0.00000000	16
17	0.0000	0.0000	0.0000	0.0000	0.0000	0.0000	0.0000	0.0000	65.0230	336.	0.00000000	17
18	0.0000	0.0000	0.0000	0.0000	0.0000	0.0000	0.0000	0.0000	65.0230	321.	0.00000000	18
19	0.0000	0.0000	0.0000	0.0000	0.0000	0.0000	0.0000	0.0000	65.0230	337.	0.00000000	19
20	0.0000	0.0000	0.0000	0.0000	0.0000	0.0000	0.0000	0.0000	61.5982	344.	0.00000000	20
21	0.0000	0.0000	0.0000	0.0000	0.0000	0.0000	0.0000	0.0000	61.5982	337.	0.00000000	21
22	0.0000	0.0000	0.0000	0.0000	0.0000	0.0000	0.0000	0.0000	.0000	0.	0.00000000	22
23	0.0000	1.8285	0.0000	0.0000	1.7081	0.1205	2.7288	0.0000	6.3858	1911.	-343263.63	23
24	0.0000	2.2429	0.0000	0.0000	0.0000	0.0000	0.0000	1.7253	3.9682	176.L	-414921.75	24
25	0.0000	2.2429	0.0000	0.0000	0.0000	0.0000	0.0000	1.7253	3.9682	176.	-350042.75	25
26	0.0000	0.0000	0.0000	0.0000	0.0000	0.0000	0.0000	0.0000	0.0000	0.	0.00000000	26
27	0.0000	2.2429	0.0000	0.0000	0.0000	0.0000	0.0000	1.7253	3.9682	280.	-345930.38	27
28	4.5986	0.7504	0.0000	0.2256	1.4825	0.0000	0.0000	0.0173	7.3843	565.	-285461.09	28
29	0.9797	0.7504	0.0000	0.2256	1.4825	0.7232	2.7288	0.0173	7.0057	237.	-314972.69	29
30	0.0000	0.5983	0.0000	0.0000	0.0000	4.8836	18.4839	0.0000	23.9808	70.	27108.020	30
31	0.0000	4.5172	0.0000	0.0000	0.0000	2.9392	18.4839	0.0000	25.9403	191.TV	-343993.78	31
32	0.0000	65.0230	0.0000	0.0000	0.0000	0.0000	0.0000	0.0000	65.0230	100.L	-7617666.0	32
33	0.0000	65.0230	0.0000	0.0000	0.0000	0.0000	0.0000	0.0000	65.0230	203.L	-7484639.5	33
34	0.0000	2.2429	0.0000	0.0000	0.0000	0.0000	0.0000	0.0000	2.2429	126.L	-261645.48	34
35	0.0000	4.1027	0.0000	0.0000	1.7081	3.0597	21.2127	0.0000	30.0832	126.	-585161.56	35
36	0.0000	96.9783	0.0000	0.0000	0.0000	0.0000	0.0000	0.0000	96.9783	40.L	-11470845.	36
37	0.0000	96.9783	0.0000	0.0000	0.0000	0.0000	0.0000	0.0000	96.9783	94.L	-11371764.	37
38	0.0000	6.3458	0.0000	0.0000	1.7081	3.0597	21.2127	0.0000	32.3261	367.	-747724.94	38

TABLE XV-2

PARAMETRIC STUDY FOR INTEGRATED SYSTEM – CONFIGURATION NO. 2
50 kW NET POWER

INPUT CONDITIONS			SYSTEM PERFORMANCE					
Case No.	Parameter Varied (1)	Value of Parameter	Gross Power (KW)	Recovered Heat (KW)	Current Density (ASF)	MeOH Consumption (Lb. Moles/ Hr)	Efficiencies (2)	
							EO	EO + Heat
1	Burner Loss	10%	57.2	100.7	168	1.7253	34.1	81.3
2	(Baseline Case)		57.2	96.6	169	1.7253	34.1	78.5
3	Cooling Water	50°F	57.2	101.8	169	1.7253	34.1	78.5
4	Cooling Water	60°F	57.2	107.1	169	1.7253	34.1	78.5
5	H_2 Utiliz.	0.7	57.1	109.3	173	1.9684	29.9	77.2
6	H_2 Utiliz.	0.75	57.1	101.6	171	1.8371	32.0	77.6
7	Burner Enrich.	1.1	57.2	96.5	169	1.7252	34.1	78.5
8	Burner Enrich.	1.4	57.2	96.7	169	1.7255	34.1	78.5
9	Air Temp.	35°F	57.2	95.0	169	1.7249	34.1	78.8
10	Air Temp.	105°F	57.2	97.7	169	1.7259	34.1	77.7
11	Cell Temp.	350°F	57.2	96.5	144	1.7252	34.1	78.5
12	Cell Temp.	400°F	57.2	96.6	191	1.7254	34.1	78.5
13	H_2O/C	1.1	57.2	99.5	162	1.7589	33.4	78.2
14	H_2O/C	1.5	57.1	94.3	173	1.7045	34.5	78.7
15	O_2Utiliz.	0.2	57.2	95.9	175	1.7270	34.0	76.8
16	O_2 Utiliz.	0.3	57.2	96.3	172	1.7253	34.1	77.9
17	O_2 Utiliz.	0.5	57.2	96.8	165	1.7256	34.1	78.8
18	Inverter Eff.	0.85	60.6	101.8	169	1.8283	32.1	76.4
19	Inverter Eff.	0.95	54.1	91.8	169	1.6319	36.0	80.1

(1) Baseline Conditions: Inverter efficiency = 0.9, O_2 utilization = 0.4, H_2O/C = 1.3, Cell temperature = 375°F, Air temperature = 70°F, Burner enrichment = 1.2, H_2 utilization = 0.8, Cooling water temperature = 40°F, Burner heat loss = 20%, Cell voltage = 0.6, Mechanical efficiency = 97%.

(2) EO = Overall electrical efficiency, EO + heat = Electrical plus heat recovery efficiency (based on lower heating value)

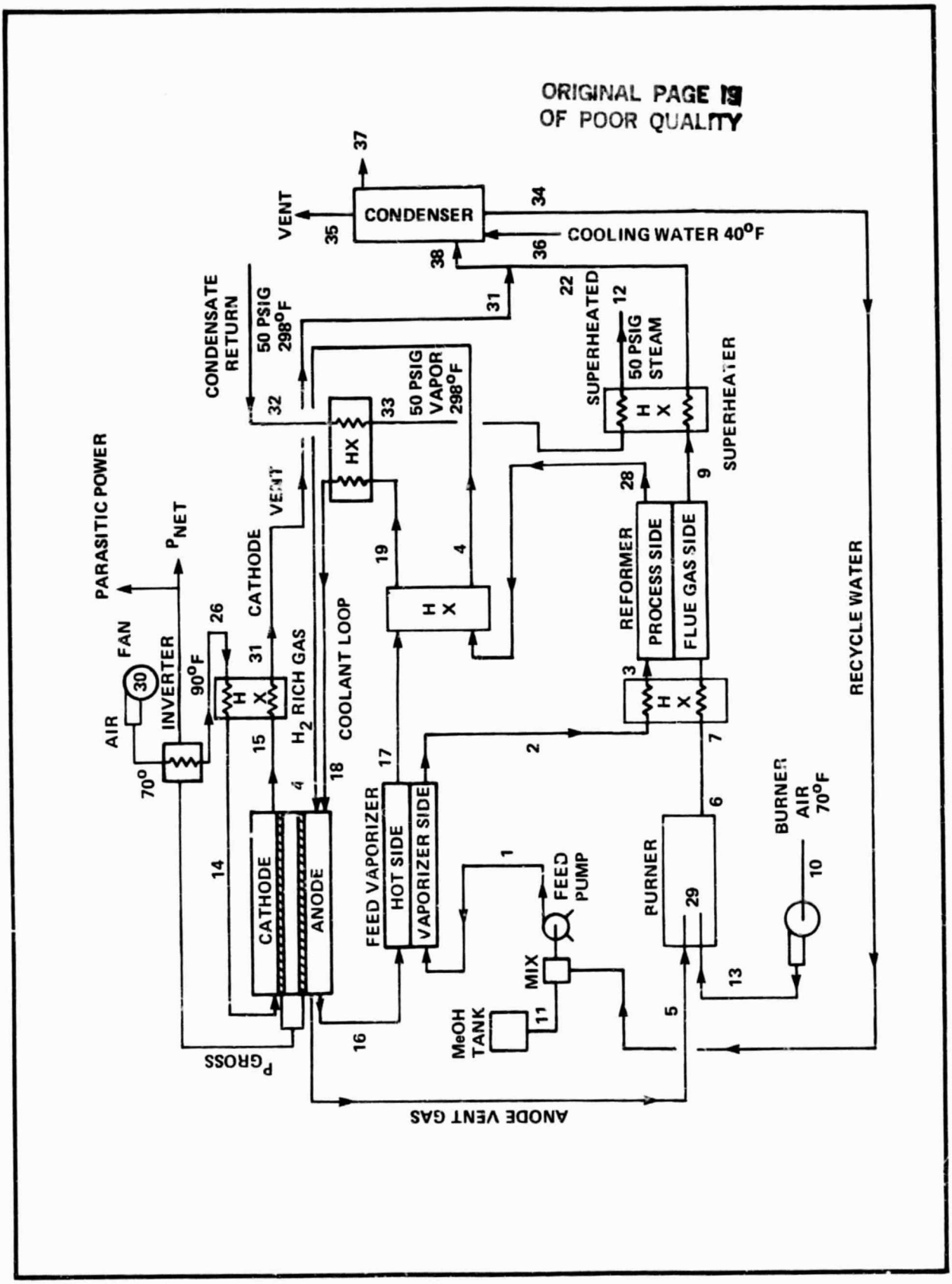

FIGURE XV-2. ON-SITE INTEGRATED ENERGY SYSTEM NO. 3

Alternatively, the total quantity of steam could be increased by producing saturated steam at 298°F (50 psig). Figure XV-3 shows the distribution of available energy for the three cases discussed. This illustrates the flexibility of the fuel cell system in providing heat of varying quality to interface with various heating, ventilating and air conditioning systems.

In association with the systems analysis and optimization activities, corresponding system costs were estimated using equipment cost estimation techniques from the chemical process industry. Costs were adjusted by the plant cost index as published in Chemical Engineer. The size of equipment for a 50kW unit is small compared to that commonly used in the chemical process industry but is large enough to be estimated. As an example, the cost of the first unit (adjusted to third quarter 1980) for Configuration #2 would be about $1600/kW (not including the stack). Obviously, this cost would be far lower for the "Nth" unit.

CONCLUSIONS

- The steady-state system model provides the basis for parametric optimization studies for on-site systems.

- The optimization of system configuration is strongly dependent on the characteristics of the specific on-site application.

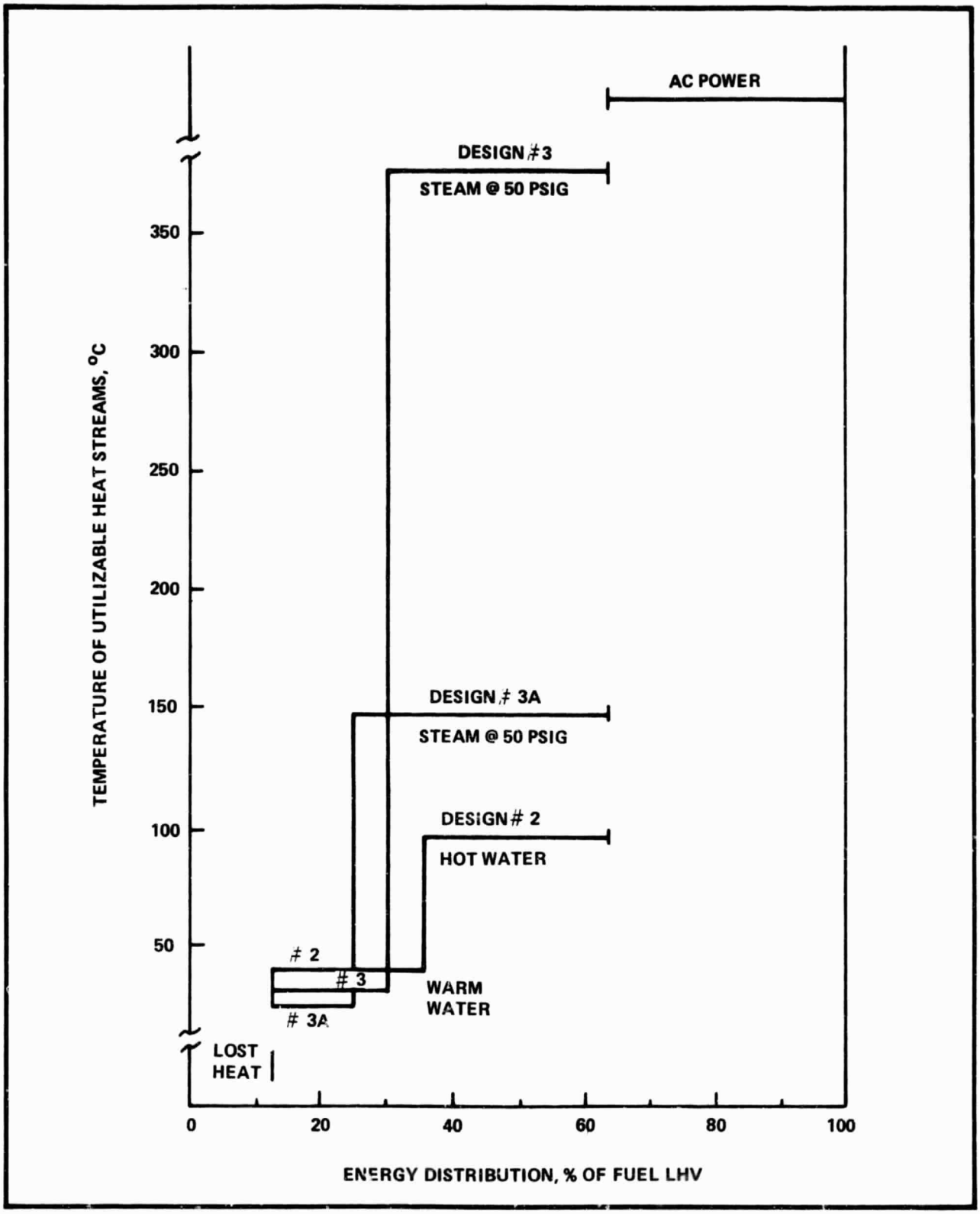

FIGURE XV-3. QUALITY OF UTILIZABLE HEAT FOR VARIOUS SYSTEM CONFIGURATIONS

SECTION XVI

POWER CONDITIONING SUB-SYSTEM

A power conditioner is required for most applications to convert the DC voltage of the fuel cell to AC voltage. Although the performance characteristics of a 5kW power conditioner could not be expected to approach those for the 50 KW unit, this equipment would provide the 5kW sub-scale system with many useful features; these include grid tie-in, load programming and AC load capability for demonstration purposes. Accordingly, specifications were established for the 5kW unit as follows:

Input Voltage Range	-	40-60 VDC
Output Voltage	-	277 VAC, 60 Hz, Single Phase
Output Power Range	-	0-5000W

Output Power to be Voltage Programmable
0-5VDC Signal to be Equivalent to 0-5kW

The Inverter to be capable of Stand-Alone
or Tie-Line Operation

The following Safety Features required:
Automatic Overload, including Short Circuit Protection
Automatic Resetting upon Overload Removal
Automatic Shutdown for Input Overvoltage
or Undervoltage

Most AC power sources for low and intermediate power levels consist of oscillators and solid state linear power amplifiers. They are inefficient, bulky, overweight, and limited in performance for overloads and extreme power factor loads.

The Abacus Controls AC power source takes advantage of modern digital technology and generates a sinewave by digital synthesis. A pulse pattern for a sinewave is stored on a memory integrated circuit for each of three phases over a 360° period. Voltage amplitude control is accomplished by increasing or decreasing the dwell time at zero volts in the stored pulse pattern. The pulse pattern has no harmonic of the fundamental frequency less than the eleventh, and the eleventh and higher harmonics are easily filtered in a simple LC filter.

By operating the power stage of the AC power source in a switching mode rather than as a linear amplifier, efficiency is improved from 35% to 90% in the output stage. By eliminating all of the low order harmonics digitally, no bulky filters are required, and a lightweight design results.

A current limit signal overrides the voltage feedback signal when an overload exists. The output can withstand a short circuit indefinitely. Upon removal of an overload, return to voltage regulated output is automatic. Because of switching mode operation without tuning filters, operation into zero lead or zero lag power factor loads does not damage or impair the operation of the AC power source.

Reliability results from low parts count, parameter derating, and low temperature rise. The digital sinewave synthesis design has these characteristics along with a history of satisfactory field performance.

Digital sinewave synthesis is the application of digital techniques to generate AC power from DC power. Switching power circuits, digital filtering, and three-phase pulse patterns stored on a memory IC result in high efficiency, reliability, and performance, with relatively low price, size, and weight.

Because of the fact that the 5kW sub-scale system is limited to a nominal 50-volt operating voltage, the efficiency of the 5kW power conditioner will be relatively low (70-80%). However, the power conditioner for the 50kW module will have a nominal input voltage of 200 volts and, hence, a much less significant IR-loss. This will result in power conditioning efficiencies in excess of 90%.

CONCLUSIONS

- Although the sub-scale (5kW) power conditioner is relatively inefficient (because of the low input voltage), it will be of considerable value in 5kW system testing due to its grid tie-in and load programming capabilities.

- The design characteristics of the 50kW system should allow power conditioner efficiency in excess of 90%.

SECTION XVII
SYSTEM CONTROL

A. CONTROL SUBSYSTEMS

The typical interrelationships of the components of an integrated fuel cell system are illustrated in the on-site system reference schematic of Figure XV-1. The sources of signals that can be used for control purposes are listed in Table XVII-1.

Optimum operation of this system requires a close and controlled interaction between three separate control subsystems that use these signals. Although each of these subsystems is described below, it is important to note that the overall control system can only be understood by the sometimes complex interaction of these subsystems. The subsystems include:

1. Sequential Control Subsystem

Start-up sequential control involves the sequencing of the following events during start-up of the system:

- Heating reformer and fuel cell
- Production of hydrogen by the reformer
- Generation of DC power by the fuel cell
- Conversion of DC power to AC power
- Application of power to a load

Shutdown sequential control basically sequences these events in a reverse order during shutdown of the system. The various steps are carried out interactively so as to avoid subjecting the stack to conditions that tend to cause corrosion.

2. Process Control Subsystem

Process control insures proper maintenance of the following operating parameters of the system during start-up, steady-state operation and shutdown:

- Reformer catalyst bed temperature
- Fuel cell stack temperature
- Reformer methanol/water fuel feed rate (As a function of fuel cell current draw)

TABLE XVII-1

SIGNAL SOURCES IN THE INTEGRATED SYSTEM

Symbol	Description	Function
TS1, TS2	Burner flame temperature sensors	Control
TS3	Reformer catalyst bed temperature	Process Control
TS4	Flue gas temperature	Readout only
TS5	Fuel cell stack low temperature	Start-up Control
TS6	Fuel cell stack high temperature	Process Control
TS7	Coolant temperature at start-up furnace inlet	Readout only
TS8	Coolant temperature at start-up furnace outlet	Readout only
TS9	Coolant temperature at stack inlet	Readout only
TS10	Coolant temperature at stack outlet	Readout only
TS11	Coolant temperature at fuel vaporizer inlet	Readout only
TS12	Coolant temperature at fuel vaporizer outlet	Readout only
TS13	Fuel vapor temperature at reformer inlet	Readout only
TS14	Reformate temperature at reformer outlet	Readout only
TS15	Reformate temperature at fuel cell inlet	Readout only
TS16	Anode gas temperature at fuel cell inlet	Readout only
TS17	Reformer combustion chamber temperature	Control
TS18	Reactant air temperature at reformer outlet	Readout only
TS19	Reactant air temperature at stack	Readout
TS20	Reformer flue gas temperature	Readout
TS21	Start-up furnace combustion chamber temperature	Control
TS22	Start-up furnace flue gas temperature	Readout
PS1	Pressure sensor in H_2 exit manifold	Readout
HS	Hydrogen leak detector in air exit manifold	Control
FS1	Combustion air flow switch	Control
FS2	Combustion air flow switch	Control
FS3	Coolant flow switch	Control
X1, X2	Igniters	Control
RV1, RV2	Relief valves	Control
S1, S2	Solenoid valves	Control
CV1, CV2, CV3	Check valves	Control

- Fuel cell reactant air flow control
  (As a function of reformer fuel feed flow)
- Fuel cell current output

3. Safety Interlock Subsystem

The safety interlock subsystem shuts down the system when any of the following conditions occur:

- Fuel cell stack temperature out of normal limits
- Reformer catalyst temperature out of normal limits
- Interruption in flow of heat transfer fluid
- Low methanol/water fuel supply
- Abnormal fuel cell voltage-current values
- Abnormal temperatures of burners

B. CONTROL HARDWARE

A Z80 microprocessor was selected for systems control. All hardware selected for use with the Z80 microprocessor is standardized for compatibility with the STD BUS concept conceived by Pro Log Corporation in 1972 and developed jointly with Mostek Corporation. Several companies now market STD BUS compatible hardware.

Included in the hardware purchases was a small keyboard and alphanumeric display unit which will be accessible to the operator of the fuel cell system. Commands to start and stop the system are made through this keyboard/display unit, and system messages can be read on this unit.

C. CONTROL SOFTWARE

Since all control system hardware was and is being purchased, design of the control system is software oriented. Engelhard has a Tektronix MDL80002A microprocessor development laboratory to support this software design effort.

Figure XVII-1 shows the general preliminary system block diagram for the software design. Sequential control is part of the start-up and shutdown blocks, process control occurs in the adjust parameters block, and safety interlocks are active in the malfunction check block. Four of the five required software routines for process control have been developed.

A block diagram for the reformer methanol/water feed rate control is shown in Figure XVII-2. The methanol/water feed rate for a given fuel cell output current is predetermined. A table of pump rate values is generated from these predetermined values and programmed into the read only memory (ROM) of the computer system. For a given current the microprocessor will look into a corresponding location in the ROM and output a control signal that will obtain the required pump feed rate. This same signal is scaled so that it will also control the speed of the blower that feeds reactant air to the fuel cell.

Figure XVII-3 shows the block diagram for temperature control for the fuel cell stack or reformer. Figures XVII-4 and XVII-5 show the block diagrams for burner turn-on and the burner ignition check. The burner turn-on is an example of sequence control and the ignition check routine is an example of a safety interlock routine. Additional work remains to be done in both these areas for 5kW integrated system operation early in Phase III.

D. CONCLUSIONS

- The use of a microprocessor-based control system in the 5kW integrated system will be of substantial value in the full-size system design effort.

- The control system design for the 5kW sub-scale system will be completed during the early stages of the Phase III effort.

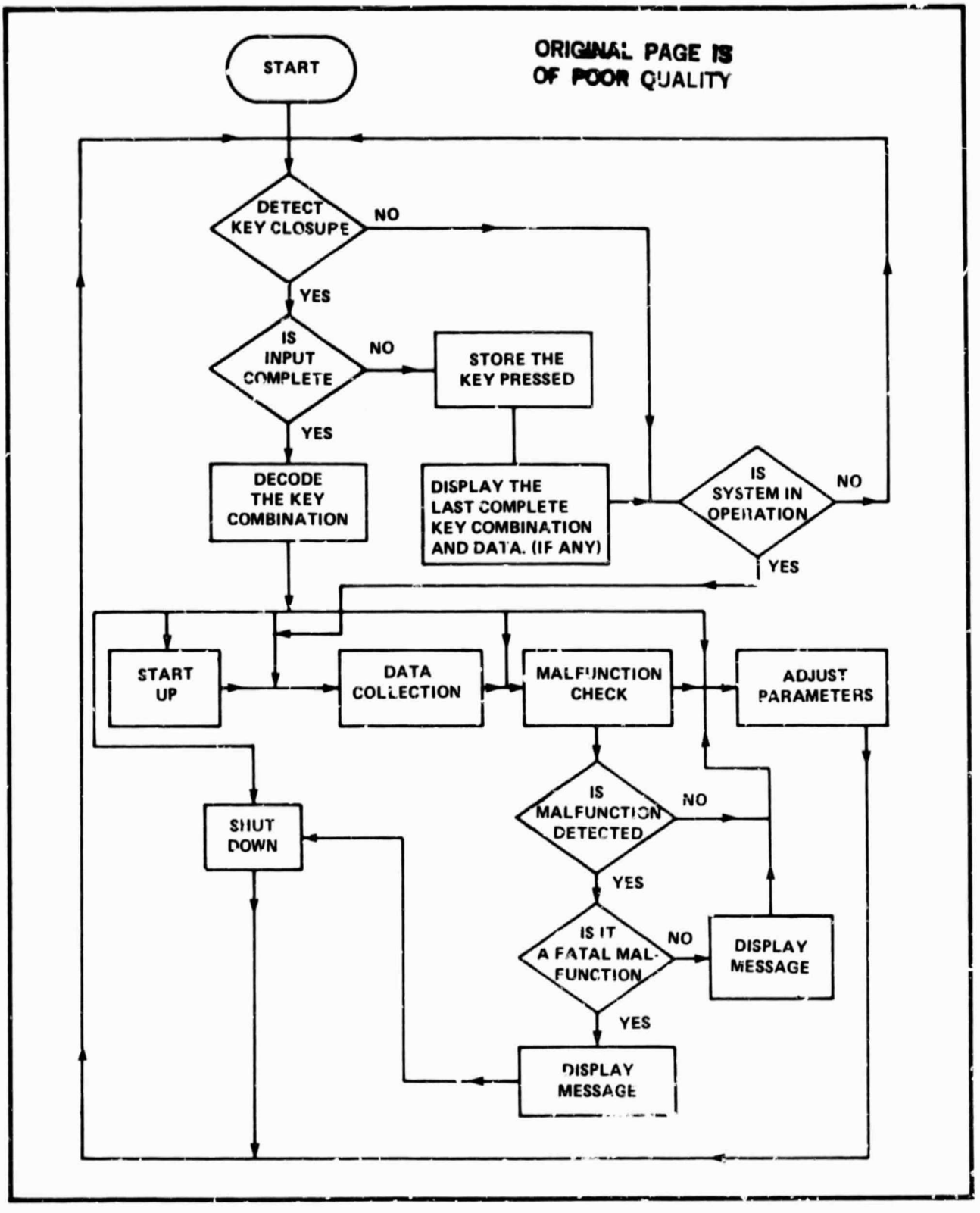

FIGURE XVII-1. CONTROL SYSTEM BLOCK DIAGRAM

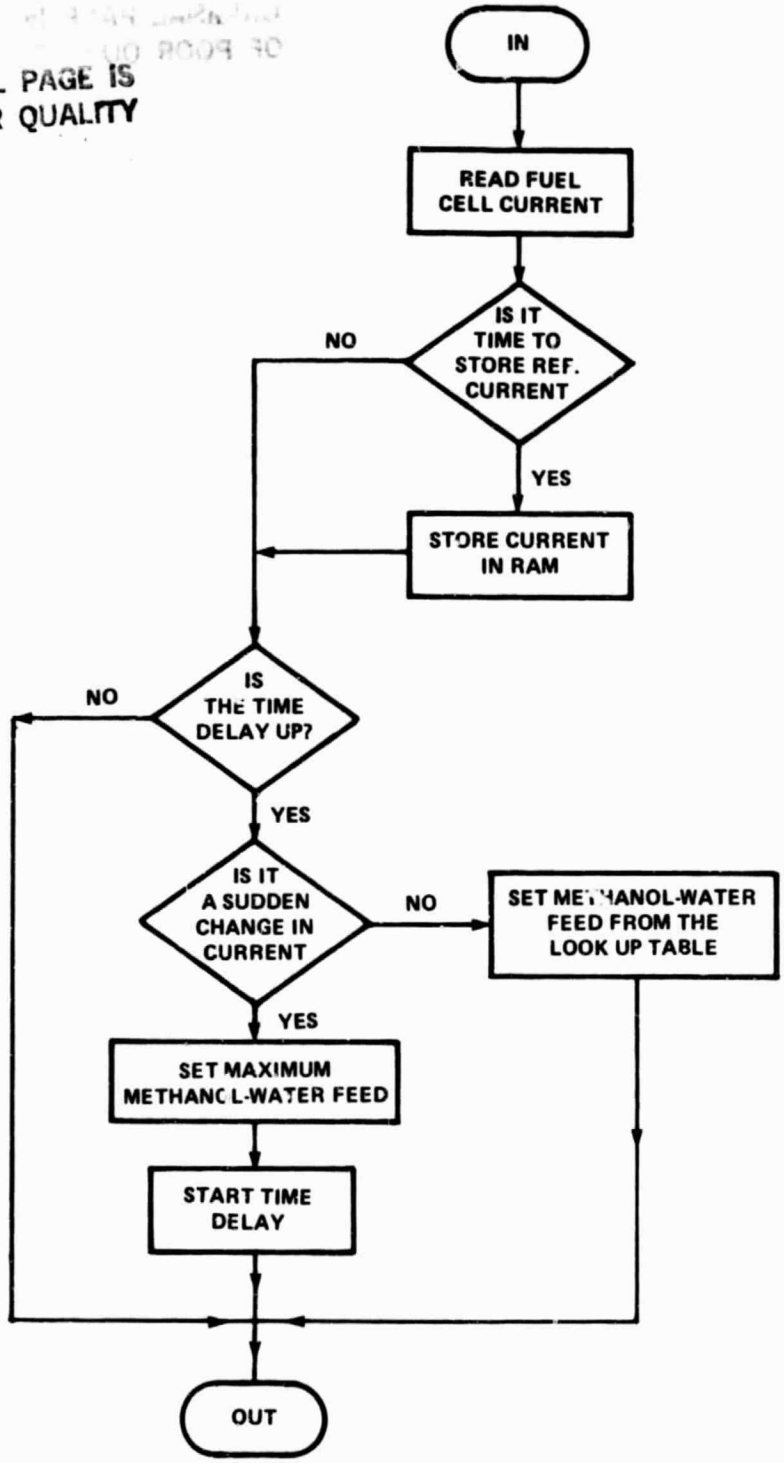

FIGURE XVII-2. METHANOL-WATER FEED REGULATION ROUTINE

C-3

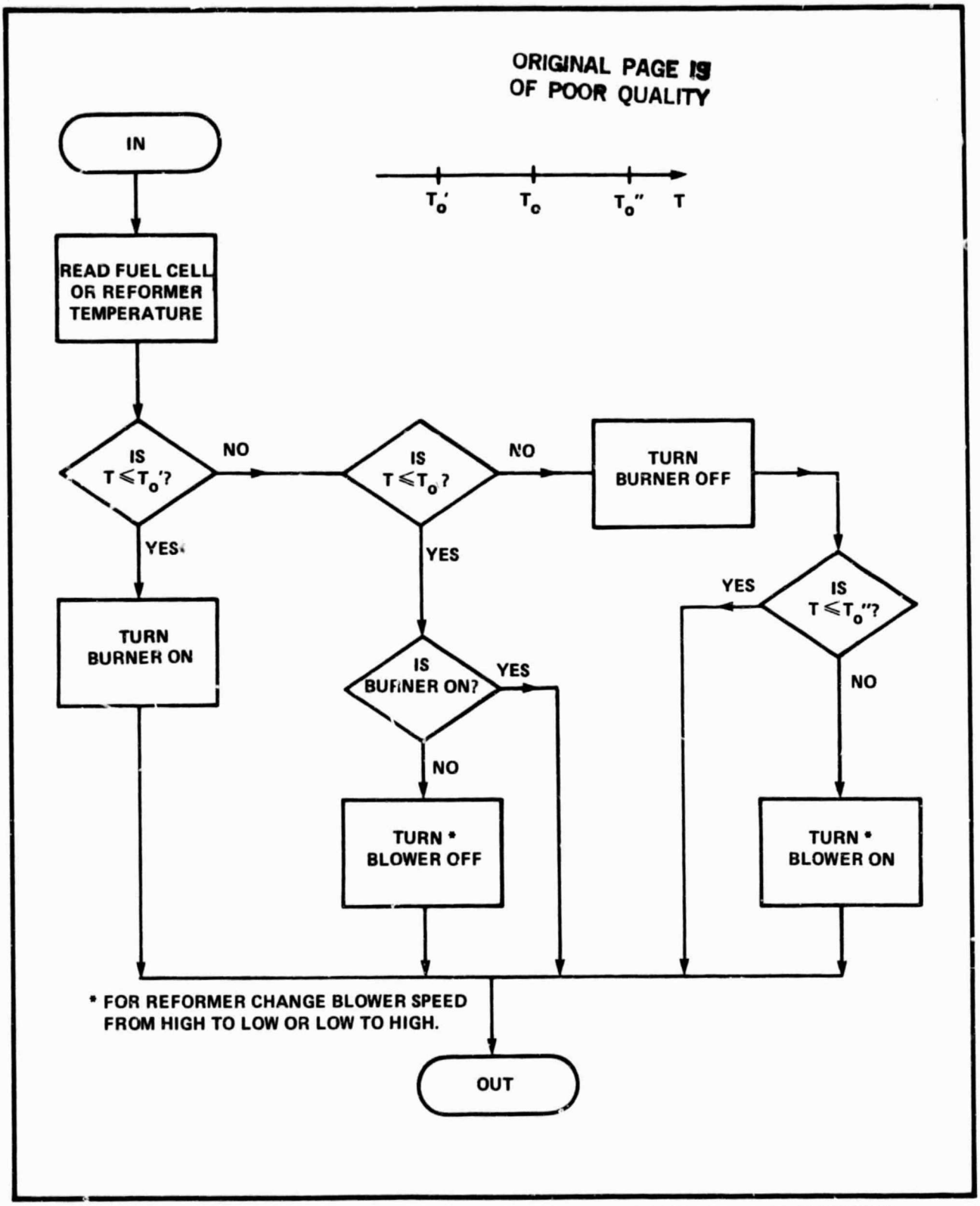

FIGURE XVII-3. FUEL CELL OR REFORMER TEMPERATURE CONTROL ROUTINE

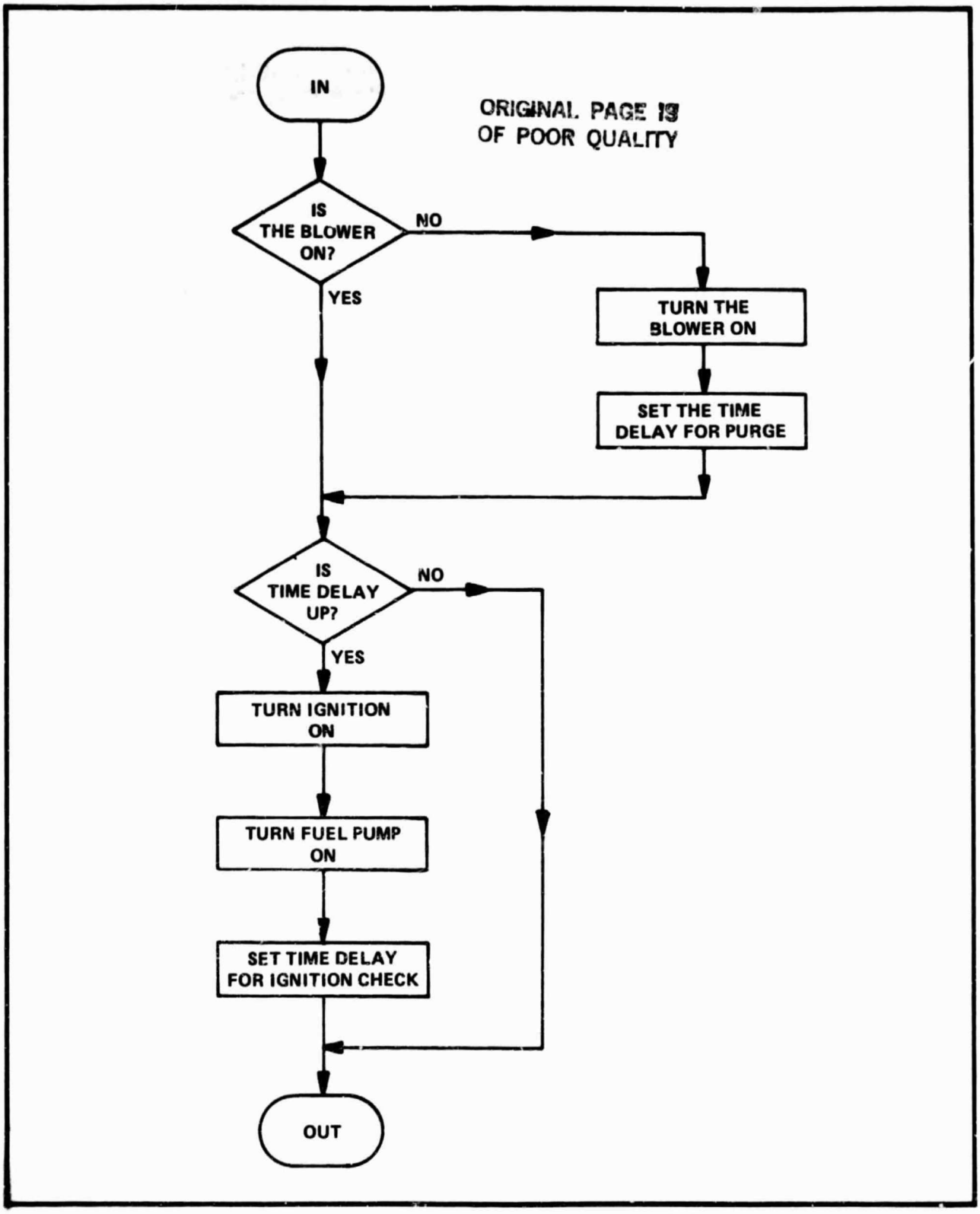

FIGURE XVII-4. BURNER TURN-ON ROUTINE

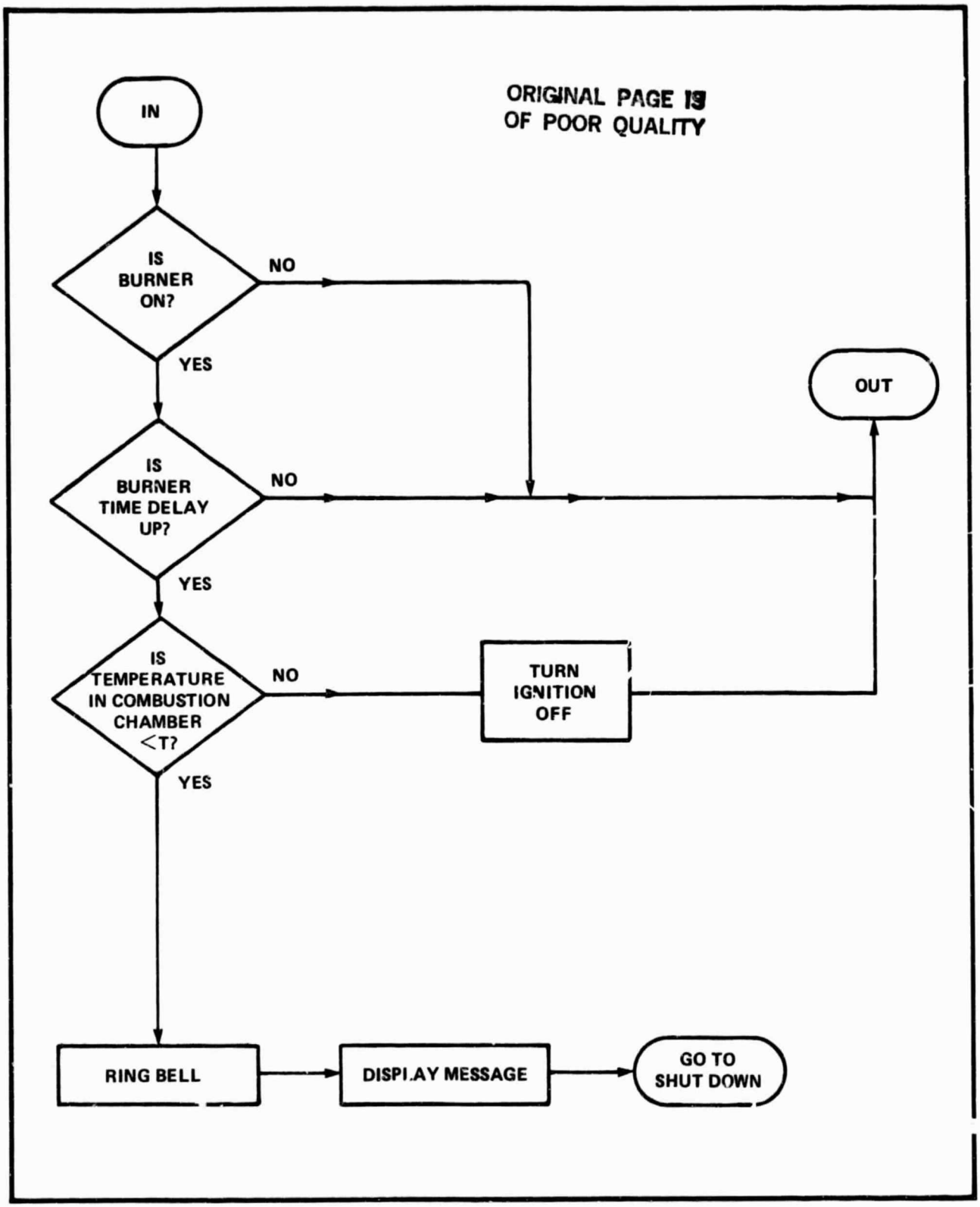

FIGURE XVII-5. IGNITION (BURNER) CHECK ROUTINE

TASK IV

LARGE STACK DESIGN AND DEVELOPMENT

The objective of this task was to prepare for the 25kW stack modules that will be developed and tested under Phase III. The main activities were stack component scale-up and preliminary large stack design. Highlights of this effort are as follows:

- Scale-up of electrodes to 13-inch x 22-inch size
- Scale-up of laminated matrix to 13-inch x 22-inch size by two candidate methods
- Successful single-cell testing of sections of scaled-up electrodes and matrix elements
- Application of scaled-up matrix elements using automated equipment
- Preliminary design of 25kW stack

These areas are discussed further in the following sections.

SECTION XVIII

PHOSPHORIC ACID STACK COMPONENT SCALE-UP

A scaled-up cell size of 13-inches x 22-inches was selected for the 25kW stack module that will be developed in Phase III. Two such stacks will be incorporated into the 50kW breadboard on-site system (see Section XIX, below).

A. ELECTRODES

The electrodes were scaled-up to the 13-inch x 22-inch size using the same constituents as in the nominal one square foot electrodes of Task I. Substrates were of the non-woven carbon paper type (Stackpole), and wetproofing methods followed Engelhard (immersion-type) techniques, as before, except that larger apparatus was required. These carbon paper substrates are currently purchased in relatively small quantities for about $1.50 per square foot. High volume production price estimates are not yet available from the manufacturer, but cost reduction by about a factor of two would be required to be consistent with electrode cost goals. Other electrode materials and the processing procedures are projected to be within cost guidelines (see Task I).

Deposition of the catalyst layer onto the scaled-up substrate was similarly accomplished according to Engelhard developed techniques with larger apparatus being used. Despite the relatively fragile nature of the substrate, handling of finished electrodes in the large size proved to be no problem.

B. MATRIX

Matrix elements were laminated onto finished electrodes initially by manual techniques. This involved both blade-coating and screen-printing as in Task I, but with larger equipment. No problems were encountered in this scale-up effort.

In light of the successful lamination of matrix elements onto 13-inch x 22-inch electrodes, attention was focused on automated equipment for this operation. A machine capable of automatic operation with substrates as large as 24-inches x 30-inches was acquired. This equipment was suitable for both blade-coating and screen-printing processes. Suitable procedures were developed for lamination onto 13-inch x 22-inch electrodes by both processes.

Matrix preparation studies indicated that the materials and projected labor costs would be consistent with the matrix cost goals of Task I (see above). This pertains to processing by either the blade-coating or screen-printing method. The blade-coating method has a somewhat lower projected labor cost provided that a simple electrode hold-down technique be perfected.

C. EVALUATION OF SCALED-UP ELECTRODES AND MATRIX ELEMENTS

Sections of scaled-up (13-inch x 22-inch) electrodes with matrix elements laminated onto them (by automated blade-coating methods) were evaluated through testing in 3-inch x 3-inch single cells. These tests, which took place early in Phase III, exhibited voltage levels at 150 A/ft^2 that were at least equivalent to the average performance of cells of the nominal one square foot size. The voltages of cells from six randomly selected sections were within a band of 20 mV from lowest to highest. (The results of these tests will be detailed in the first quarterly report under NASA Contract DEN3-241.)

D. BIPOLAR PLATES

The 13-inch x 22-inch bipolar plates will be fabricated under Phase III. CVD upgraded needled-felt will be used as the A-element, either with a resin/CVD-treated woven fabric B-element or in a new, unitized ABA configuration. The width of the continuous CVD-coating apparatus at Pfizer can accommodate the A-elements and B-elements of 13-inch width. Hence, no problems are expected in the scale-up of these elements from the 10.7-inch x 14-inch size to 13-inches x 22-inches.

Cost estimates by Pfizer for fabricating CVD-upgraded needled-felt A-elements in the 13-inch x 22-inch size using the continuous CVD process are in the $1.00 to $1.25 per square foot range (1977 dollars). This is marginally acceptable in terms of meeting the bipolar plate cost goals of Task I, considering the cost of the B-element, bonding, and final processing.

E. COOLING PLATES

The cooling plates will also be fabricated in the 13-inch x 22-inch size during Phase III. It is anticipated that these will be comprised of stamped aluminum forms and brazing sheets. The brazing operation would have to be optimized for low cost, but the larger size should pose no problems in that regard. The materials costs for cooling plate construction, including elements for interface corrosion protection, appear to be reasonably low with respect to the cost goals of Task I.

F. CONCLUSIONS

- Scaled-up (13 inch x 22 inch) electrodes and matrix elements demonstrate performance characteristics equivalent to those of their nominal one square-foot counterparts.

- Projected high-volume production costs for stack components are consistent with the goals established at the outset of the contract.

SECTION XIX

LARGE STACK DESIGN

Design effort was initiated during Phase II toward a stack module for the on-site integrated energy system breadboard that will be developed in Phase III. A 50kW integrated system size was selected, with the fuel cell subsystem to consist of two 25kW stack modules. Each 25kW stack will include 150 cells with an overall area of 13-inches x 22-inches. The design voltage is 0.63 volts per cell at a current density of 150 A/ft^2.

The preliminary design features of the 25kW stack are illustrated in Figures XIX-1 and XIX-2. The design for the reactant manifolds deviates from that of 5kW Stack No. 2 in that the hydrogen and air manifolds are independently sealed. This serves to prevent intermixing of fuel and air within the manifolds in the event of leakage at one of the vertical hydrogen manifold seals. Although a butt-seal is indicated for the vertical hydrogen manifold seal in Figure XIX-1, the independently sealed manifold arrangement does not preclude the use of a corner seal.

This design also provides for the coolant to be manifolded external to the reactant manifolds, as shown in Figure XIX-1. (If a hydrogen manifold corner seal were to be used, the coolant inlet and exit ports would have to be modified somewhat.) This approach has the advantage of minimizing the risks associated with coolant leakage, while allowing a relatively simple design for reactant and coolant manifolds. Figure XIX-1 also illustrates the simple, gusset-type reactant manifold hold down arrangement.

The stack compressive loading design features impact bars mounted on the end plates and deformable hold-down bars, as shown in Figure XIX-2. This computer aided design was found to be amenable to light weight and low cost. It is seen that the stack profile will be improved by eliminating the stack-compression springs and instead using the spring action of the hold-down bars to provide stack follow-up.

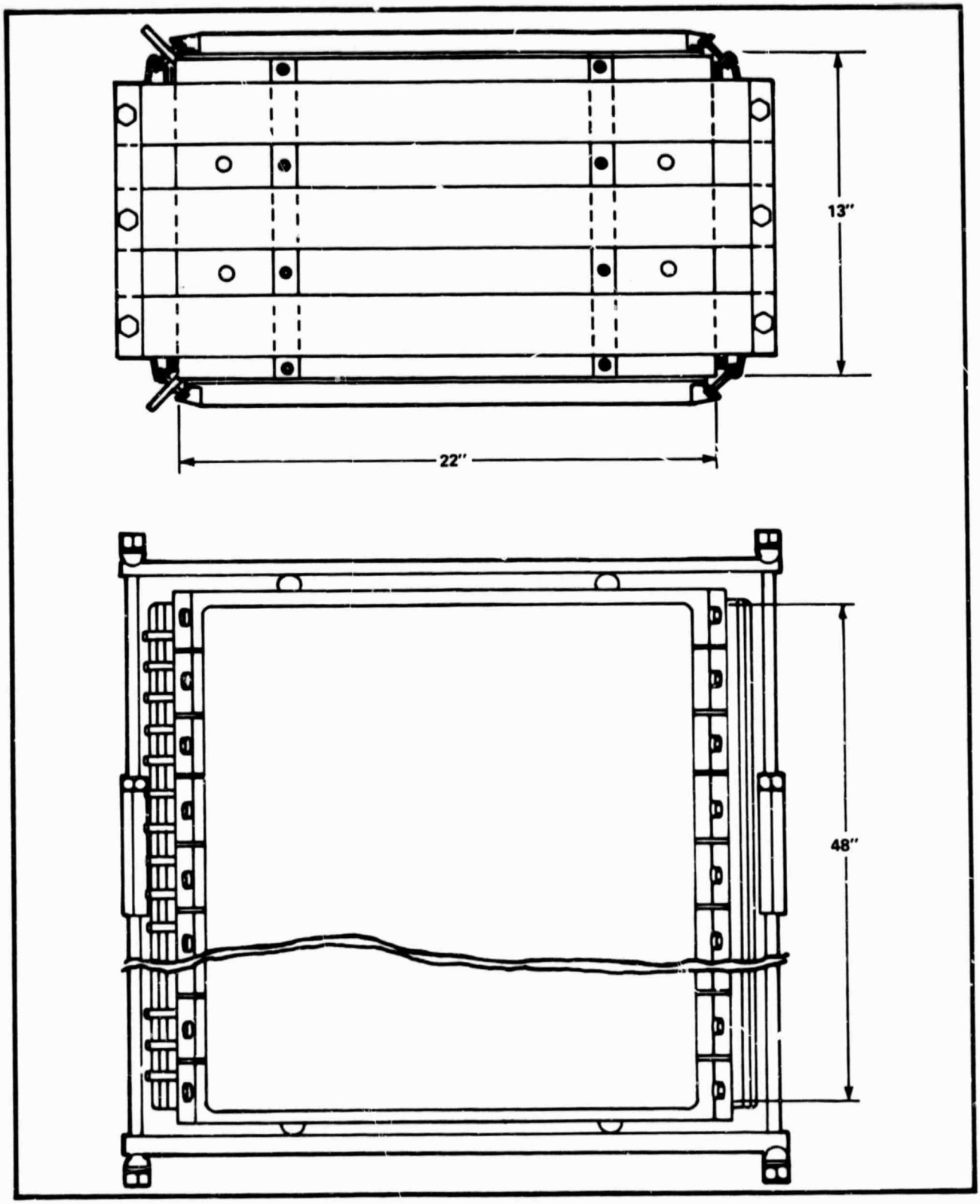

FIGURE XIX-1. 25kW FUEL CELL STACK

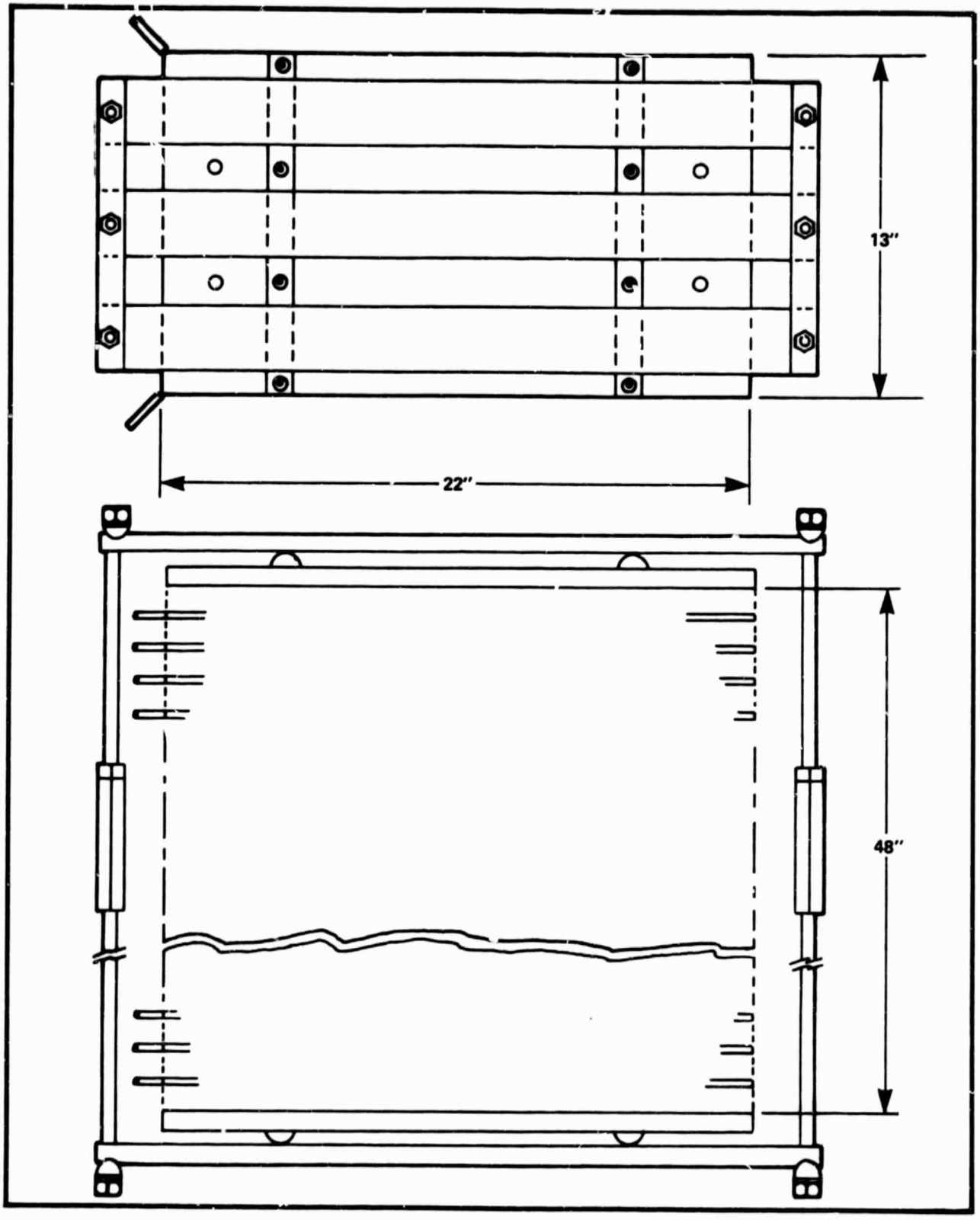

FIGURE XIX-2. 25kW FUEL CELL STACK (MANIFOLDS REMOVED)

The hold-down bars are oriented parallel to the hydrogen flow direction. This results in a shape that is suitable for modular grouping of stacks. Also, by leaving the relatively large air inlet and exit sections unencumbered, it provides attractive locations for the implementation and maintenance of an acid-management system.

CONCLUSIONS

- The design concepts for the 25kW stack that will be constructed during Phase III have been established.
- The 25kW stack design concepts are amenable to low cost.